IN-PROCESS QUALITY ANALYSIS OF LASER CUTTING

by

Zheng HongYu

BEng. (Mechanical Engineering)

Feburary, 1990

A thesis submitted for the degree of Doctor of Philosophy
of the University of London and for the Diploma of the
Imperial College of Science, Technology and Medicine

Robotics Centre
Imperial College
University of London
London SW7 2AZ
United Kingdom

Laser Laborotary
Dept. of Mechanical Eng.,
University of Liverpool
Liverpool L69 3BX
United Kingdom

BIBL.
LONDIN.
UNIV.

To:

My dear wife - Yong Ling

ABSTRACT

Laser cutting is today the most widespread industrial laser application. With its increasing use in high volume production and precise cutting processes, the need for adaptive control of the process becomes necessary to achieve optimum cutting speed, precision and high cut quality, since these often result in major savings both in processing time and in finishing operations. As the most important stage for achieving adaptive laser cutting process control, in-process monitoring of the cutting process constitutes the essential part of this project.

A review of the laser cutting process, with particular relevance to metal cutting, is presented together with a discussion of the process mechanisms and factors affecting laser cut quality. A review of state of art techniques for in-process monitoring of the cutting process and, in particular techniques for in-process quality analysis, is also given.

An automatic nozzle-beam alignment system for initial set-up is presented in chapter two. Being accurate and easy to operate, this technique could greatly assist precision laser cutting.

A new approach to the improvement of laser cut quality is reported in chapter three. This involves the use of gas mixtures instead of the usual pure gas (oxygen or inert gas) as the cutting assistant gas. Results are presented of cutting mild steel with pure oxygen, O_2/Ar, O_2/N_2 and O_2/He mixtures. Discussions on choosing optimal cutting gas composition are made.

Two distinctive arrangements based on optical detection are described in chapter four. The first uses a photodiode for off-axial detection of light emitted from the melt pool. The second method is axial detection of the light emission from the process with the aid of fibre optics. High speed filming of the process was performed at the same time to understand the dynamic behaviour of the melt pool. The second technique is believed to open a new route leading to an industrial on-line quality analysis system.

Acoustic methods for in-process monitoring of the cutting process are presented in chapter five. Two piezo-electric acoustic transducers are used to detect the acoustic stress waves generated during the processing. One transducer was put at the back of the last mirror, the other was located close to the nozzle assembly.

A technique for the in-process measurement of the cutting nozzle temperature by using thermocouples is presented in chapter six.

A novel design of a kerf scanning system for laser cut quality control is presented in chapter seven. This device is shown to be indicative of kerf width variations.

The possibility of developing an on-line control system of the laser cutting process is discussed in chapter eight.

Finally, conclusions and future work are outlined in chapter 9.

ACKNOWLEDGEMENT

I would like to give my thanks to my supervisors : **Prof. W. M. Steen, Dr. D. J. Brookfield** (Liverpool University) and **Dr. R. Hibberd** (Imperial College of London University) for their brilliant supervisions, guidance and encouragement throughout the course.

Thanks go to the present and past members of the laser group for their help and discussions:

Members at the Liverpool University :

Dr. Lin Li, Mr. Steve Plant (technician), Mrs. Heather Garnett (secretory), Mr.Jack Frith (technician), Mr. Bill W. O'Neil, Dr. S. Shah, Mr. Rehan Akhter, Miss Fiona Fellowes, Miss Sarah Sharkey, Mrs. Zhu Liu, Miss Nickii McKeown, Mr. Geoff Shannon, Mr. Qi Ning, Mr. Xiao-Liang Chen, Mr. Zhen-Yuan Zheng, Mrs. Yong Ling Wu and Miss M. M. Tan (a third-year student) .

Members at Imperial College:

Dr. Jack Gabzdyl, Mr. Russel Stracey, Mr. Nigel Willmott, Dr. Zhen-Da Chen, Mr. Jafar, Mr. G. Abbas, Mr. J. Mohanmud, Mr. Sayer and Dr. John Kamalu.

Thanks also go to the following organisations for their financial support:

The Chinese Government, The British Council and The British Oxygen Company .

My parents, brother and sisters deserve my thanks for their understanding and encouragement.

My wife, Yong Ling, deserves my very special thanks for her love, care and encouragement, which made this work possible and worthwhile.

TABLE OF CONTENTS

ABSTRACT	i
ACKNOWLEDGEMENTS	iii
TABLE OF CONTENTS	iv
LIST OF FIGURES	xi
LIST OF TABLES	xvii
GENERAL INTRODUCTION	xviii

CHAPTER ONE

LITERATURE SURVEY

1.1. Physical Mechanisms and Theories	1
1.1.1. Basic phenomena in laser cutting	1
1.1.1.1. Interactions between beam and workpiece	1
1.1.1.2. Description of the laser gas cutting process	2
1.1.2. Dynamic behaviour in laser cutting	3
1.1.2.1. Sideways burning theory	3
1.1.2.2. Mass and temperature oscillations of the molten layer	4
1.1.2.3. Oscillation of the molten layer thickness	5
1.2. Laser Cutting Performance	6
1.2.1. Quality of a laser cut	7
1.2.2. Factors affecting the cutting performance	7
1.2.2.1. Laser parameters	7
1.2.2.2. Gas flow parameters	15
1.2.2.3. Material parameters	16
1.2.2.4. Workstation parameters	19
1.2.2.4.1. Effects of cutting speed on surface roughness	20
1.2.2.4.2. Effects of cutting speed kerf width	22
1.2.2.4.3. Effects of cutting speed on dross formation	23
1.2.2.4.4. Effects of cutting speed on the extent of heat affected zone	25

1.3. Gas Composition Effects on Laser Cutting 25

1.4. Automatic Beam Alignment Techniques 28

1.4.1. Mirror alignment 28
1.4.2. Nozzle alignment 29

1.5. Monitoring of Laser Cutting Process 31

1.5.1. Monitoring of beam characteristics 32
1.5.1.1. Off-line techniques 32
1.5.1.2. On-line techniques 33
1.5.2. Monitoring of workstation characteristics 41
1.5.3. State of art work on in-process cut quality sensing and control 42
1.5.3.1. Monitoring of the shower of sparks 42
1.5.3.2. Monitoring of laser beam reflections 44
1.5.3.3. Thermal detection of the cut front temperature 45
1.5.3.4. Direct observation of the geometry of the cut kerf 46
1.5.3.5. Monitoring of light emission from the cut front 47

1.6. Conclusions 48

CHAPTER TWO

AUTOMATIC NOZZLE-ALIGNMENT SYSTEM FOR INITIAL SET-UP

2.1. Background and Principle 50

2.2. System Design 51

2.2.1. Hot nozzle development 54
2.2.2. Development of the X-Y stage 56
2.2.3. Selection of drives 57

2.3. System Control 61

2.3.1. Hardware construction 61
2.3.2. Software development 63

2.4. Experimental Procedures and Results 66

2.4.1. Experimental procedures 67
2.4.2. Results and discussion 67
2.4.2.1. Hot nozzle detection 67
2.4.2.2. Off-line test of the automatic nozzle alignment system 71

2.5. Chapter Summary 73

CHAPTER THREE

EFFECTS OF GAS COMPOSITION ON LASER CUTTING PERFORMANCE

3.1. Introduction and Background 74

3.1.1. Heat balance on the cut front 74
3.1.2. Drag effect on the cut front 80

3.2. Experimental Procedures 82

3.2.1. Laser apparatus and equipment 83
3.2.2. Experimental set-up 83

3.3. Results and Discussion 85

3.3.1. Influences of cutting speed and gas composition on kerf width 86
3.3.2. Gas effects on dross clinging problem 95
3.3.2.1. Results at a fixed cutting speed 95
3.3.2.2. Results at the maximum cutting speed 98
3.3.3. Effects of gas composition on cutting speed 100
3.3.4. Optimum speed range as a function of gas composition 101

3.4. Chapter Summary 104

CHAPTER FOUR

OPTICAL METHODS FOR IN-PROCESS MONITORING OF LASER CUTTING PROCESS

4.1. Introduction and Background 105

4.2. Apparatus and Equipment 110

4.3. Off-axis Monitoring of the Cut Face 112

4.3.1. Experimental set-up 112
4.3.2. Results and discussion 115
4.3.2.1. Factors affecting the detected signal strength and stability 115
4.3.2.1.1.Effect of cutting speed 115
4.3.2.1.2.Effect of gas flow on signal strength and stability 124
4.3.2.2. Signal variation with cut quality 128

4.4. Axial Viewing of the Cut Face 130

4.4.1. Experimental set-up 130
4.4.2. Results and discussion 131

4.5. Applicability to In-process Inspection and Control 135

4.6. Chapter Summary 137

CHAPTER FIVE

ACOUSTIC METHOD FOR IN-PROCESS MONITORING OF LASER CUTTING PROCESS

5.1. Introduction and Background 138

5.1.1. Generation of thermal-mechanical stress waves 138

5.1.2. Generation of photon pressure stress waves 141

5.2. The Measurement of the Acoustic Waves 142

5.3. Experimental Set-up 144

5.4. Results and Discussion 146

5.4.1. Factors affecting the overall signal strength 146
5.4.1.1. Signals detected by transducer P1 146
5.4.1.2. Signals detected by the transducer P2 158
5.4.2. Signal variations with cut quality 161
5.4.2.1. Signals detected by P1 161
5.4.2.2. Signals detected by P2 164

5.5. Chapter Summary 168

CHAPTER SIX

THERMAL METHODS FOR IN-PROCESS MONITORING OF LASER CUTTING PROCESS

6.1. Introduction and Background 170

6.2. Experimental Set-up 172
6.3. Results and Discussion 173

6.3.1. Causes for the temperature signals 173
6.3.2. Signal variations with cut quality 175
6.3.2.1. Signal variations due to the nozzle-beam misalignment 175
6.3.2.2. Signal variations with process parameters 183

6.4. Chapter Summary 189

CHAPTER SEVEN

KERF SCANNING SYSTEM

7.1. Introduction 190

7.2. Kerf Scanning System for Straight Line Cutting of a Flat Plate 190

7.2.1. Principle of the system operation 190
7.2.2. Mathematical Background 193
7.2.3. Experimental results 198
7.2.4. Scanning a cut with dross adhesion 199

7.3. Kerf Scanning System for Straight Line Cutting of an Uneven Plate 200

7.3.1. Two-polygon System 200
7.3.1.1. Derivation to obtain the angle of the beam 201
7.3.1.2. The relationship between the scanning distance along X-axis and the scanning time 203
7.3.2. Effects of the scanning beam size on the signal shape 206
7.3.3. Design of an on-line kerf scanning system 206
7.3.3.1. Mechanical design of the two polygon system 206
7.3.3.2. Requirements for an on-line application 209

7.4. Chapter Summary 212

7.5. Chapter Acknowledgement 212

CHAPTER EIGHT

ON-LINE QUALITY CONTROL OF LASER CUTTING

8.1. Introduction 213

8.2. Principle of an On-line Laser Cutting Control System 215

8.3. Possibility of Using the Axial Optical Detection Device in the Control System 216

8.4. Possibility of Using the Acoustic Mirror Detection System in the Control System 217

8.5. Possibility of Using the Kerf Scanning System in the Control System 217

8.6. Chapter Summary 218

CHAPTER NINE

CONCLUSIONS AND FUTURE WORK

9.1. Conclusions 219

9.2. Future Work 220

REFERENCES 221

PUBLICATIONS 233

APPENDIXES

Appendix A BBC Programming for the Nozzle/Beam Alignment 234

Appendix B The BOC Model 901 2 kW CO_2 Gas Laser 236

Appendix C Mechanical Design of the Two-polygon System 241

LIST OF FIGURES

Fig. 1 -1. Geometry and main effects of laser cutting.

Fig. 1 -2. Typical striation pattern on laser cut surface of mild steel.

Fig. 1 -3. Model showing periodic cutting process.

Fig. 1 -4. The thickness of the molten layer h_0 against the cutting speed υ_c for various gas flow velocities υ_g.

Fig. 1 -5. Quality of a laser cut.

Fig. 1 -6. Cutting carbon steel with CO_2 laser.

Fig. 1 -7. Examples of TEM_{pq} modes.

Fig. 1 -8. Illustration of focussing and depth of focus.

Fig. 1 -9. Gaussian intensity distribution.

Fig. 1-10. Reflectivity versus angle of incidence for cold iron irradiated by a low power CO_2 laser.

Fig. 1 -11. The measured reflectivity at different laser beam intensities shows a sharp decrease at the threshold intensity for plasma formation.

Fig. 1 -12. Classification of materials in terms of their absorptivity and incandescence resistance.

Fig. 1 -13. Variation of roughness of cut face with cutting speed.

Fig. 1 -14. Cut front length of 1 mm mild steel sheet.

Fig. 1 -15. Fine and coarse striation pattern of a cut.

Fig. 1 -16. Variation of kerf width with cutting speed.

Fig. 1 -17. Effect of cutting speed on the amount of dross clinging.

Fig. 1 -18. Description of the cut with a large amount of clinging dross at a low cutting speed.

Fig. 1 -19. Description of the cut with a little amount of clinging dross at a higher cutting speed.

Fig. 1 -20. Description of the cut with rough kerf zone.

Fig. 1 -21. Variation of heat affected zone with cutting speed.

Fig. 1 -22. Laser cutting of 0.5 mm and 1.0 mm stainless steel using mixed gases as assistant cutting gas.

Fig. 1 -23. Effects of decentralising on kerf width.

Fig. 1 -24. Effects of decentralising on surface roughness at different speeds.

Fig. 1 -25. Illustration of the operation of the LBA.
Fig. 1 -26. Typical output from the LBA showing a near TEM_{01} mode pattern.
Fig. 1 -27. Hollow needle beam sampler.
Fig. 1 -28. Illustration of the detecting unit.
Fig. 1 -29. Acoustic mirror detection system.
Fig. 1 -30. Registration of the shower of sparks.
Fig. 1 -31. Striation and spark showers.
Fig. 1 -32. Detection of angular distribution of laser light passing through the cut kerf.
Fig. 1 -33. Correlation between roughness R_m and temperature in the kerf T_s at various cutting speeds.
Fig. 1 -34. Observation of the cutting process by an endoscope.
Fig. 1 -35. On-line cut quality detection by vision system.
Fig. 2 -1. Principle of nozzle-beam alignment.
Fig. 2 -2a. Laser head.
Fig. 2 -2b. Lens holder.
Fig. 2 -3. Seebeck effect.
Fig. 2 -4. Three wire thermocouple system.
Fig. 2 -5. Typical temperature gradient for type K thermocouple.
Fig. 2 -6. Photo of the X-Y stage.
Fig. 2 -7. Schematic drawing of the gas sealing.
Fig. 2 -8. The unipolar stepper motor drive board.
Fig. 2 -9. The 1.8^0 step drive sequence.
Fig. 2 -10. The torque-speed characteristics.
Fig. 2 -11. Pull-out performance for the 1.8^0 stepper motor.
Fig. 2 -12. Drive board connection.
Fig. 2 -13. Feedback control system for the nozzle alignment.
Fig. 2 -14. Flowchart for pulse train generation.
Fig. 2 -15. Flowchart for the movement control in X axis.
Fig. 2 -16. General experimental set-up for laser cutting process.
Fig. 2 -17. Typical nozzle clipping signals.
Fig. 2 -18. The calorimeter.
Fig. 2 -19. Clipping signals and power drop.
Fig. 2 -20. Calculation of the nozzle dimension L.
Fig. 3 -1. Photo of the workstation.
Fig. 3 -2. Photo of the A.L.L. LBA.
Fig. 3 -3. Photo of the gas mixture instrument.

Fig. 3 -4. Laser beam mode structure from the LBA.
Fig. 3 -5. Classifications of the laser cut surface roughness.
Fig. 3 -6. Measurement of HAZ width.
Fig. 3 -7. Classifications of dross adhesion.
Fig. 3 -8. Kerf width versus cutting speed for O_2/N_2 mixtures.
Fig. 3 -9. Kerf width versus cutting speed for O_2/Ar mixtures.
Fig. 3 -10. Kerf width versus cutting speed for O_2/He mixtures.
Fig. 3 -11. Kerf width versus 1/υ for pure oxygen.
Fig. 3 -12. Kerf width versus 1/υ for pure N_2.
Fig. 3 -13. Kerf width versus 1/υ for O_2/N_2 mixture, oxygen content at 50%.
Fig. 3 -14. Kerf width versus 1/υ for O_2/N_2 mixture, 95% O_2.
Fig. 3 -15. Kerf width versus 1/υ for pure He.
Fig. 3 -16. Kerf width versus 1/υ for O_2/He mixture, O_2 content at 50%.
Fig. 3 -17. Kerf width versus 1/υ for O_2/He mixture, O_2 content at 95%.
Fig. 3 -18. Kerf width versus 1/υ for pure Ar.
Fig. 3 -19. Kerf width versus 1/υ for O_2/Ar mixture, O_2 content at 50%.
Fig. 3 -20. Kerf width versus 1/υ for O_2/Ar mixture, O_2 content at 70%.
Fig. 3 -21. Kerf width versus 1/υ for O_2/Ar mixture, O_2 content at 95%.
Fig. 3 -22. Kerf width versus 1/υ for O_2/N_2 mixture, O_2 content at 70%.
Fig. 3 -23. Kerf width versus 1/υ for O_2/He mixture, O_2 content at 70%.
Fig. 3 -24. Relationship between gas velocity, gas composition and dross clinging problems for O_2/N_2 mixtures.
Fig. 3 -25. Relationship between gas velocity, gas composition and dross clinging problems for O_2/Ar mixtures.
Fig. 3 -26. Relationship between gas velocity, gas composition and dross clinging problems for O_2/He mixtures.
Fig. 3 -27. Relationship between gas velocity, gas composition and dross clinging problems for O_2/N_2 and O_2/Ar mixtures at maximum cutting speeds.
Fig. 3 -28. Relationship between gas velocity, gas composition and dross

clinging problems for O_2/He mixtures at maximum cutting speeds.
Fig. 3 -29. Effects of gas composition on maximum cutting speed.
Fig. 3 -30. Optimum speed range as a function of gas composition at the low gas velocity, 43 m/s.
Fig. 3 -31. Optimum speed range as a function of gas composition at the gas velocity of 86 m/s.
Fig. 4 -1. Power spectral density for blackbody radiation.
Fig. 4 -2. The Fastax high speed camera.
Fig. 4 -3. The relationship between the photodiode output and the illumination lux.
Fig. 4 -4. The BPW21 and human eye spectral sensitivity.
Fig. 4 -5. Experimental set-up for the off-axis monitoring of the cut face.
Fig. 4 -6. Determination of the maximum viewing angle.
Fig. 4 -7. The chart recorder.
Fig. 4 -8. The laser beam mode structure from the LBA.
Fig. 4 -9. Signals at the cutting speed of 10 mm/s.
Fig. 4 -10. Signals at the cutting speed of 20 mm/s.
Fig. 4 -11. Signals at the cutting speed of 30 mm/s.
Fig. 4 -12. Signals at the cutting speed of 40 mm/s.
Fig. 4 -13. Signals at the cutting speed of 60 mm/s.
Fig. 4 -14. Signals at the cutting speed of 70 mm/s.
Fig. 4 -15. The correlation between the signal RMS and the cutting speed.
Fig. 4 -16. The correlation between the signal RMS and the kerf width at the speed of 10 mm/s.
Fig. 4 -17. Melt pool behaviour at a low cutting speed, 10 mm/s.
Fig. 4 -18. Illumination of the cyclic cutting process.
Fig. 4 -19. Melt pool behaviour at a high cutting speed, 60 mm/s.
Fig. 4 -20. Signal at the gas flowrate of 95 L/min..
Fig. 4 -21. Signal at the gas flowrate of 52 L/min..
Fig. 4 -22. Signal at the gas flowrate of 40 L/min..
Fig. 4 -23. Experimental set-up for monitoring the process from the last mirror.
Fig. 4 -24. The axial signal from a rough cut.
Fig. 4 -25. The axial signal from a cut with too much dross clinging.
Fig. 4 -26. The axial signal from a partially penetrating cut.
Fig. 4 -27. The axial signal from a cut with medium dross adhesion.

Fig. 4 -28. The axial signal from a good cut.
Fig. 4 -29. The description of the first quality control parameter, $\Delta V\%$.
Fig. 4 -30. The flowchart of an alarm system.
Fig. 5 -1. Orientation of sections for rectangular and round X-cut crystal plates.
Fig. 5 -2. Schematic drawing of the experimental set-up for monitoring the acoustic waves in laser cutting.
Fig. 5 -3. The piezoelectric transducer spectral sensitivity.
Fig. 5 -4. The smart acoustic monitor.
Fig. 5 -5. Illustration of a circular plate deflection.
Fig. 5 -6. The acoustic signal spectrum analysis for a non-penetrating cut.
Fig. 5 -7. Effect of dross on acoustic signals (P_1).
Fig. 5 -8. Kerf width effect on overall signal strength (P_1).
Fig. 5 -9. Kerf width and roughness effect on signal strength (P_1).
Fig. 5 -10. Effect of dross on acoustic signals detected by P_2.
Fig. 5 -11. Kerf width effect on overall acoustic signal strength (P_2).
Fig. 5 -12. Kerf width effect on signal strength (P_2).
Fig. 5 -13. Signals from a poor cut (P_1).
Fig. 5 -14. Signals with too much dross.
Fig. 5 -15. Signals with too much dross adhesion (P_2).
Fig. 5 -16. The angle of the flowing gas stream from the nozzle exit.
Fig. 6 -1. Construction of the hot nozzle.
Fig. 6 -2. Experimental set-up for testing the back reflected power.
Fig. 6 -3. Temperature signals with and without the aperture.
Fig. 6 -4. Signals for a good cut.
Fig. 6 -5. Cut face striation pattern for a good cut.
Fig. 6 -6. Signals form a terminated cut.
Fig. 6 -7. Dross adhesion and surface striation pattern.
Fig. 6 -8. Signals for cuts with dross adhesion.
Fig. 6 -9. Signals for cuts with too much dross adhesion.
Fig. 6 -10. Dross adhesion on one side of the cut edge.
Fig. 6 -11. Signals when the nozzle clipped.
Fig. 6 -12. Signals recorded by thermocouples at location 3 & 4 for a good cut.
Fig. 6 -13. Signals for a cut with dross clinging on one side of the cut edge.
Fig. 6 -14. Signals at optimal cutting speeds.

Fig. 6 -15. Signals at the cutting speed of 51 mm/s.
Fig. 6 -16. A rough cut.
Fig. 6 -17. Signals at a low cutting speed, 25 mm/s.
Fig. 6 -18. Signals at a high cutting speed, 75 mm/s.
Fig. 6 -19. Signals at a high gas flowrate, 95 L/min..
Fig. 6 -20. Signals at a low gas flowrate, 65 L/min..
Fig. 6 -21. Experimental set-up for monitoring the plasma stability.
Fig. 6-22. Signals obtained at the cutting speed of 40 mm/s, gas flowrate of 95 L/min..
Fig. 7 -1. Operation of the laser beam kerf scanning system.
Fig. 7 -2. A schematic diagram of the scanning system.
Fig. 7 -3. A typical signal scanning a clean cut kerf.
Fig. 7 -4. A geometric drawing of the scanning system.
Fig. 7 -5. The correlation between the scanning distance and the scanning time.
Fig. 7 -6. The theoretical correlation between the scanning distance and the scanning time within a short time period.
Fig. 7 -7. The empirical relationship between the kerf width and the time interval.
Fig. 7 -8. A typical signal scanning a cut with HAZ and dross adhesion.
Fig. 7 -9. The two-polygon unit.
Fig. 7 -10. The mathematical representation of the two-polygon system.
Fig. 7 -11. The correlation between the scanning distance and the scanning time in the two-polygon system.
Fig. 7 -12. The linear correlation between the scanning distance and the scanning time in the two-polygon system.
Fig. 7 -13. Effects of the scanning beam size on the signal shape.
Fig. 7 -14. A schematic drawing of the synchronising system.
Fig. 7 -15. Location of the photodiode.
Fig. 7 -16. The introduction of the He-Ne beam.
Fig. 7 -17. A schematic drawing of an on-line kerf scanning system.
Fig. 8 -1. Laser cutting process parameter interrelations.
Fig. 8 -2. Block diagram of an on-line laser cutting control system.

LIST OF TABLES

Table 1 -1. Data of gas and melt properties.
Table 1 -2. Some representative results of cutting speeds for typical materials with CO_2 laser.
Table 1 -3. Off-line techniques for laser beam measurement.
Table 1 -4. Methods for in-process monitoring beam characteristics.
Table 2 -1. Specifications of the type K thermocouple.
Table 2 -2. Specifications of the X-Y stage.
Table 2 -3. Specifications of the stepper motor.
Table 2 -4. Truth table (C = A EOR B).
Table 2 -5. User port.
Table 3 -1. Thermal properties of gases at 300 K, 1 atmosphere.
Table 3 -2. Convective heat of gases.
Table 3 -3. Heat balance on the cut front.
Table 3 -4. Shear stress caused by different gases at the gas flow velocity of 70 mm/s.
Table 3 -5. Process parameters.
Table 5 -1. Cut quality assessment.
Table 5 -2. Cut quality assessment.
Table 5 -3. Cut quality assessment.
Table 5 -4. Cut quality assessment.
Table 5 -5. Cut quality assessment.
Table 5 -6. Determination of the constant A".
Table 5 -7. Expected signal strength and dross blocking effect.
Table 7 -1. Values of x and t.

GENERAL INTRODUCTION

Since 1960, when the first laser was operated, extensive research and development have been undertaken leading to a rapid growth in laser types, output power and scope of applications [1-3]. The CO_2 laser in particular has been finding wide use in almost every aspects of laser materials processing such as cutting, welding, cladding and heat treatment. It is currently the most powerful material processing laser with commercial laser being offered up to 25 kW [32-33]. The pulsed Nd: YAG laser having a short wavelength (1.06 μm) and high pulse rate, is being widely used in laser drilling, marking and cutting of thin materials [33,41]. The excimer laser is attracting interest from researchers and manufacturers due to its very short wavelength (around 0.308 μm) which is more readily absorbed than longer wavelength and the energy of its photons which make non-thermal processing possible [41]. In fact, the excimer laser is finding many new application areas in material perforation, wire stripping and marking [32-33]. The CO laser technology provides an alternative wavelength (5 μm) [41] to the CO_2 laser. It shows promise of improved absorption and efficiency. It is being further investigated. Japan claims to be the pioneer in this field [214]. With all these varieties the laser is becoming more and more important in industry as a powerful and efficient tool.

Being one of the most mature applications, laser cutting has been widely accepted by industry, for instance, in metal sheet cutting. The advantages found for laser cutting are [3, 37]:

(i). narrow kerf giving a saving in materials;
(ii). narrow heat affected zone giving low thermal distortion;
(iii). smooth cut edge;
(iv). absence of tool wear;
(v). a wide range of materials can be cut with equal ease;
(vi). easy automation and manipulation.

The cut quality as the most important characteristics of laser cutting is

however affected by a variety of factors such as laser power, beam mode structure, cutting speed and cutting gas flow rate and composition. It is desirable to develop a fully automated process for high volume industrial production and precise cutting applications, since there are some unstable phenomena occurring during the cutting process. For example, the absorbed laser power fluctuates, either due to periodic changes of the absorption coefficient as, for instance, in the case of plasma formation [7,8,23] or due to periodic fluctuations of laser power itself, for instance, due to the effect of the laser radiation reflected back from the workpiece and coupled again into the laser resonator [25]. The beam mode structure is also time dependent [127-128]. The reactive gas flow changes due to the formation of turbulence during the cutting process [9]. The cutting speed may vary at corners due to momentum of a CNC table. The workpiece thickness and surface conditions may vary as well. All these variations could lead to reduced cut quality and reduction in process efficiency. Therefore it is necessary to make on-line control of the process to guarantee the high quality and high productivity of the cutting process.

As the most important stage of an on-line control system, in-process monitoring of the laser process has been the main research area. This includes three aspects: sensing and measuring the quality parameters; measuring laser beam characteristics and measuring the workstation characteristics. The basic requirements for an in-process quality analysis include: a reliable signal of the cut quality; fast response time; fast signal processing and omnidirectional operation [178,180]. In-process monitoring of the laser parameters includes the measurement of laser power, beam mode structure and beam diameter. Workstation characteristics usually include cutting speed control and nozzle to workpiece distance control.

Laser beam alignment is widely acknowledged as a prime factor in attaining good cut quality. To achieve highly accurate beam alignment is of special interest for precise cutting applications. Research is usually divided into two areas: mirror-beam alignment and nozzle-beam alignment respectively .

It is being realised that the cutting gas composition may have great effects on laser cutting quality and on cutting speed [55,110]. Thus the

cutting gas composition could play an important part in improving cutting performance as an operating parameter.

The nozzle/beam alignment technique to be discussed in chapter 2 and the gas effects to be discussed in chapter 3 do not seem approriate to the title of the thesis. However, they are included for specific reasons. It is essential to have the laser beam accurately aligned before the cutting process starts. Furthermore, this nozzle/beam alignment technique could, in future, be part of in-process control. The effects of gas composition on laser cutting process are interests of many companies because of the effect on process quality. The British Oxygen Company thus funded this project. The gas effects could also be relevant to in-process control, for example, it would be possible to control gas pressure to ensure optimal cutting. Therefore, these two chapters are presented as parts of the thesis.

The development of an on-line control system using an expert system for the laser materials processing is receiving more and more attention due to the multi- parameter nature of the processing [182,191]. Interests are specially concentrated on setting up a data base, which represents the relationships between the in-process sensing signals and cut quality, and relationships between cut quality and relevant parameters in a clear manner so that they can be easily accessed for on-line decision-making and correction.

The objectives of this project are therefore: first, to develop sensors and instruments for in-process monitoring and measuring of cut quality parameters; second, to investigate techniques for nozzle-beam alignment; third to investigate the improvement of cut quality by optimising the cutting gas compositions and finally to discuss the possibility for on-line diagnosis of the cutting process.

CHAPTER ONE
LITERATURE SURVEY

In this chapter a review of the literature on the laser cutting process is given. This is discussed in the following sections: physical mechanisms of the process, factors affecting cut quality and previous work on measuring and sensing the process.

1.1. Physical Mechanism and Theories

1.1.1. Basic phenomena in laser cutting

1.1.1.1. Interactions between beam and workpiece

The laser cutting process is normally a thermal process [1-5]. When a laser beam strikes an opaque surface, heat transfer occurs by photon/electron interactions with free or bound electrons. These interactions raise the energy state of electrons in the conduction band. The excited electrons then interact with lattice phonons or give back their radiation as reflected radiation [3,5]. The affected phonons cause lattice vibration which is detected as heat. The laser energy is thus converted to heat which raises the surface temperature and may cause melting or boiling depending on the amount of laser power absorbed and the materials to be cut. In general, laser cutting can be effected in six different ways [3]:

(i). Vaporisation: The beam energy heats the substrate to above its boiling point and material leaves as vapour and ejecta.

(ii). Melting and blowing: The beam energy melts the substrate and a jet of inert gas blows the melt out of the cut region.

(iii). Burning in reactive gas: The beam energy heats the material to the kindling temperature which then burns in a reactive gas jet; the jet also clears the dross away.

(iv). Thermal stress cracking or controlled fracturing: The beam energy sets up a stress field in a brittle material e.g. glass such that it can guide a crack in any direction.

(v). Scribing: A variant on (i) whereby a blind cut is used as a stress raiser allowing mechanical snapping along the scribed lines.

(vi). Etching: The direct breaking of C-C bonds of organic materials by high energy photons. For example, this happens when an excimer laser beam strikes on organic polymers [199] .

1.1.1.2. Description of the laser gas cutting process

The process of laser cutting with reactive gas assistance ((iii) above) can be illustrated in Fig. 1 -1.

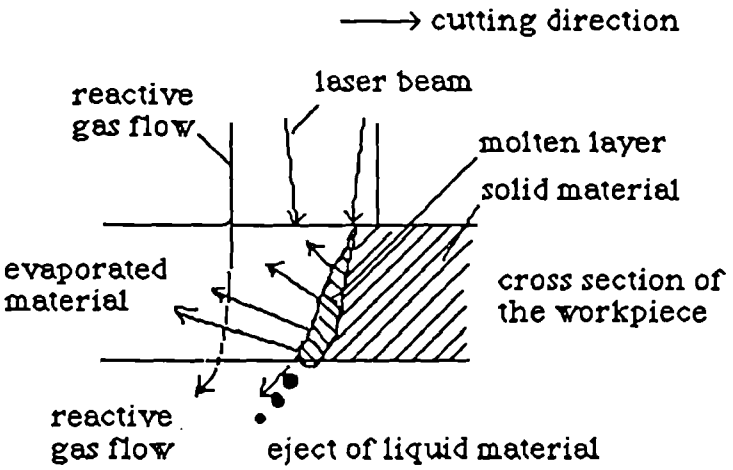


Fig. 1 -1. Geometry and main effects of laser cutting [6].

The focussed laser beam and the coaxial gas stream impinge on the upper surface of the workpiece at the cut front. Part of the gas stream and the laser beam are reflected. The latter is strongly affected by plasma formation [7,8] and by the surface properties as to be discussed later in this chapter. The remainder of the laser beam enters the kerf and either strikes on the cut front or the kerf edge or passes straight through. The cut front absorbs the majority of the radiation [6,9-14] resulting in the formation of a thin molten layer for materials which melt. The molten layer forms the border between the already existing kerf and the uncut material. The reactive gas stream acts at the cutting front in three ways simultaneously. Firstly, by mass transfer causing a chemical reaction with the melt forming, for example, oxides. This creates another heat source. Secondly, by heat transfer from convective cooling. This cooling effect is usually negligible being only a few watts compared to the input of

a few hundreds of watts [1,3]. Thirdly, by momentum transfer causing a drag force to eject molten material from the kerf. These gas actions will be further discussed in chapter three .

1.1.2. Dynamic behaviour in laser cutting

It is widely acknowledged that laser cut surfaces are characterised with a periodic striation pattern due to the dynamic behaviour of the laser cutting process (Fig. 1 -2) [9 -22]. This fairly regular striation is the main cause of the cut surface roughness. Thus the investigation into its formation mechanism has attracted interests from many researchers. In fact, several theories and models have been developed.

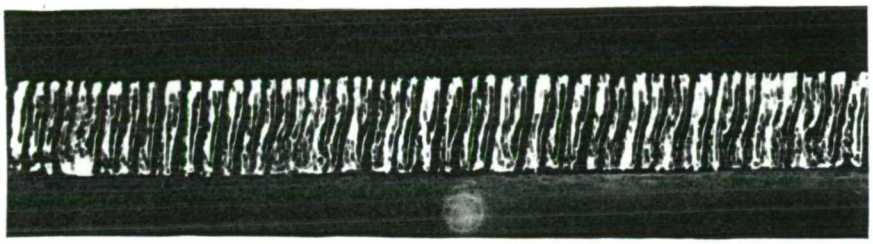


Fig. 1 -2. Typical striation pattern on laser-cut surface of mild steel.

1.1.2.1. Sideways burning theory [15]

The periodic cutting phenomena was observed by using high speed film camera looking at the leading face of the cut [15, 21-22]. A model to explain this observed phenomena was correspondingly proposed as shown in Fig. 1 -3 .

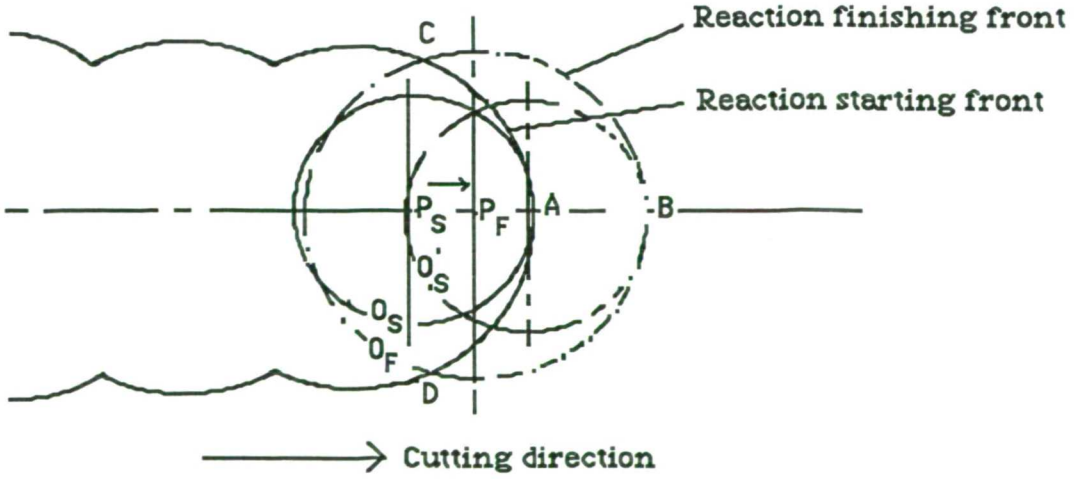


Fig. 1 -3. Model showing periodic cutting process [15].

Figure 1 -3 exhibits the top view of the model proposed to explain the formation of striations. The circles O_s and O_f, whose centres are P_s and P_f, are contours of equal laser power density, e_s, and, e_f, respectively. On coming in contact with the edge of the face CAD, the power density of circle O_s is sufficient to start the oxidation reaction. The reaction front moves along the x-axis at speed υ_r which is faster than the laser beam traverse speed until the power density is unable to sustain the the reaction at the reaction finishing power density, e_f [15]. The oxidation reaction spreads in all directions where there is material so that the region CADBC is removed. Then there is no action until the circles O_s reaches the cutting front at B again. This cyclic burning process, i.e. ignition- burning-extinction, leaves a circular arc and a ridge at C, which is a coarse striation pattern often observed with slow cuts.

1.1.2.2. Mass and temperature oscillations of the molten layer [9]

This theory is based on the oscillating behaviour of the molten layer. The molten layer formed at the cut front plays an important role in laser cutting, since it converts radiation and reaction energy to heating of the workpiece and carries out materials removal by evaporation from its surface and by ejection of liquid material at the lower surface of the workpiece due to the drag effect of the gas stream. Hence there exist energy and mass variations of the molten layer during the cutting process. The energy variation contains both energy gain by absorbed radiation and by reaction and energy loss by several mechanisms such as heat conduction, evaporation, convection and melting of new solid material during the movement of the liquid layer in the cutting direction [9]. The energy loss is strongly dependent on the gas flowrate and gas composition which control the burning reaction, and cutting speed which control the process of evaporation, heat conduction and melting of solid material. The mass variation contains, on the one hand, new mass melted, obviously dependent on the cutting speed. On the other hand, it contains mass loss due to evaporation and convective flow removal due to drag force from the reactive gas flow, the former depending on the temperature of the melt and the latter depending on the thickness of the molten layer and

its fluidity. A difference between energy gain and loss and between mass gain and loss of the liquid layer could be caused either by resonance with fluctuations of laser power or reactive gas flow or cutting speed [9,11]. The fluctuation of laser power is either due to periodic changes of absorption e.g., in the case of plasma formation [7,8], or due to the periodic variation of the laser power itself, for instance, due to the effect of the laser radiation reflected back from the workpiece and coupled again into the laser resonator [23,24,25]. The reactive gas flow can also show periodic fluctuations due to the turbulence generated in the kerf [9]. These variations result in the unstable situation of the molten layer, i.e. the oscillations of its temperature and mass. As the molten layer moves in the cutting direction, these oscillations of temperature and mass lead to a spatial fluctuation of the kerf that causes the formation of a striated structure of the cut [9,26].

1.1.2.3. Oscillation of the molten layer thickness[19]

As discussed above the dynamic behaviour of the molten layer on the cutting front may be the cause of the formation of the surface striation. A similar theory but from different approach is proposed to investigate the oscillation of the molten layer thickness [19]. It is argued that the molten layer thickness is one of the main factors controlling the melt flow characteristics and thus the formation of the surface striation. The thickness is shown to be affected by factors such as the cutting speed, the gas flow velocity and the densities and viscosities of the gas and the melt as shown in Fig. 1 -4, which was drawn based on the data from table 1 -1.

Table 1-1. Data of gas and melt properties [19]

gas density at the nozzle $kg\ m^{-3}$ (Air)	gas density at surface temperature $kg\ m^{-3}$ (Air)	dynamic gas viscosity at surface temperature $kg\ m^{-1}\ s^{-1}$ (Air)	melt viscosity $kg\ m^{-1}\ s^{-1}$ (Fe)
1.3	0.2	4.5×10^{-5}	5×10^{-3}

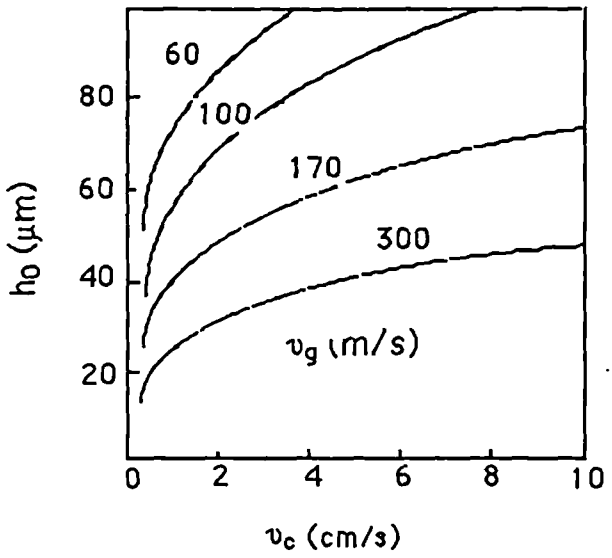


Fig. 1 -4. The thickness of the molten layer h_0 against the cutting speed v_c for various gas flow velocities v_g [19].

It is easily seen that by increasing the gas flow velocity, the molten layer thickness is decreased because the removal is more efficient. By increasing the cutting speed, the layer thickness increases since more molten material is produced per unit time in the cutting kerf. When a gas with higher density or viscosity (at the same gas flow rate) is used for cutting, the layer thickness can be reduced [19]. Because of the unstable situation of the molten layer as discussed in 1.1.2.2., this thickness varies during the cutting process causing unsteady melt flow, which may result in the periodic striation formation on the cut faces.

1.2. Laser Cutting Performance

Laser cutting has experienced wide acceptance in industry due to the process characteristics of high cutting speed, easy automation and good cut quality. It is necessary to clarify what characteristics a good cut should have and what parameters affect the cut quality and the maximum cutting speed.

1.2.1. Quality of a laser cut

It is agreed that a good laser cut should have the following characteristics [1-3, 6, 8, 15, 27, 28] (Fig. 1 -5):

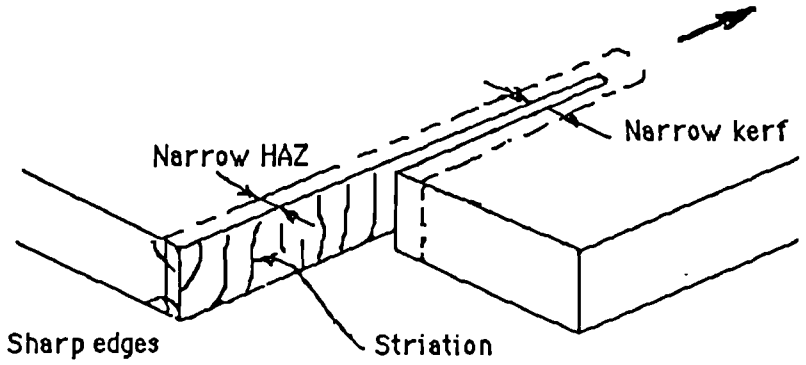


Fig. 1 -5. Quality of a laser cut [6].

(i). Sharp corners at entry and at lower edges;

(ii). Narrow kerf width: a measure of the amount of material removed due to the combined action of laser beam -workpiece interaction and the burning reaction;

(iii). Narrow Heat Affected Zone (HAZ);

(iv). Smooth cut faces: a measure of surface striation depth and wavelength;

(v). Non-adherent dross: materials clinging to the bottom edges. The quantity of dross particles depends on the flow and melting conditions of the molten materials [28] and the surface tension at the lower edges [19] .

1.2.2. Factors affecting the cutting performance

Parameters involved in laser cutting process can be grouped into four main aspects: laser parameters, gas flow, material properties and workstation parameters [3,17,29,30,31].

1.2.2.1. Laser parameters

(i). Laser power

Laser power is one of the most important parameters which define the

cutting speed and penetration [3,32,33,34]. Figure 1 -6 shows a typical relationship between laser power, cutting speed and thickness for carbon steel with O_2 assistance.

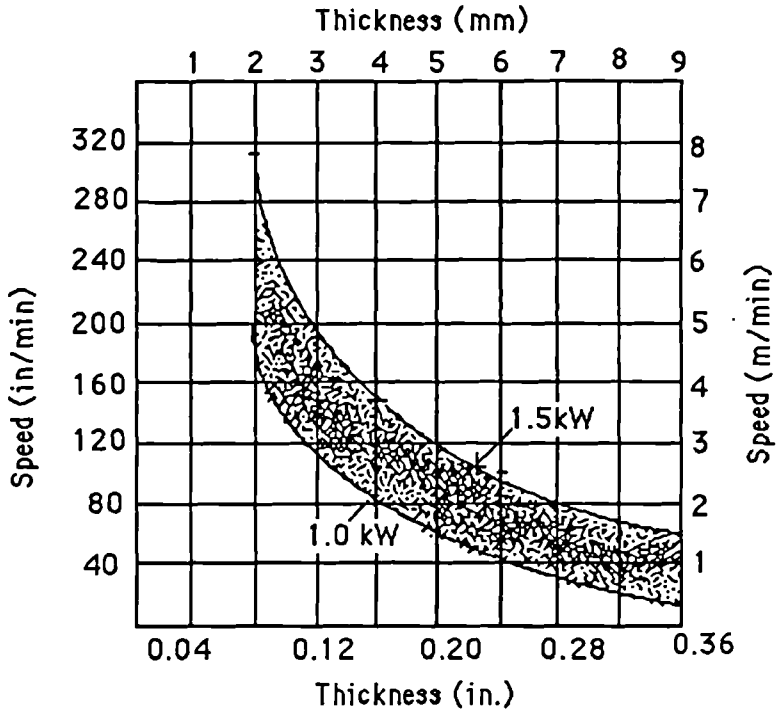


Fig. 1 -6. Cutting carbon steel with CO_2 laser [33].

As can be seen, for a given material thickness, the maximum cutting speed increases with an increase in laser power. Similarly, for a given cutting speed, thicker material can be cut at higher power. Using these curves, an estimate can be made of the cutting speed expected for a given laser power and material thickness.

The relationship between the laser power, thickness and the cutting speed is also theoretically investigated supporting the above results [3]. In which it is demonstrated that most cutting data is approximately correlated against $P/\upsilon t$ = f(material property), i.e.

$$P/\upsilon t = \eta W \rho \, (C_p \Delta T + L_m + m' L_f) \qquad (1\text{-}1)$$

where

P = absorbed energy

$= P_i(1 - r_f)$ (W);

P_i = incident power (W) ;

r_f = reflectivity ;

η = reciprocal of the process efficiency ;

υ = cutting speed (m/s);

W = kerf width (m);

t = workpiece thickness (m);

ρ = workpiece density (kg/m^3);

Cp= workpiece specific heat (J/kg·K);

ΔT= temperature rise to melting point T_m (K);

L_m= latent heat of fusion (J/kg) ;

m' = mass fraction melted which subsequently evaporates;

L_f = latent heat of evaporation (J/kg) .

In this model, all the absorbed energy which is not used for melting (e.g. heat loss by radiation, convection or conduction) is accounted for in the efficiency term, η .

(ii). Beam mode structure

Laser beam mode structure is a description of the power distribution across the beam and has a characteristic pattern depending on the dominant transverse electromagnetic modes (TEM_{pq}) for a stable resonator, where 'pq' is related to the number of nulls in the beam pattern in radial and azimuthal directions respectively for beams of cylindrical symmetry, and two orthogonal directions for beams of rectangular symmetry. Some low order beam modes are shown in Fig. 1 -7.

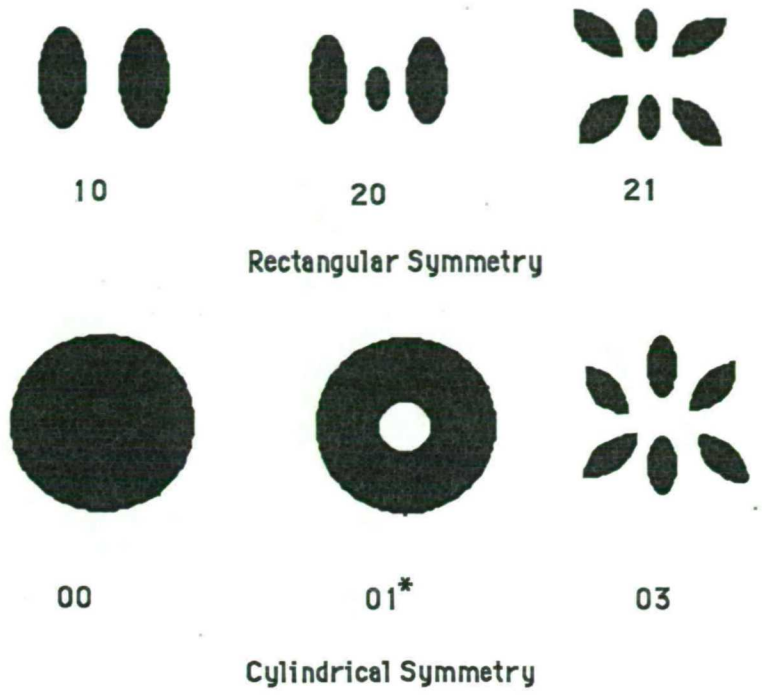


Fig. 1- 7. Examples of TEM_{pq} modes [37].

Since the order of the mode has great effects on both the focussed spot size and the depth of focus [35,39], which affect the laser power density, the beam mode structure becomes extremely important in laser materials processing. Higher-order mode beams diverge more rapidly, focus to larger spot sizes and have shorter depth of focus than Gaussian beams. The spot size for TEM_{pq} of circular modes is given as below [35]:

$$r_0 = \frac{\lambda f(2p + q + 1)}{\pi r_L} \qquad (1\text{-}2)$$

where

r_0 = the focussed spot radius (m) ;

λ = the laser beam wavelength (m);

f = the focal length of the lens (m);

r_L = the radius of the beam entering the lens (m);

p = the number of radial nulls;

q = the number of azimuthal nulls.

The depth of focus for TEM_{pq} of circular modes is given as:

$$d = \pm \pi \sqrt{\rho^2 - 1}\ \frac{r_0^2}{(2p + q + 1)\lambda} \qquad (1\text{-}3)$$

where d, is the depth of focus, defined as the distance over which the power density is within $\pm$ 10% of peak power density (Fig. 1 -8) ; ρ is a factor determined by the application. Essentially, ρ determines the amount by which the spot size can vary and still produce acceptable results. This is clearly different for different applications. Generally, more than a 10% variation in spot size will cause a substantial degradation of quality in cutting [35].

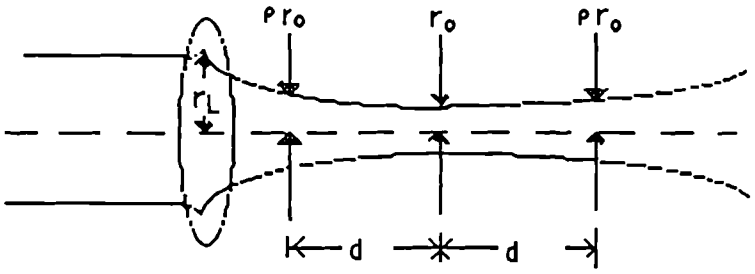


Fig. 1 -8. Illustration of focussing and depth of focus [35].

In cutting, it is generally desirable to achieve highest possible speed and therefore the highest possible power density. Thus the lowest order mode is desirable (TEM_{00} or Gaussian mode for stable resonators) [35,36,37]. In fact, the Gaussian beam structure has been shown to give best cut quality in terms of smoothness and kerf width due in main to the increased speeds possible [38].

The Gaussian beam distribution , as shown in Fig. 1 -9, can be written as :

$$I = I_o \exp\left(-\frac{2r^2}{r_0^2}\right) \qquad (1\text{-}4)$$

where

r = the radial distance from the beam axis;

r_0 = a definition of spot size: at $r = r_0$, $I/I_0 = 1/e^2 = 0.135$;

I = the intensity at a distance r;

I_0 = the peak intensity.

The maximum intensity occurs at the centre of the beam and is given in terms of the total power, P_t, by[37]

$$I_0 = \frac{2P_t}{\pi r_0^2} \qquad (1\text{-}5)$$

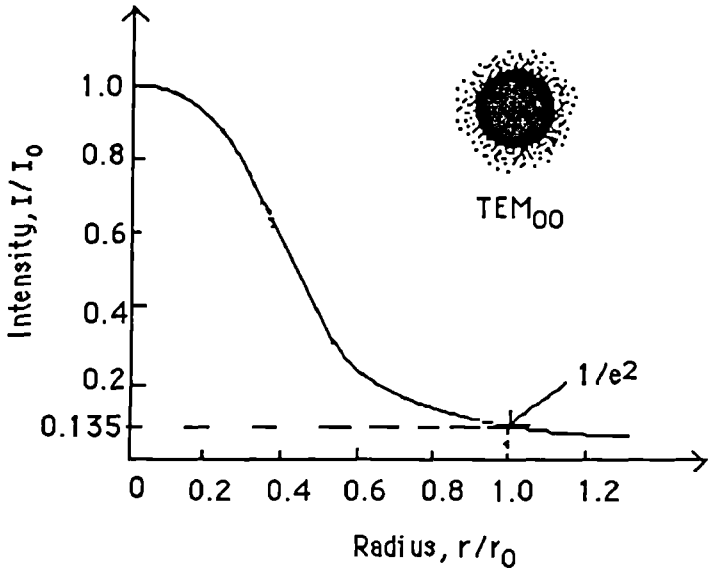


Fig. 1 -9. Gaussian intensity distribution [37].

(iii). Focusing optics

For a Gaussian beam (TEM_{00}), when the $1/e^2$ definition of the spot size is used, the spot size can be worked out from equation (1-2) as :

$$r_0 = \frac{\lambda f}{\pi r_L} \qquad (1\text{-}6)$$

and the depth of focus, d, is given as:

$$d = \pm \pi \sqrt{\rho^2 - 1}\ \frac{r_o^2}{\lambda} \qquad (1-7)$$

From equations (1-6) and (1-7), it can be stated that the shorter the focal length of the focussing optics the smaller the spot size and thus the depth of focus. The spot size determines the power density at a given laser power and affects the kerf width, while the depth of focus affects the depth of penetration. Therefore, the focussing optics directly influence the cut quality.

(iv). Beam coupling with the workpiece

The coupling of energy into the workpiece is of great importance in all laser processes, and so for laser cutting too. The absorption is a function of workpiece reflectivity, (i.e. absorption =(1- reflectivity) for an opaque material). It is affected by many factors such as surface conditions [3, 40,42], the incidence angle of the laser beam [17,40], the state of beam polarisation [17] , the wavelength of laser emission [37,41] , plasma coupling [3,7-8] and temperature of the workpiece. It thus varies during the process.

The workpiece surface condition such as the reflectivity and surface oxidation affects the beam absorption. Theoretically, the lower the reflectivity the better the beam absorption. A oxidised surface will have better absorptivity.

The beam incidence angle affects significantly the reflectivity as shown in Fig. 1 -10, where R_p and R_s are the reflectivity for light polarised respectively parallel and perpendicular to the plane of incidence. It can be seen from this graph that the absorptivity is strongly dependent on the plane of polarisation of the beam particularly when the angle of incidence is large. In laser cutting , the angle of incidence on the cut front is normally larger than 80^0 [17] . When the laser beam is plane-polarized, cutting in the direction of polarisation (direction parallel to the electric field) has been shown to be optimum to give fastest speed, smoothest and most constant kerf width [3,17,35,40,43,44]. "Circular" polarisation in which the electric field vector is made to rotate is

necessary for contour cutting due to its ability to produce even and homogeneous kerfs in any direction [36,45] .

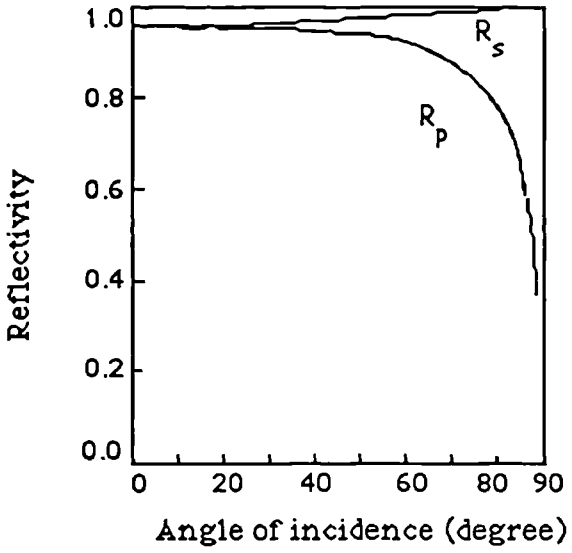


Fig. 1 -10. Reflectivity versus angle of incidence for cold iron irradiated by a low power CO_2 laser [40].

The absorptivity depends also on the wavelength of the beam as described by the inverse Bremsstrahlung, in which the absorption coefficient is proportional to the square of the wavelength [8,23,48]. The absorptivity will be higher for the beam with shorter wavelength.

Laser-induced plasma has a considerable effect on beam absorption mechanisms [3,7-8, 46-48]. It is clearly seen in Fig. 1 -11 that the plasma forms when the laser intensity approaches a critical value. Instantaneously, the absorption rises to higher values via perhaps coupling with the electrons in the plasma. However, in some other circumstances, absorption by the plasma can lead to decoupling due to the separation of the plasma from the workpiece surface [7-8,37].

The absorption is also dependent on the workpiece temperature. Generally speaking, the higher the workpiece temperature the higher the absorption coefficient.

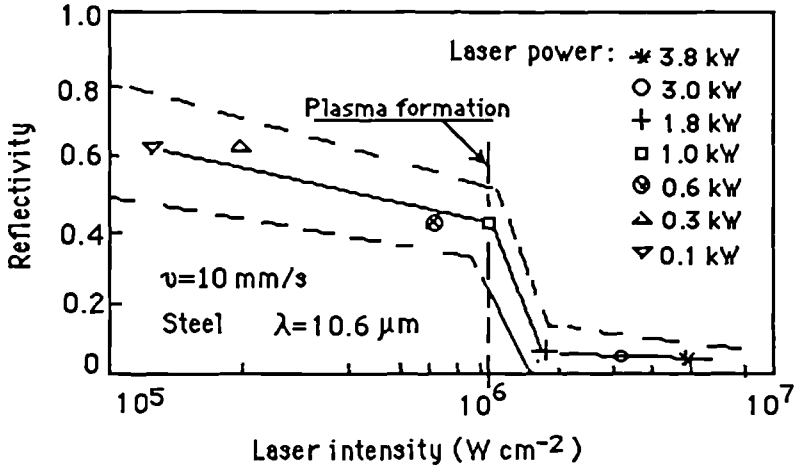


Fig. 1 -11. The measured reflectivity at different laser beam intensities shows a sharp decrease at the threshold intensity for plasma formation [7].

1.2.2.2. Gas flow parameters

In laser gas cutting, the dominant functions of the gas flow are the mass transfer to cause chemical reaction and momentum transfer to eject molten material and dross. Thus it has been shown that the nozzle design and gas flow have considerable effects on the cutting performance [18,28,29,49-58]. The assistant gas is introduced either off-axis or co-axis to the laser beam through a nozzle. The coaxial method is however most commonly used since it is axisymmetric and necessary for omnidirectional cutting. It also has the advantage of providing protection for the beam focussing optics against damage by ejected debris.

(i). Nozzle diameter: The basic requirements for the nozzle diameter are : first it must be big enough to pass the laser beam and to make beam-nozzle alignment easier; second the exit pressure should be high enough to provide momentum to blow the dross away without using too much gas [3].

(ii). Nozzle standoff distance: The distance between the nozzle exit and the workpiece (often called nozzle standoff distance or nozzle height) is crucial. It should be kept as close to the workpiece as possible to keep the pressure high on the workpiece, but must be high enough off the

workpiece to prevent possible mechanical jamming due to the splattered dross or severe back pressure on the lens. It should also avoid the shock waves discussed below.

(iii). Nozzle gas pressure: It has been widely acknowledged that increasing the gas pressure or gas flow rate increases the cutting speed and metal cut quality [3, 51, 54]. However, if the nozzle pressure is very high (but still within the pressure limit which the focussing lens can withstand) then the gas flow becomes choked or even supersonic for convergent nozzles. This results in shock waves [3, 51, 54, 59-60] between the nozzle tip and the workpiece. These shock waves can cause significant reduction in cutting pressure at some specific values of the standoff distance, and thus may impede dross removal [49,54,61-64]. In some cases, where very high gas pressure is required, non-circular nozzles such as lobed nozzle can be used which has been shown to reduce the tendency to form Mach shock discs [54].

(iv). Gas type : The type of gas used in laser cutting affects how much heat is added to the cutting action by chemical reaction. This obviously affects the cutting speed. Usually, oxygen is used for cutting most metals since much heat is generated from the exothermic reaction with oxygen[3, 32-33] . For example, in the case of cutting steel as much as 60% of the heat input comes from the exothermic reaction [22]. However in some situations, it is necessary to use inert gas to reduce oxides or dross clinging problem [65]. The effects of gas type and gas mixtures on laser cutting performance are further discussed in section 1.3 and will be fully investigated in chapter three of this thesis.

1.2.2.3. Material parameters

The ease with which a material can be cut and the quality of the resulting cut depend also on the material properties. In general, there are three main factors regarding the material properties, i.e. the thermal properties, the mechanical properties and the chemical properties. A classification of materials based on these material properties is shown in Fig. 1 -12 [74] .

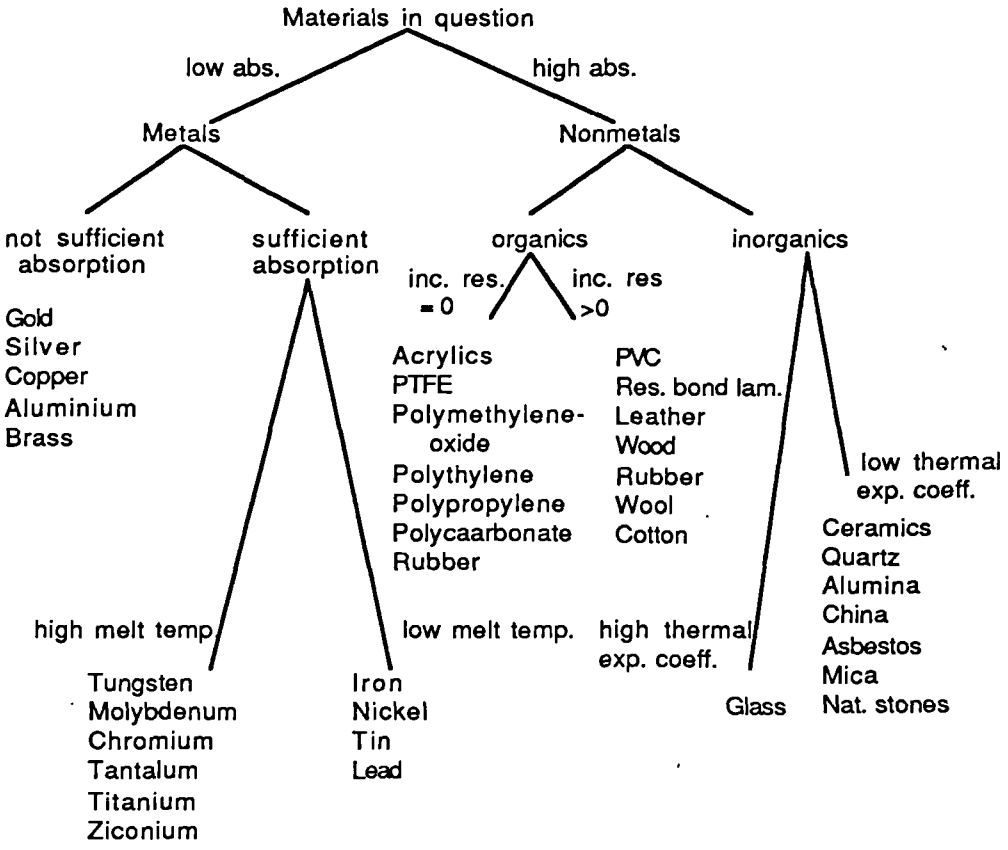


Fig. 1 -12. Classification of materials in terms of their absorptivity and incandescence resistance [74].

(i). Thermal properties

The main thermal properties concerned in laser cutting process are the reflectivity and conductivity of the workpiece. The reflectivity determines the beam absorption process, while the heat conductivity determines how much of the absorbed energy is lost through heat conduction. Therefore, these two factors affect the overall process efficiency and cut quality. Highly reflective as well as conductive materials such as copper, aluminium and gold (materials in column 1 in Fig. 1 -12) are thus difficult to cut, since only a small portion of the beam energy is absorbed. However, the surface reflectivity changes its value during the processing due to the formation of plasma and the changing angle of the cut face to the incident beam as discussed before. Therefore, laser cutting of these materials becomes easier once cutting starts. In fact, good results were reported for cutting thin sheets of copper (0.6 mm) at speeds up to 2.5 mm/s [67, 68] , where a near Gaussian mode structure

was used, together with suitable power density and extremely careful control of the positioning of the focal spot on the workpiece surface. Successful cuts of other highly reflective materials were also reported elsewhere [66, 69-73, 93] (table 1 -2).

Laser cutting of materials with sufficient absorptivity such as steel and titanium (column 2 and 3 in Fig. 1 -12) can be easily cut with good cut quality [75 -78, 80, 88, 90, 95] (table 1 -2).

Laser cutting of materials with high absorptivity and low conductivity such as paper, plastics and wood (column 4 and 5 in Fig. 1 -12) are easily cut even at low powers with very high cutting speeds [79, 81 -87, 91 -92, 94, 96 -100, 102, 105] . For example, 0.33 mm thick of gloss paper was cut at the speed of 667 mm/s at the laser power of 60 W (table 1 -2).

(ii). Mechanical property

The main mechanical property concerned in laser cutting is the stress resistance property. Brittle materials such as glass and ceramics (column 6 and 7) tend to crack during cutting and will thus need special treatment such as preheating and post-cut tempering [75, 80, 90, 96 -100] . They are usually cut by scribing followed by mechanical fracture [101 -103].

(iii). Chemical properties

The main chemical properties concerned in laser cutting are the heat of reaction and the melting point of oxides. The former determines the amount of heat input from the oxidation reaction into the cutting process and thus affects the cutting speed. The melting point of the oxides resulting from the burning reaction affects the melt fluidity and thus may cause dross clinging at the bottom cut edges. For example, when laser cutting of stainless steel, chromium oxides having a high melting point are formed some of which deposit at the cut edges forming clinging dross. This dross may be difficult to remove and may thus affect the subsequent welding or finishing process. The mechanism of dross formation will be further discussed later in this chapter.

A summary of some representative cutting results for typical

materials is shown in table 1 -2.

Table 1 -2. Some representative results of cutting speeds for typical materials with CO_2 laser (selected from [3, 67, 33,90]).

Material	Thickness (mm)	Power (W)	Gas	Cutting Speed (mm/s)
Mild steel	2.0	2000	oxygen	83.3
	2.54	2000	oxygen	35
Stainless steel	2.0	1000	oxygen	66.7
	2.8	2000	oxygen	20
Titanium	1.6	300	oxygen	25
	3.5	2000	oxygen	8.33
Aluminium	0.5	500	oxygen	36.7
	3.0	1000	oxygen	16.7
Copper	0.6	500	oxygen	2.5
glass quartz	2.0	500	none	20
glass ruby	0.4	100	none	33.3
Ceramics (Aluminium oxide)	0.75	100	none	25
Paper (gloss)	0.33	60	air	666.7
Plastic ABS	6.3	500	inert gas	100
Plastic Nylon	0.2	200	air	60
Wood Hard	19	500	inert gas	8.33
Wood Soft	25.4	2000	air	33.3

1.2.2.4. Workstation parameters

The cutting speed affects the cut face melt pool size and flow as well as the extent of any burning reaction and heat flow into the workpiece. Thus the quality of cut edge is perhaps most affected by the cutting speed both from the point of view of the striation pattern (section 1.2.2) and the

extent of the HAZ [28, 31, 104, 106-113].

1.2.2.4.1. Effects of cutting speed on surface roughness

Figure 1 -13 shows the effect of the cutting speed on surface roughness. It clearly shows that increasing the cutting speed would greatly improve the surface roughness. This can be explained by the sideways burning theory. At low speeds, the oxidation reaction moves faster than the laser traverse speed. There is then a considerable side burning resulting in very rough edge [3, 15, 21, 22]. With the increase in cutting speed, the laser traverse speed matches the oxidation reaction speed leading to a fine striation pattern. However, if the cutting speed is further increased above the optimum valuc, the surface becomes rough again. This can be explained by figure 1 -14, where the concept of "cut length difference" is introduced. It is actually a representation of the inclined angle of the surface striation pattern. It is seen from this figure that the cut length difference, |(a - b)|, increases sharply with the cutting speed after the optimum cutting speed.

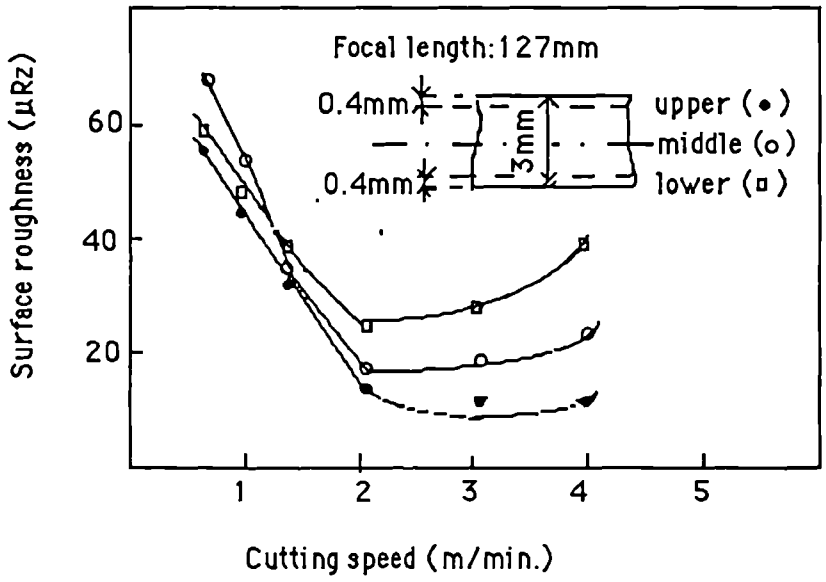


Fig. 1 -13. Variation of roughness of cut surface with cutting speed. Mild steel, 1 kW laser power, 46.9 kPa oxygen pressure [15].

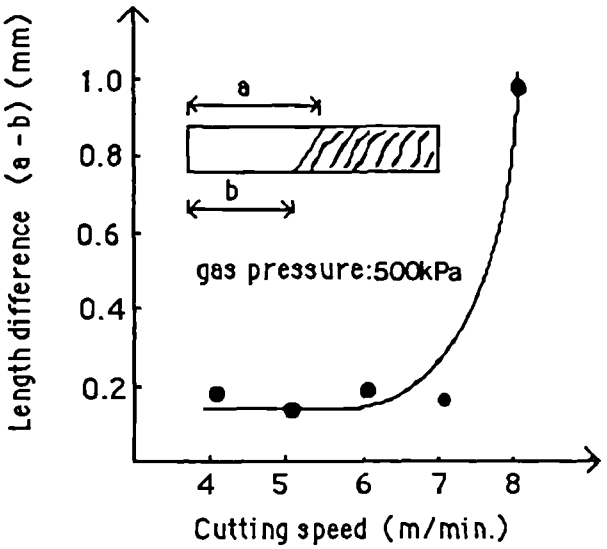


Fig. 1 -14. Cut front length of 1 mm mild steel sheet. Cut with CW CO_2 laser at 350 W and various cut speeds and oxygen pressures [104].

It has been noticed that the upper part of the cut face is generally smoother than the lower part [9,15]. This phenomenon could be understood in terms of the formation of two separated liquid layers, one near the upper surface of the workpiece and one at the lower surface [9]. The reactive gas flow enters the kerf at subsonic speeds, but is heated due to the interaction with the hot liquid layer [6, 114], as it penetrates into the bulk of the workpiece. The density of the gas flow is accordingly reduced and thus the speed of the gas flow is raised. After a critical distance from the surface, the flow becomes turbulent or even sonic. From that point on, a second molten layer exists that shows different properties due to the interaction with the turbulent gas flow. That molten layer has a lower temperature, since the 'peak' of the laser beam has already struck the upper part of the cut leaving only the 'tail' of the beam and reflections previous from the cut face to heat this lower part. The oscillations of the second liquid layer can be excited by the fluctuations of the turbulent gas flow. Since the frequency of the oscillations of the liquid layer depends strongly on the temperature [9], the upper molten layer and the the lower molten layer must show different oscillation frequencies and different drag angles. Generally the oscillation frequency increases with rising temperature of the melt, thus the wavelength of the upper pattern must be shorter than that of the lower pattern. In other words, the upper part of the cut face is smoother than the lower part and with a more regular striation frequency and drag angle (Fig. 1 -15). Similar results were

reported elsewhere [105,106,108,113].

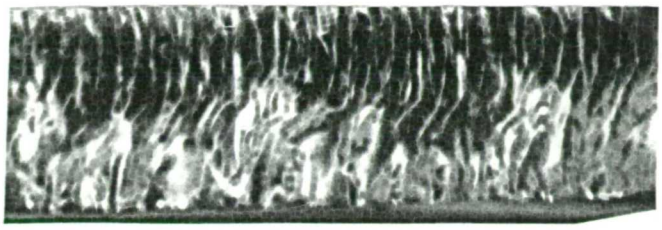


Fig. 1 -15. Fine and coarse striation patterns of a cut. Cut performed at the cutting speed of 40 mm/s, laser power of 1570 W and gas pressure of 300 kPa. Material: 1 mm thick of mild steel.

1.2.2.4.2. Effects of cutting speed on kerf width

A typical plot of kerf width versus traverse speed in 4 mm thick of mild steel is shown in Fig. 1 -16.

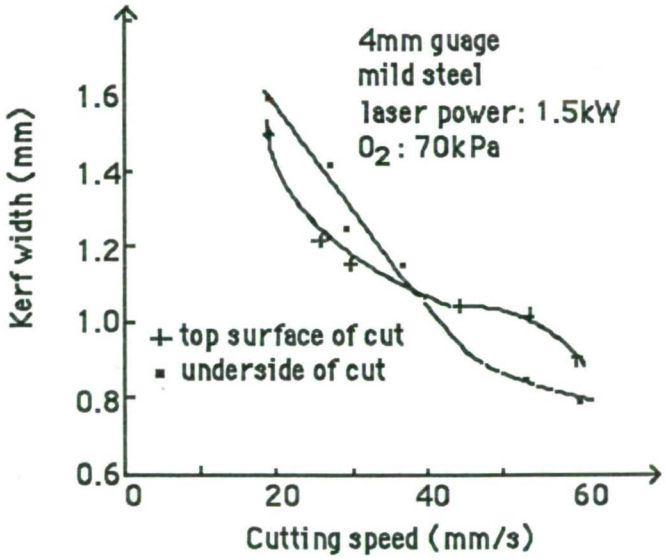


Fig. 1 -16. Variation of kerf width with cutting speed [3].

Generally, the kerf width decreases with increasing cutting speed. This can be explained by the sideways burning theory. At low cutting speed, there is considerable side burning due to the laser beam traverse speed being slower than the speed of oxidation reaction as discussed before, and thus resulting in a wide rough kerf. Similar results were

observed by other researchers as well [106,108,110-112].

1.2.2.4.3. Effects of cutting speed on dross formation

The dross clinging phenomenon was observed with high speed camera and the relationship between the height of the clinging dross H_D and the cutting speed v_b is shown in Fig. 1 -17.

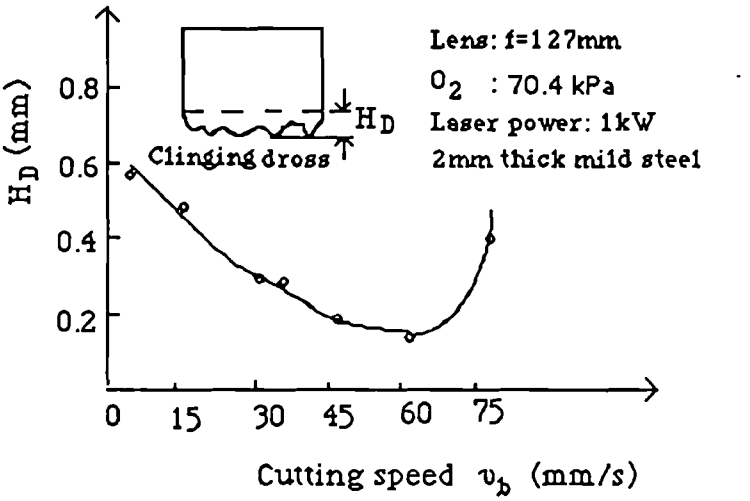
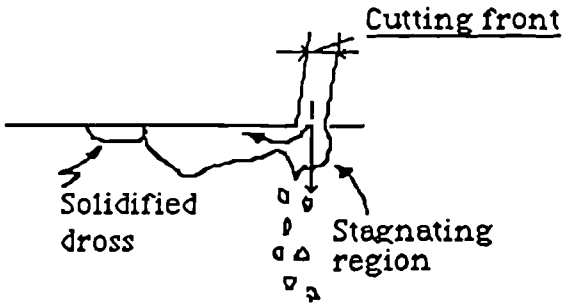


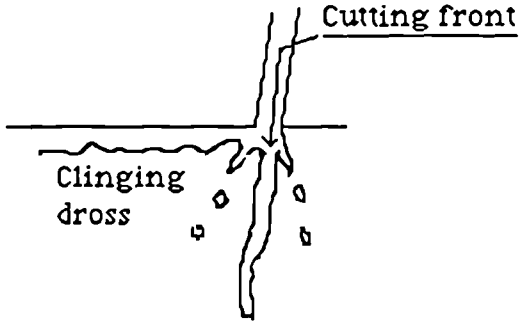
Fig. 1 -17. Effect of cutting speed on the amount of dross clinging [28].

It is seen that at low cutting speeds, the cut is accompanied with a large amount of clinging dross. The molten flow briefly stagnates on the bottom edge. A part of this molten flow is ejected as a large number of small spherical dross particles by the shear force of the gas flow. Simultaneously, the other part flows backwards along the bottom edge and is finally solidified as clinging dross (Fig. 1 -18). This phenomenon changes remarkably with cutting speed [28]. When the cutting speed is high, the amount of dross adhering is reduced. The backward flow, as shown in Fig. 1 -18, is weak in this case, and a long pendant stream forms at the base of the cut front (Fig. 1 -19). Thus most of the spherical dross particles are formed at the leading edge of this pendant part. When the cutting speed is further increased, the laser beam may fail to fully penetrate causing the angled striation patterns on the cut edge (Fig. 1 -20) [3,28]. The dross fails to clear quickly from the bottom edge leading to a rough edge.



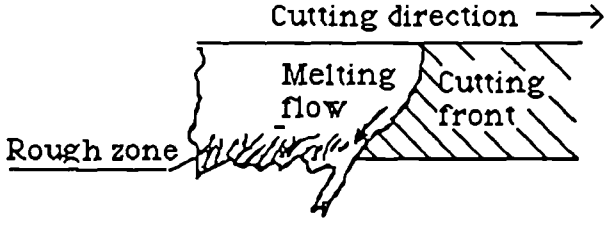
Cutting speed: 1.4 m/min.
O_2 : 70 kPa
Laser power: 1kW
Thickness: 2mm mild steel

Fig. 1 -18. Description of the cut with a large amount of clinging dross at low cutting speed [28].



Cutting speed: 3m/min
Other conditions: the same as in Fig.1 -18.

Fig. 1 -19. Description of the cut with a little amount of clinging dross at higher cutting speed [28].



Cutting speed: 5m/min
Other conditions: the same as in Fig.1 -18.

Fig. 1 -20. Description of the cut with rough kerf zone [28].

1.2.2.4.4. Effects of cutting speed on the extent of heat affected zone

The relationship between the cutting speed and the heat affected zone (HAZ) has been studied by many researchers [3, 104, 106] and is illustrated in Fig. 1 -21 (HAZ was measured by surface oxidation marks).

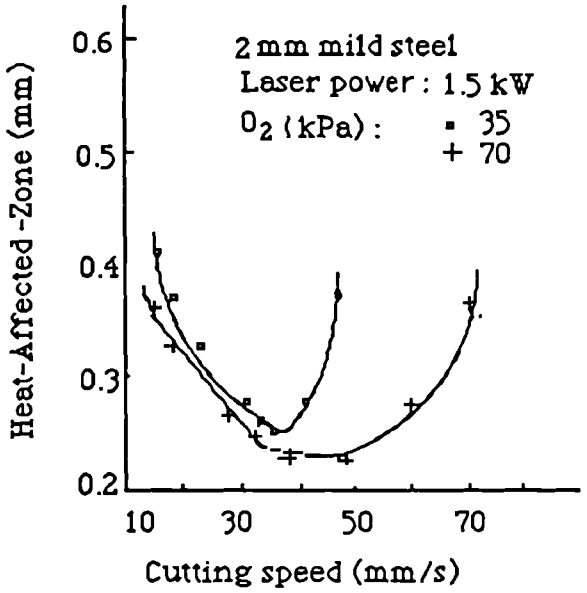


Fig. 1 -21. Variation of heat affected zone with cutting speed [3].

As can be seen from this figure that the width of the HAZ decreases with increasing the cutting speed. This is because the energy input per unit time decreases with increasing cutting speed so affecting the HAZ [104] . When cutting speed is further increased, the dross fails to clear quickly from the bottom edge resulting in a sharp rise in the HAZ [3]. In fact, there is a strong correlation between the extent of the HAZ and the quantity of the adherent dross. This correlation is roughly seen by comparing Fig. 1 -17 and 1 -21. At the gas pressure of 70 kPa, both curves have similar trends against cutting speeds, i.e. where there is a large quantity of dross adherent there is a correspondingly wide HAZ.

1.3. Gas Composition Effects on Laser Cutting

The gas parameters have been discussed in 1.2.2.2. Here a more detailed discussion concerning the gas composition effect on laser cutting performance is presented, since this is particularly relevant to some of the author's work.

In laser cutting applications most of the materials are cut with the aid of either an inert gas such as nitrogen and argon (fusion cutting) or a reactive gas such as oxygen (reactive fusion cutting).

In fusion cutting the laser beam merely melts the workpiece, while the inert gas jet has the sole task of removing the molten materials from the cut. The physical mechanism involved in this process is similar to that of the reactive fusion cutting process (section 1.1) but simpler due to the absence of exothermic reactions. It can be summarised as follows [3]. The laser beam strikes the workpiece surface, some of its energy is reflected while the rest is absorbed, evaporating a small hole ("keyhole"), which acts as a blackbody and absorbs all the laser energy. Initially, the "keyhole" is surrounded by molten walls. The inert gas enters the "keyhole" and blows the molten material out of the bottom of the hole. While the workpiece moves forward, the leading edge of the "keyhole" is traversed leaving a slot (cut kerf). The laser beam now strikes only the leading edge of this cut kerf from which a steady or pulsing flow of molten material is blown. In general, the cut appearance is characterised by a narrow HAZ edges free of oxides, due to the lack of chemical burning reaction, and free of dross if the gas flow is correct. However the cutting speed is usually much lower than that with reactive gas cutting due to the absence of the contribution from the exothermic combustion energy [65,116].

In oxygen assisted cutting, the process is similar but at the cut face the laser beam heats up the workpiece to its ignition temperature initiating the oxidation reaction in a defined area. The exothermic reaction heat increases the energy input, raising the maximum cutting speed [116].

However, it was reported that laser oxygen cutting of some materials e.g. stainless steel, imposes some limitations on further processing of the cut components since the material is burnt away forming different types of iron-oxides and chromium-oxides (slag) [55,115,116]. Because of the high melting point the slag solidifies before it is blown out of the kerf during the cutting process. The slag is partly pressed into the molten zone in the cut kerf and partly placed as a burr on the lower edge of the cut kerf. This slag is difficult to remove, and thus may cause problems in cut

finish or in subsequent welding. When using special gas mixtures slag free cuts can be achieved without significant reductions in the cutting velocity [55, 115] (Fig. 1 -22). This is further discussed in this thesis in chapter three.

Figure 1 -22 shows the cutting velocity as a function of the gas concentration when cutting 0.5 mm and 1.0 mm stainless steel. The cutting gas mixtures were two-component gases, i.e , gases based on an inert gas mixed with oxygen. As can be seen from this graph, in the concentration range 100-90% oxygen the cutting speed decreases rapidly compared to normal oxygen cutting, from 14 m/min to 7 m/min cutting of 0.5 mm thick stainless steel and from 7 m/min to 4 m/min when cutting 1.0 mm material. However in the concentration range 90-70% oxygen there is a tendency to increasing cutting velocity most distinct for 0.5 mm thickness. It seems that helium mixtures in general show the highest cutting velocity possibly due to its small molecule size thus having least blocking effect for oxygen diffusion to the burning front. In the range of 70-55% oxygen the cutting velocity is constant followed by a decrease in the range of 55-40% oxygen.

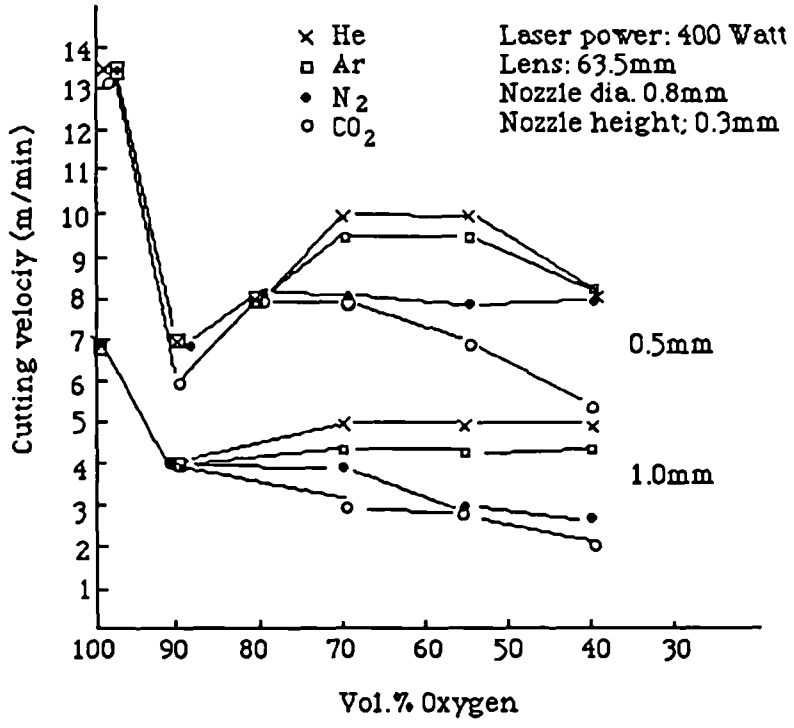


Fig. 1 -22. Laser cutting of 0.5 mm and 1.0 mm stainless steel using mixed gases as assistant cutting gas [55].

In this work, TIG welding of the laser cut stainless steel was tested using the following gas mixtures:

100% O_2 , cutting at 7.0 m/min;

60% He + 40% O_2 , cutting at 5.2 m/min;

Air (78% N_2 + 21% O_2), cutting at 1.5 m/min;

100% Ar, cutting at 0.4 m/min.

The evaluation of the welds was done in two steps: direct visual inspection of the welds and by metallurgical examinations. The results were however the same from both methods and can be summarised as follows:

(i).Workpiece cut by 100% O_2 was not weldable: In most cases there was no joining of the edges. In some cases the workpiece was partly joined with many holes and considerable porosity. The partly joined area was only welded at the surface.

(ii). Other workpiece were welded normally.

Therefore, laser cutting of stainless steel using proper gas mixtures was shown to be beneficial in terms of oxide free cuts and good weldability for further processing.

Laser cutting of other materials using mixed gases may also lead to interesting results. The gas effects on cut quality (dross adhesion, surface roughness and HAZ) are important and have yet to be established. This will be presented in this thesis in chapter three.

1.4. Automatic Beam Alignment Techniques

Beam alignment after the output window of the laser cavity involves two aspects, i.e., mirror alignment and nozzle alignment.

1.4.1. Mirror alignment.

In the current laser materials processing system, the laser beam is usually delivered to the workstation through a long distance from the

laser generator. This requires an accurate alignment of the beam. Manual alignment is very time consuming and may not be accurate. In addition, long path lengths are more susceptible to accidental disturbances such as misalignment. Therefore methods for on-line automatic beam alignment system are necessary. Unfortunately, very few methods are available.

A technique placing four acoustic sensors on the back of the mirrors is being developed both at Imperial College and Liverpool university (U.K.) to make sure that the laser beam always strikes on a fixed point on the beam guidance mirror (the last mirror) [176, 205]. . Experiments have shown that the maximum root-mean-square (RMS) value of the sensor output is obtained when the laser beam strikes the mirror where the central axis of the sensor is located. The magnitude reduces when the laser beam moves away from the sensor. Thus the mirror can be adjusted by rotating proper angles until signals from the all four sensors are equal.

A device was developed by Loosen[213] to measure the beam position. This device consists of four metal wires, which are automatically and repetitively moved into the beam for a short time resulting in the heating of the wires. By measuring and processing of temperature-time functions of the wires electronically, the beam position can be investigated [213].

1.4.2. Nozzle alignment.

In the laser cutting process it is important that the laser beam is perfectly centred with respect to the co-axial cutting nozzle, since even slight deviations can have noticeable effects on cut quality [118-122]. Figure 1 -23 shows the effects of decentralising on kerf width. Kerf width generally increased with misalignment. Figure 1 -24 shows the effects of decentralising on surface roughness. It also shows a general trend of deterioration with misalignment. The effect of cutting speed on surface roughness can be quite clearly seen. At higher cutting speeds the variation of the surface roughness with the beam misalignment is more pronounced because of the lower roughness values obtained when the beam was well centred [118].

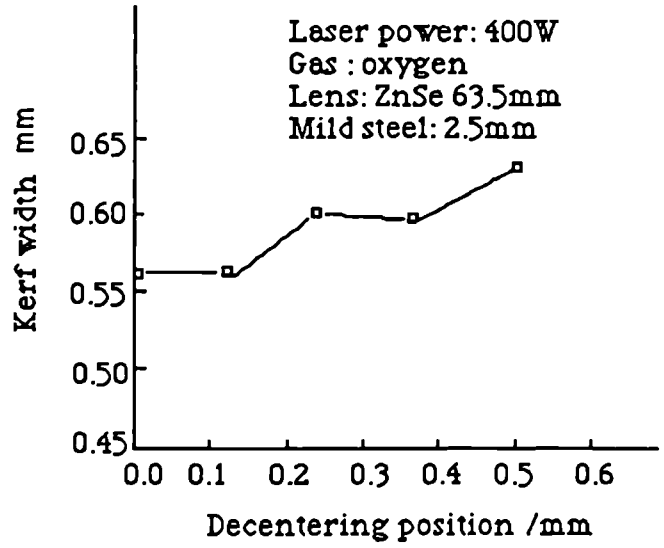


Fig. 1 -23. Effects of decentralising on kerf width for a 1.5 mm nozzle, with a standoff of 1 mm, cutting speed at 15 mm/s [118].

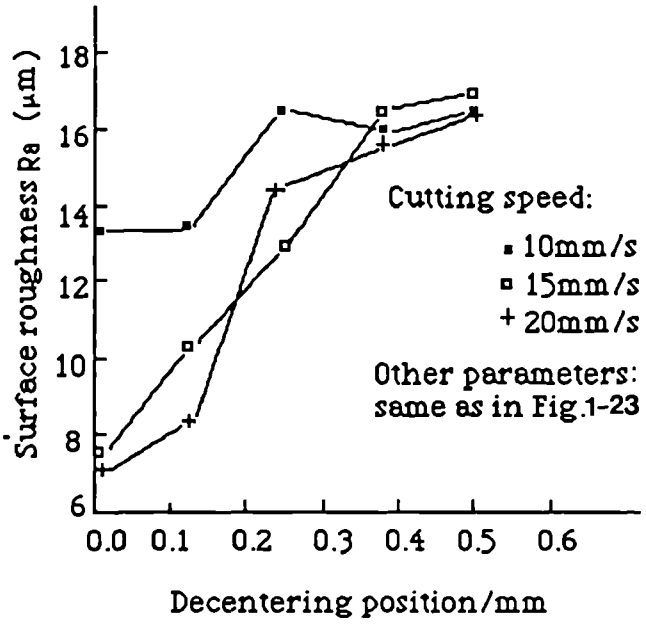


Fig. 1 -24. Effects of decentralising on surface roughness at different speeds [118].

There are many different methods currently being employed for centring the beam within the nozzle. One such method is to use a piece of material (workpiece) with a smear of grease on its surface. Placing the

workpiece in the focal position and firing a laser together with the assistant gas pulse leaves a pattern in the grease which clearly identifies the centre of the jet and also marks the laser spot. A magnifying glass can then be used to assess the alignment of the two marks to an accuracy of perhaps $\pm$ 0.05 mm [29, 118] . The presence of any anomalous streaks in the grease pattern also indicates the presence of nozzle damage sufficient to influence the gas flow [29]. This method is widely used but not accurate enough for very fine laser cuts, since minor misalignment e.g. 0.05 mm could have noticeable effects on kerf width (Fig. 1 -23) and surface roughness (Fig. 1 -24).

Another method often employed is to cut wood in the two axes of the work table and to inspect for side burning on the top of the cut. If there is side burning on one side of the cut it means that the laser light is touching the opposite side of the nozzle and the nozzle should be adjusted accordingly [120]. This method requires experience and takes a long time.

The direction of sparks generated when a laser pulse strikes on a piece of alumina ceramic can also be used as a guide to centring. When the nozzle and beam are misaligned the sparks fly in a preferred direction. The approximate nozzle centre can be found by adjusting the nozzle until the sparks are generated radially. The accuracy of this method again largely depends on experience and the method can be time consuming.

The use of a power meter below the nozzle has also been reported [119]. The nozzle centre is found by adjusting the nozzle so that a maximum power output is obtained. Obviously, this is also a trial and error method and could take a long time to achieve correct alignment. A different method is discussed in this thesis in chapter two.

1.5. Monitoring of Laser Cutting Process

As already discussed in section 1.2, laser cut quality is influenced by several parameters such as laser beam quality, the gas flow and the cutting speed. In order to examine the cut quality in-process the first step must be to identify in-process if the cut quality is acceptable. The next step is then to optimise the cut quality by the on-line adjustment of the cutting parameters. Thus, signals which need to be monitored from a laser

process fall into three categories [122-124]: beam characteristics, workstation characteristics and in-process monitoring of workpiece cut quality. The last category is the most complex and forms the central topic of this Ph.D project.

1.5.1. Monitoring of beam characteristics

Laser beam characteristics are usually defined as : laser power, beam mode structure, beam divergence and beam diameter. There has been considerable research into developing techniques for measuring these parameters. These methods can generally be classified into two groups: off-line methods and on-line methods.

1.5.1.1. Off-line techniques

Off-line methods for laser parameter measurement are to use the whole laser beam for the measurement. Thus the laser beam can not be used for processing during the measurement. The commonly used techniques were reviewed in references [132, 192] and listed in Table 1 -3 .

Among these methods the water flow calorimeter is the most commonly used device for high power CO_2 laser, since it also acts as a convenient beam dump. Pyroelectric or thermopile beam power meters are often used for the measurement of low power lasers (below 1 kW). Pyroelectric sensor array, photodiode sensor array, thermo-resistor arrays and thermopile arrays are the most popular commercial instruments for the off-line measurement of beam diameter and beam profile but only suitable for low power lasers (less than 1 kW). Beam printing in a piece of perspex is often used in practice as an easy , quick way of checking the beam profile. The other methods e.g. thermal printing are also used for measuring beam size and beam profile.

Table 1 -3. Off-line techniques for laser beam measurement

Method	Principle	Beam profile	Power	Charac-teristics	References
Burn pattern	Thermal damage (acylic/polymethyl-methacrylate/)	Yes	No		151,132,156, 160-163
Thermography	Thermal image plate /thermal paper	Yes	No	Low power	130,152,153, 159
Water flow calorimeter	Thermal	No	Yes	low sensi-tivity	166
Photon drag	DC potential in Ge	Yes	Yes	high power pulsed only	141,158,163
Infrared vidicon	Video image	Yes	No	low power beam	154
IR /CCD Camera (charge coupled device)	Thermal image	Yes	No		122,130,149
Thermopile	Thermal	No	Yes	less than 1kW	140
Spherical cone	Thermal	No	Yes	Focussed beam	131,159
Thermal resistor array	Thermal	Yes	Yes	less than 1kW	146
Pyro-electric sensor array	Optical	Yes	Yes	IR beam less than 1kW	167-168
Photodiode array	Opto-electric	Yes	Yes	Visible / less than 1kW	169-170
Heating plate & use of micro-phone/thermo-couple	Photo-acoustic/	No	Yes	pulsed beam	171
	Thermal	Yes	Yes	unfocused beam	155
Ge-Cu/ HgCdTe sensor	Quantum	No	Yes	Low power	129,131

1.5.1.2. On-line techniques

On-line methods take a small portion of the laser beam even when the laser beam is used for processing and use this to analyse the whole beam. The commonly used techniques for this purpose were well reviewed by some researchers [123,132,164]. Based on these references a summary of the commonly used methods was made and shown in Table 1 -4.

Table 1 -4. Methods for in-process monitoring beam characteristics .

Method	Principle	Beam profile	Beam power	Charac-teristics	References
Beam scanning sampler	Rotating needle	Yes	Yes	Continuous IR beam	list 1a -1d as below
Partially transmissive back end mirror	Beam splitting	Yes	Yes	Off-line meter can be used	131,132,165
Beam splitter	Beam splitting	Yes	Yes	Off-line meter can be used	130,156,
Perforated mirror	wave front sampling	Yes	Yes	focused beam	133
Choppers	rotating blade /mirror	Yes	Yes	Continuous beam	134,150,169, 166,168,167
	hollow needle	Yes	No	Continuous	135
Heating a gas	Thermal	No	Yes	Pulsed or continuous	136-138
Transparent flat plate	Optical scattering	No	Yes	Fast response	139
Heating of wire	Thermal	Yes	Yes	Continuous	142
Acoustic mirror	Photon-stress	Mode	Stability	Fast response	123,143,147, 148
Thermopile mirror	Thermal	Yes	Yes	Continuous	145
Thermo-couple mirrors	Thermal	No	Yes	Position dependent	144,157

According to the type of sensors used, the procedure of measurement and the instrument design, the on-line beam monitoring can be grouped into the following categories:

1). Beam scanning sampler: This method employs usually a wire or a needle or a mirror to scan through the laser beam to abstract a small fraction of the beam for measurement. The direct information from this kind of instrument is the laser beam intensity distribution. Due to the restriction of the sampling rate, this type of instrument is mainly used for continuous laser beams. Thus four different devices can be found using this technique.

1a). Laser beam analyser (LBA): This device was invented at Imperial

College (UK) by G.C. Lim and W.M. Steen in 1982 [127]. The operation of the device is briefly illustrated in Fig. 1 -25.

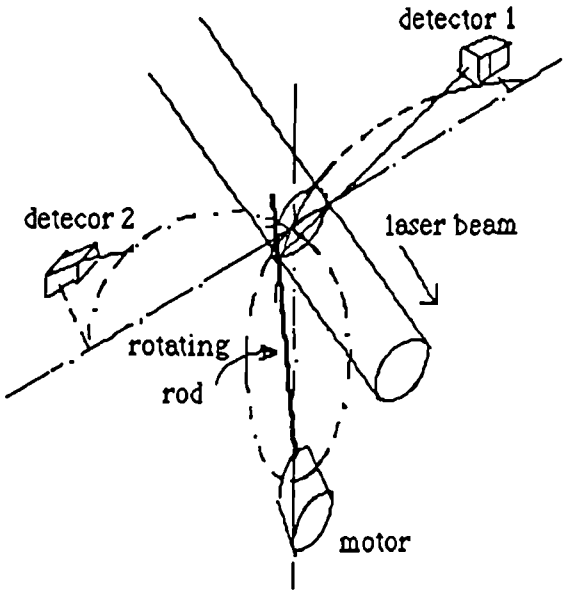


Fig. 1 -25. Illustration of the operation of the LBA [124].

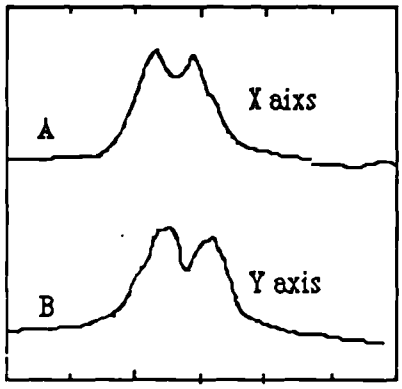


Fig. 1 -26. Typical output from the LBA showing a near TEM_{01} mode pattern [124].

A thin , highly reflective straight rod is attached radially to the axis of a synchronous motor. The rod rotates in a plane perpendicular to the beam. Since there are two pyroelectric detectors, two simultaneous orthogonal passes of the beam are made by a single pass of the thin reflective rod. The output signals from the detectors are amplified with built in amplifiers and then fed into an oscilloscope which displays the beam profile in the two orthogonal axes directly. By arranging for the peak signals of the two traverses to be of the same intensity the beam can be correctly centred [124] . Schematic traces from this analyser are shown in Fig. 1 -26.

The signals can be further analysed to derive the principle variables required: the beam diameter, relative central power, approximate power distribution, and approximate overall power [124]. The LBA can also measure other variables of considerable in-process value. For example, if the take-off location points (A,B) shown in Fig. 1 -26 move relative to each other then the beam has moved. The amount by which the beam has

wandered can be calculated and an adjustment made in order to ensure that regardless of guidance mirrors being subjected to various thermal movements the beam will remain correctly aligned [124]. Another example is that if small peaks occur before the take off location this usually signifies that the laser cavity mirrors need tuning [124]. A further example is the daily check on the state of of the system optics by comparing the mode structure from day to day [124]. The latest computer attachment [126] to the LBA allows the storage of two digitised mode structures with full comparative read out. Further mode structures can be stored and analysed mathematically by transferring the digital signal to a personal computer. These digitised mode structures can be analysed to indicate the diameter of the beam, or give a reading of the power envelope area (approximately proportional to the overall power) or the maximum power within any particular recorded mode [124]. Since the information is digital it can therefore be used to adaptively control the laser power. An in-process laser power monitoring and feedback control system based on an LBA was reported [164]. The basic principle of this system is as the follows. The signals from the LBA are converted into laser power by integrating the area beneath the curves or using the RMS signal of the output. The RMS signal was then chosen as the power sensing signal. The analogue signal from the display was passed to an analogue/digital converter and via a control unit in which it was compared to a controllable reference signal. The signal generated from the comparator was used to control the laser tube current and thus the laser power [164].

1b). Multifacet rotating mirror: Developed by Juptner (Germany) in 1986 [166] , this device uses a mirror-wheel with eight mirror stripes arranged spoke-like at an angle of 45^0 to the beam axis. The thin side of the mirror stripes are provided as plane reflectors. At any one time only one of the mirrors is in the area of the transmitted beam. This mirror reflects one small line of the laser beam at an angle of 90^0 onto the revolution axis, where three pyroelectric detectors are mounted in a distance of 16 mm relative to each other. The signals are then fed into a micro-processor for digital analysis and video display. Since 24 lines of the signal can be obtained for each revolution of the wheel, a three dimensional image of the laser beam mode can thus be displayed.

1c). Chopper blade laser beam sampler: Developed by Austin (U.S.A.)

in 1986 [193] , this instrument including two parts: mode viewing and power sensing. The mode viewing was realised by deflecting a small portion of the laser beam (less than 1%) with a high speed (2400 r.p.m) aluminium chopper to a luminescent phosphorous plate, which was being viewed by a TV camera. The power sensing was effected by using another chopper, which consists of two polished nickel blades and is rotated across the laser beam onto a thermopile network. The thermopile network then converts the laser heat energy to an electrical signal which is proportional to the laser power.

1d). Hollow needle beam sampler: This was developed at Fraunhofer-Institute of Laser Technique (W. Germany) by Beyer et.al. in 1986 [135]. The device was specially developed for monitoring focussed laser beams. As shown in Fig. 1 -27, the laser beam is sampled through a hollow rotating needle and reflected inside the needle down to a pyroeletric sensor. To get the whole beam profile the needle is moved linearly perpendicular to the beam in such a way that each cut line through profile is detected with every rotation of the needle. As a result the whole beam can be sampled in a short time (9 seconds approximately) and three -dimensional beam profile obtained.

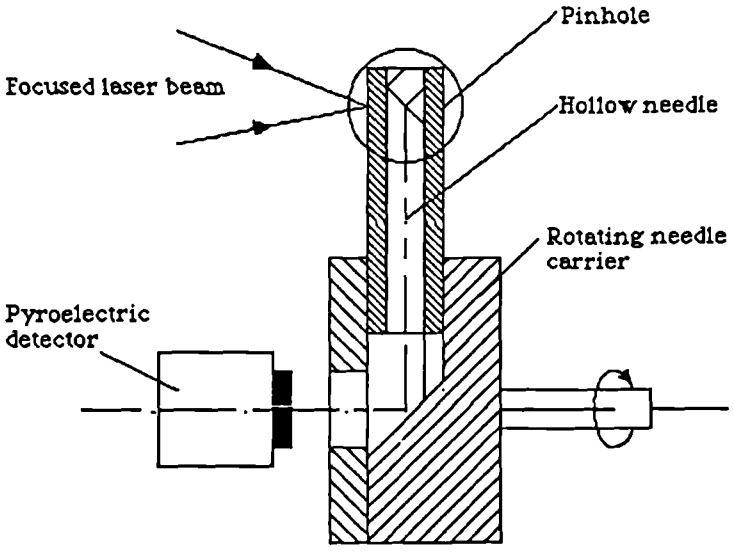


Fig. 1 -27. Hollow needle beam sampler [135].

1e). Perforated mirror: This device was developed by the Culham Laboratory (U.K.) [133]. A hole-matrix diffraction grating is used as the

final mirror which transmits a small fraction of the power. Insertion of a lens in the beam transmitted through the hole-matrix results in a diffraction pattern in the focal plane. This pattern is a matrix of separated principle maxima, each with an intensity distribution which is a good approximation to the intensity distribution of the main beam in the far-field [133]. Thus analysis of the focussed beam which has passed through the mirror gives estimates of the focused main beam power, shape, position and polarisation state.

2). Beam splitting: These devices are used to split the laser beam so that a small portion of the beam is continuously directed to the detectors. A distinctive feature of this type of instrument is that most of the off-line beam measuring devices can be used for on-line monitoring.

2a). Partially transmitting mirror for beam splitting: An instrument was developed at Electrotechnical Laboratory (Japan) by Ikeda in 1986 [156]. This device uses partial transmitted mirror (silicon wafer coated with gold for 1-3% power transmission) and a reflecting prism for beam sampling. The transmitted signal is directed to a second silicon wafer for further attenuation and then to a HgCdTe infrared sensor for measurement. The horizontal scanning is carried out with the rotating prism driven by a motor. The vertical scanning is achieved with rectilinear motion of the prism and sensor. The signals are analysed by a microcomputer to map out the beam profile.

2b). Partially transmissive back end mirror: Two examples based on this principle can be found.

The first instrument was developed by Delta Development Co. (U.S.A.). It simultaneously monitors both the pulse shape and average power of the high-power CO_2 lasers [165]. The basic principle is to measure the laser power through a 1% transmitting mirror at the laser cavity's non-output end. A wedged beam splitter routes the bleed power to two detectors: a pyroelectric detector for wave form monitoring; and a platinum resistance bolometer for measuring the power.

The second device using an integrating sphere and partial

transmissive back end mirror was developed by Drenker at Fraunhofer Institute of Laser Technology in 1988 (Germany) [131]. The detecting unit consists of a pyroelectric detector and a thermopile mounted to an integrating sphere (Fig. 1 -28). The portion of the beam penetrating through the partially transmitted rear back end mirror is collected by a focusing mirror and directed into the sphere where the distribution of the intensity is homogenised by multiple reflections, which guarantees that the intensity of the radiation impinging onto both detectors is proportional to the entire beam power. Signals from both detectors are electronically corrected and combined to a single output signal which is proportional to the beam power over a band width of 300 kHz.

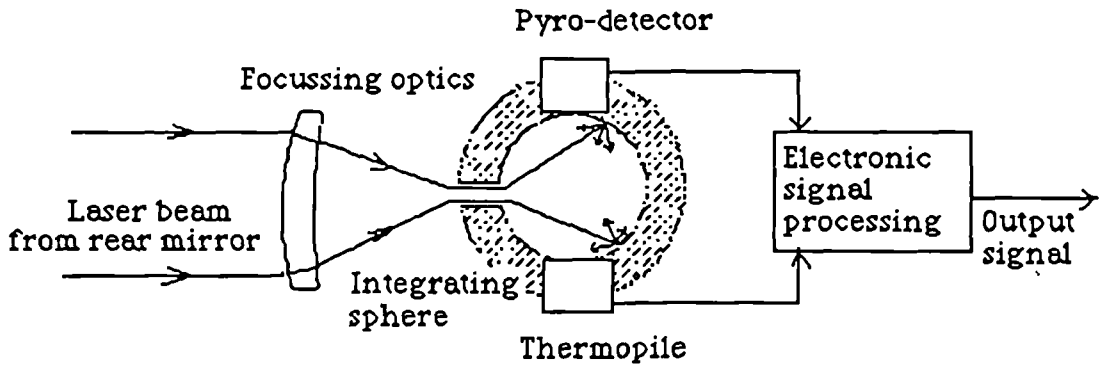


Fig. 1 -28. Illustration of the detecting unit [131].

3). Beam scatter: A transparent flat plate was used by Crow (U.S.A.) [139] in the laser beam path. Four photodiodes were attached to the sides of the plate to catch the scattered laser beam. The signals were summed up to obtain the average laser power through calibration. This method is for visible beam monitoring.

4). Thermal mirror: Several instruments have been developed based on this principle [144,145,157]. By placing a thermocouple or a thermopile or thermal resistor arrays at the back of the mirror laser power or beam profile can be determined without disturbing the laser beam. This technique however requires the redesign or modification of the existing laser mirrors.

5). Heating of gas: The principle of this technique is as follows [136-138]. A gas chamber is position in the beam path thus the gas is

heated by the laser. The changes of gas temperature or gas pressure can be then detected by either a temperature detector or a pressure sensor or a microphone. This method requires that the laser beam is pulsed or chopped or the gas density is modulated for effective sensing. Since little energy is lost in heating up the gas, this method does not disturb the use of the laser beam for processing. It is mainly useful for very high power beams (> 10 kW).

6). Heating a wire: This method uses a thermoresistive wire to scan across the laser beam so that the change of the resistance by the laser heating can be detected. The signals can then be related to the laser beam power and possibly to the beam profile [142].

7). Acoustic mirror: This technique was developed at Imperial College (U.K.) by Weerasinghe and Steen in 1984 [147]. The basic system set-up is shown in Fig. 1 -29. By placing an acoustic emission (A.E.) transducer at the back of the last mirror, changes of the laser beam characteristics can be detected including the power density and wander [123,124,148]. One of the advantages of this method is its fast response to very high frequency changes of the laser beam (up to 2 MHz), which could be used for monitoring the pulsed laser beam as well. This method can be used for measuring very high power laser beam due to its non-intrusion of the beam. However this device experiences difficulties in providing individual information on laser beam profile, diameter, and laser power.

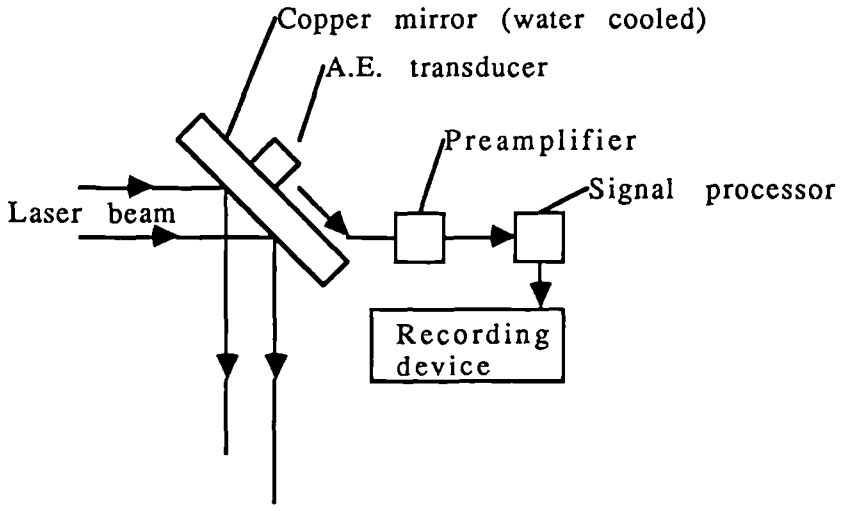


Fig. 1 -29. Acoustic mirror detection system [124].

1.5.2. Monitoring of workstation characteristics

The monitoring of workstation characteristics includes the position and traverse speed control of the workstation and the focal position control (nozzle standoff control). The movement of the workstation is usually realised by a CNC table equipped with encoders and tachometers. Thus both position and velocity can be accurately controlled [172].

The nozzle standoff distance (nozzle height) is a crucial parameter in laser cutting as discussed in section 1.2.2.2. Thus the nozzle standoff has to be on-line controlled to guarantee a high cut quality.. This is particularly necessary in the case of contour shape cutting. The following methods are usually used for the nozzle height control.

(i). Ride-on nozzle assembly: This method uses a special nozzle assembly using floating Z axis with bearings "sitting" on the workpiece. Thus the nozzle height is kept the same during processing. The contacting feature limits its use for high speed contour cutting.

(ii). Capacitive nozzle: This technique was patented by Rofin-Sinar Co. (Germany) for autofocussing in laser cutting. A collar shape capacitive sensor was fitted to the nozzle to detect the nozzle standoff distance. The signal is then fed back to a servo control system to maintain the desired nozzle height with an accuracy of $\pm$ 0.2 mm [173]. This system, however, requires that the workpiece must be an electrical conductor so that it forms part of a capacitor. It is also vulnerable to problems with surface debris and proximity of edges.

(iii). Laser diode probe: An optical height sensor consisting of a laser diode and an optical position sensitive device (PSD) was developed by Mitsubishi Electric Co. in Japan in 1985 [174]. Its principle is that the change of the reflected beam position on the PSD is proportional to the change of the nozzle height. Thus the signals detected from the PSD can be fed into a servo controller for height control.

(iv). Infrared height sensing: Based on an infrared distance sensor, an automatic height sensing system was developed by L. Li at Imperial College, London (U.K) [192]. An accuracy of $\pm$ 0.1 mm for dynamic slope

position control was reported.

Other methods include inductive sensing, feeler and pressure sensing etc. as summarised by Steen [175].

1.5.3. State of art work on in-process cut quality sensing and control

A few papers [17,166,177-186,188,191] have discussed the different techniques for in-process quality analysis of the laser cuts. Based on different indirect methods of quality detection these methods fall into the following groups.

1.5.3.1. Monitoring the shower of sparks

This technique employs either photodetectors or video cameras underneath the workpiece to detect the intensity distribution and the angle (direction) of the sparks shower. Usually, a good correlation between the cut quality and the sensor signals can be obtained [17, 177,179,182]. One disadvantage of the method is the restrictions on the sensor positions as outlined in [178], namely, limited space, evaporated material or implementation into industrial machines with moving optics. Three typical arrangements using this technique can be found.

(i). Registration of the shower of sparks: This arrangement was reported in 1986 [177]. Its operation can be shown as Fig. 1 -30, where a photoconductive cell was used to detect the light emitted from the shower of sparks.

It was found that when the cut was of good quality, the photoconductive cell was illuminated homogeneously, and a high level signal was measured. In other cases, when for example beads of clinging dross formed, an unsteady signal was observed resulting in a corresponding lower level of the sensor signal, but with a higher fluctuation.

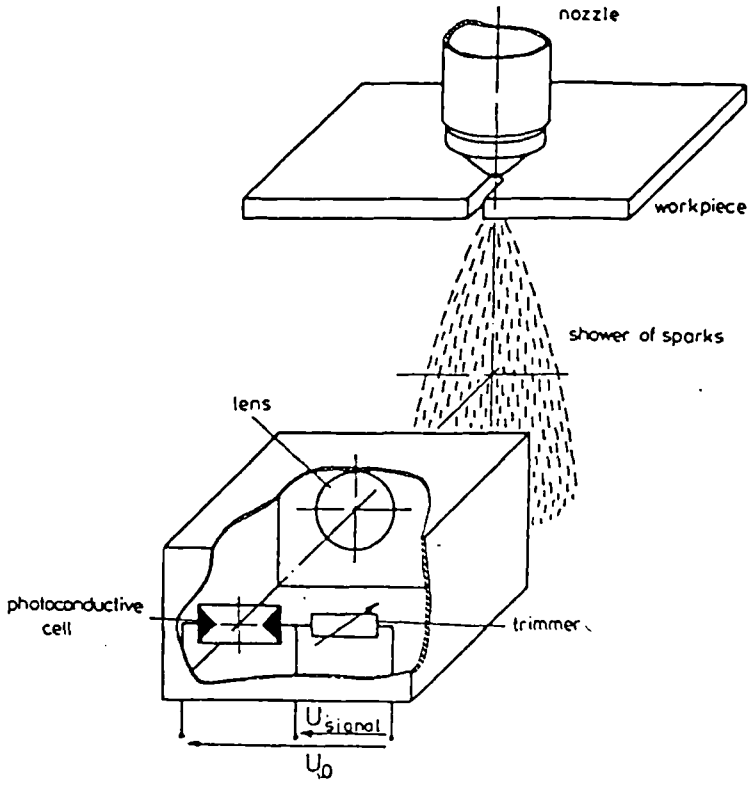


Fig. 1-30. Registration of the shower of sparks [177].

(ii). Viewing the cone pattern of the sparks: A "smart" laser cutter was developed at ETCA (France) [179,182], where a TV camera was employed to monitor the spark cones produced during the laser cutting process. The cone angle and symmetry were found to be related to the cut quality. Different operating parameters (e.g. cutting speed, gas flow rate and laser power) resulted in different cone patterns. For instance, if no cone was present, this meant that the laser beam was not penetrating the plate due to, for example, too low power density. If molten materials were clinging to the bottom edge, the cutting speed was probably too low or the gas assistance was inadequate. If a very inclined cone was observed, this possibly meant that the cutting speed was too high. All these observations were simultaneously processed by a real-time image processor. Then a rule-based decision making system estimated the cut quality, searched for optimum operating parameters according to appropriate rules and adjusted

the operating parameters to guarantee a good cut.

(iii). Viewing the angle of the shower of sparks: An attempt to correlate the angle of the shower of sparks from the cut kerf with the angle of striations of the cut surface was made [17]. Figure 1 -31 shows an example of this correlation. The results showed that the main angle of the spark-shower corresponded to the angle of the striations at the lower part of the cut face.

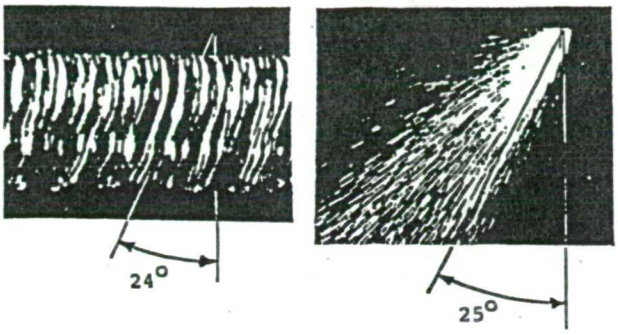


Fig. 1 -31. Striations and spark-showers, at cutting speed of 90 mm/s, gas pressure of 400 kPa and laser power of 600 W. Material: 2 mm thick of mild steel [17].

1.5.3.2. Monitoring of the laser beam reflections.

This technique measures the laser beam reflections from the cut kerf either in the downward or the backward (up through the cutting optics) direction. A system using a pyroelectric sensor to study the angular distribution and intensity of the laser light emerging down through the cut kerf during the cutting process was developed [178]. The basic set-up is shown in Fig. 1 -32. The detecting unit consisted of a lens collimating the light emerging from the bottom of the cut front into the pyroelectric detector. In front of the detecting unit an aperture with a 4 mm bore was placed in order to protect the detecting unit against molten materials from the cutting process. Relationship between cut quality (good, acceptable or poor) and the light intensity was indicated. This method again has restrictions for industrial machines due to it being underneath the plate .

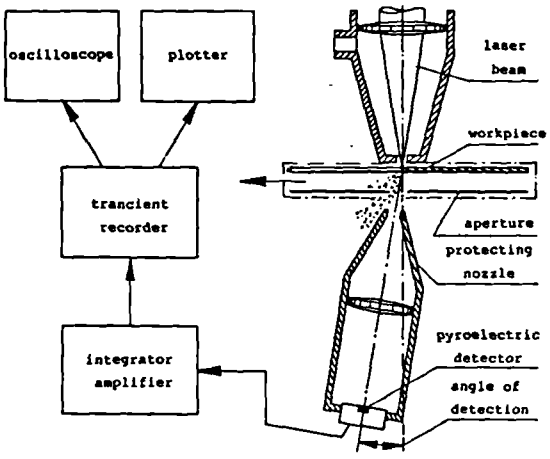


Fig. 1 -32. Detection of angular distribution of laser light passing through the cut kerf [178].

The detection of the backward reflection of the laser beam for laser cutting process has not been reported so far. In chapter five of this thesis back-reflected acoustic signals are discussed. These back reflection signals were applied to the laser welding process as reported in [124, 187, 189].

1.5.3.3. Thermal detection of the cut front temperature.

This method uses a radiation pyrometer with a wavelength of (8.05 $\pm$ 0.15) μm to measure the intensity of the infrared radiation from the cut front [177]. The pyrometer was positioned off-axis with an angle to the workpiece to look at the cut front. The correlation between roughness Rm and temperature in the kerf Ts at various cutting speeds were shown in Fig. 1 -33. It was argued that the heat loading to the workpiece is minimal (i.e. the energy transfer to the cutting process itself is maximal) if the cutting process results in an optimum cut quality. If the cutting speed is too low there is more energy from the laser presented than is needed for cutting; if the cutting speed is too high the molten material cannot be blown out of the kerf as quickly as necessary so that the heat contact to the cutting surface is elongated. The temperature signals are however strongly dependent on the cutting direction because of the viewing angle

of the radiation pyrometer.

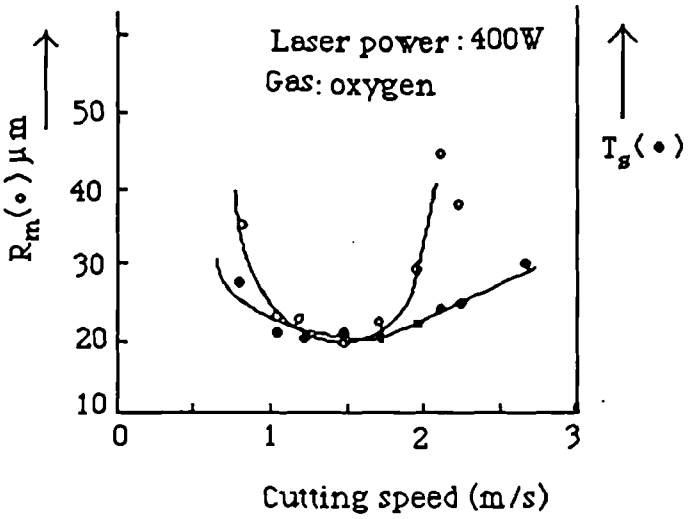


Fig. 1 -33. Correlation between roughness Rm and temperature in the kerf T_s at various cutting speeds (mild steel, 3 mm thick) [180].

A pyrometer was also used for measurement of the surface temperature during the laser hardening process [180]. It was shown that there was a strong correlation between the surface temperature and the depth of focus. The use of photodiodes for axial and off-axis monitoring of the cutting process is discussed in chapter four of this thesis.

1.5.3.4. Direct observation of the geometry of the cut kerf.

The use of an endoscope together with a CCD camera makes it possible to observe the cut kerf directly [177, 188]. Figure 1 -34 illustrates the operation of the system. According to the report, characteristic faults of the cut kerf can be easily identified such as cut without complete separation and parts of the clinging dross bridging the bottom of the kerf. However, this method cannot indicate any valuation of the grade of the roughness of the cut faces, and requires real-time image processing which is usually quite slow.

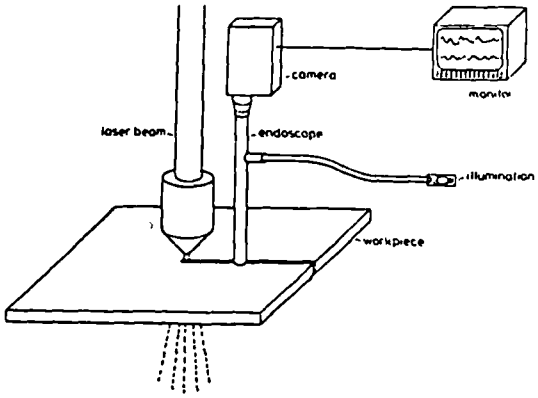


Fig. 1 -34. Observation of the cutting process by an endoscope [177].

1.5.3.5. Monitoring of the light emission from the cut front

The principle of this technique is to detect the light emission during the cutting process including light emitted from the cut front, plasma and sparks. Thus several different approaches can be found.

(i). Vision system: As shown in Fig. 1 -35, the system employs a CCD camera viewing the cut front through the focal lens and via a GaAs -window, which was antireflection-coated on both sides transmitting 99% of the laser beam but was reflective to visible lights [178]. In front of the visible camera different apertures were placed in order to reduce spherical aberration arising from the simple fact that $\sin\theta$ is not truly equal to θ except at $\theta = 0^{o}$ [190] and adjust the camera illumination. It was found that in case of too slow cutting speeds, the light emission from the cut kerf was varying both in spatial distribution and in intensity. In the case of correct cutting speeds, the light emission was stable and the intensity distribution in the cut kerf was fairly uniform. The light emission from the cuts performed with too high velocity was also reasonably constant, but the intensity was high in the front area of the cut kerf [178]. This method is believed to provide enough information to evaluate the cut quality but may have difficulty in minimising both the image sampling and the computing time in order to cope with the laser cutting process.

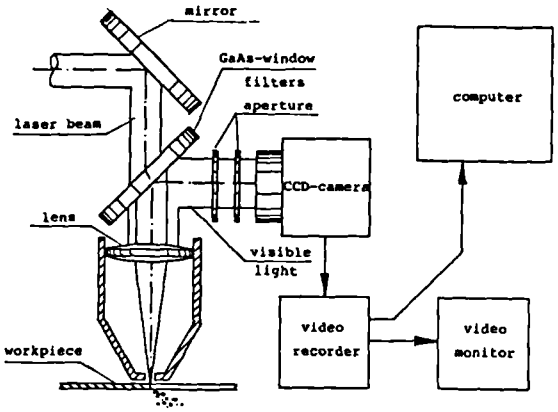


Fig. 1 -35. On-line cut quality detection by vision system [178].

(ii). Optical detection of the plasma transmittance: The effect of process-induced surface plasma on laser cut quality was investigated by measuring the transmittance of a He-Ne laser beam passing through the surface plasma [183-184]. The He-Ne beam was positioned parallel to the workpiece and orthogonal to the CO_2 beam axis. Two photodiodes were positioned 5 mm apart and 30 mm away from the irradiated spot. This allowed the photodiodes to see the same spatial locations in the plasma. Results showed that the laser cut quality drops once the surface plasma size increases, due to which the transmittance of the He-Ne beam decreases, i.e. , the signals detected decreases [183]. This was explained by stating that the plasma forms an intermediate medium between the CO_2 laser beam and the workpiece surface. Therefore it absorbs the incident laser beam and transmits less energy into the workpiece. This results in the presence of transiently hot plasma on the workpiece surface. On the other hand , plasma also acts as a heat source increasing the clinging dross [183]. This method may experience difficulty in positioning the He-Ne beam and the photodiodes when curved cuts are performed.

1.6. Conclusions

The physical mechanisms involved in laser cutting are reasonably well understood. The main factors which affect the cut quality are also

understood. The main potential for laser cutting is believed to be in the area of automation. As the most important stage to achieve an automated laser cutting system, methods for in-process cut quality analysis will be investigated in the thesis.

The basic criteria for an in-process laser cut quality analysing device are: a reliable signal of cut quality including surface roughness, dross adhesion and the extent of HAZ; a fast response time less than about 3 milliseconds; fast signal processing and omnidirectional operation.

BIBL.
LONDIN.
UNIV.

CHAPTER TWO

AUTOMATIC NOZZLE - BEAM ALIGNMENT SYSTEM FOR INITIAL SET-UP

2.1. Background and Principle

The purpose of nozzle - beam alignment is to ensure that the laser beam is perfectly centred within the cutting nozzle, since even small misalignment may have noticeable deteriorating effects on laser cut quality as discussed in section 1.4. The existing alignment techniques can be very time-consuming depending on the operator's experience, and may not be accurate enough for precise cutting [122] . Thus it is desirable to develop a system which can align the beam accurately with minimum requirement of operator's experience.

When the nozzle - beam alignment is performed, an inert gas is usually employed for keeping the nozzle cool. Obviously, the nozzle temperature is kept near constant if a laser beam travels through without clipping, since no beam-material interaction happens except by reflections from the workpiece. However, the nozzle will quickly heat up if the laser beam clips the nozzle due to the heat transfer during the beam - nozzle interaction. Based on this principle, a technique for the nozzle alignment can be designed as indicated in Fig. 2 -1, where the circle represents a cross - section of the nozzle. The operation procedures can be described as follows:

(i). Make sure that the focussed laser beam is inside the nozzle which can be bigger (in terms of exit diameter) than the one to be used for cutting. Thus first step is fairly straight forward.

(ii). Move the nozzle in one direction (say + X) step by step. Simultaneously fire the laser until the beam clips the nozzle. If a temperature detector is attached to the nozzle, the clipping state can be detected by the sudden rise of the nozzle temperature. Therefore, point 1 (Fig. 2-1) is found.

(iii). Then move the nozzle in the opposite direction (- X) until the beam clips the nozzle, where point 2 is located.

(iv). Then move the nozzle back to the centre position between the point 1 and the point 2 , point O' is found (This step can be easily done through a computer programming as discussed later in this chapter).

(v). Then move the nozzle in $\pm$Y direction respectively through the point O', points 3 and 4 can thus be found.

(vi). Finally, the centre of the nozzle (point O) is located by moving the nozzle back to the centre position between the points 3 and 4.

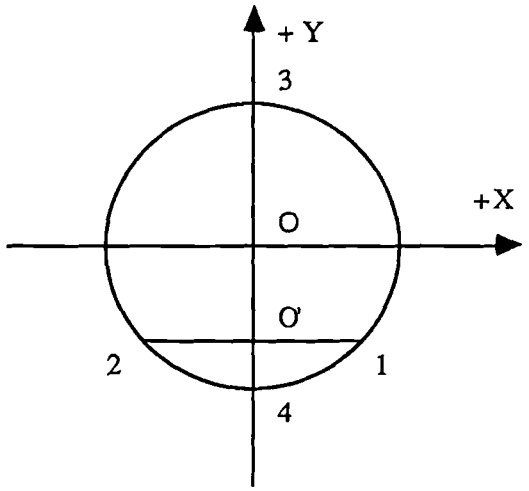
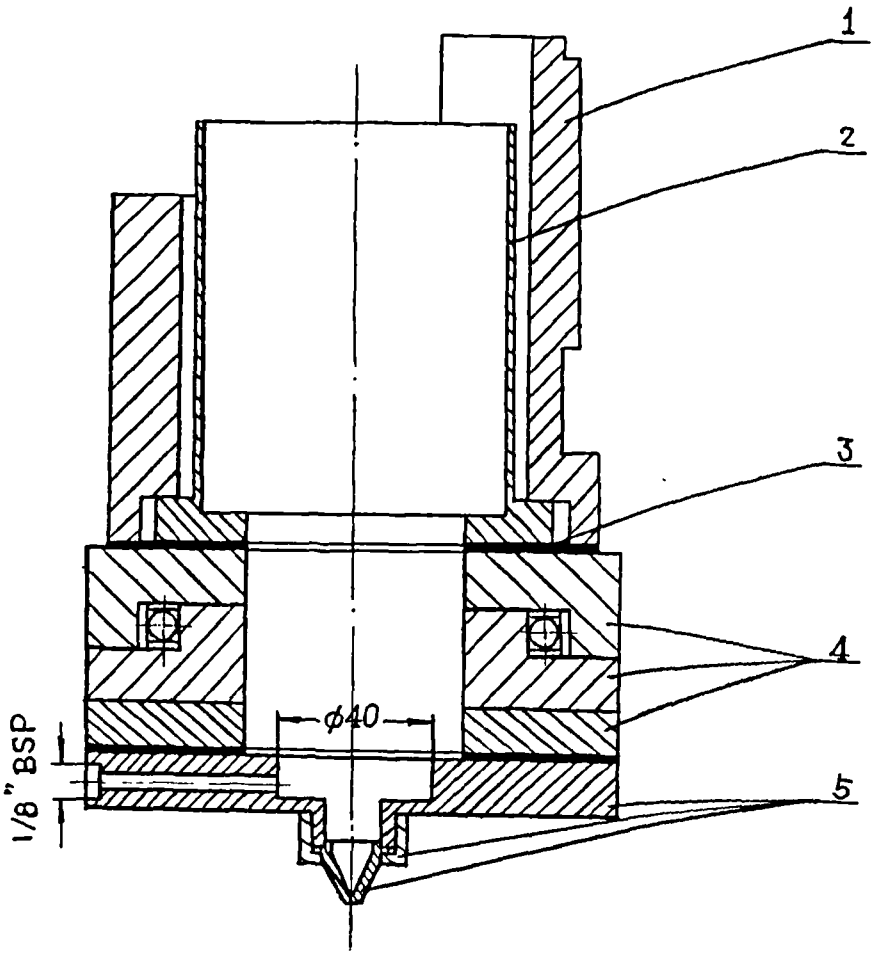


Fig. 2 -1. Principle of nozzle - beam alignment .

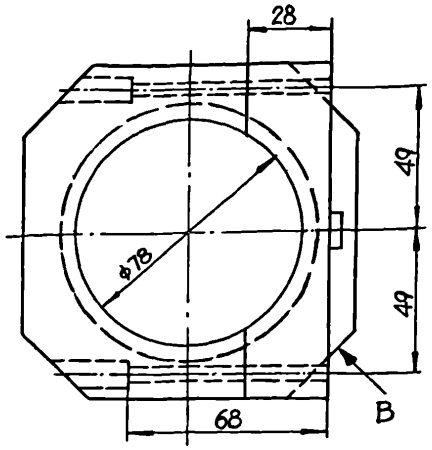
2.2. System Design

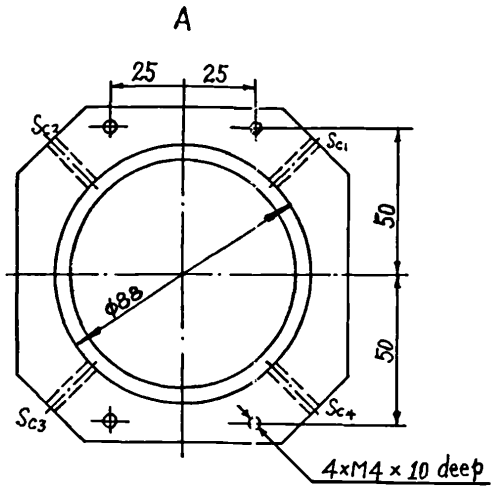
From the above discussion, it is seen that the nozzle needs to be automatically controlled. Therefore, a new laser head assembly is necessary, which makes the automatic movement control of the nozzle possible. A drawing of the new laser head assembly is shown in Fig. 2 -2a . It consists of a lens holder, a X-Y stage to be motorised and a nozzle assembly. Since the nozzle temperature needs to be detected during the nozzle movement, a thermocouple will fixed to the nozzle to form a 'hot nozzle'. The specification of the thermocouple is to be discussed in the following text. The design of the modified lens holder is shown in Fig. 2-2b. In consideration of the weight and strength, aluminium alloy is selected. Four screws S_{c1} - S_{c4} are used for holding the lens tube and for adjusting the lens position up to 5 mm in each direction when necessary. The adjustment of the focal position is done through choosing proper spacers.

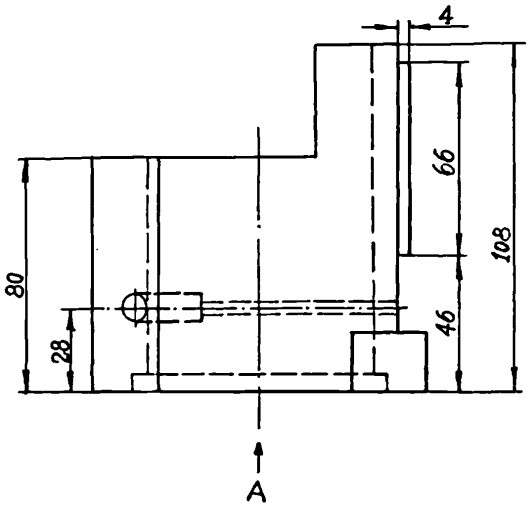


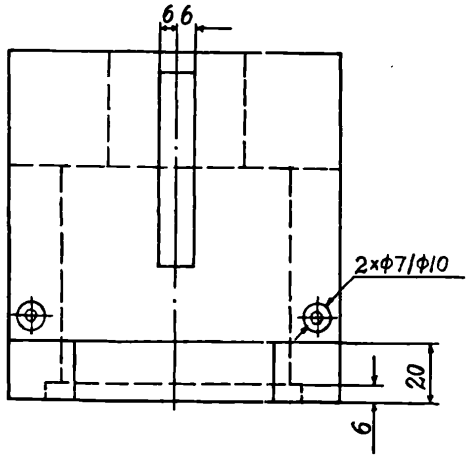
NO.	NAME	MATERIAL
1	Lens Holder	Aluminium
2	Lens tube	Aluminium
3	Sealing	Rubber
4	X-Y stage	Steel
5	Nozzle & Nozzle Assembly	Copper/Aluminium
DATE		Oct. 1987
DRAWN BY		ZHENG H.Y.
SCALE		1:2
TOLERANCE		free

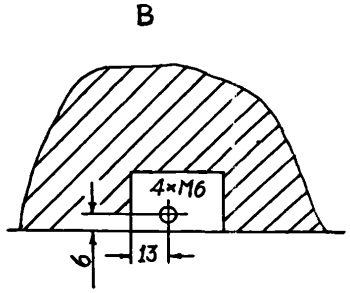
Fig. 2 -2a











REMARKS	
Approved by	
Date	
Drawn by	ZHENG H.Y.
Date	Oct. 1987
Scale	1:2
Drawing No.	Fig. 2-26

Title

LENS HOLDER

2.2.1. Hot nozzle development

Thermocouples provide an economic means of measuring temperature with practical advantages, for instance, fine wire thermocouples respond very rapidly to temperature changes [194]. The theory of the thermocouple detection can be illustrated in Fig. 2 -3, where A and B represent two different metals with the connecting junctions at temperature T_1 and T_2. The number of free electrons in a piece of metal depends on two factors: temperature and composition of the metal. Therefore there are more free electrons at higher temperature (the hotter end) than at lower temperature (cooler end) leading to the drift of the electrons in the hotter end towards the cooler end. This drift varies for A and B due to differences in their thermal conductivity forming a potential difference across the two ends, i.e., an emf (electromotive force) is formed. This emf is given by an integral over temperature [195]

$$\varepsilon = \int_{T_1}^{T_2} (Q_A(T) - Q_B(T))\, dT \qquad (2\text{ -}1)$$

where

ε = emf produced in volts;

T_1, T_2 = junction temperatures in ^0K;

Q_A, Q_B = thermal transport constants of the two metals at a given temperature .

Equation (2-1), which describes the Seebeck effect, shows the emf produced is proportional to the difference in temperature and , further , to the difference in the metallic thermal transport constants. In practice, the two constants Q_A and Q_B are nearly independent of temperature [195] . Thus an approximate linear relationship exists [195] as

$$\varepsilon = \alpha (T_2 - T_1) \qquad (2\text{ -}2)$$

where

α = constant in Volts/^0K;

T_1, T_2 = junction temperature in ^0K.

Based on the above equations, a common measurement system was used and shown in Fig. 2 -4. This shows that the measurement junction T_m is exposed to the environment (attached to the nozzle for this study) which is to be measured. This junction is formed of metals A and B as shown. Two other junctions were then connected to the measurement apparatus, e.g. chart recorder. The " reference " junctions were held at the room temperature T_R.

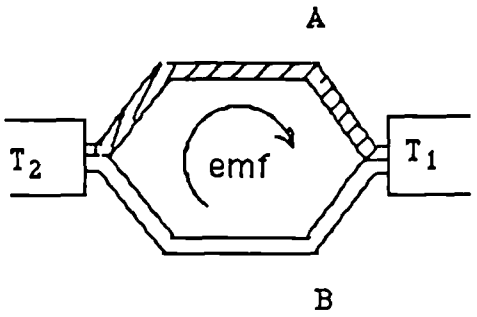


Fig. 2 -3. Seebeck effect.

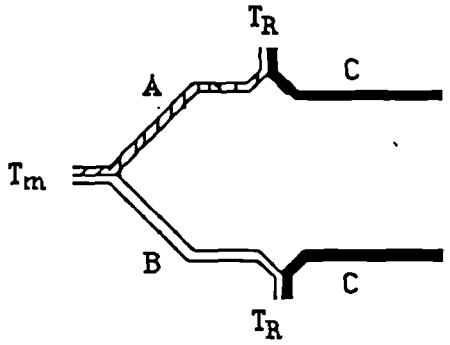


Fig. 2 -4. Three wire thermocouple system.

Being most widely used , a type K welded tip thermocouple, which is based on nickel chromium/nickel aluminium, was chosen as the temperature detector. The main specifications of the thermocouple are listed in Table 2 -1. Figure 2 -5 shows a typical curve of voltage versus temperature for type K thermocouples. From the curve, it is calculated that the sensitivity is 0.04 mV/^{0}C (typical). To make measurement easier, a signal conditioning circuit is usually employed to increase the sensitivity. A thermocouple amplifier AD595AQ (RS COMPONENTS CO. Ltd.) was chosen for this study, which can produce a high level output (10 mV/ ^{0}C) directly from the thermocouple signal.

Table 2-1. Specification of the Type K thermocouple [194]

Thermocouple wire	1 / 0.2 mm
Overall length	1 metre
Insulation diameter	0.6 mm (nom.)
Insulation material	Poly tetra fluro ethylene (PTFE)
Working temperature range	-50 ^{0}C to + 200 ^{0}C (continous) + 250 ^{0}C (spot)

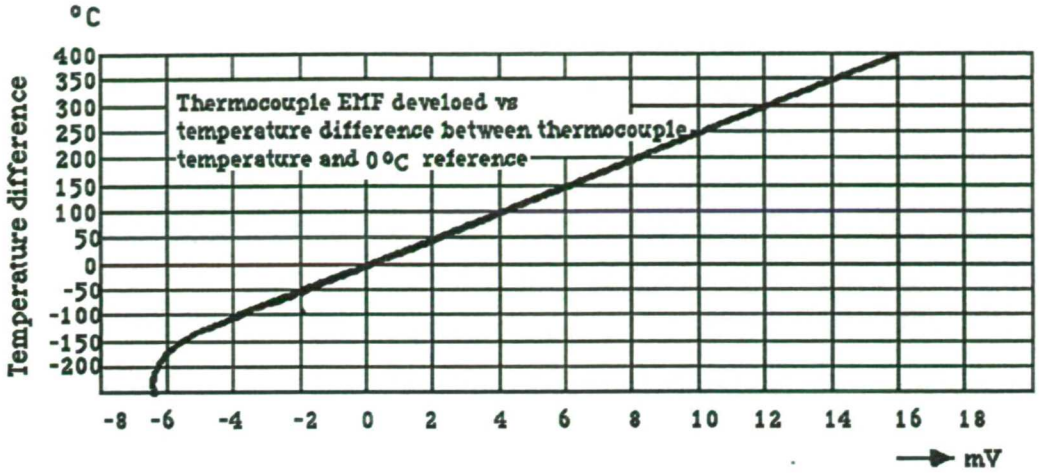


Fig. 2 -5. Typical temperature gradient for type K thermocouple [194].

2.2.2. Development of the X-Y stage

Based on positional accuracy, size and price, a two axis stage with 50 (mm) diameter through hole (manufactured by SPIRES ROBERSON) was selected (Fig. 2 -6). It is composed of three plates. The top (or bottom) and middle plates are spring loaded against the micrometer spindles for minimum backlash. The main specification is listed in table 2 -2. The micrometers were driven by two stepper motors to motorise the stage movement as will be discussed later.

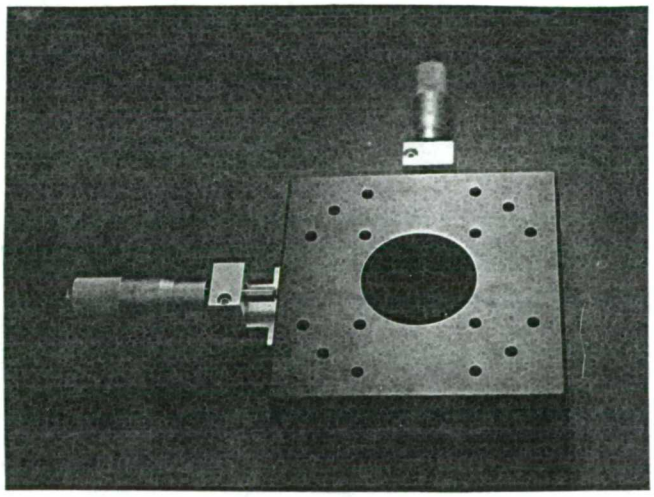


Fig. 2 -6. Photo of the X - Y stage .

Since there are gaps between the three stage plates, the assistant cutting gas will escape through these gaps causing leakage. Apart from economical reasons, this leakage will cause problems in setting the gas flowrate and further influences the cutting performance (cut quality and cutting speed). A design was thus made to solve this gas leaking problem as shown in Fig. 2 -7, where part 1 represents the top plate of the stage and was fixed to the lens holder, part 2 is the middle plate and movable, part 3 is the bottom plate holding the nozzle assembly and is movable (motorised), and part 4 is the gas sealing device equipped with " O " rings at two ends. The end A was fixed to the part 1. The end B is movable relatively to the nozzle assembly. Thus the gas leaking problem was simply solved by this design.

Table 2 -2. Specification of the X-Y stage

Size	125 mm^2
Leadscrew pitch	0.5 mm
Travel	± 12.5 mm
Minimum readout	0.01 mm
Guiding method	Ball bearing/ Steel rods
Load capacity	5.0 kg

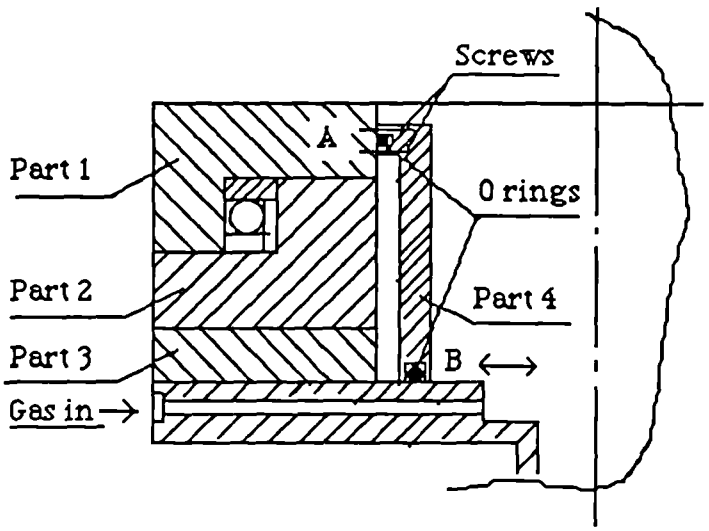


Fig. 2 -7. Schematic drawing of the gas sealing.

2.2.3. Selection of drives

In order to automatically control the movement of the X-Y stage, two identical stepper motors were selected since they can provide some practical advantages as control devices [196] :

(i). The positional error is non-cumulative.

(ii). It is possible to achieve accurate position and speed control in an open-loop system, thus avoiding ordinary instability problems. Other transducers such as tachometer and feedback transducers can often be eliminated.

The chosen motor has a 1.8 ° step angle rotation of the spindle (i.e. 200 steps per resolution). Thus the BLU (basic length unit) for the motorised stage is given by

$$\begin{aligned} \text{BLU} &= \text{lead screw pitch/ steps per resolution} \\ &= 0.5 / 200 \\ &= 0.0025 \text{ (mm)}. \end{aligned} \qquad (2\text{-}3)$$

The stepper motor is an incremental digital drive. It translates an input pulse sequence into a proportional angular movement and rotates one angular incremental, or a step, for each input pulse. The shaft position is determined by the number of pulses and its speed is proportional to the pulse frequency, i.e., the shaft speed in steps per second is equal to input frequency in pulses per second. The main specifications of the stepper motor are given in table 2 -3.

To supply power to the motor, a commercial unipolar drive board was used (RS Cat. No. 332 - 098) (Fig. 2 -8). It basically consists of a steering circuit and a power amplifier. The steering circuit translates the incoming pulses into the correct switching sequence (Fig. 2 -9) required to step the motor. The steered pulses are converted to power pulses, with appropriate duration, rise time, and amplitude for driving the motor winding. The direction can be controlled as clockwise or counterclockwise.

Table 2 -3. Specification of the stepper motor

Step angle	1.8^{o}
Step angle tolerance	± 5.4' , non-cumulative
Nominal phase (winding) parameters :	
voltage	5 V d.c.
current	1 A
resistance	5 Ω
inductance	10 mH
Holding torque	460 mNm
Working torque	320 mNm
Detent torque nominal	30 mNm
Rotor inertia	less than 1350 kg m^2
Pull-in maximum	880 steps /s
Ambient temperature	- 20^{o}C to + 50 ℃
Temperature rise, Max. (measured with two phases excited, 1 A/phase)	80 ^{o}C
Weight	600 g

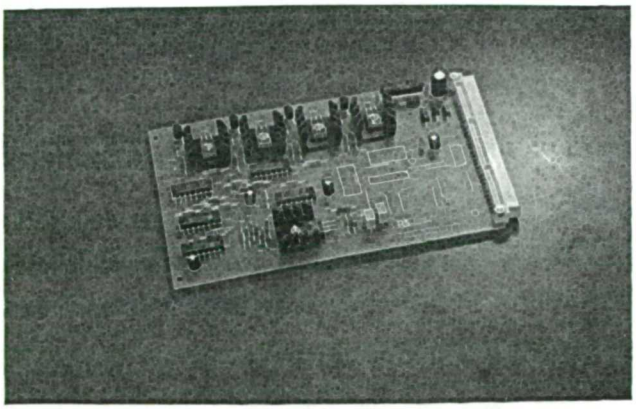


Fig. 2 -8. The unipolar stepper motor drive board.

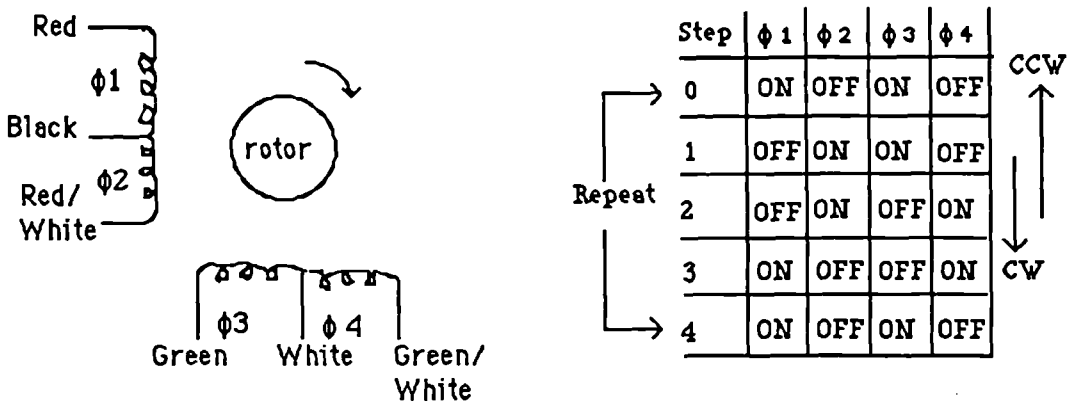


Fig. 2 -9. The 1.8 ° step drive sequence [194] .

The torque versus stepping rate characteristic for a stepper motor can be shown in Fig. 2 -10. The pull-in curve describes the maximum constant start/stop rate that a frictionally loaded motor can achieve without loss of step. This curve is dependent on the method of driving the motor and load inertia. The start/stop region decreases with increasing load inertia. The pull-out curve describes the maximum stepping rate which a frictionally loaded motor can follow without loosing steps, assuming sufficient time is allowed to accelerate the motor by ramping the frequency of the command drive circuit. Within the start/stop region the motor can be started, stopped or forced to change direction of the rotation followed by a sudden command change from the drive circuit. However, within the slew range the motor can only be accelerated or decelerated to the required speed and it cannot suddenly change direction. The pull-out performance for the selected motor using the drive board is shown in Fig. 2 -11.

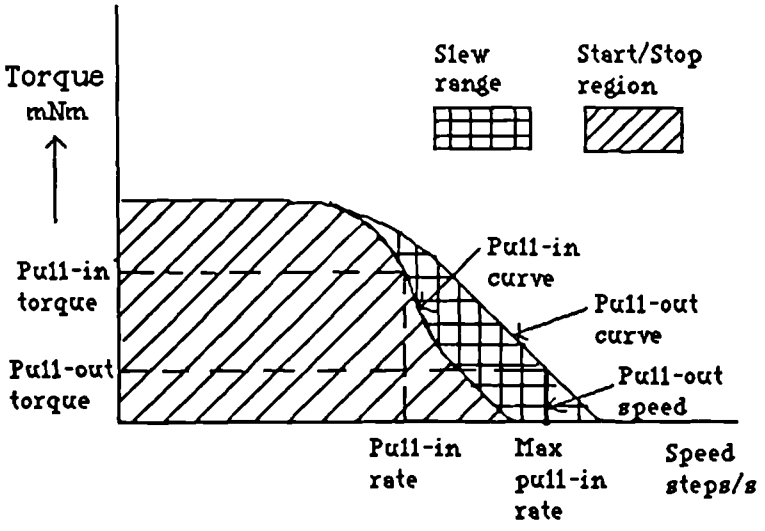


Fig. 2 -10. The torque - speed characteristics [194].

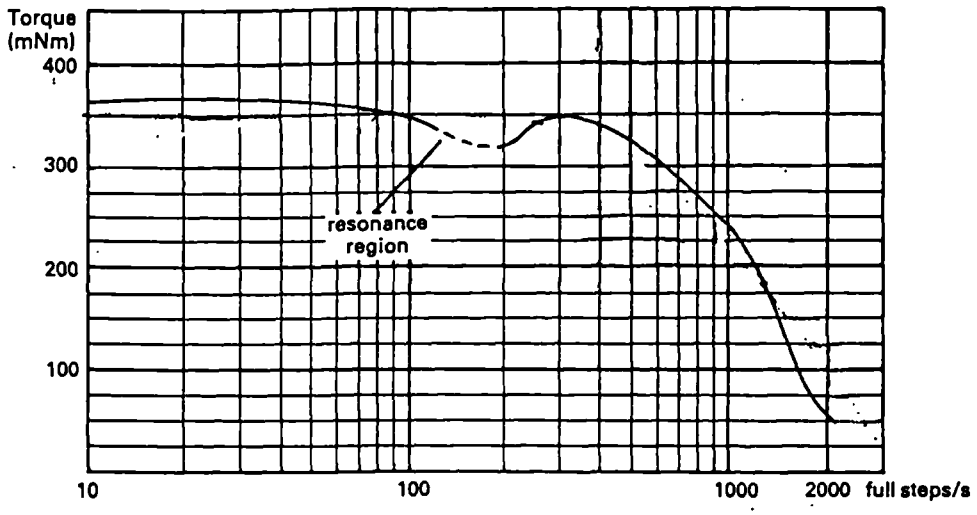


Fig. 2 -11. Pull-out performance for the 1.8° stepper motor[194].

2.3. System Control

2.3.1. Hardware construction

Figure 2 -12 shows the unipolar stepper motor drive board connections. The 25 W wirewound resistors (RS Component Ltd.) were selected based on the required resistance and the maximum power dissipated through it. The former is given as

$$R = \frac{+V_{motor} - \text{rated winding voltage}}{\text{rated wind current}} \qquad (2\text{-}4)$$

where

rated winding voltage = 5 Volts [table 2-3] ,

rated winding current = 1 A [table 2-3] ,

+ Vmotor = 24 Volts (between 15 - 30 Volts).

Thus R is calculated to be 19 Ω. The maximum power, P_m , dissipated through R is determined by

$$P_m = (\text{rated motor current})^2 R$$
$$= 19 \text{ (Watts)} \qquad (2\text{ -}5)$$

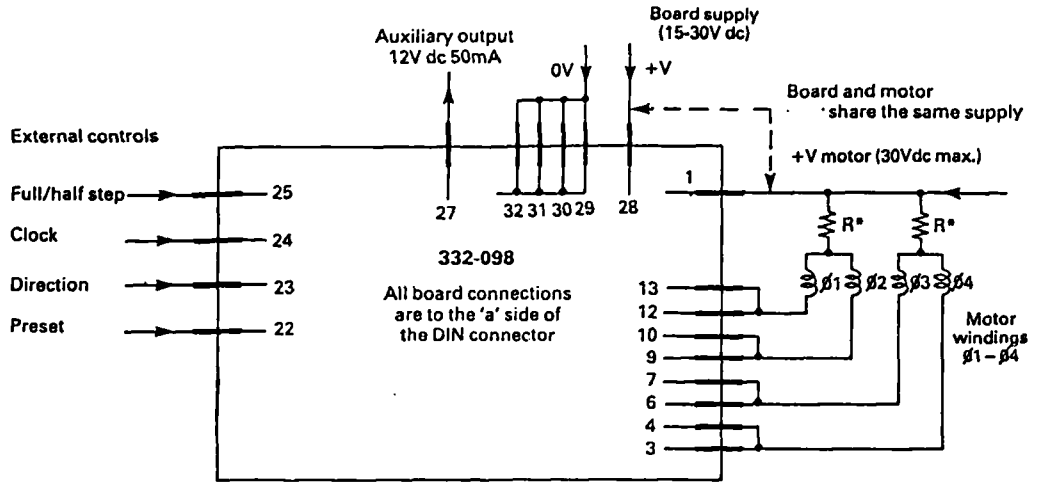


Fig. 2 -12. Drive board connections (reproduction of RS Data sheet No. 8199).

The external controls were implemented by a BBC microcomputer. A block diagram of the closed-loop control system for the nozzle alignment with feedback from the thermocouple is shown in Fig. 2 -13, where the BBC computer provides clock signals with required frequency and executes the control programme. The computer interface with the motor drive board is through the 8 bit user port, which can be read from and written to in BASIC and in assembly language through the 6522 VIA (Versatile Interface Adaptor) integrated circuit. This circuit is addressed at locations between &FE60 and &FE6F. The 8 bit bidirectional port B lines are controlled by a data direction register (DDRB) and an output register (ORB). The former specifies whether the port bits are to operate as inputs or outputs. Placing a "0" in a bit of the DDRB will cause the corresponding bit of that port to be defined as an input. A "1" will cause it to be defined as an output. When programmed as an output, a port line will be controlled by the corresponding bit in the output register. The interface to the thermocouple is through the "analogue in" port which has four input channels to accept voltages in the range 0 to 1.8 V.

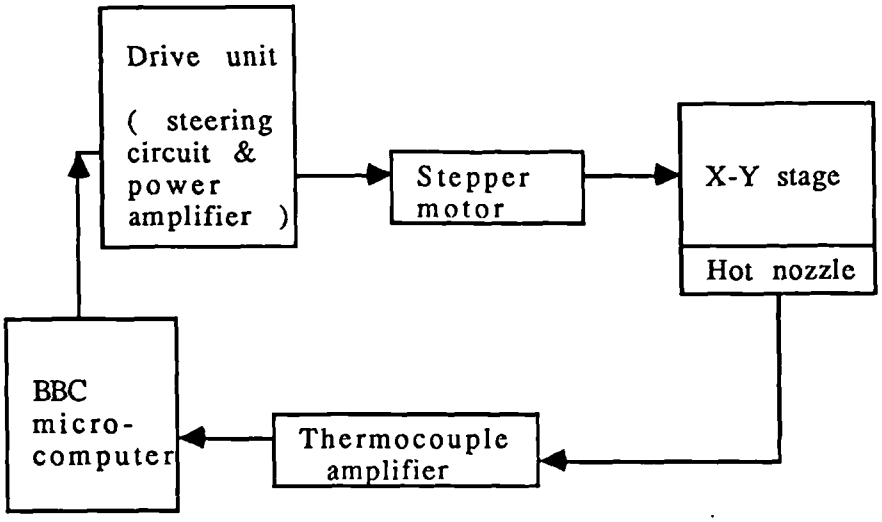


Fig. 2 -13. Feedback control system for the nozzle alignment.

2.3.2. Software development

Based on the detection principle as outlined in 2.1, a programme using BASIC languagewas written (Appendix A) to control the motion of the X-Y stage. The configuration of the port B is through the following programme:

```
?& FE62 = &FF
?U% = & FE60
?U% = 0
```

where ? is an 8 bit indirection operator. This programme describes how to read a value in the range of 00000000_2 to 11111111_2 from the port at &FE60.

A pulse is generated by turning the output line on, i.e. logic " 1 " is given to the pulse line. PB2 , i.e. bit 2 (2) , in the user port output register is selected to generate the pulse for X axis movement. Thus a pulse train (a sequence of pulses) can be produced based on Fig. 2 -14.

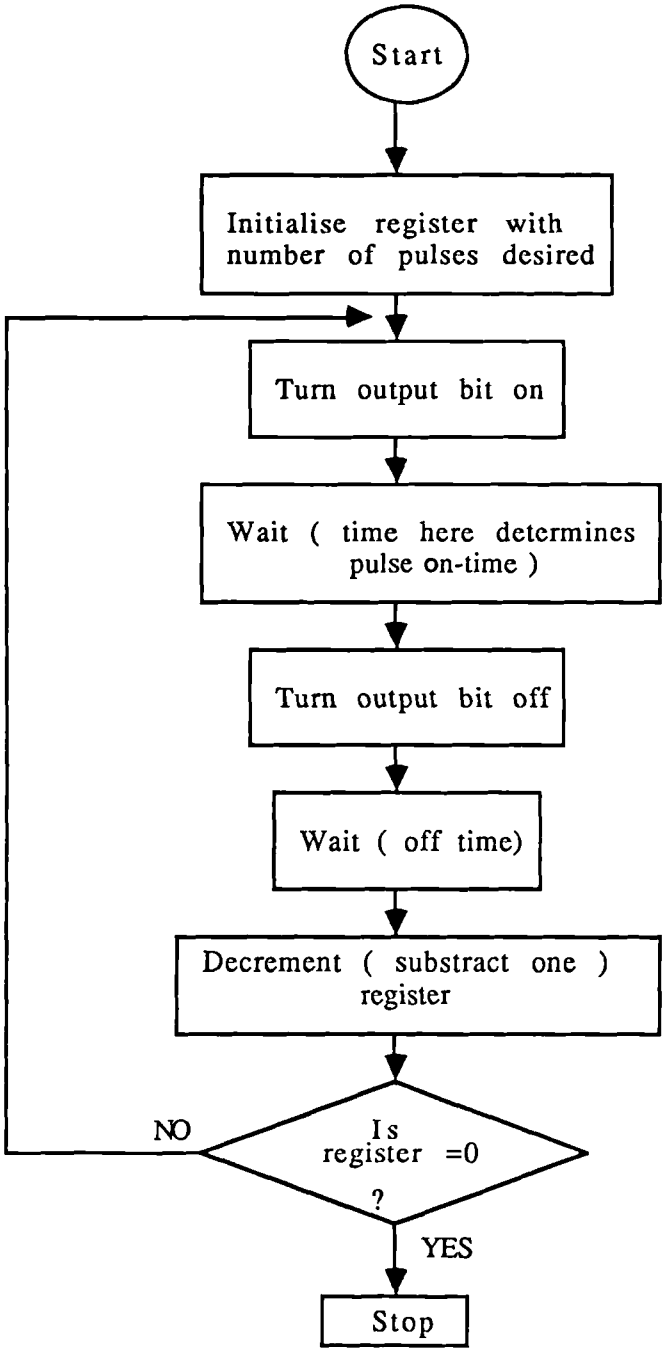


Fig. 2 -14. Flowchart for pulse train generation.

The motor rotating direction is independently controlled by a different output line (Bit 3 (4) for X axis direction). Changing direction can thus be performed by changing the bit value of this line. This is done through the logic EOR operation , i.e. , by the function

?U% = ?U% EOR 4

where the port B line PB3 (Bit 3) has been assigned as output line , i.e. U%

= "1". Thus the logic value of the Bit 3 changes from "1" to "0" (table 2 -4). The clock and direction control of the Y-axis movement can be effected in the same way. The user port function is summarised in Table 2 -5.

The thermocouple signal is read in by function ADVAL (Ch), where Ch represents the input channel number. This function converts the analogue signal into digital in the chosen channel. In practice 1.0 V input typically produces a reading of 35168 [197]. Thus a threshold of the thermocouple output can be preset using experimental results. The thermocouple signal is then compared with the threshold value in real-time. If it is higher than the threshold, the movement of the motor is then stopped. Meanwhile the laser shutter is closed.

Table 2 -4 Truth table (C = A EOR B)

A	B	C
0	0	0
0	1	1
1	0	1
1	1	0

Table 2 -5 User port

Bit	Function
2 (2)	X Clock
3 (4)	X Direction
4 (8)	Y Clock
5 (16)	Y Direction

A flowchart of the programme is shown in Fig. 2 -15. To illustrate this flowchart, consider an X axis movement. The computer counts and stores the number of steps, N, advanced in +X direction (the point 1 location in Fig. 2 -1), and returns the stage back to its original position by moving N steps in -X direction (reset the counter). Then the stage is further moved in the same direction (-X) until clipping happens again. The number of steps advanced is then recorded as M (the point 2 location in Fig. 2 -1). Then the motor is driven for (M + N)/2 steps to locate the point O' (Fig. 2-1).

The laser shutter control was investigated by L. Li [192], where the shutter control was performed by logical switching operation. The computer interfaced with the external control circuit of the laser manual operating unit sends a logic "1" signal to switch the shutter on and a logic "0" to turn the shutter off based on the feedback sensing signals.

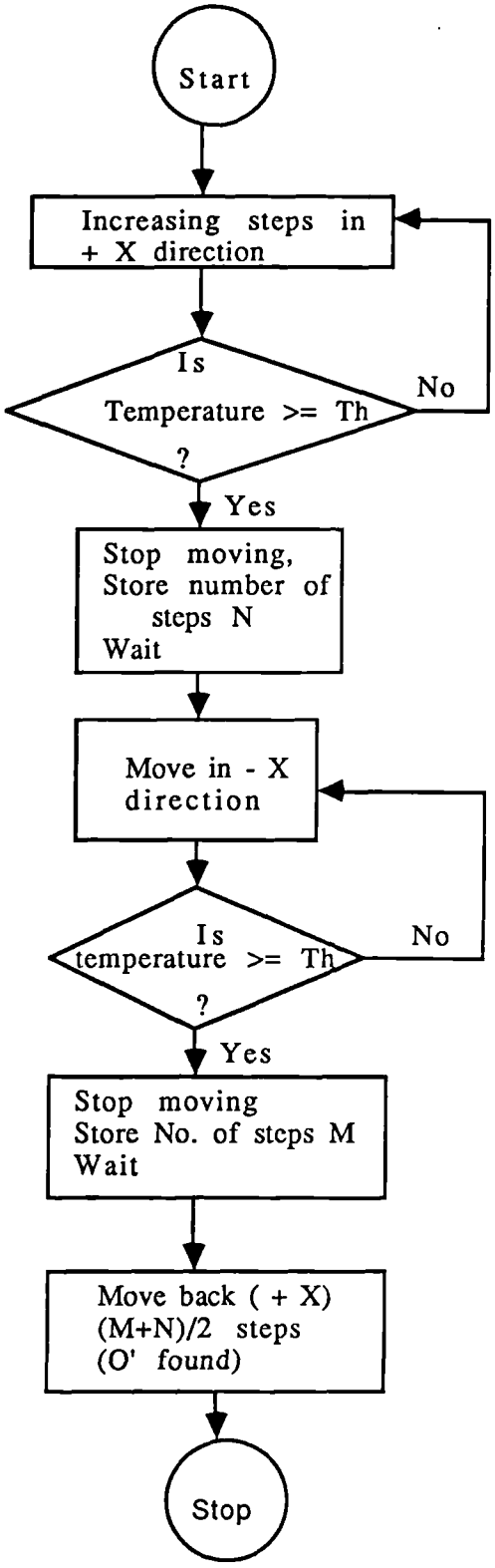


Fig. 2 -15. Flowchart for the movement control in X axis.

2.4. Experimental Procedures and Results

2.4.1. Experimental procedures

The experiments were performed by using the laser equipment at Imperial College. The laser is a 2 kW CW (continuous wave) CO_2 laser (Control Laser) with a wavelength of 10.6 μm (a more detailed description is given in the Appendix B). As shown in Fig. 2 -16, the laser beam was focussed by a ZnSe lens with a focal length of 100 mm down through a converging conical " hot " nozzle with an orifice diameter of 1.5 mm. The nozzle was manually moved step by step using the existing X-Y stage (not motorised). At each step the laser was fired for about one second. Meanwhile signals were recorded by a chart recorder. The operation parameters were set as follows:

laser power: 1.61 kW;
shielding gas : Ar .

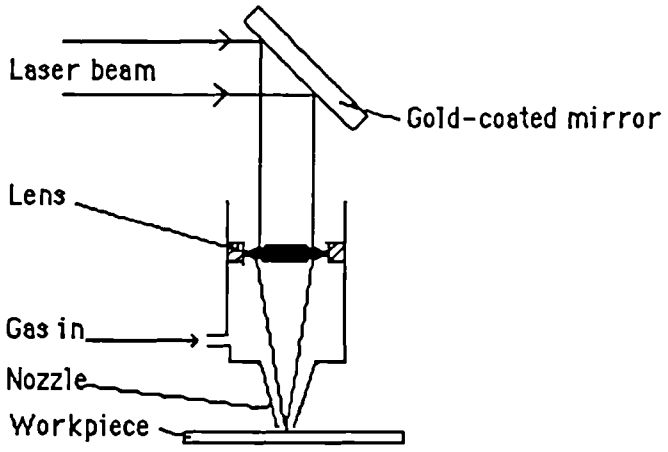


Fig. 2 -16. General experimental set-up for laser cutting process.

2.4.2. Results and discussions

2.4.2.1. Hot nozzle detection

(i). Thermocouples can well signal the clipping state. Figure 2 -17 shows the thermocouple outputs against time for both cases of X axis

movement (Fig. 2 -17a) and Y axis movement (Fig. 2 -17b).

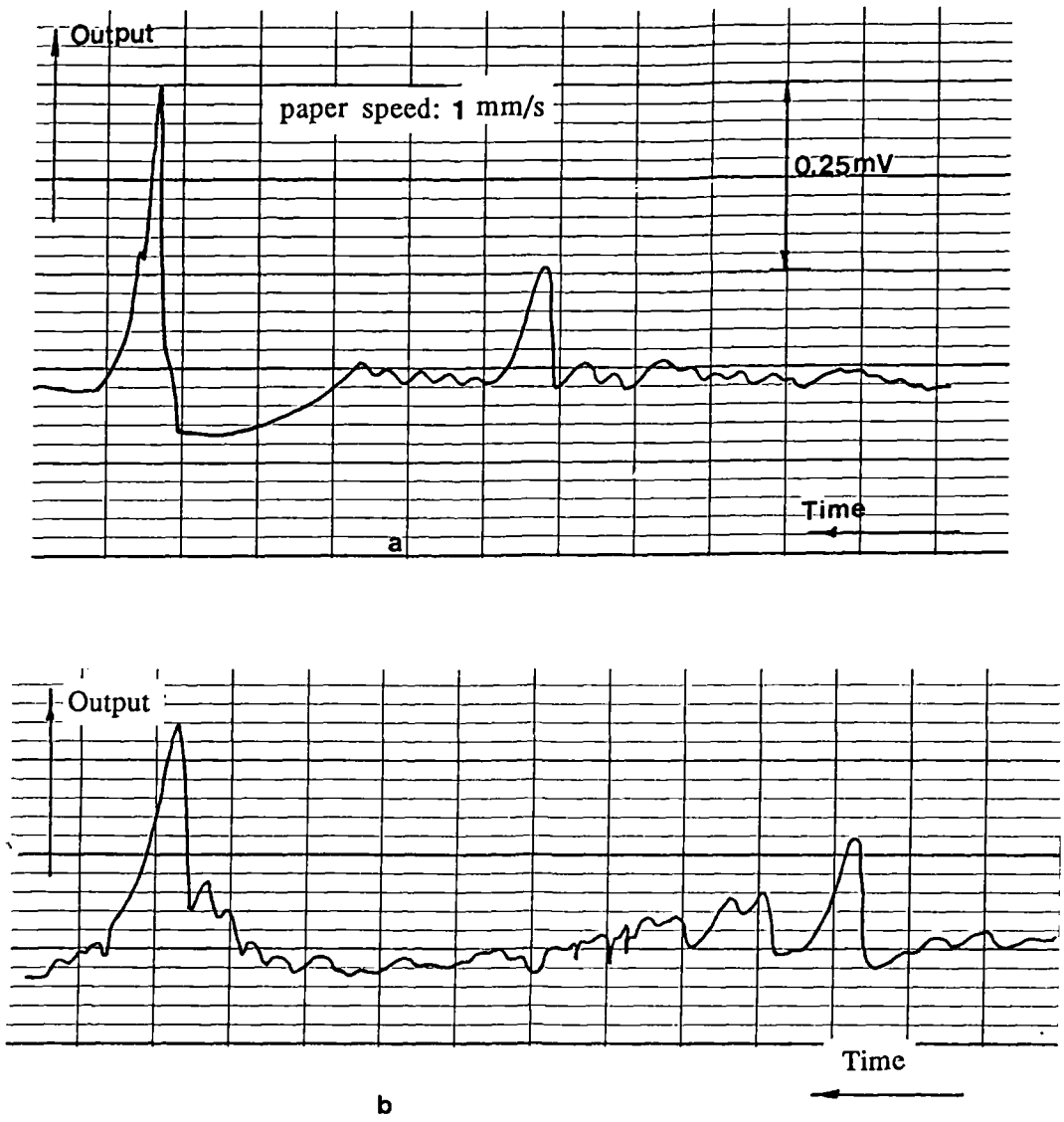


Fig. 2 -17. Typical nozzle clipping signals.

It is clearly seen in both cases that the temperature jumped to a significantly higher value when clipping occurred. The extent of the temperature increase was determined by many factors such as the laser power density, the beam incidence angle relative to the nozzle surface, the surface reflectivity and the interaction time between the laser beam and the nozzle. Since the laser power, the beam incidence angle and the nozzle reflectivity could all be assumed to be constant, it was the interaction time that controlled the nozzle temperature. The difference of the peak values at the clipping states were thus caused by the difference in the interaction time, which happened due to the manually controlled

laser shutter. This problem can be easily solved when the automatic alignment system is employed which can control the laser shutter through programming.

By repeating these experiments, it was found that the thermocouple responded to the clipping state in a very similar way. Thus the repeatability of the device is good.

By visual observation of the clipped nozzle, no damage was found. This can be explained as follows. Firstly, copper has very high reflectivity absorbing only 2-5% of the incident beam [68].. Thus the nozzle temperature could not reach a very high value in such a short time. Secondly, the flowing inert gas has a shielding effect prevènting oxidation. In fact, the nozzle temperature recorded in this experiment can be approximately worked out according to the equation (2 -2), where α is given as 0.04 mV/°C, the reference temperature, i.e. the room temperature was 22 °C. Since the peak values of the thermocouple signal varied between 0.125 - 0.50 mV, the corresponding temperature changes are thus worked out between 3.1 - 12.5 °C. Therefore, the nozzle temperature varied in the range 25.1 °C to 34.5 °C, which obviously could not cause any physical damages to the nozzle.

As discussed before, the thermocouple sensitivity can be increased to 10 mV/°C by using the thermocouple amplifier, i.e., the above signal level would vary from 31.3 mV to 125.5 mV, which falls into the acceptable range of the BBC computer "analogue in" port (0 - 1.8 V). This voltage range can be adjusted by changing the laser shutter "on" time. When 1 V output is required, the corresponding nozzle temperature would be around 100 °C, which is still well below the copper melting point (between 1000 - 1100 °C depending on its composition).

Therefore thermocouples can well signal the clipping state without any thermal damage to the nozzle.

(ii). Power meter demonstration of the detection principle. In this experiment, a water -cooled cone calorimeter (Fig. 2 -18) was positioned underneath the nozzle to indicate the power loss when the beam clips the

nozzle. In principle, all the laser beam energy would be absorbed by the cavity of the calorimeter when there is no beam clipping.

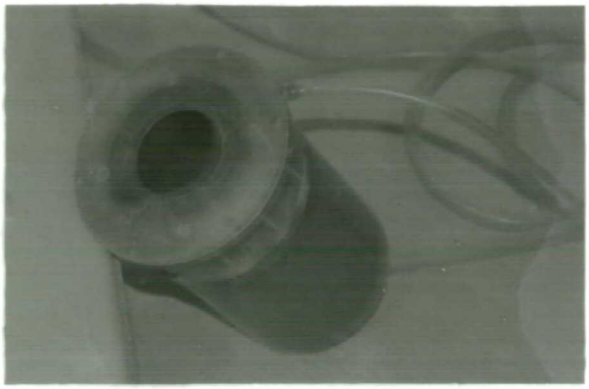


Fig. 2 -18. The calorimeter.

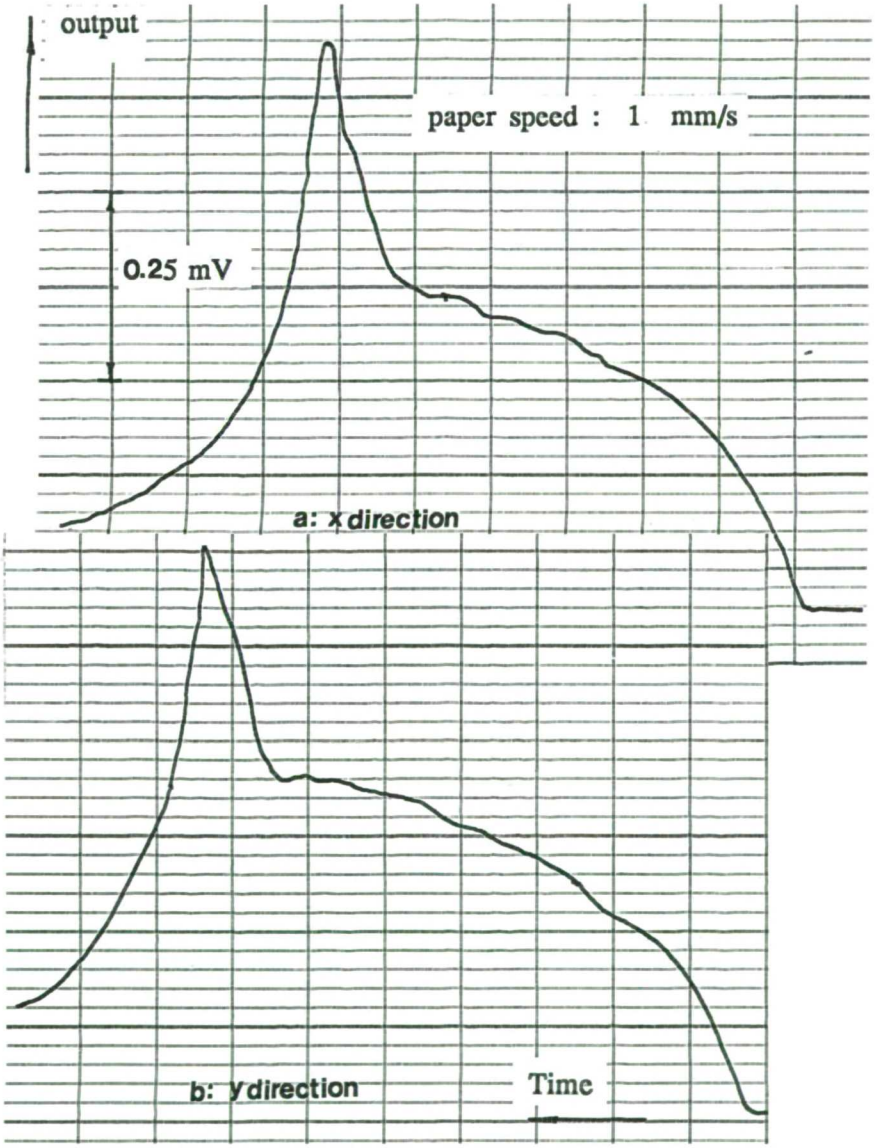


Fig. 2 -19. Clipping signals and power drop.

The operating principle of the calorimeter is based on the

measurement of the temperature difference between the water inlet and the water outlet using thermocouples whose output is directly displayed as watts of laser power on a digital wattmeter.

The laser beam was fired while the nozzle was moved. Temperature signals of the cutting nozzle were simultaneously recorded. It was observed that the power reading increased gradually and reached a nearly steady value. Then it dropped suddenly indicating the clipping state, since when the beam clipped the nozzle much of the beam was blocked from going into the calorimeter cone leading to the loss of power. The 'hot nozzle' temperature signals recorded as shown above in Fig. 2 -19, indicated sharp rises when clipping happened.

2.4.2.2. Off-line test of the automatic nozzle alignment system

A test was performed by using the motorised X-Y stage with the hot nozzle. A soldering gun was used to touch the nozzle to indicate the clipping state. The computer interpreted the incoming signals and executed the programme for controlling the stage.

The system accuracy is mainly determined by the motor positional error and the system response time. The motor positional error is the tolerance of each angular step movement. This error is non-cumulative, i.e., remains constant regardless of the number of steps advanced. As given in table 2 -3, the positional error is 5.4', which can be converted to the linear movement error, Δ, given by

$$\Delta = \Delta N * BLU \qquad (2\text{-}6)$$

where

ΔN = the corresponding steps of the positional error
= 5.4/108 (1.8^0 , i.e. 108' per step)
= 0.05 ;

BLU = 2.5 μm .

Thus the linear error is calculated to be 0.125 μm.

The system response time is mainly controlled by the thermocouple response time and the heat transfer time from where the beam clips the

nozzle to where the thermocouple is located. The type K thermocouple response time is affected by its wire diameter and the contact method between the thermocouple junction and the nozzle. The selected thermocouple has a very fine diameter and thus has a response time less than 100 ms [194]. When a semi-infinite slab of finite thickness, L, is heated, the ratio (β) of temperatures at the front and back surfaces is a function of Fourier number, F_0, which is given by[1]

$$F_0 = \frac{\alpha \tau}{L^2} \qquad (2\text{-}7)$$

where

F_0 = Fourier number;

α = thermal diffusivity of the substrate

= 1.123 x 10^2 $(mm)^2/s$ for copper at moderate temperature;

τ = heat transfer time (s);

L = a significant dimension of the system (mm).

The ratio β tends to be equal to one (i.e., the temperatures tends to be equal at the front and back surfaces) when the Fourier number, F_0, is one. This principle also applies if the heated body is small. Therefore the heat transfer time within the cutting nozzle can be estimated as below. The dimension L for the hot nozzle is defined as the distance from point A to point B (Fig. 2 -20) and is calculated to be equal to 3.355 mm. When the Fourier number is equal to one, the temperature tends to be steady across the substrate. Thus the heat transfer time , τ , is calculated from Eqn. (2-7) as 0.1 second. Therefore the response time of the nozzle alignment system as the combination of the thermocouple response time and the heat conducting time was less than 0.2 second.

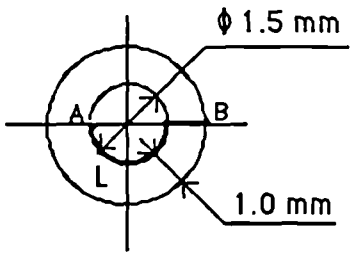


Fig. 2 -20. Calculation of the nozzle dimension L .

The system positional error, ΔE , can thus be estimated by the following equation

$$|\Delta E| = \Delta + t_r * \upsilon_m * BLU \qquad (2\text{-}8)$$
$$= 0.125 + 0.20 \times 20 \times 2.5$$
$$= 11.25\ (\mu m)$$

where

t_r = response time of the system ,

υ_m = the motor speed (steps /s).

In order to increase the system positional accuracy, the motor speed was set a low value, i.e. 20 steps per second. Obviously this positional error will be acceptable for most of the precise laser machining processes. Since the travelling distance of the system is very small (usually less than 1.5 mm), the motor speed is not crucial. In other words, the motor is driven in the region of the start/ stop region (Fig. 2 -10), in which the motor can be started, stopped or forced to change direction of rotation without losing steps. This secures the system accuracy.

The machining of the new laser head was not finished although the drawings were given to the workshop at Imperial College. Therefore on-line testing of the nozzle alignment system is not possible. However, since the principle of the alignment system and off-line testing have been proved, the on-line testing would be expected to be working well.

2.5. Chapter Summary

The detection principle of the nozzle alignment by using thermocouples has been proved through experiments. The thermocouples can well signal the nozzle clipping state. An off -line test of the automatic alignment system shows that the nozzle movement can be accurately controlled through programming to an estimated accuracy of $\pm$ 0.01 mm .

CHAPTER THREE

EFFECTS OF GAS COMPOSITION ON LASER CUTTING PERFORMANCE

3.1. Introduction and Background

As discussed in chapter one, the assistant gas plays an important role in the laser cutting process. Depending on the type of gas used, three actions can happen simultaneously (e.g. in the case of oxygen assisted laser cutting), i.e. heating by burning of the melt to form, for example , oxides in the oxygen stream; cooling by convection and drag force by the flowing gas stream.

3.1.1. Heat balance on the cut front

The exothermic burning reaction between the oxygen stream and the melt creates another heat source for the cutting process. In order to accomplish the cutting process, this burning reaction energy and the laser beam energy should be high enough to provide energy for melting the material and for compensating the heat loss due to convection, conduction and radiation. A heat balance describing the heat transfer on the cut front can be given as follows:

$$P f(1 - r) + \alpha P_{chem} = Q_{melt} + Q_{cond} + Q_{conv} + Q_{rad} \qquad (3\text{-}1)$$

where

P = incident laser power (W);

f = fraction of the laser beam striking on the surface as opposed to that passing through the kerf;

r = workpiece reflectivity ;

P_{chem} = heat generated during chemical burning reactions between oxygen and melts (W);

α = fraction of this power transferred to the process;

Q_{melt} = heat used for melting the material (W) ;

Q_{cond} = heat loss by conduction during laser beam and material interaction (W) ;

Q_{conv} = heat loss by convection to air (W);

Q_{rad} = heat loss by radiation (W) .

Each of these values can be calculated to give a quantitative concept of the heat balance on the cut front.

(i). Calculation of the laser power transferred into the process: Given that the laser output power is 1850 W (used in this study) and power loss at each mirror is 1%, the laser power after three mirrors (this is the case for the laser system used in this study) is thus given by 1850 x $(0.99)^3$, i.e. P = 1795 W.

The surface reflectivity is dependent on the polarisation direction and on the angle of incidence as discussed in chapter one. In laser cutting, the polarisation direction is usually parallel to the cutting direction to achieve optimum cutting speed, and the angle of incidence is normally larger than 80^o [17]. At this angle, absorption of around 40% is normal with CO_2 laser radiation on a steel plate [17] , therefore r ≈ 0.6.

The value of f depends on cutting speed. The higher the cutting speed, the higher the value of f. At the speed of 35 mm/s, f was given around 0.5 for the beam size of 0.5 mm in radius and a given power[1]. Thus the laser beam energy used in cutting process is given by 1795 x 0.4 x 0.5 , i.e.

$$P\,f(1 - r) \approx 359\ (W) \qquad (3\text{-}2)$$

(ii). Calculation of the chemical reaction energy: The total amount of the heat generated from the burning reactions between the oxygen and the melts is determined by the oxygen concentration at the cutting front and the material being cut. The former is controlled by the mass transfer of the oxygen to the molten layer which covers the cutting front and diffusion through this molten layer to the burning front. The oxygen mass transfer and diffusion process is a strong function of the gas composition and the gas flow velocity. The higher the oxygen content in the gas mixtures the faster the rate of the mass transfer and the rate of the diffusion process due to the increased oxygen concentration gradient. Increasing the gas flow velocity will decrease the gaseous boundary layer thickness over the melt front [206], which would increase the oxygen

gradient in the gas phase. Increasing the gas velocity would also decrease the melt thickness due to the drag force and hence aid in increasing the oxygen gradient in the liquid phase. Since the higher oxygen concentration at the cutting front leads to a faster burning reaction, more heat is generated. The maximum cutting speed is thus raised to a higher value. The power generated due to the heat of the chemical reaction is given as below [1]:

$$P_{chem} = W t \lambda \upsilon \qquad (3\text{-}3)$$

where

W = cut kerf width (m);

t = thickness of the workpiece (m);

λ = an average heat generated by the reactions, allowing for varying content of reaction (J/m^3) ;

υ = cutting speed (mm/s) .

In order to get a quantitative concept of the magnitude of P_{chem} in an actual cutting situation, the following calculation was made based on oxygen assisted laser cutting of mild steel with laser output power of 1.85 kW. The workpiece has a thickness of 10^{-3} m, i.e. $t = 10^{-3}$ m. The average cut kerf width, W , is taken as 1.0×10^{-3} m . The heat of reaction forming FeO is given as $\lambda = 3.81 \times 10^{10}$ J/m^3. The cutting speed $\upsilon = 3.5 \times 10^{-2}$ m/s as an example. Thus the burning energy used in the cutting process is calculated as:

$$\alpha P_{chem} = \alpha\ 1.0 \times 10^{-3} \times 10^{-3} \times 3.81 \times 10^{10} \times 3.5 \times 10^{-2}$$

$$= \alpha\ 1334\ (W) \qquad (3\text{-}4)$$

Since the gas stream will rapidly remove heated material from the interaction region, the value of α is likely considerably < 1.

(iii). Calculation of the convective heat loss: The convective heat loss is also governed by the flowing gas stream which carries away a portion of the heat. The heat dissipated due to this convective cooling effect of the

gas stream can be expressed as:

$$Q_{conv} = hA(T_1 - T_2) \qquad (3\text{-}5)$$

where

h = convective heat transfer coefficient ($W/m^2.K$);

A = the cooling area (approximately equal to Wt) (m^2);

T_1= the melt front temperature (K) ;

T_2 = the gas temperature (K).

The heat transfer coefficient , h , can be determined by the following equation:

$$N_u = f(Re, Pr) \qquad (3\text{-}6)$$

for gas flow in a pipe, it is given by the **Ditus Boelter equation:**

$$N_u = 0.023\ Re^{0.8} Pr^{0.33} \qquad (3\text{-}7)$$

where

Nu = hx/k (Nusselt number) ;

x = the diameter of the pipe (taken as the kerf width W) (m);

k = the thermal conductivity (W/m.K) ;

Pr = μCp/k (Prandtl number) ;

μ = the coefficient of gas viscosity (kg/m.s);

Cp = specific heat capacity (J/kg.K);

Re =ρux/μ (Reynolds number) ;

ρ = the gas density (kg/m^3);

u = gas flow velocity (m/s).

From equations (3 -5) and (3 -7), it is seen that the exact amount of the convective heat loss depends on the gas properties. Given the oxygen flow velocity u = 70 m/s , the convective heat transfer coefficient, h , can be worked out according to equation (3 -7) as h = 450.5 ($W/(m^2\ K)$) (data from table 3 -1 and table 3 -2).

Table 3 -1. Thermal Properties of Gases at 300 ^{o}K, 1 atmosphere [198]

	ρ (kg/m ^{3})	k (W/(m K))	Cp (J/(kg K))	μ (kg/m.s)	Pr
Oxygen	1.301	0.0267	920.3	20.6×10^{-6}	0.709
Nitrogen	1.142	0.0262	1041	17.8×10^{-6}	0.713
Argon	1.660	0.0173	522	22.5×10^{-6}	0.680
Helium	0.166	0.146	5190	19.8×10^{-6}	0.710

Given $(T_1 - T_2) \approx T_m \approx 2000$ ^{o}K (melting point of steel), and using the data given in (ii), the heat loss Q_{conv} is calculated as:

$$Q_{conv} = 450.5 \times 10^{-3} \times 10^{-3} \times 2000$$
$$= 0.9 \text{ (W)} \qquad (3\text{-}8)$$

The convective coefficients of other gases and the corresponding convective heat under the same conditions are calculated and shown in table 3 -2.

Table 3 -2. Convective heat of gases

	Re	h (W/(m ^{2} K))	Q_{conv} (W)
Oxygen	4.40×10^{3}	450.5	0.90
Nitrogen	4.49×10^{3}	450.1	0.90
Argon	5.16×10^{3}	327.1	0.65
Helium	0.59×10^{3}	491.9	0.98

It is seen that although the values of different gases are different, the resultant heat loss are always small, since the cooling area concerned is very small. Thus it can be concluded that the convective cooling effect is negligible compared to the energy input of hundreds of watts.

(iv). Calculation of the energy used for melting the material : The

heat used in melting the workpiece material is given as [3] :

$$Q_{melt} = \rho W \upsilon t(C_p T_m + L_m + \phi L_f) \qquad (3\text{-}9)$$

where

L_m = latent heat of fusion (J/kg);

ϕ = mass fraction vaporised;

L_f = latent heat of evaporation (J/kg);

Given $L_m = 2.66 \times 10^5$ J/kg, $L_f = 6.33 \times 10^6$ J/kg , $\rho = 7833$ kg/m^3, $C_p = 465$ J/kg.K (data from ref.[206]), $\phi \approx 0.1$ (In laser gas cutting, material is basically removed as molten droplets due to the drag effect. Therefore ϕ can be very small.) and using the data given in (ii), the heat used for melting the material is calculated as:

$$\begin{aligned} Q_{melt} &= 7833 \times 10^{-3} \times 0.035 \times 10^{-3} \{465 \times 2000 + 2.66 \times 10^5 + 0.1 \times 6.33 \times 10^6\} \\ &= 2.74 \times 10^{-4} \times \{9.3 \times 10^5 + 2.66 \times 10^5 + 6.33 \times 10^5\} \\ &= 501 \text{ (W)} \end{aligned} \qquad (3\text{-}10)$$

(v). Calculation of heat loss by conduction: The amount of conducted heat is approximately given as below [198]:

$$Q_{cond} \approx kA(T_2 - T_1)/t \qquad (3\text{-}11)$$

Given k = 54 W/m.K[198] , $A \approx Wt = 10^{-6}$ m^2 , $(T_2 - T_1) \approx T_m = 2000$ K, Q_{cond} is calculated as :

$$\begin{aligned} Q_{cond} &= 54 \times 10^{-6} \times 2000/10^{-3} \\ &= 108 \text{ (W)} \end{aligned} \qquad (3\text{-}12)$$

(vi). Calculation of heat loss by radiation: According to Stefan-Boltzmann law, the radiation energy is given as:

$$Q_{rad} = A \varepsilon \sigma T^4 \qquad (3\text{-}13)$$

where

A = radiant area, i.e. $A \approx Wt = 10^{-6}$ (m^2);

ε = emissivity $\approx$ 1;

σ = Boltzmann constant = 5.67 x 10^{-8} $W/m^2.K^4$[198].

Given T = T_m = 2000 K, Q_{rad} is calculated as :

$$Q_{rad} \approx 10^{-6} \times 5.67 \times 10^{-8} \times (2000)^4$$
$$= 0.91 \text{ (W)} \qquad (3\text{-}14)$$

A summary of the above calculated results is listed in table 3 -3.

Table 3 -3. Heat balance on the cut front

Heat input		Heat output			
Pf(1-r) (W)	α P chem (W)	Qmelt (W)	Qcond (W)	Qconv (W)	Qrad (W)
359	α1334	501	108	0.9	0.9

The following conclusions may be drawn according to this table:

a). The heat loss by convection or by radiation is negligible ;

b). The sum of the heat used for melting the material and the heat loss through conduction can be more than the energy provided by the laser power. Therefore, burning effect of the assistant gas is important, which provides another heating source.

3.1.2. Drag effect on the cut front

The drag effect is due to the shear stress of the gas stream on the molten materials. This is essential to generate a cut as opposed to a weld. The shear stress, τ , for gas flowing through a pipe can be estimated as below [198] :

$$\tau = \frac{1}{2} f_r \rho u^2 \qquad (3\text{-}15)$$

where f_r is the friction factor given by the **Blasius equation** [198], i.e.

$$f_r = 0.0791\ R_e^{\frac{-1}{4}} \qquad (3\text{-}16)$$

It is easily seen that the gas flow velocity has great influence on the shear stress, i.e. the increase of the gas flow velocity will increase the shear stress. The use of different gases also affect the stress value due to the difference in the gas densities as shown in table 3 -4, where the gas velocity u = 70 m/s was used.

Table 3 -4. Shear Stress Caused By Different Gases at Gas Flow Velocity 70 m/s

	ρ (kg/m ^{3})	f x 10^{-3}	τ (N/m ^{2})
Oxygen	1.301	9.71	30.95
Nitrogen	1.142	9.66	27.03
Argon	1.660	9.33	37.95
Helium	0.166	16	6.50

These results approximately indicate the relative magnitude of drag effects when using different gases. It is seen that the drag effect will be increased when argon gas is used, while helium gas has the least drag effect. More accurate calculations will require the gas density and dynamic gas viscosity to be taken at the cut front temperature.

As discussed in chapter one, the laser cut quality is evaluated by kerf width, width of HAZ, surface roughness and dross adhesion. Among the most important operating parameters, gas flowrate and gas composition play important parts in achieving a good cut quality. Commercially pure oxygen is widely used as the cutting gas for most metal cutting, since it has been thought to give good results with respect to attainable cutting speeds and acceptable cut qualities. However, laser cutting using pure oxygen includes certain drawbacks as outlined in chapter one (section 1.3). Oxides are formed during the melting of the material in the workpiece. A portion of the oxides and the molten material may be deposited on the underside of the kerf to form clinging dross particles which reduce the cut quality, and in the case of high alloy steels, these may be difficult to remove. When cutting with pure oxygen, HAZ and kerf width may be

increased due to the excess burning. To replace pure oxygen with inert gas would solve the above-mentioned problem, since inert gas can prevent excess burning. However this would also result in a marked reduction in the cutting speed.

Therefore, using gas mixtures as the cutting gas could be a compromise which would lead to the improvement of laser cut quality without significantly reducing the cutting speed.

3.2. Experimental Procedures

3.2.1. Laser apparatus and equipment

The experiments were performed at the Laser Laboratory of Liverpool University. The laser is the 2 kW CW CO_2 Control Laser originally installed at Imperial College. It is capable of supplying powers up to 2 kW with the wavelength of 10.6 μm (please refer to the Appendix B for a more detailed description of the laser).

The workpiece movement is controlled by a Computerised Numerical Control workstation(CNC) (Fig. 3 -1). The CNC controller manufactured by Trio Ltd. of U.K., can control the movement in X and Y direction simultaneously and can achieve a maximum traverse speed of 120 (mm/s).

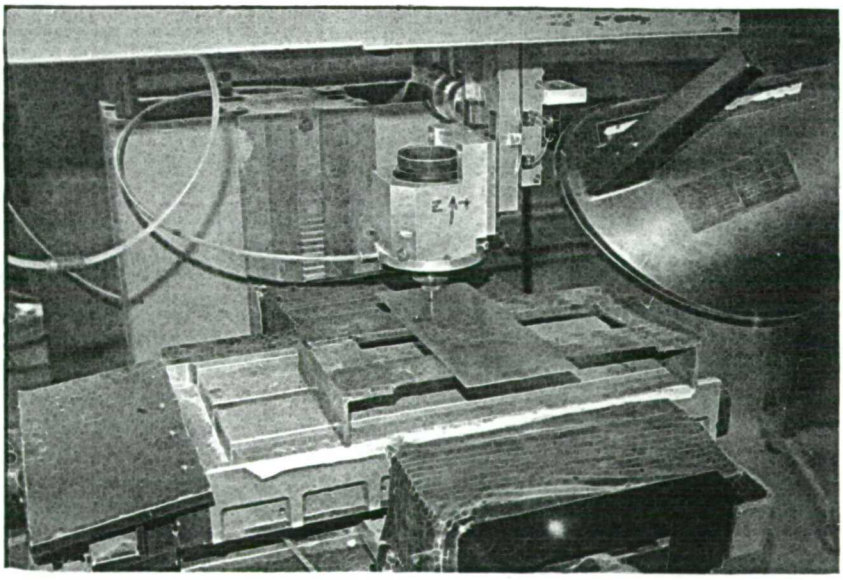


Fig. 3 -1. Photo of the workstation.

3.2.2. Experimental set-up

The experimental arrangement was the same as that shown in Fig. 2-15. The laser beam, together with the coaxial cutting gas, past through a converging conical nozzle with a diameter of 1.4 mm and was focussed onto the workpiece surface through a KCl lens with a focal length of 125 mm.

The gas mixture was based on two components, i.e. a commercial pure inert gas (99.99%) mixed with commercial pure oxygen (99.5%). The following gas and gas mixtures were used as the cutting gases for this study (in volume percent):

0 - 5 - 30 - 50 - 99.99 % Helium in Oxygen;
0 - 5 - 30 - 50 - 99.99 % Nitrogen in Oxygen;
0 - 5 - 30 - 50 - 99.99 % Argon in Oxygen.

A summary of the constant and process parameters is listed in table 3-5. To get comparable results, the lens and the nozzle were kept in good conditions and at the same position throughout the experiment. The beam mode structure was also kept nearly the same.

Table 3 -5. Process Parameters

Laser power	1850 W
Beam mode	Fig. 3 -4
Focal lens	ϕ38 x 125 mm, KCl, plano-convex
Nozzle	ϕ1.4 mm
Nozzle standoff distance	0.5 mm
Workpiece	1 mm thick of mild steel
Cutting speed	10 - 120 mm/s
Gas flow velocity	25 - 86 m/s

The laser beam mode structure is measured by a LBA (Fig. 3 -2), manufactured by the Applikationslabor fur Lasertechnik CO. of West Germany (A.L.L.) . The scanning needle has a diameter of 1.0 mm and rotates at a speed of 1500 r.p.m. (revolutions per minute). Laser powers in the range from 200 - 2000 (W) can be measured. The LBA is directly connected to an oscilloscope to display the signals in X and Y channels.

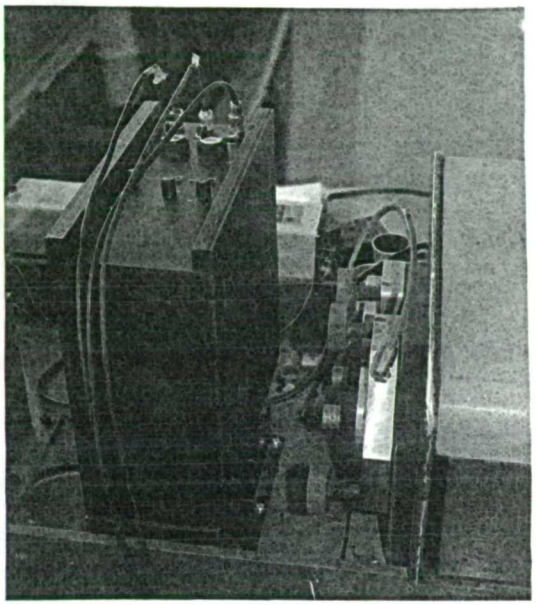


Fig. 3 -2. Photo of the A.L.L. LBA .

The gas mixture instrument is shown in Fig. 3 -3, where the gas flow rate of each component is controlled through a gas flow meter.

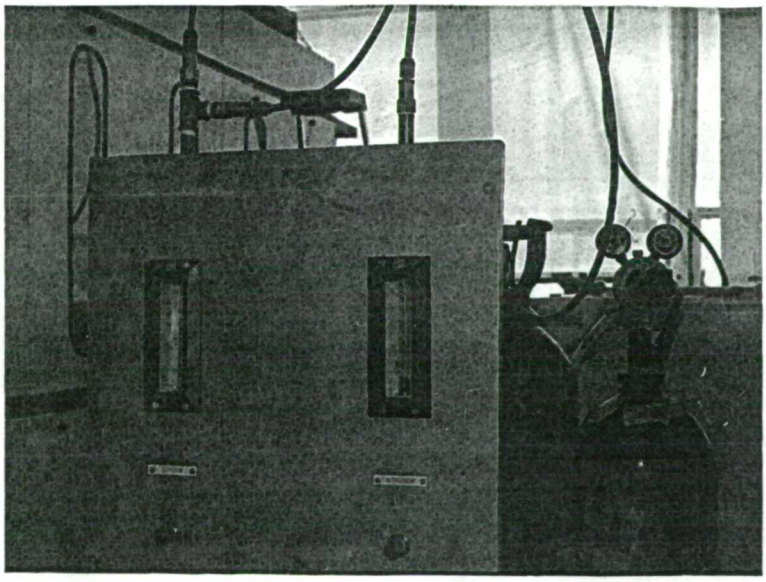


Fig. 3 -3. Photo of the gas mixture instrument.

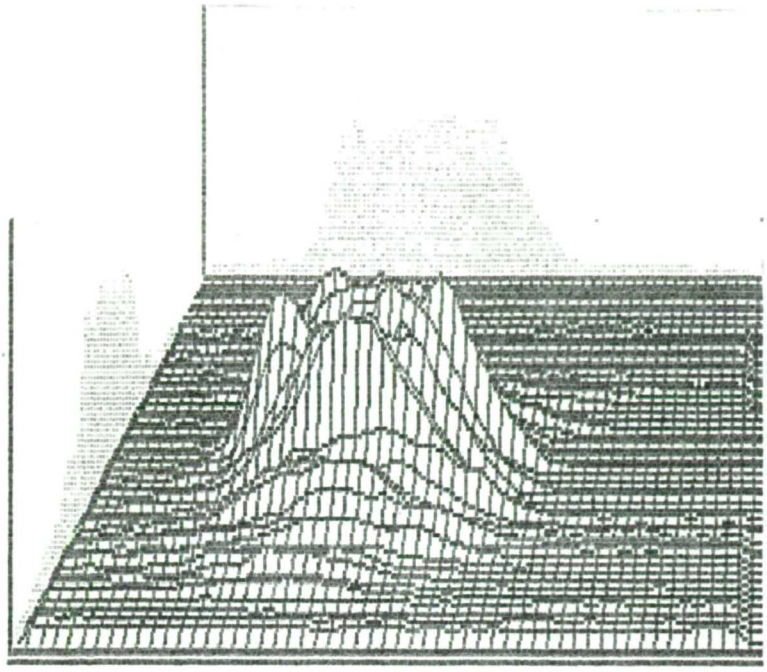


Fig. 3 -4. Laser beam mode structure from the LBA.

3.3. Results and Discussion

The laser cut quality was assessed by examination of cut kerf width, surface roughness, clinging dross and the width of HAZ. The top surface kerf width of the cut sample was measured with a microscope to an accuracy of ± 0.01 mm and average readings were taken. The surface roughness was visually examined and classified as good and poor depending on the frequency and irregularity of the striation (Fig. 3 -5). The HAZ was assessed by observing the top surface oxidation marks (Fig. 3-6).

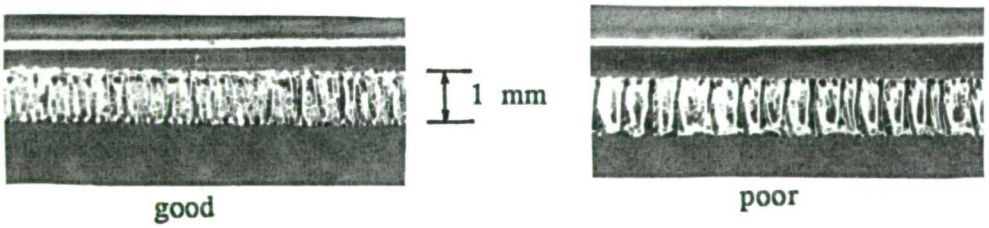


Fig.3 -5. Classifications of the laser cut surface roughness.

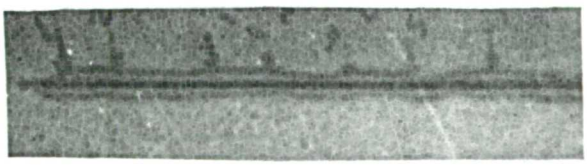


Fig. 3 -6. Measurement of HAZ width.

The clinging dross was visually examined and classified as four grades depending on the size and amount of the dross:

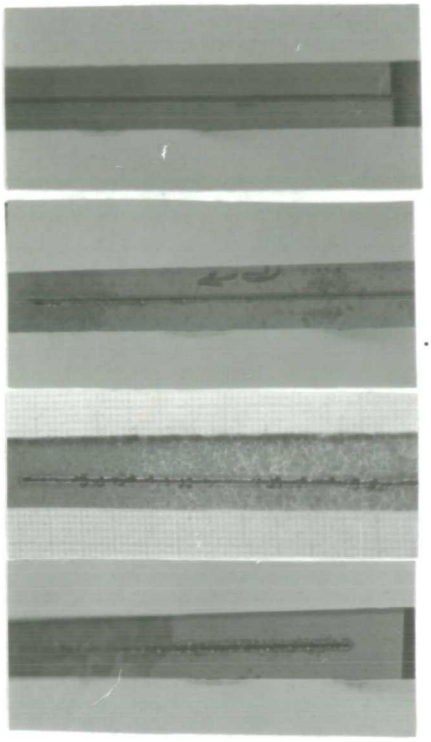


Fig. 3 -7. Classification of dross adhesion.

3.3.1. Influences of cutting speed and gas composition on kerf width

The relationships between cut kerf width and cutting speed for different gases and gas mixtures at a given gas velocity 86 m/s are shown in Figs. 3 -8, 3 -9 and 3 -10. The gas velocity here was calculated from the ratio of gas flowrate divided by the nozzle exit area , since this velocity is controllable by adjusting the gas flowrate. The use of the concept - gas velocity instead of gas flowrate is mainly because that gas flow characteristics are usually described according to the gas flow velocity, i.e. subsonic flow or supersonic flow.

The figures given in the above figure were estimated according to the area of the cut kerf being blocked by the clinging dross particles. The calculation of the gas velocity was made on the assumption that the ratio of the absolute pressure inside the lens chamber over the ambient pressure is less than 1 (subsonic flow).

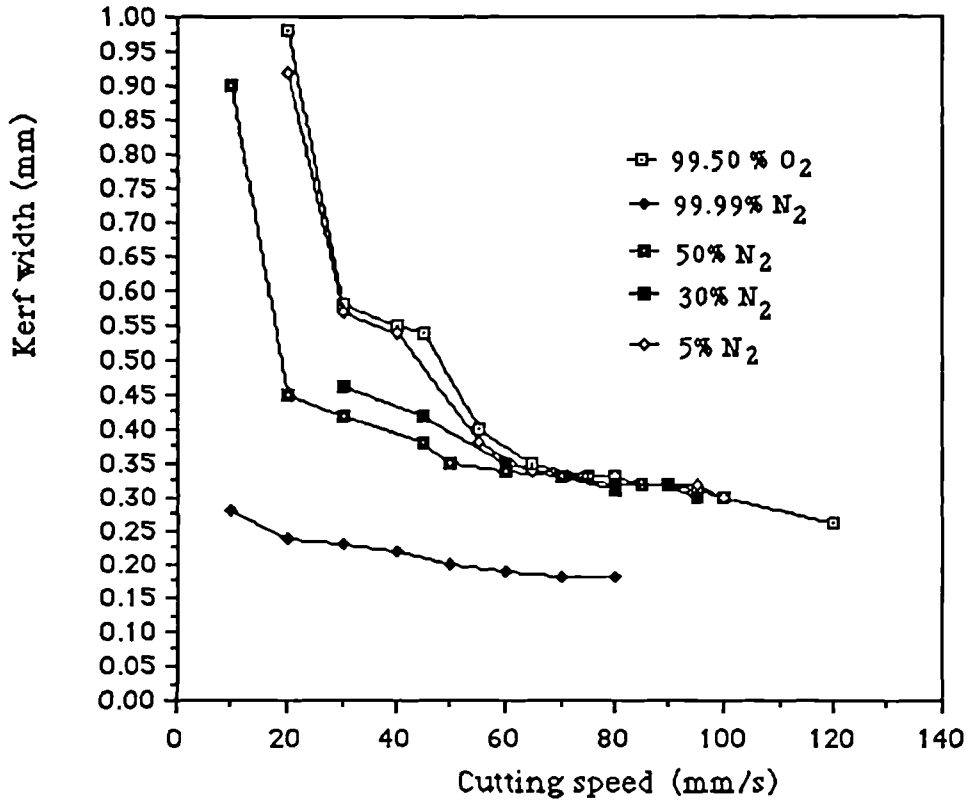


Fig. 3 -8. Kerf width versus cutting speed for O_2/N_2 mixtures.

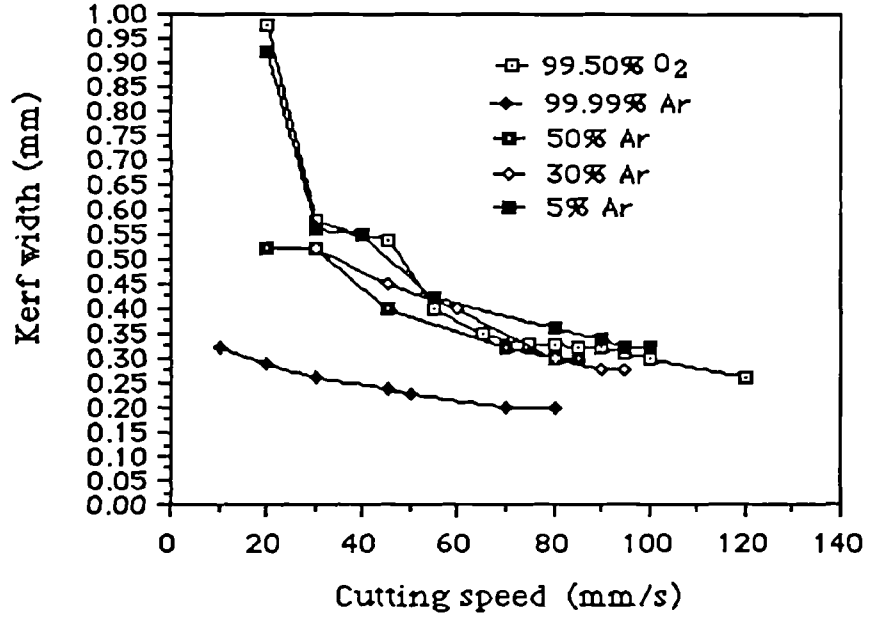


Fig. 3 -9. Kerf width versus cutting speed for O_2/Ar mixtures.

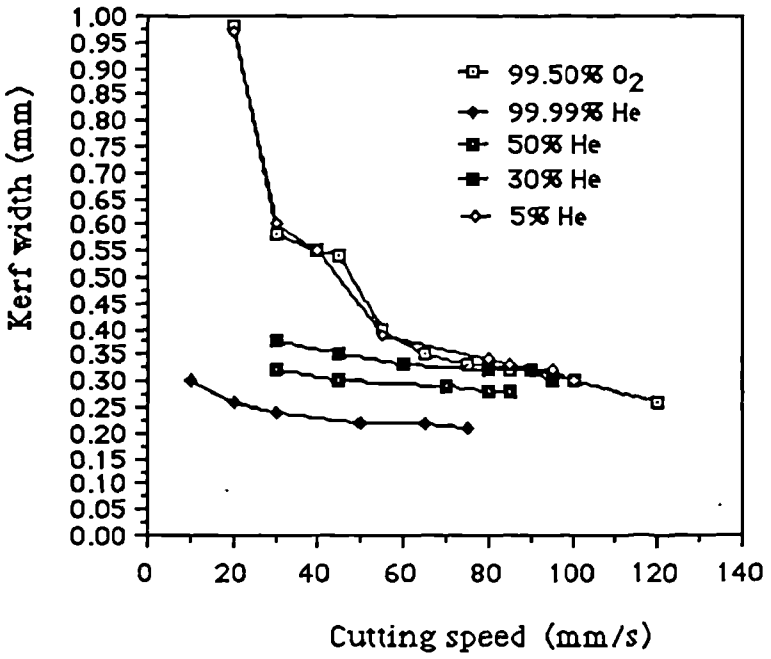


Fig. 3 -10. Kerf width versus cutting speed for O_2/He mixtures.

As can be seen from these graphs, kerf width decreased with the increase of the cutting speed for all the gases and gas mixtures. The kerf width increased, however, with the increase of oxygen content in the gas mixtures at a fixed cutting speed. At the maximum speed, the kerf width was reduced by using pure oxygen compared to the other gas mixtures. The effects of different inert gases on the kerf width were nearly the same.

(i). Oxygen assisted laser cutting. The kerf width is a measure of the amount of molten materials removed during the cutting process, and is thus determined by the amount of heat at the cutting front for a given material thickness and for a fixed laser beam spot size. The amount of heat is controlled by the laser power and the burning reaction. The spot size for a focussed beam is a function of the wavelength of the laser radiation and the beam mode structure as described by the equation (1 -3). At the low cutting speed the oxygen burning front moved faster or as fast as the laser beam traverse speed as discussed in chapter one. This resulted in intense sideways (as well as in other directions) melting of the materials. Meanwhile the longer interaction time between the laser beam and the workpiece at a slower cutting speed generated more heat in all the directions and thus melted more materials. These large amount of molten

materials were blown away by the gas jet to form a wide cut kerf. When the cutting speed was increased, the laser beam traverse speed moved faster than the oxygen burning speed, i.e. the oxidation reaction speed could not match the laser beam traverse speed. The region where the oxidation reaction could be maintained was reduced leading to a narrow kerf.

(ii). Pure inert gas assisted laser cutting. When cutting with one of the pure inert gases the input energy was purely from the laser beam interaction with the workpiece material. The amount of heat generated was thus controlled by the interaction time between the laser beam and the workpiece for a given power density and at a given gas velocity. The slower the cutting speed the longer the interaction time and thus the more heat coupled to the process. Therefore the kerf width was wide at the low cutting speeds, and was narrow at the high cutting speeds.

The lack of burning reactions when using the inert gases reduced the heat at the cut face leading to a reduced kerf width. As calculated before, the convective coefficient varies with the different gases, in particular helium gas has the largest value. However, the convective cooling effect is small for all the gases and thus negligible due to the small heat transfer areas concerned. Therefore the effect of different gases on the kerf width was almost the same.

(iii). Gas mixtures assisted laser cutting. The gas mixtures reduced the oxidation effect due to the reduced oxygen content in the gas stream. The less the oxygen content in the gas stream the less the heat was generated at the cutting front and thus the narrower the kerf width. However, this was true only at a fixed cutting speed. At the maximum cutting speeds, the kerf width obtained with pure oxygen was narrower, since a higher speed was achieved with pure oxygen assisted cutting.

(iv). The kerf width varied approximately as $1/\upsilon$. As discussed above, the melt region due to the heat from the the oxygen burning reactions and from the laser beam interactions with the workpiece determines the kerf width. The faster the cutting speed , the less the interaction time and the less the burning reaction. It is thus suspected that the kerf width may be

inversely proportional to the cutting speed. Figure 3 -11 shows this relationship for pure oxygen, where υ is the cutting speed. It is seen that the correlation coefficient, R , to this function is 98%. Similar results for inert gases and for gas mixtures are shown from Fig. 3 -12 to Fig. 3 -23.

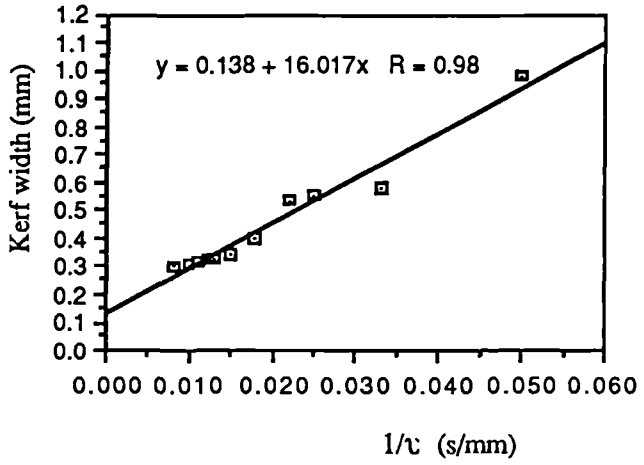


Fig. 3 -11. Kerf width versus $1/\upsilon$ for pure oxygen.

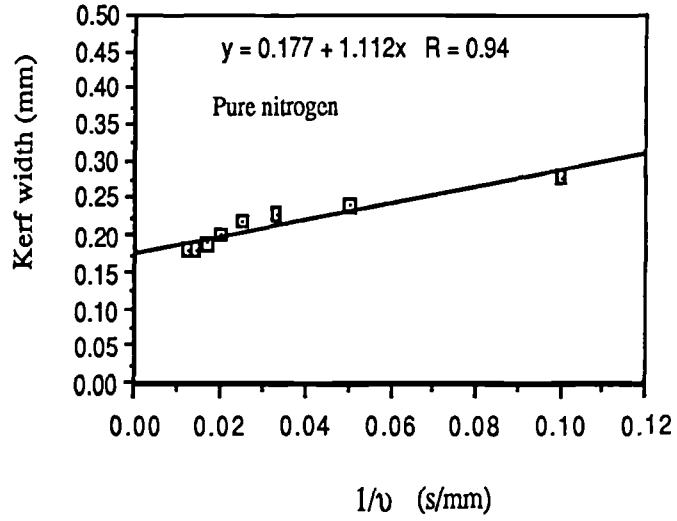


Fig. 3 -12. Kerf width versus $1/\upsilon$ for pure N_2.

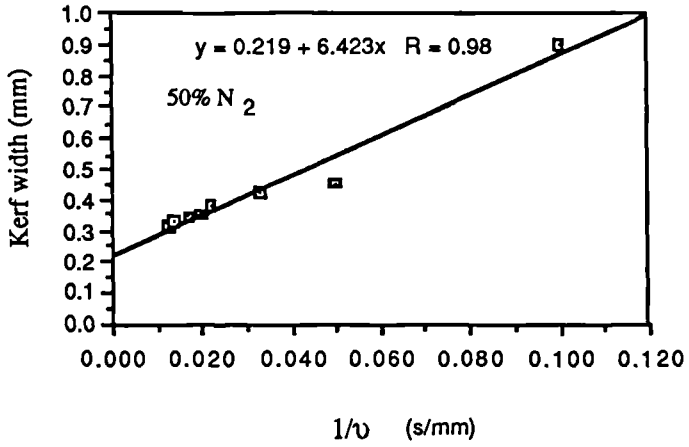


Fig. 3 -13. Kerf width versus 1/υ for O_2/N_2 mixture, oxygen content at 50%.

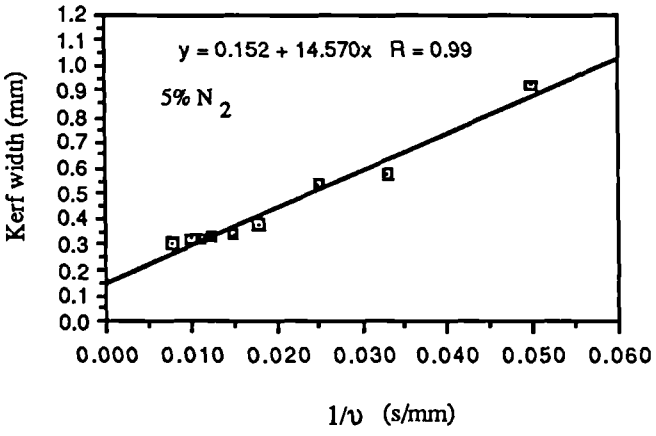


Fig. 3 -14. Kerf width versus 1/υ for O_2/N_2 mixture, 95% O_2.

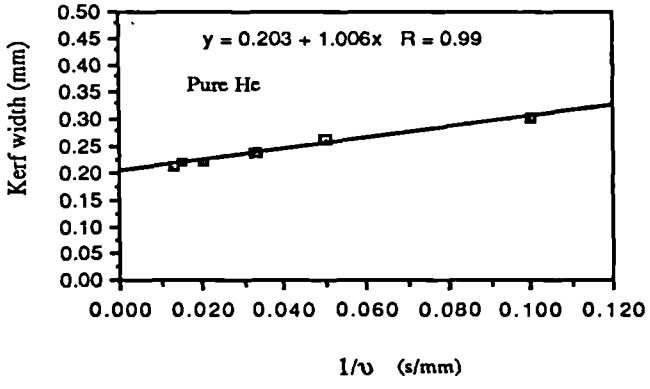


Fig. 3 -15. Kerf width versus 1/υ for pure He.

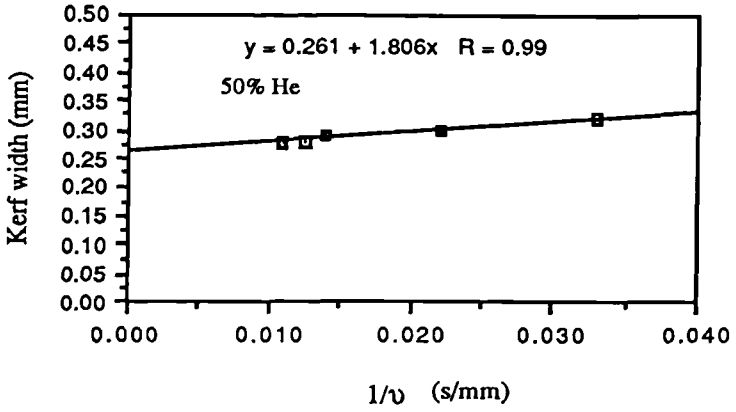


Fig. 3 -16. Kerf width versus 1/υ for O_2/He mixture, O_2 content at 50% .

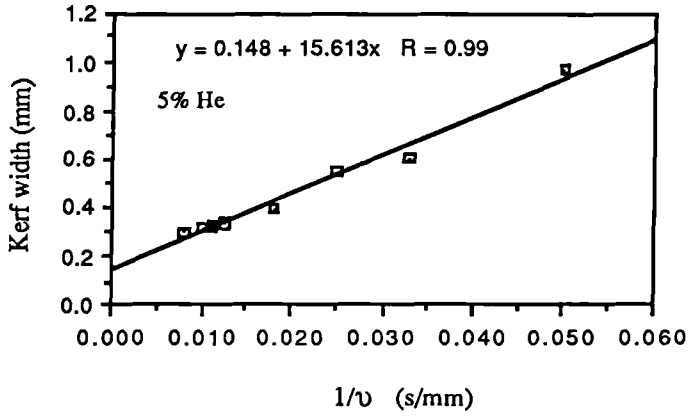


Fig. 3 -17. Kerf width versus 1/υ for O_2/He mixture, O_2 content at 95%.

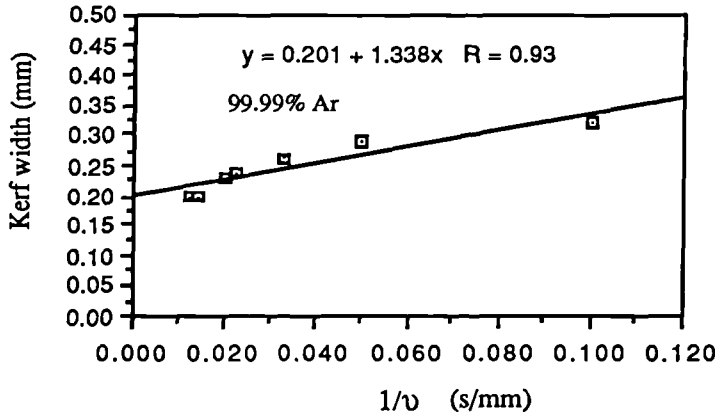


Fig. 3 -18. Kerf width versus 1/υ for pure Ar.

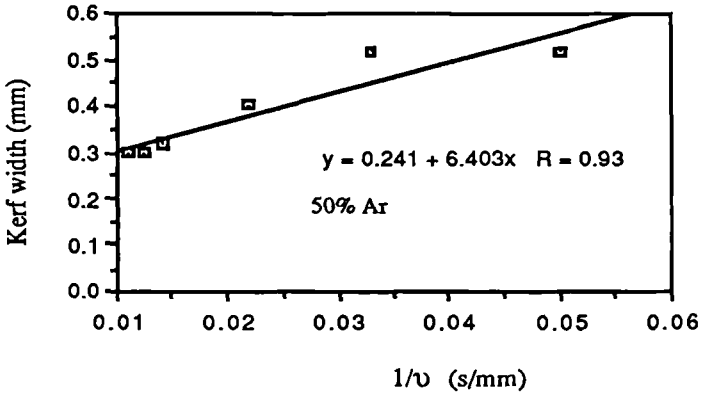


Fig. 3 -19. Kerf width versus 1/υ for O_2/Ar mixture, O_2 content at 50%.

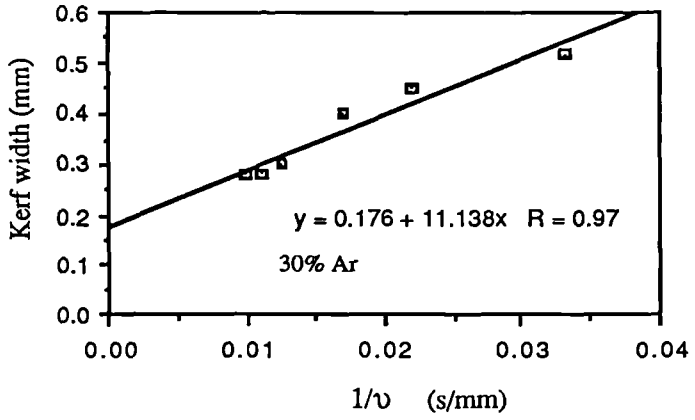


Fig. 3 -20. Kerf width versus 1/υ for O_2/Ar mixture, O_2 content at 70%.

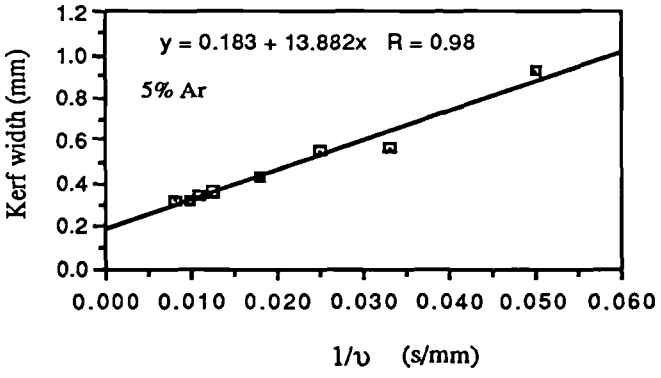


Fig. 3 -21. Kerf width versus 1/υ for O_2/Ar mixture, O_2 content at 95%.

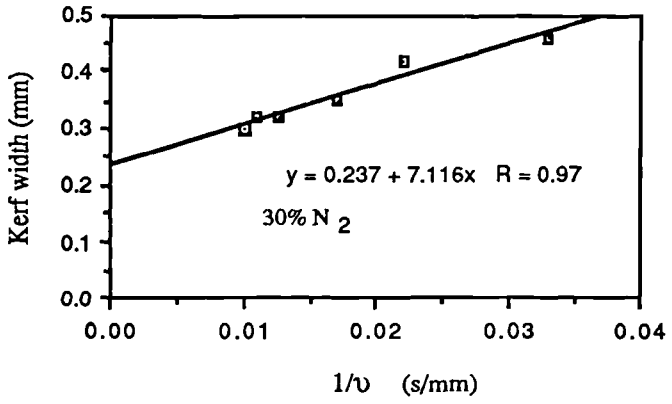


Fig. 3 -22. Kerf width versus 1/υ for O_2/N_2 mixture, O_2 content at 70%.

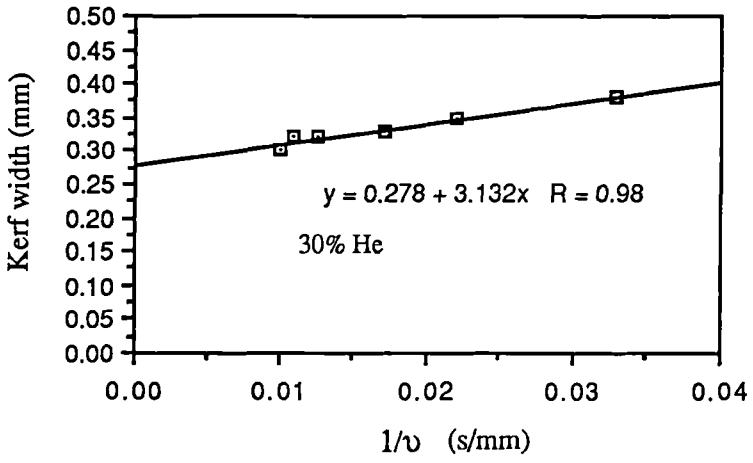


Fig. 3 -23. Kerf width versus 1/υ for O_2/He mixture, O_2 content 70%.

It is seen from these figures that the kerf width has an approximately linear relationship with 1/υ within a speed range. When the cutting speed is very high, i.e. 1/υ ≈ 0, the empirical equations would not be suitable, since then the kerf width would be expected to be zero. The correlation between the kerf width and the cutting speed can be theoretically represented according to the overall heat balance equation (1 -1) as follows :

$$W \approx \frac{P}{\eta \rho v t (C_p \Delta T + L_m)} \qquad (3\text{-}17)$$

Given values as below:

$P = 1850$ W;

$\rho = 7833$ kg/m^3 ;

$t = 10^{-3}$ m;

$C_p = 465$ J/kg·K;

$\Delta T \approx T_m = 2000$ K;

$L_m = 2.66 \times 10^5$ J/kg;

the equation then becomes:

$$W \approx 0.197 \frac{1}{\eta v} \qquad (3\text{-}18)$$

η is the reciprocal of process efficiency. Theoretically, increasing the oxygen content in the gas mixture would enhance the burning reaction thus generating more heat and therefore increase the process efficiency or decrease the value of η . In other words, the gradient would increase with increasing the oxygen content. This was in accordance with the experimental results as shown above. However, this theory cannot explain the constant in the developed empirical equation.

3.3.2. Gas effects on dross clinging problem

3.3.2.1. Results at a fixed cutting speed

Figure 3 -24 shows the relationship between the gas velocity, gas composition and the dross clinging problem for O_2/N_2 mixtures at a cutting speed of 50 mm/s. The shadow and blank areas represent the dross grading regions. The experimental points were connected by straight lines for simplicity. It is clearly seen that the dross problems were principally controlled by the gas velocity, i.e. the amount of clinging dross was reduced by increasing the gas velocity for all the gas compositions. It is also seen that when the oxygen content was high (70% or above) the dross problem became slightly worse with the increase of oxygen content in the gas mixtures.

(i). Gas velocity. The likelihood of dross clinging is mainly influenced by the melting/flowing conditions of the molten material on the cutting front. A part of the molten materials is ejected out into a large amount of small dross particles by the drag force of the gas flow as described in 3.1. Simultaneously the other part stays there, and is finally solidified into clinging dross. According to the equation (3 -15) the shear stress is proportional to the square of the gas velocity for a given gas and a given material thickness. Take the pure oxygen stream as an example, when the oxygen velocity increases from 50 m/s to 70 m/s, the shear stress is calculated to correspondingly increase from 15.79 N/m^2 to 30.95 N/m^2 (96% increase). The dross problem was correspondingly improved from grade B region to the intermediate region next to A.

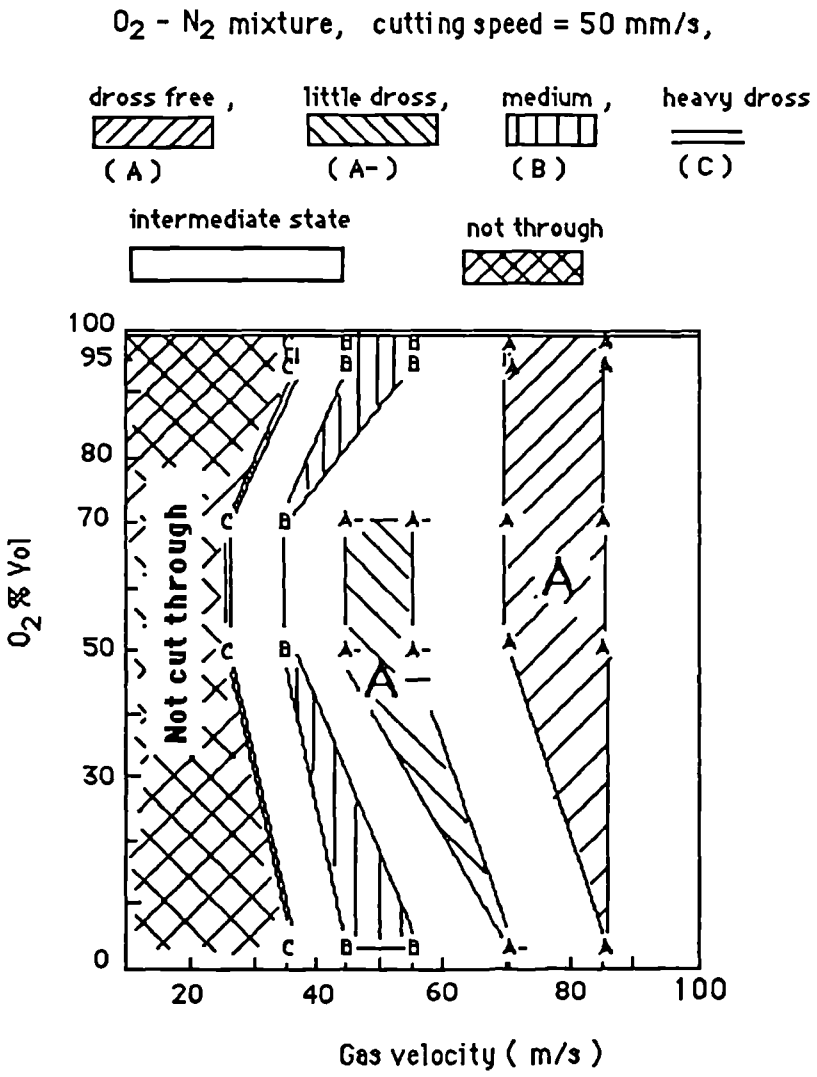


Fig. 3 -24. Relationship between gas velocity, gas composition and dross clinging problems for O_2/N_2 mixtures.

(ii). Oxygen content. With the increase of the oxygen content in the gas mixture more heat was produced and a wider kerf was resulted as shown in Fig. 3 -6. Therefore the amount of molten material to be blown away per unit time was increased, i.e. the momentum of the molten materials increased, which required stronger drag coefficient from the gas flow. Therefore, at a given cutting speed and gas flow velocity, the dross problem was observed to get worse for those gas mixtures with high oxygen content. This was particularly so at relative low gas velocity as observed in the above graph.

Similar relationships between the gas velocity, gas composition and the dross clinging problem for O_2/Ar and O_2/He mixtures are shown in Figs. 3 -25 and 3 -26 respectively.

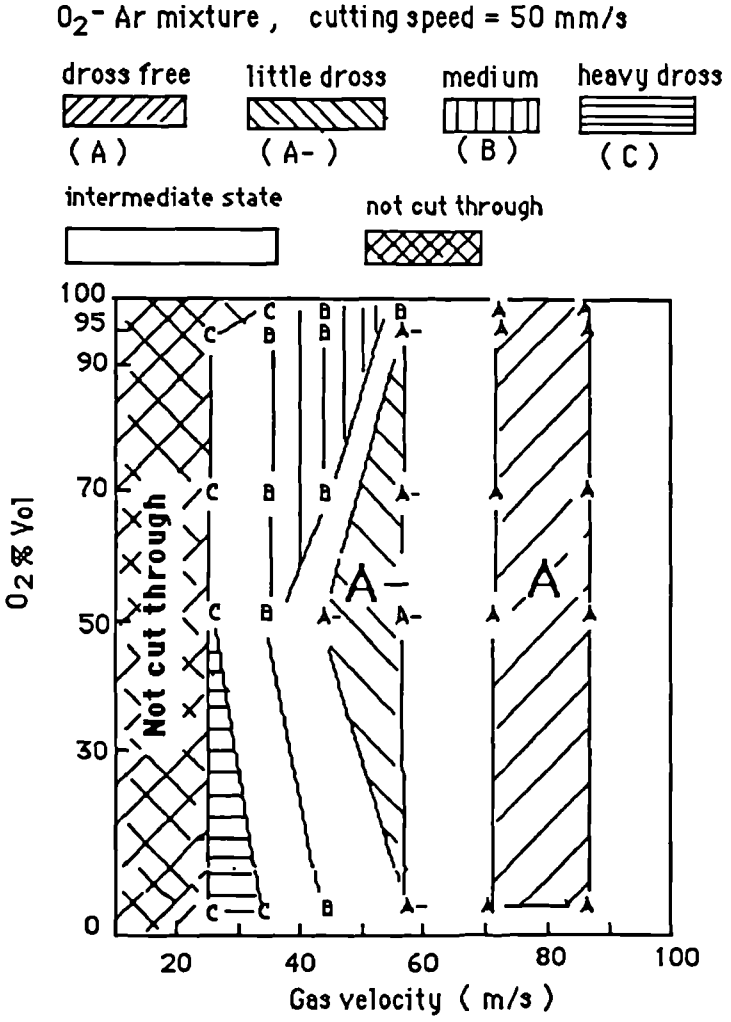


Fig. 3 -25. Relationship between gas velocity, gas composition and dross clinging problems for O_2/Ar mixtures.

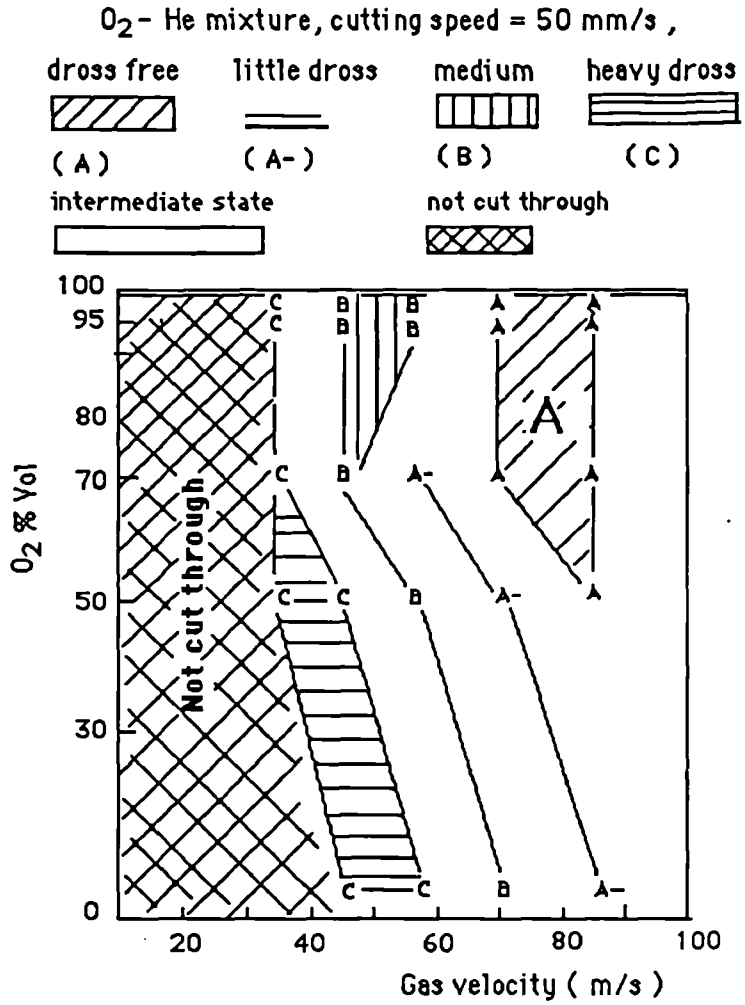


Fig.3 -26. Relationship between gas velocity, gas composition and dross clinging problems for O_2/He mixtures.

Since the drag effects of different gases are different as shown in Table 3- 4, the removal of the molten materials is thus expected to be most efficient with O_2/Ar mixtures and least efficient with O_2/He. This can be seen when these two graphs are compared. For example, when oxygen content was 50% and the gas velocity at 70 m/s, the dross clinging problem was classified as grade A in Fig. 3 -25 but grade A- in Fig. 3 -26.

Since the shear stress values produced by argon, nitrogen and oxygen stream are rather close, the difference in the removal efficiency of the molten materials by using O_2/Ar and O_2/N_2 mixtures was not obvious.

3.3.2.2. Results at the maximum cutting speed

Figures 3 -27 and 3 -28 show the effect of the gas velocity on the dross grade for O_2/Ar, O_2/N_2 and O_2/He mixtures at the maximum cutting speeds. Since the O_2/Ar and O_2/N_2 mixtures had similar effect, they were plotted in the same graph as Fig. 3 -27. The maximum speed is defined here as the highest achievable cutting speed with acceptable cut quality (dross grading B or above).

It is seen that increasing the gas velocity improved dramatically the dross adhesion problem due to the increased drag effect as discussed earlier. Increasing the oxygen content had , however, a different effect from those observed in Figs. 3 -24 to 3 -26. This can be explained as follows. A higher cutting speed is usually obtained with increasing the oxygen content as to be discussed in the following section, therefore the maximal cutting speed with pure oxygen assistance was much higher than those with gas mixtures assistance. This higher speed led to a narrower kerf as shown previously in Figs. 3 -8 to 3 -10. Thus the amount of molten materials blown away per unit time was reduced. In other words the removal of the molten dross was more efficient.

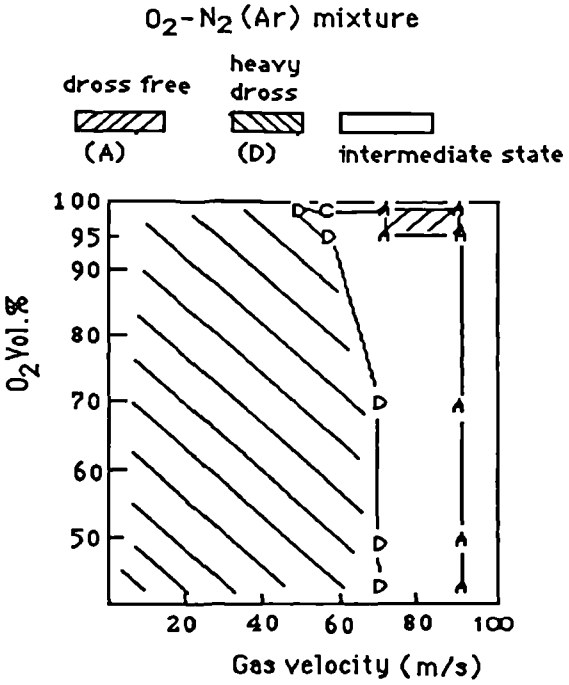


Fig. 3 -27. Relationship between gas velocity, gas composition and dross grade for O_2/N_2 and O_2/Ar mixtures at maximum cutting speeds.

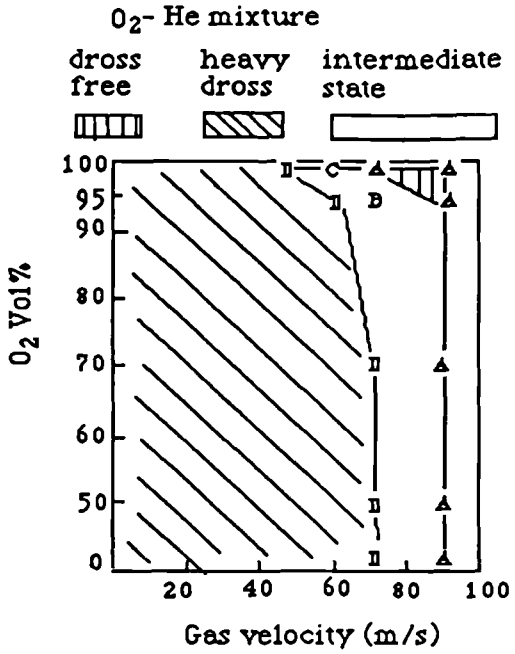


Fig.3 -28. Relationship between gas velocity, gas composition and dross grade for O_2/He mixtures at maximum cutting speeds.

3.3.3. Effects of gas composition on cutting speed

Figure 3 -29 shows the correlation between the maximum cutting speed and the gas velocity for different gas mixtures.

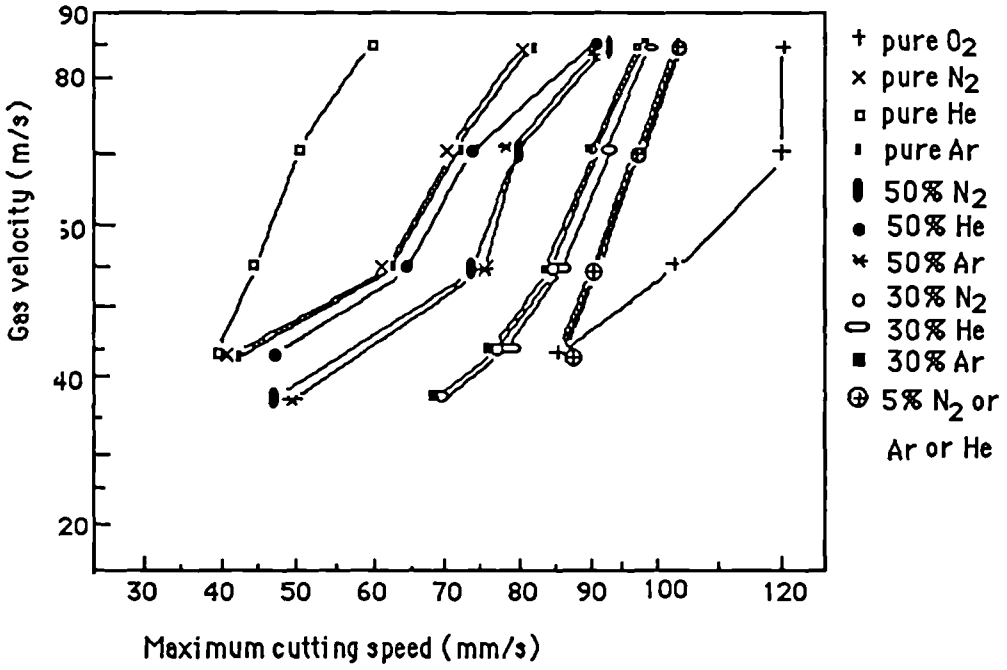


Fig. 3 -29. Effects of gas composition on maximum cutting speed.

It can be seen that for a given gas composition, the maximum speed increased with increasing the gas velocity. For a given gas velocity, an increase in the oxygen content resulted in the increase of the maximum speed. Using pure oxygen as the cutting gas, the cutting speed was high even at the low gas velocity. The explanations are given as below.

(i). In chapter one, it has been shown that the molten layer thickness would increase with the cutting speed at a given gas velocity (Fig. 1 -4). Thus if the speed is too high, the dross fails to clear quickly, which results in a sharp rise in the HAZ and cutting failure. The kerf loses its near parallelism and a rough surface results. It is also seen from Fig. 1 -4 that the molten layer thickness decreases with increasing gas flow velocity, since the removal of the molten material is more efficient with a higher gas velocity. Therefore, a higher maximum speed can be achieved at a higher gas velocity.

(ii). A higher cutting speed was obtained by increasing the oxygen content. This was due to the chemical reaction between the oxygen and the workpiece, which generated heat. Namely, more energy was put into the process, which facilitated the cutting process. For example, in the pure oxygen assisted cutting, the maximum speed reached 120 mm/s, while using the gas mixture with 30% inert gas, the maximum speed reached only 95 mm/s.

(iii). The addition of the inert gases to the oxygen stream had deleterious effect on the cutting speed depending on type of gas used. Helium had the slowest cutting speeds due to its lowest density and hence reduced drag coefficient. Argon and nitrogen behaved almost the same since their drag coefficients are quite similar as discussed before. However, when the oxygen content was high (70% or above), the deleterious effects of the three gas mixtures with oxygen on the cutting speed were observed to be similar. This was due to the fact that the drag effect was mainly controlled by oxygen at such a high oxygen content and that the drag effect of oxygen is similar to Ar and N_2 as calculated at the beginning of this chapter.

3.3.4. Optimum speed range as a function of gas composition

The relationships between overall cut quality, volume percent of oxygen and cutting speeds at two levels of gas velocities are shown in Figs. 3 -30 and 3 -31. The areas shown cover the operating conditions for good cuts. A good cut is here defined as a cut with little dross (grade A- or above), smooth surface, narrow kerf and narrow HAZ.

(i). Results at a low gas velocity (43 m/s) are shown in Fig. 3 -30. It is seen that at a given speed good cuts were achieved with pure O_2 and with 50% or less Ar or N_2 mixtures (O_2/Ar and O_2/N_2 gave similar results, hence they are presented together on the figure), and with 30% He or less gas mixtures. When the content of inert gas was more than the above specified values, cut edges were not clean. This can be understood from the low heat input due to the reduced chemical burning reactions, which could not maintain the molten -temperature long enough to allow dross to be blown away. It is interesting to notice that the helium mixture had a relatively narrower range while Ar or N_2 mixtures had a larger range. This was due to their different effects on cutting speed and on the extent of dross adhesion as discussed before. It is also seen that pure O_2 had a wider speed range when the cutting speed was high, while the gas mixtures had a wider speed range when the cutting speed was low.

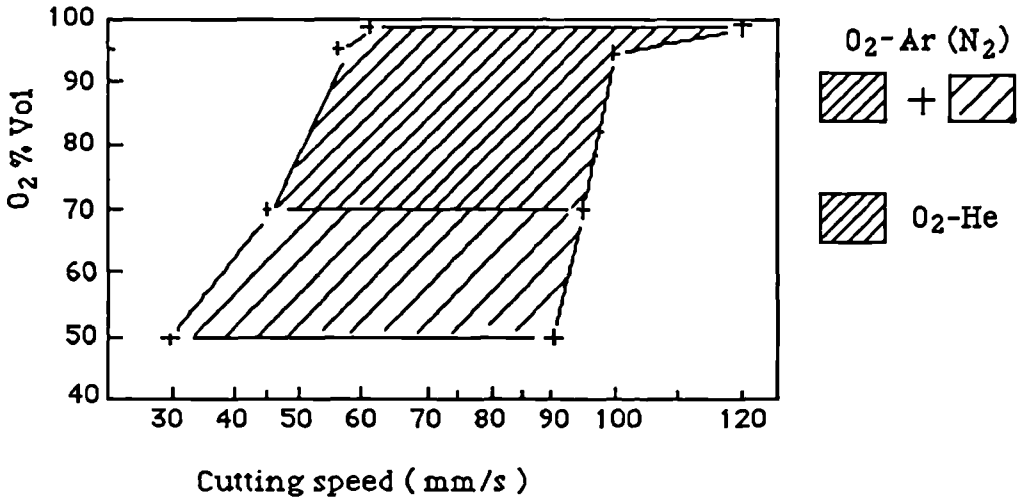


Fig. 3 -30. Optimum speed range as a function of gas composition at low gas velocity, 43 m/s.

(ii). Results for a high gas flow velocity (86 m/s) are shown in Fig. 3 -31.

Basically, good cuts were achieved at certain speeds for all the gas mixtures even at the low oxygen content. This was possibly due to the increase of the drag effect given by gas flow, which may compensate for the loss of the amount of energy caused by the reduction of the oxygen content. In particular, it is noticed that excellent cuts with dross free, narrow HAZ, narrow kerf and smooth surface were obtained with gas mixtures with inert gas contents at 30% and 50%. Although good cuts were obtained with pure inert gases, the maximum cutting speed stopped at 80 mm/s. The gas flow velocity, i.e. the gas pressure inside the laser head chamber, could not be raised higher due to such factors as the focussing lens.

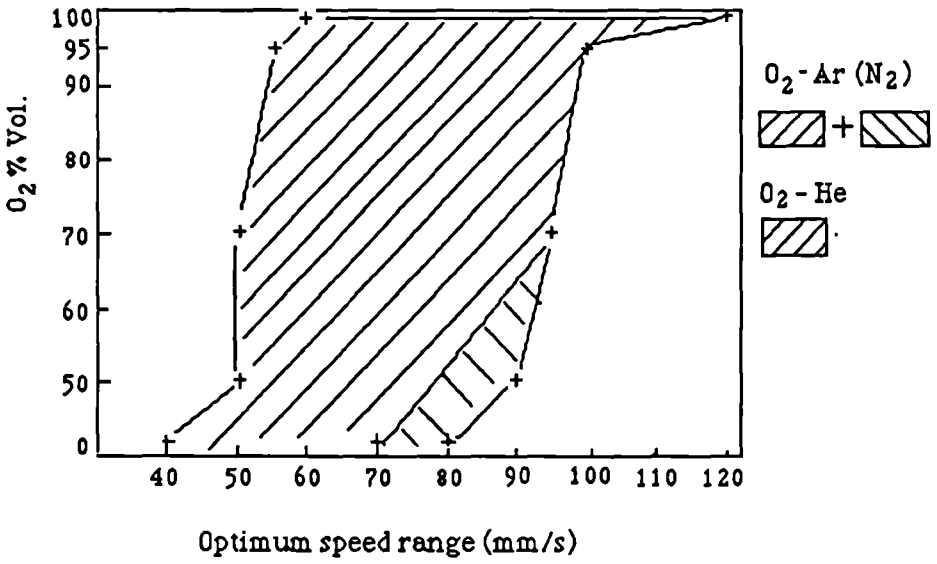


Fig. 3 -31. Optimum speed range as a function of gas composition at the gas velocity of 86 m/s.

From the above discussion, general models defining the optimum speed ranges at both the high and low gas velocities can be drawn. Based on the data shown in Fig. 3 -30, the following equation is produced:

$$(2.7 + 57.1 * \text{Vol\%}) \leq \upsilon \leq (64.5 + 46.8 * \text{Vol\%}) \qquad (3\text{-}17)$$

$$(R = 0.99) \qquad (R = 0.82)$$

where Vol% is the oxygen content in the gas mixture in volume percent, R is the correlation coefficient to the corresponding function. This model represents the approximate optimum cutting speed range as a function of

the gas composition at the low gas velocity. At the high gas velocity, a different model is produced as below:

$$(39.9 + 17.7 * \text{Vol\%}) \leq \upsilon \leq (77 + 31.8 * \text{Vol\%}) \qquad (3\text{-}18)$$

$(R = 0.96)$ $(R = 0.87)$

This indicates the approximate optimum speed range at the high gas velocity.

3.4. Chapter Summary

A study has been made of the effect of various gas mixtures on the cut quality. Results are presented of cutting with pure oxygen, O_2/Ar, O_2/N_2, O_2/He mixtures, and pure inert gases. The following points can be drawn:

(i). Kerf width was found to be approximately inversely proportional to the cutting speed. A wider kerf was obtained with increasing oxygen content at a fixed speed. At the maximum speed, however, the kerf width was reduced with the pure oxygen assistance.

(ii). Clinging dross problems are principally controlled by gas velocity at a given cutting speed. Increasing the gas velocity would reduce the amount of dross particles. At the maximum cutting speed, increasing the oxygen content would also reduce the amount of clinging dross particles.

(iii). The maximum cutting speed can be increased with the increase of gas velocity. Pure O_2 will cut faster at a given gas velocity. Helium gas mixtures had a somewhat lower cutting speed than the other gas mixtures. However, when the inert gas content was small (< 30%), Helium behaved similar to Ar and N_2.

(iv). There existed optimum speed ranges as a function of gas composition and gas velocity. At the low gas velocity, the optimum speed range was approximately represented by equation (3 -17), while at the high gas velocity, the optimum speed range was approximately indicated by equation (3 -18).

(v). A patent held by Nielson [115] on laser gas mixtures may restrict the free use of the patent content.

(vi). The results presented here gave detailed gas effects on laser cutting of mild steel, while Nielson' work (Fig. 1 -22) was based on laser cutting of stainless steel. In Fig. 1 -22, the cutting speed increased with reducing the oxygen content in the range of 70 - 90%, which is hard to be understood from the point of view that oxygen plays a crucial part in assisting the cutting process. This phenomena was not observed by the author of the thesis.

CHAPTER FOUR

OPTICAL METHODS FOR IN-PROCESS MONITORING OF LASER CUTTING PROCESS

4.1. Introduction and Background

As discussed before, laser cut quality is affected by a variety of factors such as laser power, beam mode structure, cutting speed, gas flow velocity and gas composition. Some of these factors may change their values during the cutting process. For example, the absorbed laser power fluctuates due to the following reasons. Firstly, the absorption coefficient of the cut front varies with the beam incidence angle (Fig. 1-10) possibly according to the striation pattern. Secondly, the absorption coefficient is affected by any plasma formation. At the formation of the plasma, the absorptivity is significantly increased due to inverse Bremsstrauhlung effects, in which the absorption coefficient is proportional to the square of the wavelength as discussed in chapter one (Fig. 1 -11). Thirdly, the laser power itself fluctuates due to the optical feedback effect as discussed in chapter one as well as the mode instability in the laser cavity to be discussed in chapter five. The gas flow also may change during the processing due to the turbulent flow from the nozzle and the irregular movement of the cutting front (chapter one, section 1.2.2.2. Gas flow parameters). The cutting speed may vary due to the vibration of the CNC table. Also, the workpiece thickness and surface conditions may vary over the surface of the workpiece. Any of these variations could lead to reduced cut quality and reduction in process efficiency. It is thus desirable to develop an on-line quality control system particularly for high volume production and precision cutting applications. The first stage of an on-line control system is in-process sensing. Thus in-process sensing and monitoring of the cut quality parameters constitute the main part of this thesis. In this chapter and the following chapters different approaches including optical, acoustic and thermal methods will be described.

Since laser cutting is normally a thermal process, the melt pool

temperature is likely to be an indicator of the cut quality. In laser cutting of metals, the melt pool temperature is controlled by the heat balance on the cut front between the heat input and the heat loss. Increasing the input heat will obviously increase the melt pool temperature. The input heat comes from two sources: the absorbed laser beam power and the oxygen burning reaction with melts.

The absorbed beam power depends on the input laser power level, the absorptivity of the cut front and the cutting speed. The absorptivity of the cut front is determined by the surface reflectivity, i.e. absorptivity = 1 - reflectivity. The latter is a function of the beam incidence angle and polarisation as given below [17]:

$$R_p = \frac{\tan^2(\phi_1 - \phi_2)}{\tan^2(\phi_1 + \phi_2)} \qquad (4\text{-}1)$$

and

$$R_s = \frac{\sin^2(\phi_1 - \phi_2)}{\sin^2(\phi_1 + \phi_2)} \qquad (4\text{-}2)$$

where R_p is the reflectivity for light polarised in a plane parallel to the plane of incidence and R_s is the reflectivity for light polarised perpendicular to the plane of incidence. The angles ϕ_1 and ϕ_2 are the angle of incidence and the angle of transmission respectively. The angle of transmission, ϕ_2, is given as [17]:

$$\sin\phi_2 = \frac{\sin\phi_1}{n^*} \qquad (4\text{-}3)$$

where n* is the complex index of refraction of the workpiece and is determined by the workpiece permittivity, ε_r, as below [17]:

$$n^* = \sqrt{\varepsilon_r} \qquad (4\text{-}4)$$

The workpiece permittivity is a function of the wavelength of the incident

light, in the case of CO_2 laser beam (λ = 10.6 μm), the permittivity of steel is given as ε_r = 1414[17]. Thus n* is calculated as 37.6. Given the incidence angle ϕ_1 as 85^0 and 40^0 respectively, the corresponding angles of transmission, are calculated as 1.52^0 and 0.98^0. Therefore, R_p is worked out as 0.28 and 0.87 respectively. Similarly, R_s is worked out as 0.99 and 0.92 respectively. It is thus seen that the increase in the incidence angle would greatly reduce the reflectivity of R_p, i.e. the absorptivity of the workpiece would be greatly increased. The reflectivity of R_s also changes with the beam incidence angle but only slightly.

The cutting speed affects the fraction of the beam striking the cut front compared to that passing straight through the kerf. Increasing the cutting speed will cause more of the beam to strike the cut front thus more energy input into the process. Increasing the power level will obviously increase the heat input thus the melt pool temperature.

The oxidation reaction energy, αP_{chem}, is a function of cutting speed and the burning area as discussed in chapter three. Increasing the cutting speed would have two contradictory effects on the heat generation. On the one hand, it causes more melting which can react with oxygen per unit time and thus generates more heat. On the other hand, it decreases the kerf width thus the burning area and further reduces the amount of melting which can react with the oxygen. The fraction factor, α, is affected by the extent of the burning reaction having a higher value with a complete burning reaction.

From the above discussion, it is easily seen that the melt pool temperature is a function of process parameters which determine the cut quality parameters. Therefore, in-process cut quality analysis can possibly be achieved by measuring the transient temperature of the melt pool.

The temperature measurement can be effected by optical methods measuring radiant energy. Stefan-Boltzmann law states that the radiant

energy is proportional to the temperature to the fourth power for a fixed radiant area and emissivity (equation(3 -13)). This indicates that the radiant energy can be very sensitive to the temperature and the melt pool size. According to this law, the relative change in the radiant energy, $\Delta E\%$, can be given as:

$$\Delta E\% = \frac{E_2 - E_1}{E_1} \times 100\% = \left(\frac{E_2}{E_1} - 1 \right) \times 100\%$$
$$\approx \left(\frac{A_2 T_2^4}{A_1 T_1^4} - 1 \right) \times 100\% \qquad (4\text{-}5)$$

where E_1, E_2 are the radiant energy and A_1, A_2 are the melt pool size at temperature T_1, T_2 respectively. It is seen that any change in the melt pool temperature or in the melt pool size would cause corresponding changes in the radiant energy. For example, given the temperature change of 1%, i.e. T_1 = 2000 K and T_2 = 2020 K, and assuming the radiant area is unchanged, the relative change in the radiant energy , $\Delta E\%$, can be worked out as 4.1%.

If a photodiode is employed, the signal strength detected will be proportional to the emitted radiant energy over the waveband sensitivity of the photodiode, $S(\lambda)$, and the solid angle between the photodiode and the cut face - the view factor, F_{12}. The waveband sensitivity, $S(\lambda)$, is the ratio between the sensitivity at wavelength λ and the maximum sensitivity. This entirely depends on the type of photodiode chosen for the measurement. The solid angle is defined by the ratio of area subtended (i.e. the effective detecting area of the photodiode) divided by the distance squared (the distance between the photodiode and the cut face). The emitted energy per unit time and per unit area from a blackbody over the waveband λ to $\lambda + d\lambda$, is given by Planck's law as [200]:

$$W_{B\lambda} d\lambda = \frac{C_1}{\lambda^5 [\exp (C_2 / \lambda T) - 1]} d\lambda \qquad (4\text{-}6)$$

where

$W_{B\lambda}$= power spectral density for blackbody radiator (Watts/m^3), as shown in Fig. 4 -1 ;

T = absolute temperature (K) ;

λ = wavelength (m) ;

$C_1 = 1.19 \times 10^{-16}$ Wm^2 ;

$C_2 = 1.439 \times 10^{-2}$ m K .

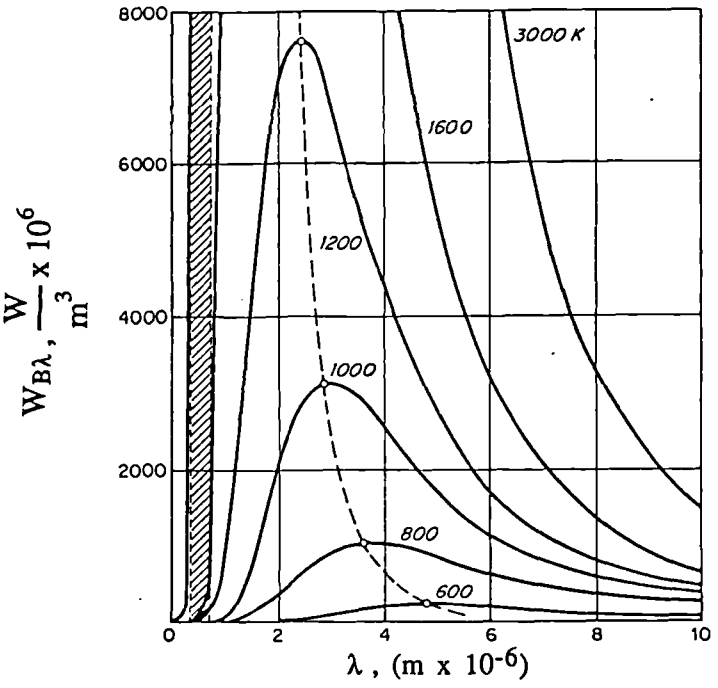


Fig. 4 -1. Power spectral density for blackbody radiation [200] .

The energy striking the detector E(T) is thus given as [200]:

$$E(T) = \varepsilon(T, \lambda)\ e^{-bl}\ S(\lambda)\ F_{12} \frac{C_1}{[\exp(C_2/\lambda T) - 1]\ \lambda^5} d\lambda \qquad (4\text{-}7)$$

where

$\varepsilon(T, \lambda)$ = surface emissivity ;

b = absorption coefficient for the transmissivity of the space between the cut face and the detector (this space may be smoke filled and has a varying transmissivity) ;

l = the thickness of the space .

Thus for a given rise in temperature of the melt pool the signal strength will rise, but not linearly.

This temperature dependent signal is, however, only part of the light source. Further signals would arrive at the photodiode from reflections off cut edges and radiation from sparks. The former is dependent on the surface reflectivity, while the latter is most dependent on where the sparks emerge and the size and quantity of the sparks. The sparks emerging on the photodiode side would have particularly strong effect on the signal strength.

Different methods for in-process monitoring the light intensity generated during the laser cutting process have been reviewed in chapter one, where TV cameras or photodetectors were employed to monitor the shower of sparks or to look at the cut front directly. However, all these methods have certain drawbacks such as sensor location and processing time of the signal, which make the implementation of an in-process monitoring system difficult.

This chapter describes an experimental study based on two distinctive detection methods, i.e. off-axis and axial viewing of the cutting process respectively. They both gain their signals by the direct viewing of the cut face. A visual image of the cutting action will be recorded by using a high speed camera at the same time as the photodiode. This visual image will help to understand the dynamic behaviour of the melt pool and explain the detected signal. The design of an on-line alarm system will be discussed.

4.2. Apparatus and Equipment

The experiments were performed by using the 2 kW CW CO_2 laser at the Laser Laboratory of Liverpool University (Please refer to the Appendix B for the detailed description of the laser equipment). The workpiece movement was controlled by the CNC workstation as shown in Fig. 3 -1. The laser beam mode structure was measured by the LBA shown in Fig. 3 -2.

The camera used is a Fastax High Speed Camera, Category III (Fig. 4-

2). It has a maximum speed of 4,000 frames per second. The film speed is not uniform and therefore the timing light within the unit marks the film at 1 ms intervals to facilitate accurate measurements. The camera has a number of lenses and the 125 mm focal length was chosen for a stand-off distance of 750 mm for convenience. The camera was mounted on a stand mobile in the vertical and horizontal axes, the camera itself movable on a pivotal axis about the vertical. The objective lens is focussed onto the area on which the laser beam is incident, which is 0 - 5 mm in diameter. The film used was Kodak RAR film 2498 and had a length of 38.1 m.

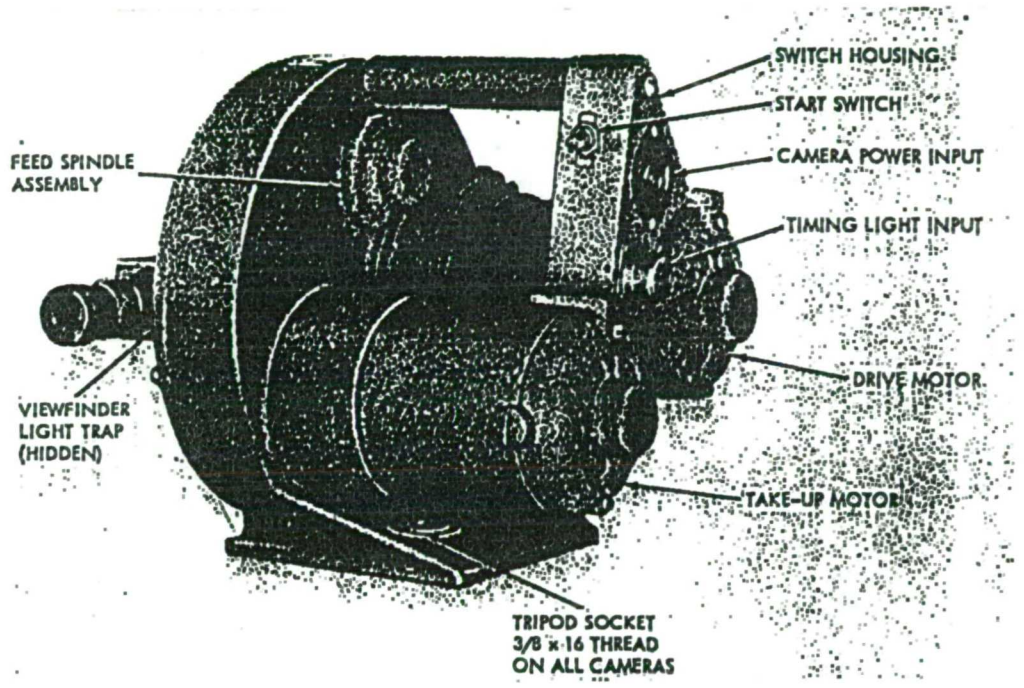


Fig. 4 -2. The Fastax high speed camera.

A silicon photodiode BPW21 housed in a hermetically sealed case with a flat window was chosen from the RS Component Co. Ltd.. It is designed for use in the photovataic mode, i.e. the photodiode generates a voltage which is proportional to incident electromagnetic (EM) radiation intensity as shown in Fig. 4 -3. The photodiode has a response time 3.5 μs, a wavelength range of 460 nm - 750 nm and a sensitivity approximating the human eye response as shown in Fig. 4 -4. It is clearly seen that direct or specular reflections of the laser beam would not be recorded since 10.6 μm radiation is outside the sensitivity band of the detector.

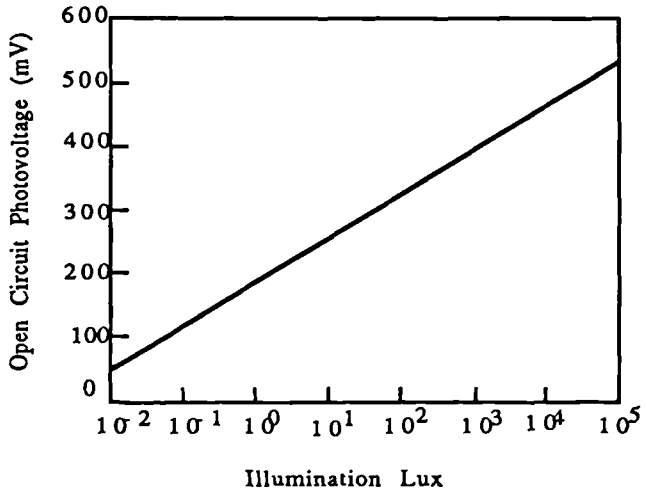


Fig. 4 -3. The relationship between the photodiode output and the illumination lux (reproduction of the RS data sheet No. 4462).

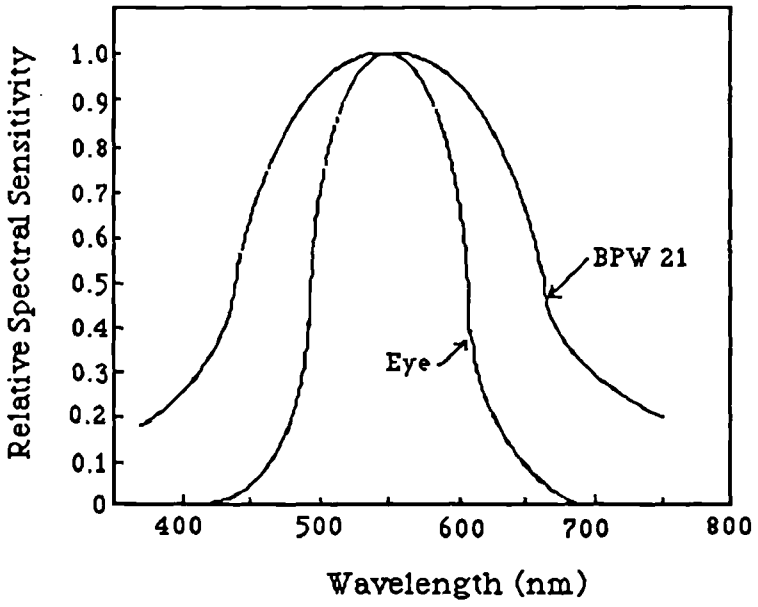


Fig. 4 -4. The BPW21 and human eye spectral sensitivity (Reproduction of the RS data sheet No. 4462).

4.3. Off- axis Monitoring of the Cut Face

4.3.1. Experimental set-up

The experimental set-up for monitoring the light emission from the

cut face is shown in Fig. 4 -5. The laser beam was focussed onto the workpiece surface through a KCl lens having a focal length of 125 mm. The beam, together with the coaxial cutting gas, O_2 , past through a converging conical nozzle with an orifice diameter of 1.40 mm. The standoff distance between the nozzle and the workpiece was 0.8 mm. The workpiece material was 1 mm thick mild steel.

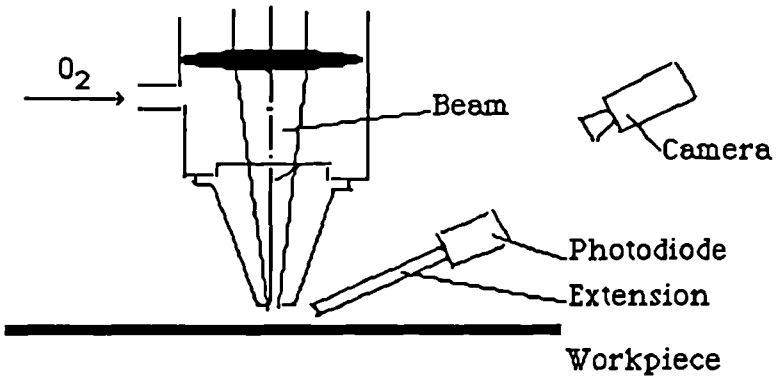


Fig. 4 -5. Experimental set-up for the off- axis monitoring of the cut face.

The detection unit consists of the photodiode fitted with an aperture in the form of an extension tube at an angle about 25° to the workpiece surface. This angle was actually the maximum possible angle at which the photodiode was still able to look at the cut front (the best in-depth view of the cut face). This angle, α , as shown in Fig. 4 -6, can be determined as below:

$$\alpha = \arctan\frac{0.8}{0.7 + 1.0} \approx 25^0 \qquad (4\text{-}8)$$

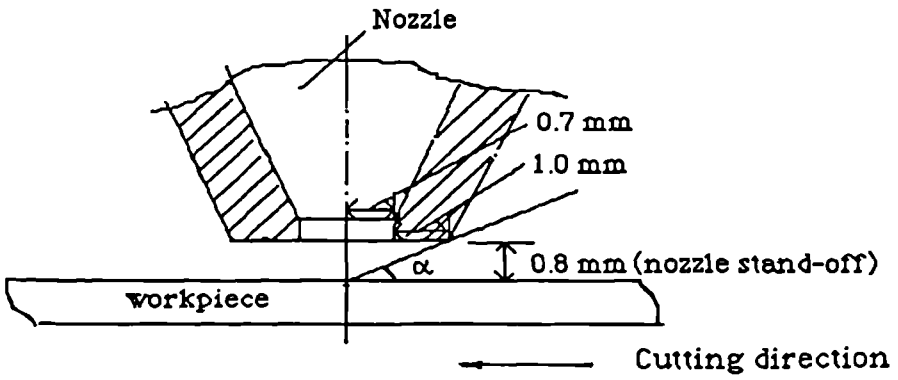


Fig. 4 -6. Determination of the maximum viewing angle.

The function of the extension tube is twofold. Firstly, it protects the photodiode from flying sparks. Secondly, it functions as an aperture to confine the sensor's receiving angle to only view the cut face. This eliminates stray reflections from the nozzle tip, outside lights, sunshine and other sources. The signal was recorded by a chart recorder which is shown in Fig. 4 -7.

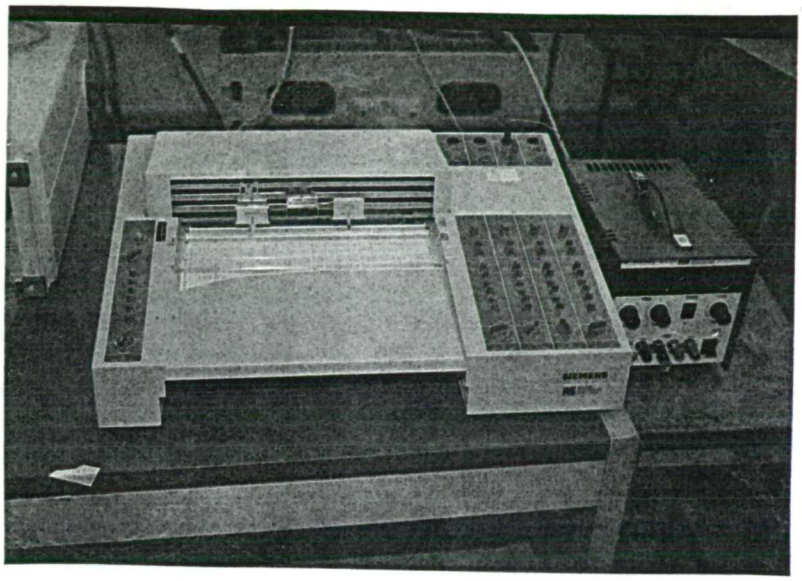


Fig. 4 -7. The chart recorder.

The high speed camera was operated at the same time as the photodiode for certain cuts (to be discussed later) and positioned at about 25^0 to the workpiece and at a small angle to the photodiode in order to look at the leading face of the cut.

The experiments were so arranged that the relationship between signals and cut quality could be established. Various cut edge appearances were obtained by varying some of the process parameters as shown in table 4 -1. The laser beam mode was recorded by the LBA as shown in Fig.4-8.

The cut edge quality was assessed based on the amount of dross adhesion, extent of HAZ, kerf width and the surface roughness, which was measured on a Talysurf instrument.

Table 4 -1. Experimental Arrangement

Cut quality (effect)	Preset process parameters (cause)		
	cutting speed	gas flowrate	others
rough cut	too slow	high	
too much dross	high	low	
lack of penetration	too high	low	
HAZ variation			misalignment or clinging dross
good cut	high	high	

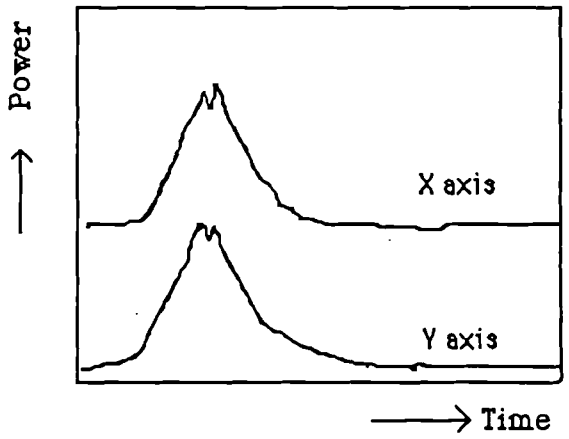


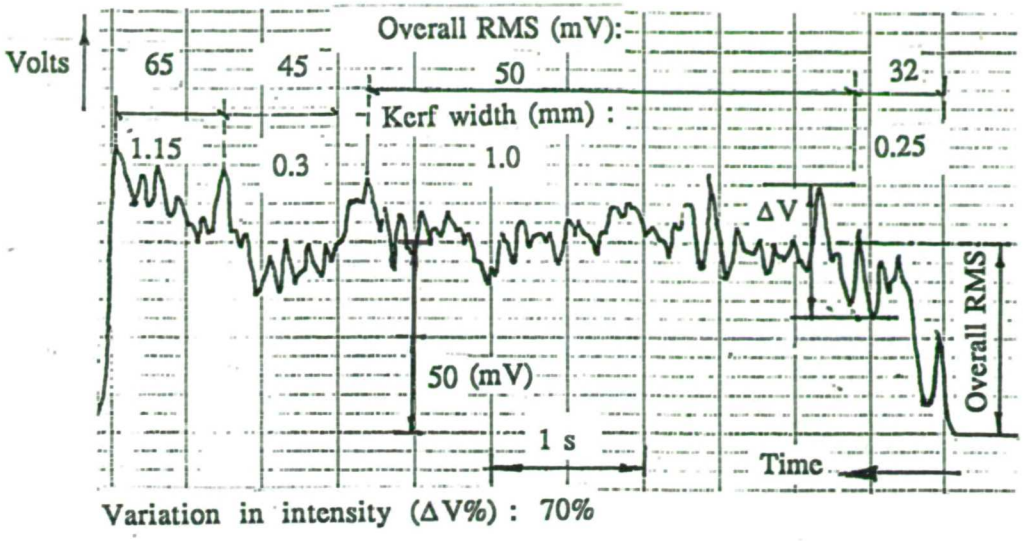
Fig. 4 -8. The laser beam mode structure from a LBA.

4.3.2. Results and discussions

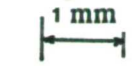
4.3.2.1. Factors affecting the detected signal strength and stability

4.3.2.1.1. Effect of cutting speed

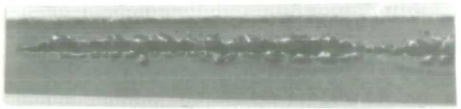
The signals at different cutting speeds together with the resultant cut edge appearances and the cut surface roughness are shown in Figs. 4 -9 to 4 -14. Gas flow rate and laser power were kept constant at 79 L/min. and 1.63 kW respectively.







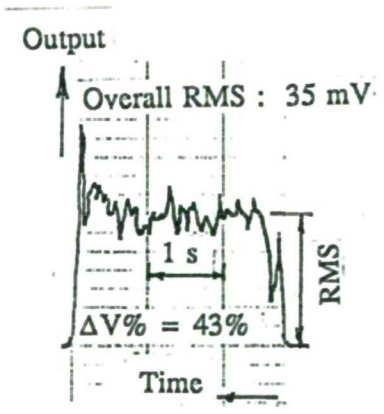
Striation pattern

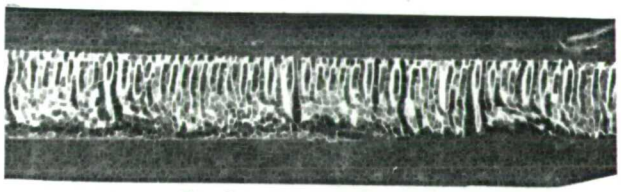


Dross adhesion , Kerf variations

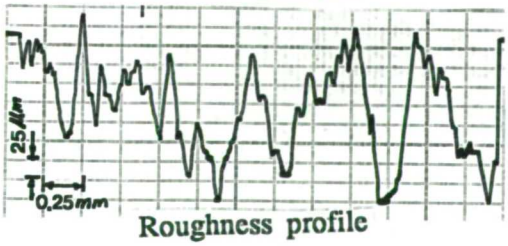
Comment : rough cut, wide kerf and HAZ variations

Fig. 4 -9. Signals at the cutting speed of 10 mm/s.





Surface striation



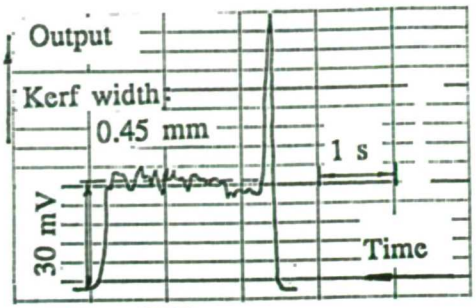
Roughness profile

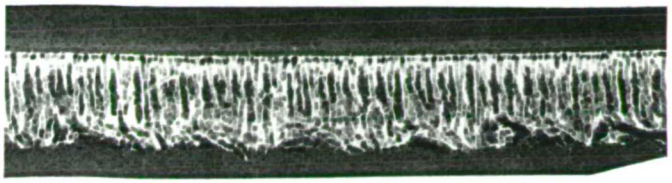


Dross adhesion

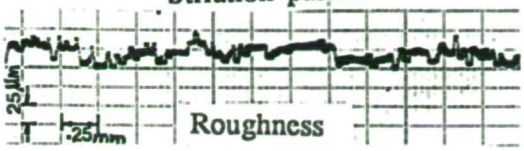
Comment: much dross, HAZ variation.

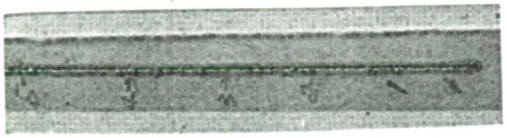
Fig. 4 -10. Signals at the cutting speed of 20 mm/s.





Striation pattern

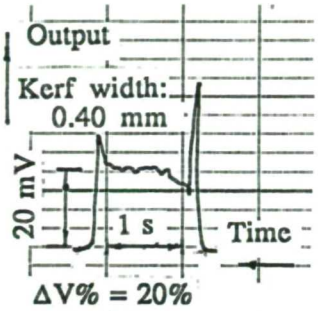


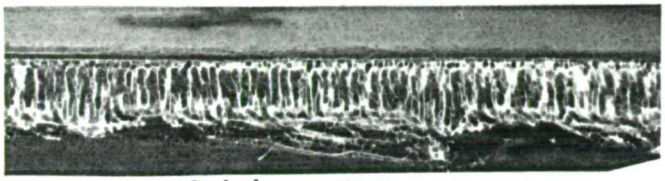


Dross adhesion

Comments: medium dross.

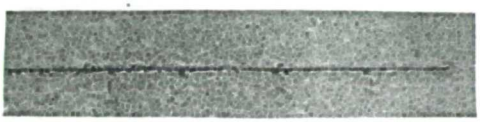
Fig. 4 -11. Signals at the cutting speed of 30 mm/s.





Striation pattern

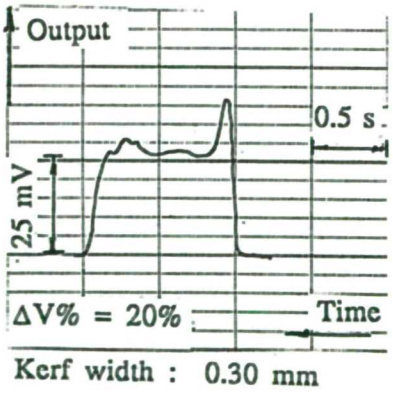


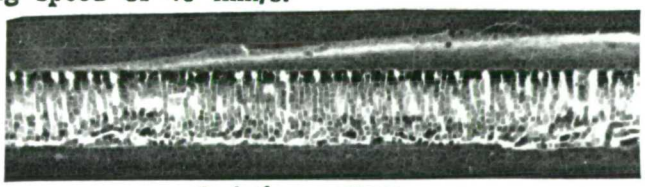


Dross adhesion

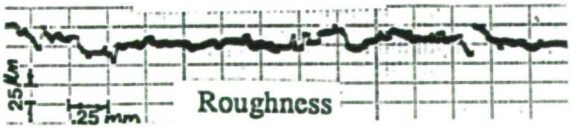
Comments : little dross on one side of the cut.

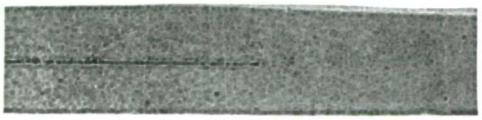
Fig. 4 -12. Signals at the cutting speed of 40 mm/s.





Striation pattern





Dross adhesion

Comments : good cut

Fig. 4 -13. Signals at the cutting speed of 60 mm/s.

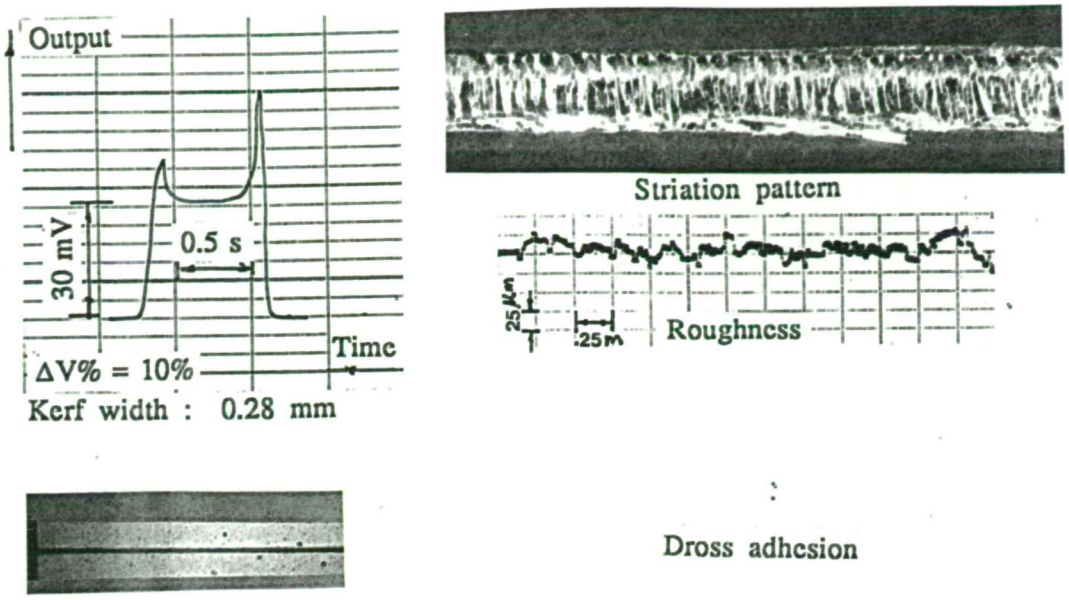


Fig. 4 -14. Signals at the cutting speed of 70 mm/s.

(i). Initial and final signal peaks:

As can be seen from the above figures, there are peaks in the responses at the start and finish of each cut. The start peak was generally caused by the upward directed flash at the formation of an initial keyhole. The peaks at the end of the cut were mainly caused by some edge effect. Where the cut terminated before the workpiece edge, such is the case in Fig. 4 -11, no final peak was observed. It is thus likely that this final peak was due to a view of sparks flying clear of the underside of the sample, or a dross build up on the sample edge. In this thesis, only the steady state cutting is concerned, therefore end effects are not considered further in the following text.

(ii). Overall signal strength:

The overall signal strength is determined by the amount of radiation arriving at the detector both directly and by reflection from the melt front, hot cut faces, sparks and hot dross. Thus the area of the melt front (equation (4 -5)), which is related to the kerf width, the emissivity of this area, which is a function of the surface roughness [201], as well as the

temperature, which is affected by the cutting speed, affect the overall signal strength.

The correlation between the signal strength RMS and the cutting speed is shown in Fig. 4 -15.

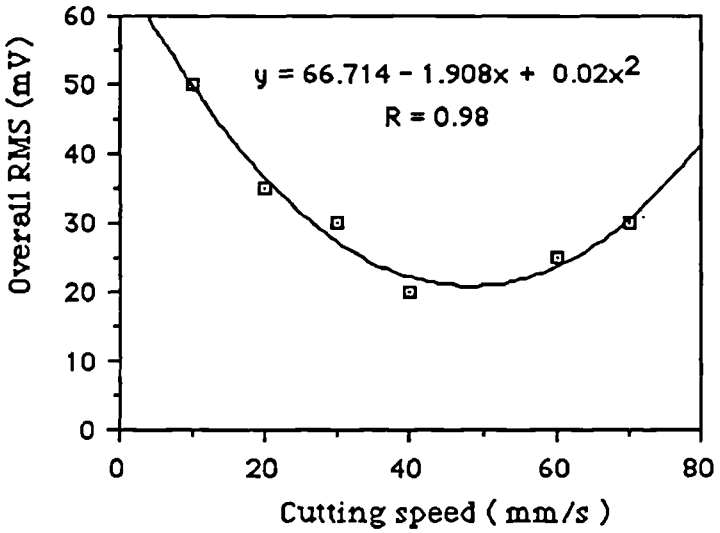


Fig. 4 -15. Correlation between the signal RMS and the cutting speed.

It is seen that the signal strength varied differently with the cutting speed at the low speed range and at the high speed range. At the low speed range, the overall signal RMS decreased with increasing the cutting speed due to the following reasons. Firstly, at a lower speed, the kerf was generally wider allowing more of the sparks to be present in the view field of the photodiode. Secondly, the burning reaction was more effective at a lower cutting speed as to be discussed later. At the high speed range, however, the laser beam/workpiece interaction is dominant in controlling the process heat input. Increasing the cutting speed, would increase the fraction of the beam striking the cut front and thus increase the cut front temperature, which led to the increase in the signal RMS.

In order to establish the direct correlation between the signal RMS and the kerf width, the cutting speed had to be kept unchanged since which affected the kerf width and the signal strength. Fortunately, it is noticed from Fig. 4 -9 that the kerf width of this cut varied over the workpiece due to the changes in the surface conditions (the absorptivity) and due to the unstable burning process. Therefore the kerf width of

different values was measured and related to the signal RMS as shown in Fig. 4 -16.

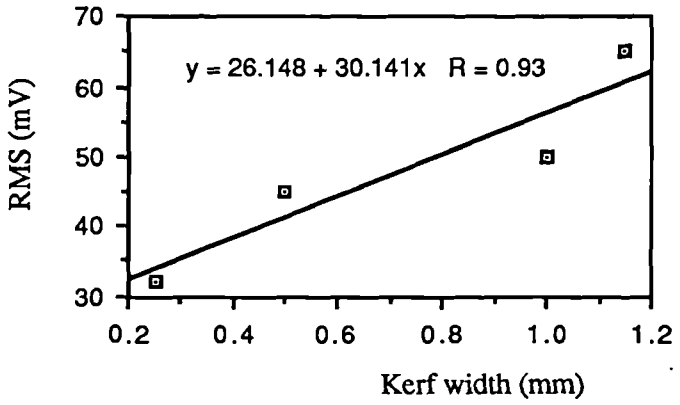


Fig. 4 -16. The correlation between the signal RMS and the kerf width at the speed of 10 mm/s.

It is seen that the signal RMS increased with the kerf width due to the larger viewing angle of the sparks when the kerf width was wider, which also increased the radiation area. The variation of the signal RMS with surface roughness is hard to separate experimentally.

The quantity of the clinging dross particles would also affect the signal strength. Firstly, they are additional heat sources emitting lights. Secondly, they could reflect lights upward to increase the signal strength (blocking effect). These dross effects are further discussed in later section (4.3.2.1.2.: Signals at different gas flowrates).

(iii). Signal stability:

a). Slow cutting speeds: The signal stability depends on the stability of the light emission from the melt pool, that is the stability of the melt pool temperature and size, and extent of the sparks and molten dross visible to the photodiode. The dynamic behaviour of the cut front would thus indicate the stability of the light emission.

Figure 4 -17 shows a typical set of movies indicating the transient state of the cut front at a slow cutting speed (10 mm/s). These movies were

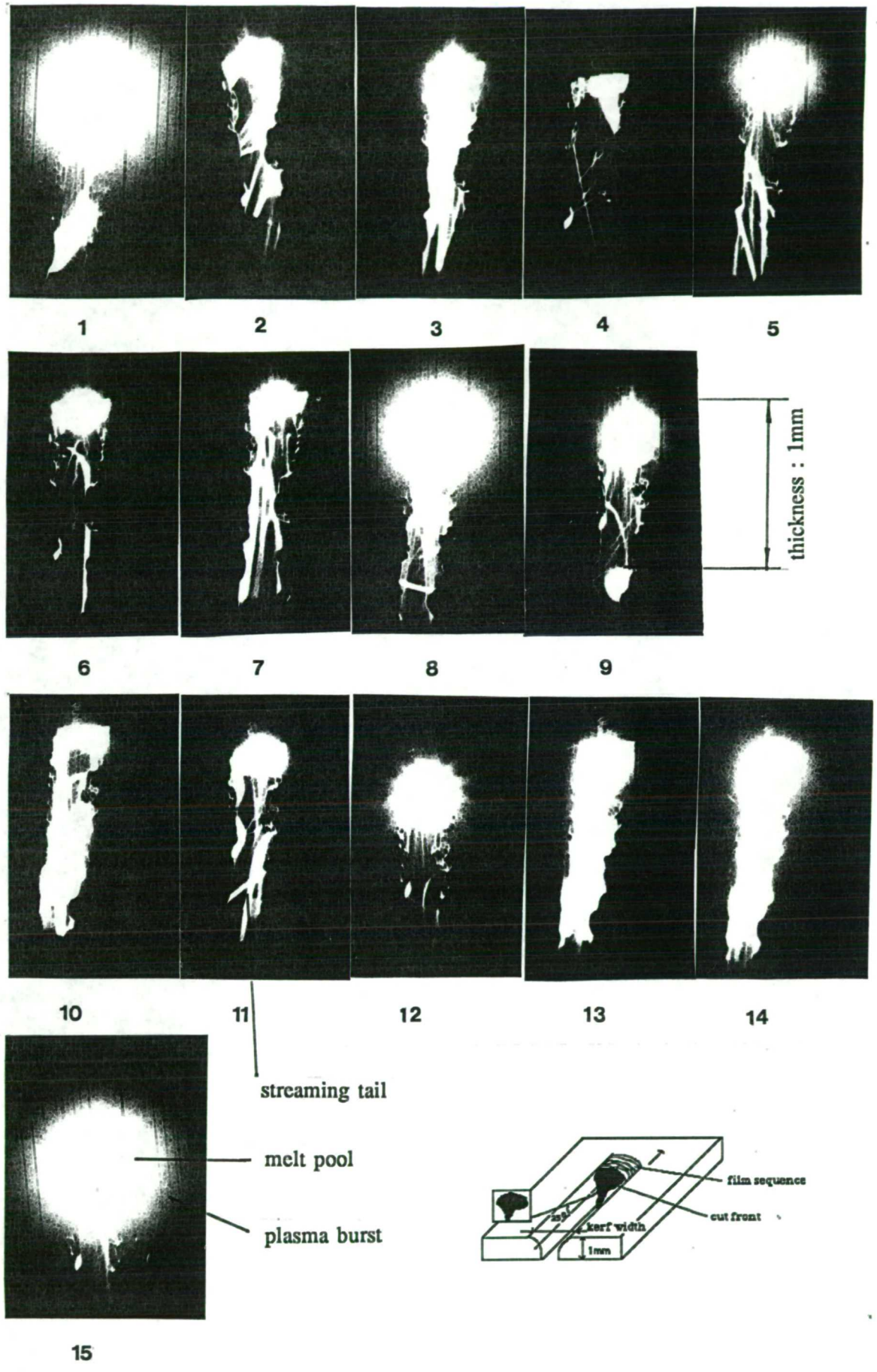


Fig. 4 -17. Melt pool behaviour at a low cutting speed, 10 mm/s.

taken continuously by the high speed camera at the same time as the photodiode (signals were recorded as shown in Fig. 4 -9). But the movies shown in Fig. 4 -17 are not located against the corresponding locations on the detected signal (Fig. 4 -9). The time interval between each picture was about 6.5 ms.

It is seen that each picture consists of three parts: plasma burst, melt pool and streaming tail. The melt pool is shown as the bright spot indicating a high temperature region. The area surrounding the melt pool indicated the action of the plasma burst due to the beam/workpiece interaction. It is seen that the melt pool varied both in shape and size in a periodic way , i.e. from a flare (picture 1) to smaller spots (picture 2 to 7) and then a flare again (picture 8). This process was repeated in pictures 8 to 15. The period for one cycle was about 45.5 ms (7 x 6.5 ms), i.e. 22 Hz, which agreed approximately with the frequency of the surface striation as already shown in Fig. 4 -9.

From these cyclic behaviour of the melt pool, a burning flow pattern can be proposed as shown in Fig. 4 -18, in which the sequence of the diagrams is corresponding to that shown in Fig. 4 -17.

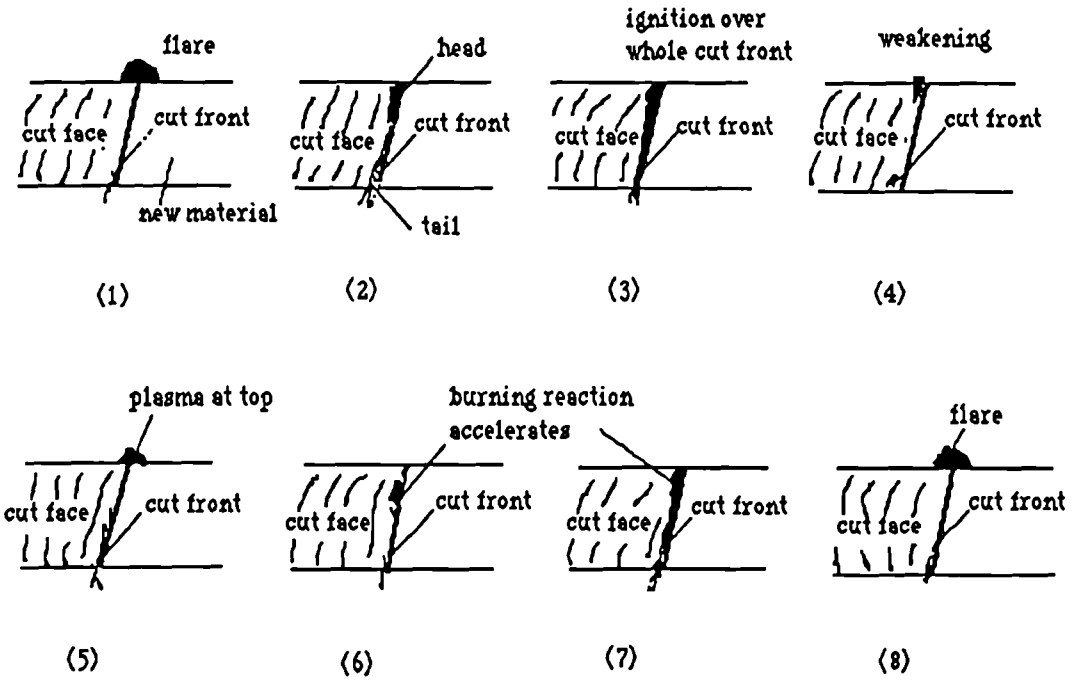


Fig. 4 -18. Illustration of the cyclic burning process.

The first diagram was a big flare, which indicated a intense burning reaction at the top surface possibly due to the burning rate moved ahead of the laser beam as discussed before in chapter one [15, 21]. Then the burning reaction moved downward and were confined in the cut kerf leading to a smaller spot and a stream tail, which showed the flow of the melt. Diagram 3 showed a bright zone across the whole cut front indicating the possible ignition of the whole cut front from top to bottom. The burning process then tended to die down due to the increased slag covering the melts or due to the reduced fraction of the laser beam striking the cut front. The slag may include FeO, Fe_2O_3 and Fe_3O_4 as discussed in chapter three. The latter happened since the beam could not quite match up the movement of the cut front. In diagram 5, a flare appeared again but smaller than the previous one. This flare was possibly due to the plasma burst as the result of the beam/workpiece interaction when the laser beam eventually caught up the burning reaction when it was slowing down. The workpiece temperature was thus raised up due to this beam/workpiece interaction. This increased temperature would accelerate the burning reaction, i.e. the burning rate started to increase. Diagrams 6 & 7, indicated this acceleration of the burning reaction when considering the increased bright area in the picture 7 compared with diagram 4 (Fig. 4 -17). In the last diagram, a big flare similar to the first one appeared, which indicated that the burning reaction moved ahead of the laser beam again. The whole cycle repeated from pictures 9 to 15.

From the above discussion, it is seen that the burning rate oscillated during the cutting process, which agreed with the unsteady situation of the molten layer covering the cut front, i.e. the oscillation of the temperature as discussed in chapter one [1.1.2.2.]. This periodic oscillation of the burning rate was thus responsible for the formation of the surface striation.

The tail part as already mentioned represents the radiation from melt being blown clear. It too varied in size and shape depending on the quantity of clinging dross, the extent of the view through the kerf width, the direction of the spark ejection, quantity of the sparks from the underneath which were visible and the cut face radiation and reflections.

Therefore, the variations in size and shape of both the head (melt pool and the plasma burst) and tail parts (quantity and direction of the sparks being ejected) would be responsible for the large variations in the signal detected .

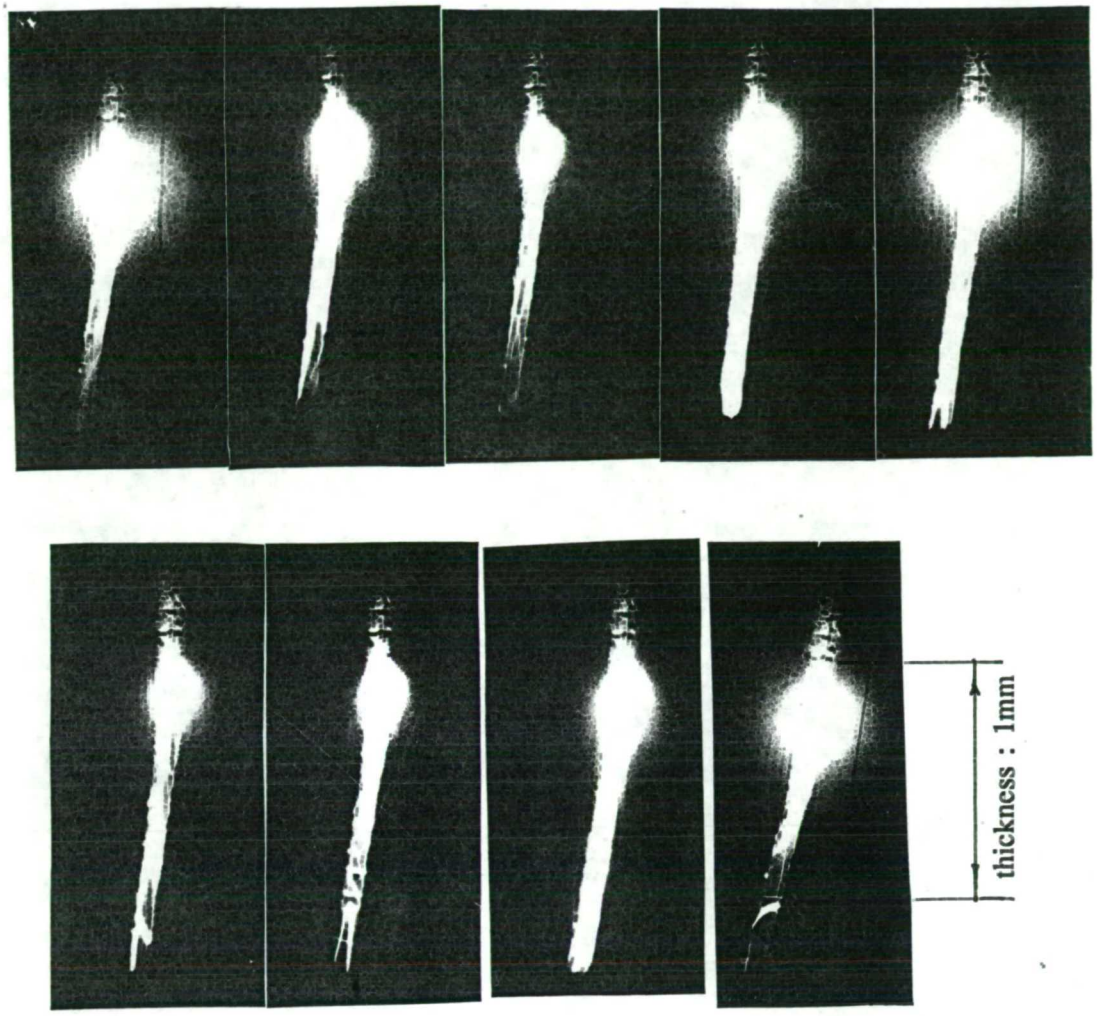
b). High cutting speeds: At higher cutting speeds the signal was smoother for fully penetrating cuts as illustrated in Figs. 4 -12 to 14. These can also be explained by the dynamic behaviour of the cut front. Figure 4-19 shows a typical set of the high speed movies showing the light emission from the cut front and the ejection of the sparks. These pictures were taken at the cutting speed of 60 mm/s. It is seen that each picture consists again of three parts, i.e. plasma burst, melt pool and streaming tail. The plasma burst and the melt pool showed a similar cyclic burning pattern as before. But the period was shorter having 4 x 6.5 = 26 (ms), i.e. 38.5 Hz.

It is also seen from these movies that the variations in size and shape of the melt pool were much smaller than those shown in Fig. 4 -17. The tail part indicated a quite steady flow of melt out of the cut region and possibly a reduced view of intermittent spark emission from the underside. This reduced view would be expected due to the fairly constant and narrow kerf width. Therefore, the light emission from the cut front was relatively stable at the high cutting speeds resulting in the steady signals shown in Figs. 4 -12 to 14.

4.3.2.1.2. Effect of gas flow on signal strength and stability

The detected signals and the resultant cut edge appearances at different gas flow rates are described in the following text, where the cutting speed and laser power were kept constant at 70 mm/s and 1.63 kW respectively.

(i). Very high gas flow rate (95 L/min.) : When the gas flowrate was very high, the signal was shown in Fig. 4 -20. It is seen that the overall signal strength was 51.5 mV, which is much higher than that of 30 mV shown in Fig. 4 -14 where lower gas flowrate was used. This was probably due to the increase in kerf width and an increased cut front temperature



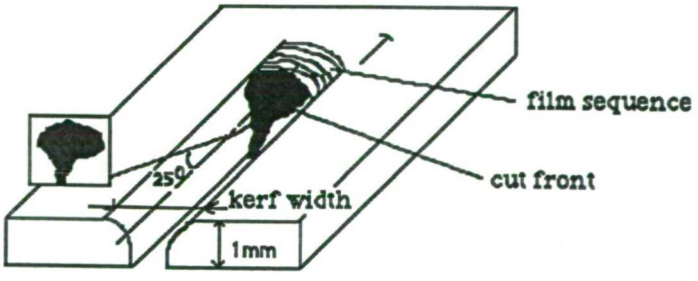
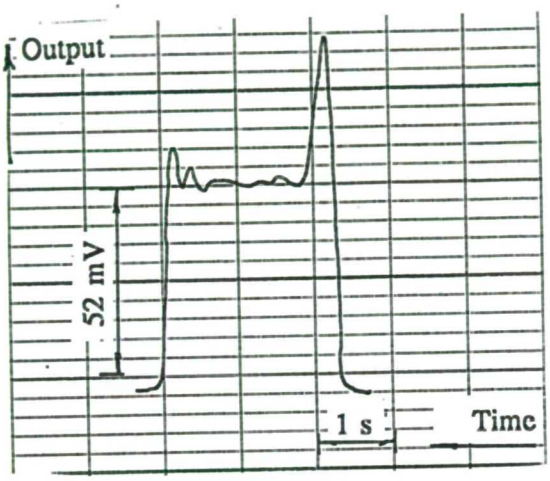


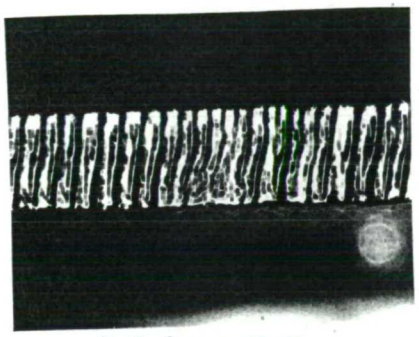
Fig. 4 -19. Melt pool behaviour at a high cutting speed, 60 mm/s.

at this high gas velocity. The kerf width values for these two cuts are 0.66 mm and 0.42 mm respectively. The increased cut front temperature was due to the increased oxygen concentration in the melt stream at higher gas flowrate, which caused a stronger burning reaction. The rougher surface of the cut as shown in Fig. 4 -20 may have further enhanced the signal strength by increasing the emissivity.





Roughness



Striation pattern

Comments: wide kerf

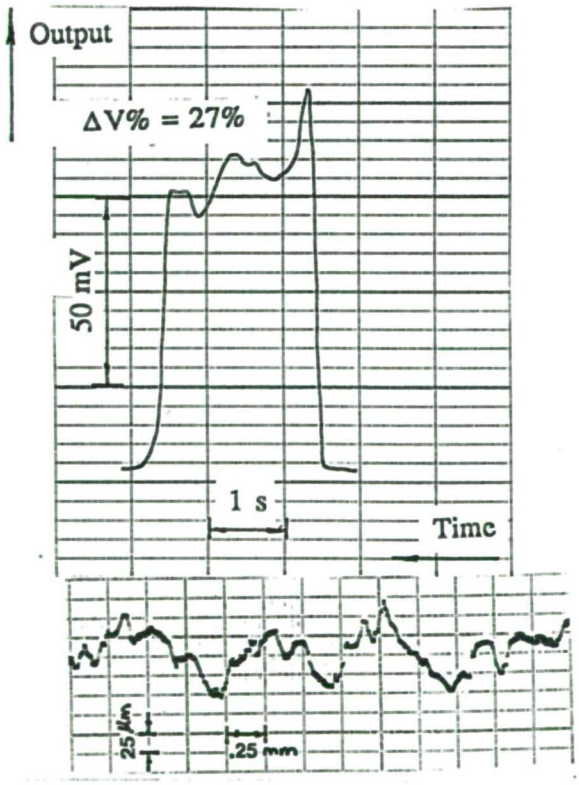
Fig. 4 -20. Signal at the gas flowrate of 95 L/min..

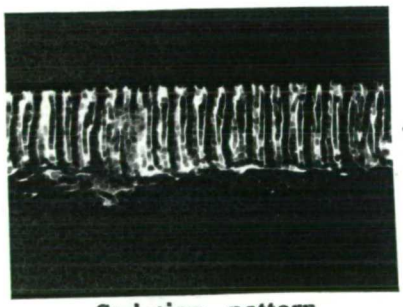
(ii). Optimum gas flowrate (79 L/min.): When the assistant gas flowrate was optimum, a good cut with little dross and smooth surfaces was obtained (refer to Fig. 4 -14). The signal was smooth with little variation in signal strength due to the following reasons:

Firstly, the dross effect: In laser cutting, the assistant gas has a drag effect as discussed before, which blows the molten dross particles out of the cut kerf. In fact if there is no or very little gas assistance then a weld would result not a cut. Thus the drag effect is of importance. At high gas flowrates, the molten dross particles were more effectively scoured from

the kerf leaving less dross. The dross effect on the signal intensity was thus minimised. Secondly, the laser beam - workpiece interaction was generally stable at high cutting speeds as discussed earlier (Fig. 4 -19), and thus gave relatively stable light emission from the melt pool. Thirdly, the constant kerf width of this cut reduced the viewing of the intermittent spark emissions, which was responsible for the signal variations. Finally, the smooth surface gave stable radiated and reflected energy and may thus contribute to the steady signal.

(iii). Low gas flowrate (52 L/min.): At a lower gas flowrate the signal shows some instability but a higher intensity with the overall RMS value of 75 mV (Fig. 4 -21). The cut had much dross adhesion due to the insufficient gas flow. These clinging dross particles reflected the sparks upward leading to higher light intensity. The instability was also associated with the drag force being insufficient to remove the melt as a steady stream.





Striation pattern

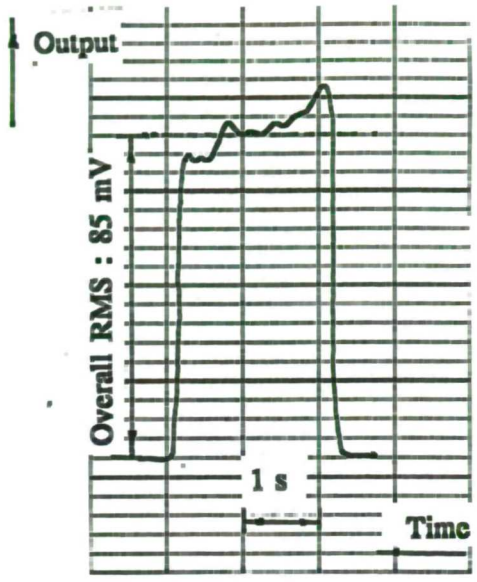
Roughness

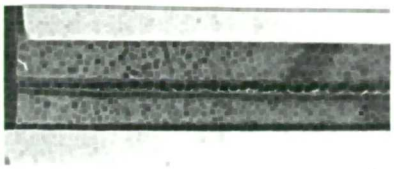
Comments : too much dross

Fig. 4 -21. Signal at the gas flowrate of 52 L/min..

(iv). Very low gas flowrate (40 L/min.) : At very low gas flowrate,

the cut failed to get through. The process-generated sparks were thus all present above the workpiece leading to a massive view of the sparks by the photodiode. Therefore, a strong signal with the overall RMS value of 85 mV was observed as shown in Fig. 4 -22.





Dross adhesion

Comments : not penetrating

Fig. 4 -22. Signal at the gas flowrate of 40 L/min..

4.3.2.2. Signal variation with cut quality

As discussed above, the signal varied at the different cutting speeds and gas flowrates, which determined the cut quality. Thus the signal was expected to be indicative of the cut quality.

(i). Rough cut: When the cutting speed is low and gas flow rate is high, a rough cut can usually be obtained, such is the case already shown in Fig. 4 -9. The cut edge appearance was characterised by having a deep striation pattern (The surface profile was too rough to measure by the Talysurf Instrument, but the deep striation pattern can be seen from the

picture given in the figure), considerable dross clinging to the bottom edge, large variations in kerf width and in the width of HAZ. The signals obtained showed large variations in both amplitude and frequency (the relative signal variation, $\Delta V\% \approx 70\%$, please refer to equation (4 -9) for the definition of $\Delta V\%$). The reason of this variation is considered to be due to the following causes. Firstly, there was the unstable emission due to the dominant cyclic burning process as discussed in 4.3.2.1.1. Secondly, the signal varied due to the varying view of dross and sparks. The view varied with the varying kerf width/striation pattern and the quantity of dross or sparks visible and also varied as droplets formed or the burning reaction proceeded at varying rates. Thirdly, the temperature of the cut face would vary with time due to the cyclic nature of a burning reaction. Fourthly, where dross adhered the HAZ became large and hence formed a further radiant source visible to the detector.

The in-process high speed filming of the melt pool as already shown in Fig. 4 -17 proved that there were large variations in the melt pool shape and size at this speed resulting in the large variations in the signals detected.

(ii). Cut with dross adhesion: When the cutting speed was high but gas flowrate was low, a cut with much dross adhesion and consequent variations in HAZ was obtained (refer to in Fig. 4 -21). Its cut edge had considerable dross clinging to both sides of the bottom edges, variations in HAZ on the top of surface and a relatively rough surface profile. The signal showed some variations in amplitude ($\Delta V\% = 27\%$) but in a lower frequency compared to the signal for a rough cut due to the higher cutting speed. The signal variation was due to the dross/HAZ effects and due to the insufficient drag force causing unsteady melt flow.

(iii). Good cut: When the cutting speed and gas flow rate were optimum, the good cut was obtained as already shown in Fig. 4 -14. It had little dross clinging to the bottom edge, constant and narrow kerf width, constant HAZ on the top and a smooth cut surface. Since the cutting speed was high, the laser beam/workpiece interaction was dominant in controlling the heat input. This generated more stable melting at the cut face and hence a more stable signal. The dross/HAZ effect, kerf width effect and surface roughness effects were all minimised.

The in-process high-speed filming of the 'good' cut (Fig. 4 -19) showed that the 'head' and 'tail' only varied in a small scale in size and shape. Thus the light emission from the cut front was stable leading to the steady signal detected.

4.4. Axial Viewing of the Cut Face

The objective of this set of experiments was to investigate the possibility of using an axially mounted fibre optics and a photodiode to inspect the cut quality in real time by direct viewing of the laser cutting process through the final beam guidance mirror.

4.4.1. Experimental set-up

The experimental set-up is shown in Fig. 4 -23. The final beam guidance mirror had a 1 mm diameter hole drilled through it at 45°. A thin polymer fibre cable was fitted into the hole, but set back from the mirror face. It has good transmissivity to visible wavelengths (peak wavelength range of 301 - 561 nm) and could work at temperature up to 85°C. The photodiode was attached to the fibre to look directly at the cut face. Since this viewing angle was down the optic axis of the process, it was independent of the cutting direction.

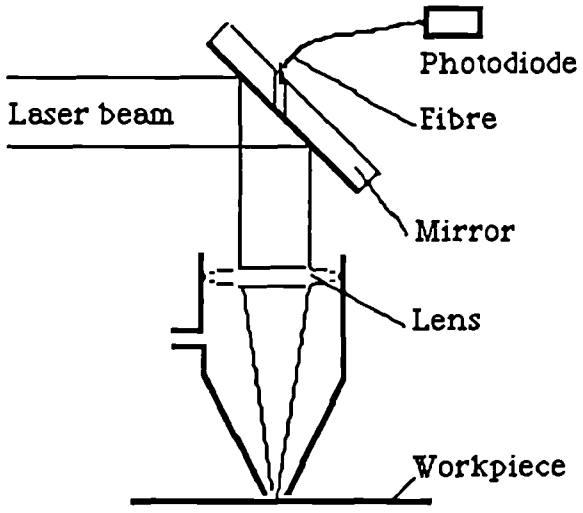
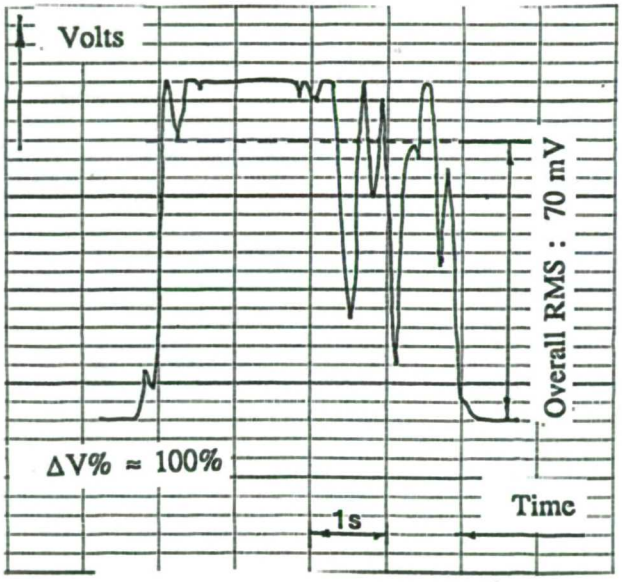


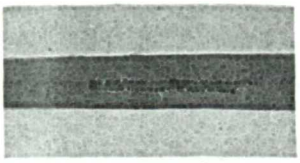
Fig. 4 -23. Experimental set-up for monitoring the process from the last mirror.

4.4.2. Results and discussion

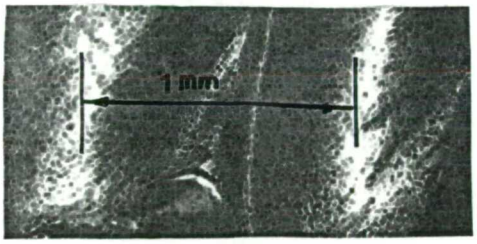
A systematic variation of parameters was made to establish a relationship between signals and cut quality. The laser power was kept as 1.63 kW. The material cut was 1.0 mm thick mild steel sheet. Signal traces and the corresponding cut edge appearances from cuts made under different conditions were investigated as below.

(i). Signals from a rough cut: A rough cut with wide kerf width and large variations in HAZ was obtained at the cutting speed of 10 mm/s and the gas flow rate of 53 L/min.. The recorded signal is shown in Fig. 4 -24.





Dross adhesion



Striation pattern

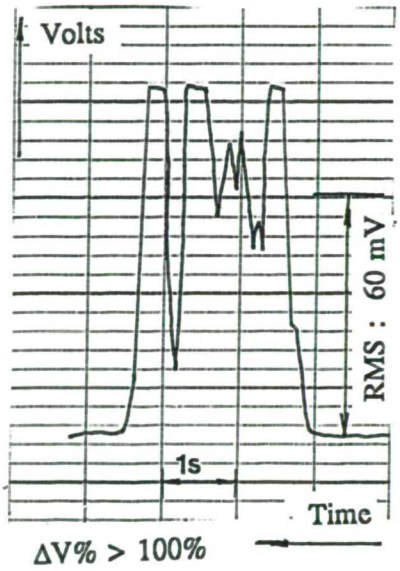
Comments : large variations in kerf width

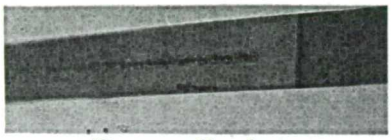
Fig. 4 -24. The axial signal from a rough cut.

It is seen that there were wide variations in the signal strength having an overall RMS value of 70 mV and an average amplitude variation of 100%. The overall signal strength and the amplitude variations are considerably larger than those observed with the off-axis viewing system (the overall RMS = 50 mV and the signal variation, ΔV% = 70%). The signal is quite clearly different from the trace of Fig. 4 -28(shown later) which

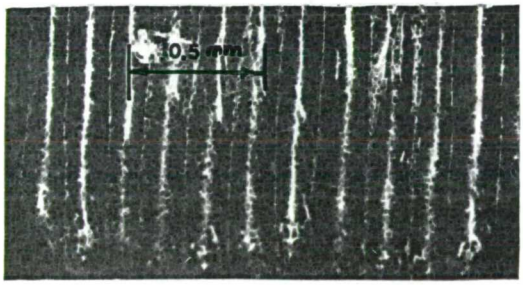
was given by a good cut. This suggests that a useful control signal is available. These signal variations can be explained as before due to the unsteady light emission from the cut front and the varying viewing of the sparks. The flat parts of the signal indicated that the chart recorder pen was out of scale due to the strong signal.

(ii). Signals from a cut with much dross: A cut with much dross, rough surface but narrower kerf was obtained at the cutting speed of 30 mm/s and the gas flow rate of 40 L/min.. The recorded signal is shown in Fig. 4 -25. The overall RMS was 60 mV, which was lower than that shown in Fig. 4 -24 for a rough cut. But the average signal variation was high, i.e. $\Delta V\% > 100\%$.





Dross adhesion

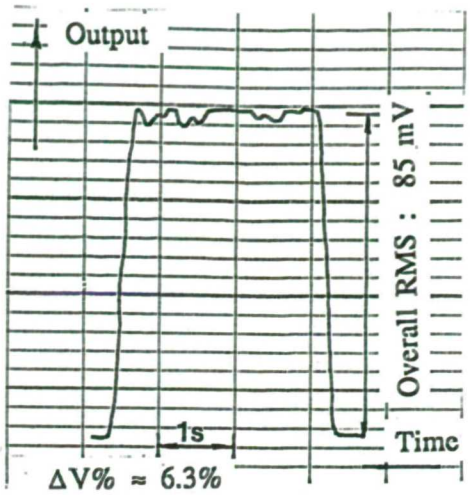


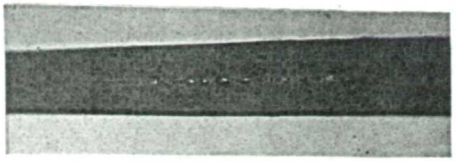
Striation pattern

Comments : constant kerf width but with too much dross adhesion.

Fig. 4 -25. The axial signal from a cut with too much dross clinging.

(iii). Signals from a partially penetrating cut: At the cutting speed of 40 mm/s and the low gas flowrate of 40 L/min., a partially penetrated cut resulted leading to a full view of the massive flying sparks above the workpiece. The detected signal was thus very strong having an overall RMS value over 85 mV as shown in Fig. 4 -26. However, the variations in the signal strength were small ($\Delta V\% \approx 6.3\%$) due to the increased cutting speed thus the relative stable emission from the cut front.



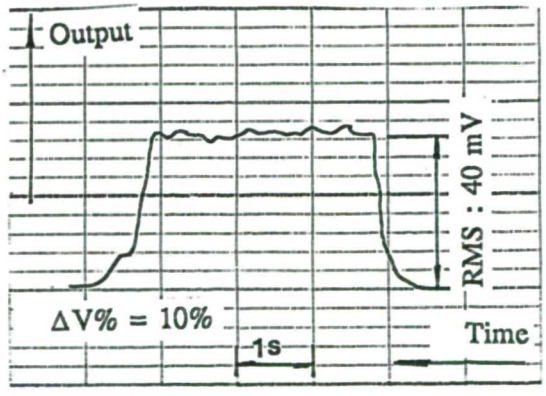


Dross adhesion

Comments : not penetrating.

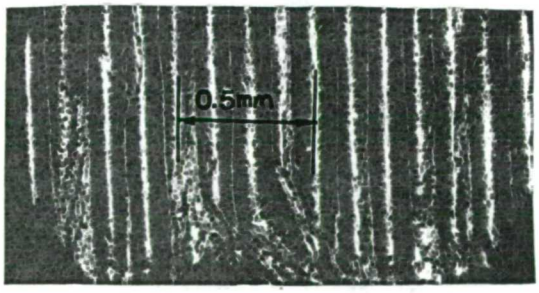
Fig. 4 -26. The axial signal from a partially penetrating cut.

(iv). Signals from a cut with medium dross adhesion: Figure 4 -27 shows the signal obtained at the cutting speed of 35 mm/s and at the gas flowrate of 52 L/min.. The resultant cut edge was also shown in this figure. The cut had medium clinging dross and quite constant kerf and HAZ. The cut surface was smooth. The signal strength and the amplitude of the signal variation were 40 mV and 10% respectively, which were very much reduced compared to the signals in Figs. 4 -24 to 4 -26.





Dross adhesion



Striation pattern

Comments: medium dross

Fig. 4 -27. The axial signal from a cut with medium dross adhesion.

(v). Signals from a good cut: At the cutting speed of 40 mm/s and the gas flowrate of 79 L/min., a good cut with little dross, smooth surface, narrow kerf and narrow HAZ was obtained. The detected signal is shown in Fig. 4 -28, which was smooth ($\Delta V\% \approx 10\%$) and of low overall intensity (overall RMS = 20 mV). This significant reduction in intensity is probably due to the steeper cut face reducing the viewing angle and also sending the sparks down and away from the view of the detector. With cuts not clearing properly the viewing area is greatly increased and the quantity of sparks visible will rise abruptly as the cut face angle changes, when viewed directly from above, as here. This variation in the cut face angle was used as a control signal by Burg *et.al.* [179]. They viewed the angle of the cut face by the discharge angle of the spark cone from beneath the cut as discussed in chapter one. The constant kerf and smooth surface also contributed to the steady signal.

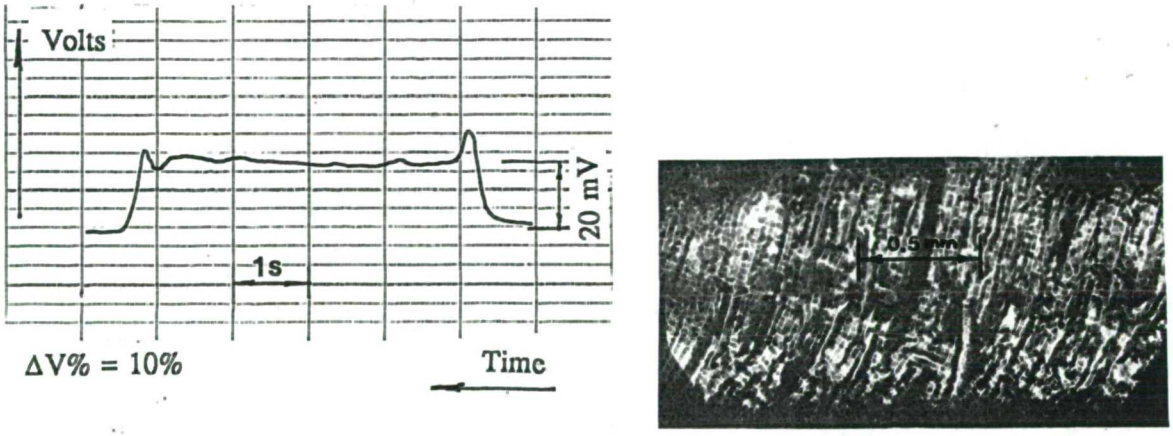


Fig. 4 -28. The axial signal from a good cut.

Thus the signal gained from this axial view point is probably a very sensitive one to cut quality. The axial signals were considerably stronger than those off-axis signals. Also the amplitude variation observed for rough cuts was larger. Thus this viewing position appears preferable. It has the further advantage of being axisymmetric and therefore independent of the cutting direction.

4.5. Applicability to In-process Inspection and Control

The off-axis measuring technique illustrated that radiation signals detected by a photodiode could indicate the cutting behaviour. However the signal varied with the alignment of the detection unit and the cutting direction and may not therefore be suitable for an omnidirectional cutting process.

The axial detection unit meets all the basic requirements for an in-process monitoring system. The signal was strong and varied greatly from good to bad quality cuts. The response time of the photodiode is short. It is simple to insert into a beam guidance train without significantly interfering with the mirror efficiency or cooling system.

From the signals obtained it can be concluded that a good cut would give smooth and low level signals, while a poor cut (e.g. a rough cut) would give noisy (large variations) and high level signals. This lead us to introduce two control parameters, i.e. the percentage of variations of the sensor output ($\Delta V\%$) and the overall RMS value (root-mean-square value) as shown in Fig. 4 -29. The calculation of $\Delta V\%$ is given by

$$\Delta V\% = \frac{\Delta V}{\text{Over all RMS value}} \times 100 \qquad (4\text{-}9)$$

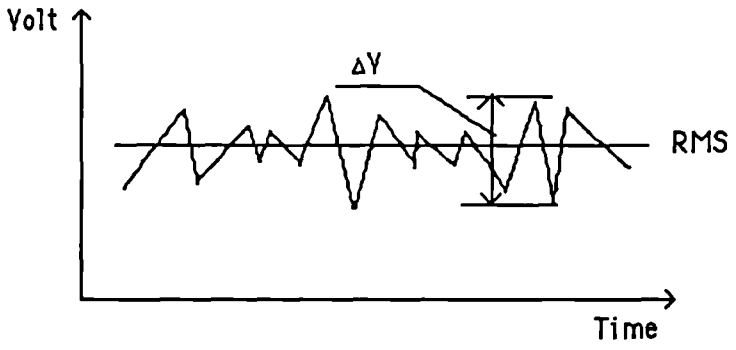


Fig. 4 -29. The description of the first quality control parameter $\Delta V\%$.

The values of these two parameters were found for the material studied (1mm thick of mild steel) by axial detection to be :

a). good : $\Delta V\% \approx 10\%$ and the overall RMS = 20 (mV) ; cut edge was clean and smooth;
b). ok : $\Delta V\% \approx 10\%$ and overall RMS = 40 (mV); cut with medium dross adhesion;
c). bad : $\Delta V\%$ nearly 100% or above and the overall RMS = 70 (mV); rough cuts or cuts with too much dross.
d). not cut: overall RMS > 85 mV.

This detection system could therefore be used for in-process monitoring of the laser cutting process so that appropriate actions such as an alarm, part rejection, or the stopping of the process could be made on a mass production line. A simple flowchart showing the sequences of developing an alarm system is shown in Fig. 4 -30. The computer has the functions of recording and processing signals. The received signals can be analysed to give the overall RMS intensity and the variations in intensity. These two principle parameters would then be compared to some threshold values. If they exceed the threshold value of either of these two parameters the computer would send a command to operate the alarm. The operator will then decide what actions need to take.

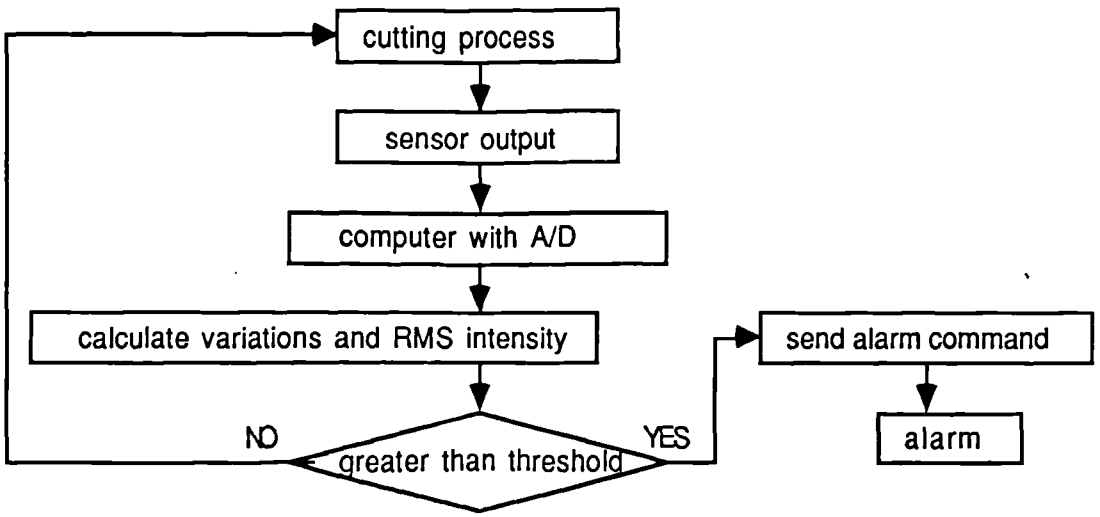


Fig. 4 -30. The flowchart of an alarm system.

It could also be possible to make an on-line fault diagnosis of the laser cutting process based on rules concerning the metal cutting process. For example, the following rules can be made from this study:

a). If the $\Delta V\%$ value and the overall RMS value are greater than the thresholds, there is a large oscillation of the signals, then the cut possibly has a rough surface or much clinging dross;
b). If the $\Delta V\%$ value and the overall RMS value are within the threshold, there is a small oscillations of the signals, then the cut possibly has a smooth surface and little dross;
c). If the $\Delta V\%$ or the overall RMS changes, e.g. decreasing within the threshold, then the quantity of the dross is probably reduced (this can be seen by comparing the two signals in Figs. 4 -27 and 4 -28).

4.6. Chapter Summary

Two experimental studies for in-process monitoring of the laser cutting process were investigated. Detected signals from the photodiode were analysed and related to the dross adhesion, kerf width and surface roughness. The off-axis detection unit provided reliable and fast information about the cut quality but has a disadvantage of directional dependency. The axial monitoring method through the final beam guidance mirror could meet all the basic requirements for an industrial control system by providing reliable information about the cut quality, with fast detection and is independent of cutting direction. The design of an on-line alarm system was discussed.

CHAPTER FIVE

ACOUSTIC METHOD FOR IN-PROCESS MONITORING OF LASER CUTTING PROCESS

5.1. Introduction and Background

An acoustic signal can be obtained from a mirror reflecting power from a fast axial flow CO_2 laser [123-124]. In the first experiment observing this phenomenon shown in Fig. 1 -29, acoustic signals at greater than 100 kHz were detected. These acoustic signals were used in monitoring laser welding process [187]. It may thus be useful for monitoring laser cutting process. A few theories exist to explain the mechanism of these laser-induced waves. These theories basically follow two principles[124], i.e. the generation of the thermal-mechanical stress waves and the photon pressure.

5.1.1. Generation of thermal-mechanical stress waves

When the surface of a body is subject to a sudden heating ("heat shock") there will be temperature gradients in the surface layer. These temperature gradients produce, as a result of thermal expansion, strains in the surface layer and lead to the generation of stress waves which propagate away from the heated surface. If the heating is of very short duration (a few nanoseconds), very high frequency and shock waves can be produced. In the case of interaction between the CO_2 laser beam and the mirror, the heat shock can be related to the fast oscillations in the beam power or fluctuations in the back reflected energy from the workpiece. The latter could be related to the state of the processing or the cut quality as to be discussed later. The beam power oscillations could be caused by the following reasons:

(i). Superposition of axial and transverse modes: Axial (longitudinal)

mode of the laser cavity is defined as the number of half-wavelengths of the electromagnetic field that can be contained between the reflectors. This number, n, is given as [204] :

$$n = \frac{2L}{\lambda} \qquad (5\text{-}1)$$

or

$$n = \frac{2L\nu}{c} \qquad (5\text{-}2)$$

where

L = the length of the cavity (m) ;

λ = the wavelength (m);

c = velocity of light, 3 x 10^8 (m/s);

ν = the frequency of the beam (1/s).

From equation (5 -2) the frequency separation $\Delta\nu_{axial}$ between adjacent modes (Δn =1) is given by [204]

$$\Delta\nu_{axial} = \frac{c}{2L} \qquad (5\text{-}3)$$

The modes of oscillation of the laser cavity consists, therefore, of a large number of frequencies each is given by Eqn.(5-2) and separated by c/2L. The superposition of these axial modes results in a temporal fluctuation of the total power. Since the cavity length of laser cavity is 6 m for the fast-axial flow 2 kW Control Laser, the frequency separation of the axial modes is 25 MHz for this laser.

The frequency separation of the transverse modes, $\Delta\nu_{tr}$, is given as [204]:

$$\Delta\nu_{tr} = \frac{c}{\pi R} \qquad (5\text{-}4)$$

where R is the radius of curvature of the spherical mirror and is 15 m for the Control Laser. Since the transverse mode determines the intensity distribution, the superposition of the transversal modes results in a spatial fluctuation of the centre of weight of the intensity distribution [204]. The frequency of the transverse modes is around 6 MHz for the Control Laser.

Therefore, the superposition of the axial and transverse modes leads to a power oscillation of 25 MHz, which is much higher than the observed frequency of the acoustic waves.

(ii). Relaxation oscillations and mode instabilities: Power oscillations in the region of 50 kHz to 5 MHz are caused by two phenomena, i.e. the relaxation oscillations and the mode instabilities. The relaxation oscillations in the case of continuous excitation may be induced by optical feedback [204]. Optical feedback may occur due to the back reflected laser beam from the workpiece entering the laser cavity. These back reflected laser beams are amplified there and return as amplified damped oscillations. The mode instabilities may be induced by nonlinear gain saturation [204]. The frequency of the relaxation oscillations, f, is given as [187] :

$$f = \frac{1}{2} \left| \frac{(g/g_e) - 1}{t_s t_c} \right|^{\frac{1}{2}} \qquad (5\text{-}5)$$

and the decay time or the damping coefficient is given as [187] :

$$T_d = \frac{2\, t_s}{(g/g_e)} \qquad (5\text{-}6)$$

where

g = unsaturated gain;

g_e = gain at threshold;

t_s = lifetime of the upper excited laser level;

t_c = resonator lifetime.

These two equations describe the laser response to a step disturbance, i.e. the laser power relaxes with the indicated frequency to the steady state value. For example, given $g/g_e = 1.8$, $t_s = 0.4$ ms and $t_c = 0.4$ ns , relevant to the Control Laser [187], the frequency of relaxation oscillations is calculated as 1.1 MHz with a damping coefficient T_d of 0.44 ms. This frequency is in the order of that of the acoustic signals detected in the final beam guidance mirror.

However, it is worthwhile to point out that the experiment reported in

reference [123] was performed in a laser system where the distance of the workpiece from the laser cavity was short (about 1.5 m) [123]. In this particular arrangement, the back-reflected beam from the workpiece may be strong enough to disturb the beam amplification inside the cavity leading to the power oscillations. When the distance of workpiece from the laser cavity is long such is the case for this study (around 6 m), the intensity of the back-reflected beam into the cavity would be very much reduced after being reflected by a few mirrors. Therefore, the optical feedback effect would be expected to be weak in this case. In fact, when several pizeoclectric transducers were positioned on different mirrors in the beam path, it was found [205] that the transducer on the final beam guidance mirror gave the strongest response, while the one close to the the laser cavity gave the weakest signal. This indicated that the optical feedback effect would be small if the workpiece has a long distance to the laser cavity.

(iii). Variations of pumping power and resonator losses: Power fluctuations in the low frequency range between Hertz and kilo-Hertz are due to variations of pumping power and resonator losses. The variation of the pumping power is mainly caused by plasma instabilities and current ripples, while the resonator losses are due to mechanical and thermal instabilities of the laser structure, leading to, for example, mirror misalignment and resonator length alterations [204]. This frequency range is much lower than that of the detected signal.

5.1.2. Generation of photon pressure stress waves

It is an important feature of electromagnetic waves that they are able to transport momentum as well as energy. When an electromagnetic wave is reflected by a metal surface, the wave induces electric currents in the surface skin-layer which are in phase with electric and magnetic fields **E** (V/m) and **H** (A/m) and consequently there is a non-zero force of interaction between the current and **H**. The force per unit area is termed radiation pressure or photon pressure [203]. It was shown [203] that the magnitude of the photon pressure for a normally incident wave is twice

the energy density of the incident wave, i.e. :

$$q = 2\xi \tag{5-7}$$

where q is the magnitude of the photon pressure ($N.m^{-2}$) and ξ is the energy density of the incident wave. The energy density of the incident wave, ξ, is determined by the radiant flux density as follows [209]:

$$\xi = \frac{B_x}{c} \tag{5-8}$$

where

B_x = the radiant flux density (W/m^2);

c = velocity of light, 3×10^8 (m/s).

Therefore the photon pressure, q , is given as

$$q = \frac{2B_x}{c} \ (Nm^{-2}) \tag{5-9}$$

When the incident wave is at an angle e.g. 45^0 to the surface, the photon pressure would be expected to be smaller than that given by Eqn.(5-9), since the portion of the wave which is parallel to the surface will have no photon pressure effect. Thus the magnitude of the photon pressure for an incident wave at an angle of 45^0 may be given as :

$$q = \frac{2B_x}{c} \sin 45^0 \tag{5-10}$$

In laser materials processing, the photon pressure comes from the main laser beam, the back reflected laser beam and the radiant energy from the process (e.g. the visible light). From the above discussions, it is seen that both theories could explain the acoustic signals detected in the last mirror. However, a comparison between the magnitude of the two effects is necessary to determine the main cause for the detected acoustic signals. This is to be discussed in later section.

5.2. The Measurement of the Acoustic Waves

The measurement of acoustic signals is most commonly achieved by using piezoelectric transducers operating on the Piezoelectric Effect. The piezoelectric effect is a property of the crystal structure and is linked to an asymmetry in it which can be characterised by the appearance of one

or several polar axes. These are crystal axes in which one direction differs from the opposite direction so that any rotation of the crystal in which the front and back ends of such an axis are interchanged never gives the same position of the crystal. The pizeoelectric effect is best analysed by using plates cut from the crystal at right angles to an X-axis, as shown in Fig. 5 -1.

In this so-called X-cut, the Z-axis and one Y-axis are located in the plane of the plate. Any pressure on this plate slightly reduces its thickness because it is elastic. This shifts the electrically charged elements of the crystal lattice in a way relative to each other such that the plate becomes polarised. As a result free positive charges appear on one side of the plate, and negative charges on the other. This can be readily detected [202]. Usually, discharge of the electric charge, metal electrodes, e.g. silver layers are used, which are firmly attached to both sides of the plate. These layers form an electric capacitor with the crystal as dielectric. In the presence of polarisation, resulting from pressure exerted on the plate, the capacitor is charged to a voltage measurable by an instrument.

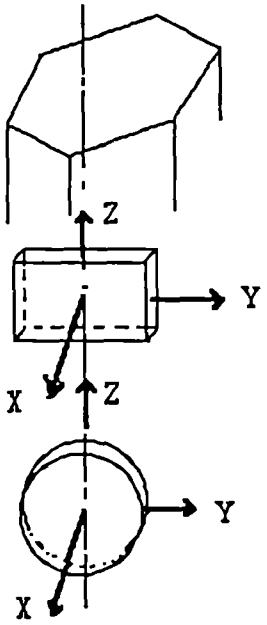


Fig. 5-1. Orientation of sections for rectangular and round X-cut crystal plates[202].

The above-described direct piezoelectric effect can be represented by:

$$Q = jF \tag{5-11}$$

where

Q = the electric charge (coulomb);

j= piezoelectric constant, i.e. the charge sensitivity to force (coulombs $newton^{-1}$);

F = the applied force (newton).

It is seen that the electric charge produced on the crystal surfaces is proportional to the force applied on them. Therefore if the force changes, the produced voltage will change correspondingly. Based on this piezoelectric effect, piezoelectric transducers can be used for receiving acoustic waves.

The objective of this study is therefore to find out the correlation between the acoustic signals generated during laser cutting process and the laser cut quality.

5.3. Experimental Set-up

The experimental set-up is shown in Fig. 5 -2, where two piezoelectric transducers were located at different positions. The transducer P_1 was coupled onto the rear of the gold-coated last mirror and would detect mechanically coupled vibration. Grease was used to increase contact between the transducer and the mirror ensuring good acoustic coupling. The transducer P_2 was positioned close to the cutting nozzle and would detect acoustic waves transmitted through air.

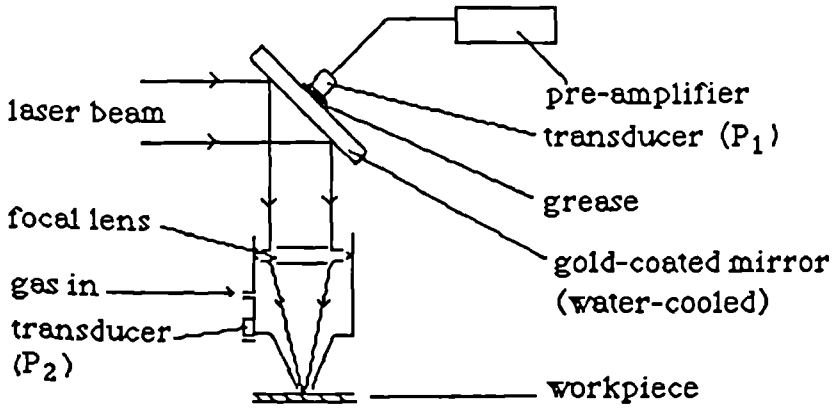


Fig. 5 -2. Schematic drawing of the experimental set-up for monitoring the acoustic waves in laser cutting.

The piezoelectric transducer was selected from Dunegan and Physical Acoustic Corporation (Mode number: WD No. 671). It provides an approximately "flat" frequency response from 100 kHz - 1 MHz as shown in Fig. 5 -3. The experimental set-up shown in Fig. 5 -2 consists of a preamplifier (Dunegan/PAC) with a gain of 60 dB used to increase the transducer's sensitivity and a "Smart Acoustic Monitor" (Fig. 5- 4, Dunegan/PAC), which was equipped with a fast R.M.S. device (time constant = 0.1 second) producing the acoustic signal R.M.S. values.

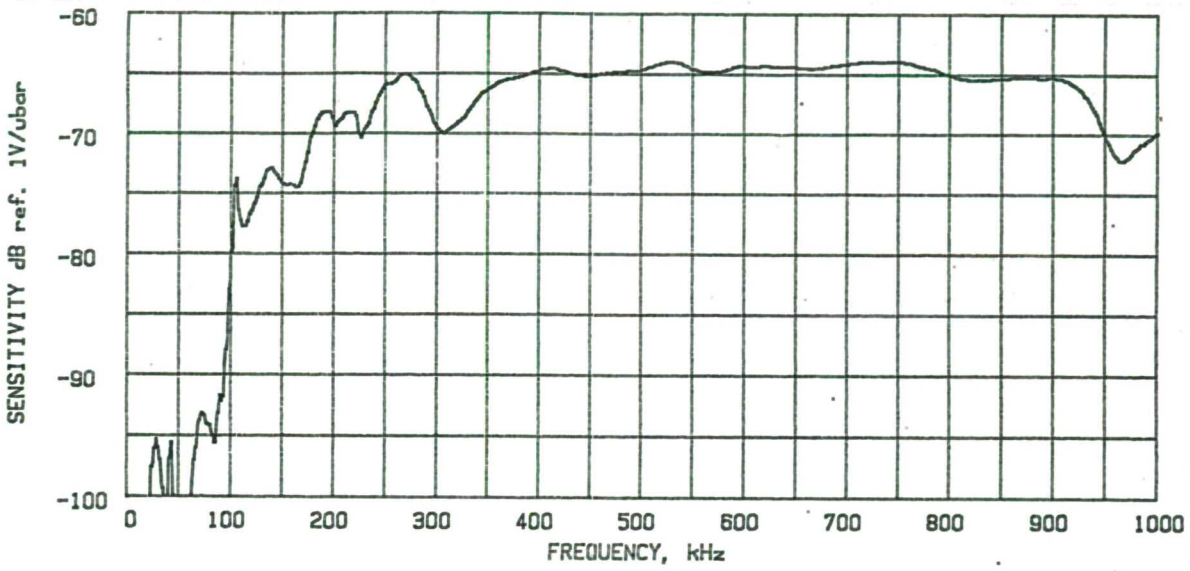


Fig.5-3. The piezoelectric transducer spectral sensitivity (reproduction from the Dunegan product manual).

As can be seen from Fig. 5 -3, the sensitivity of the transducer before amplification is around - 65 dB, which can be converted into $10^{(-65/20)}$ = 5.62 x 10^{-4} (V/μbar), i.e. 5.62 x 10^{-3} V/Nm^{-2} according to the definition of decibel. After the preamplifier, the sensitivity would be (-65 + 60) = -5 dB, i.e. $10^{(-5/20)}$ = 5.62 V/Nm^{-2}.

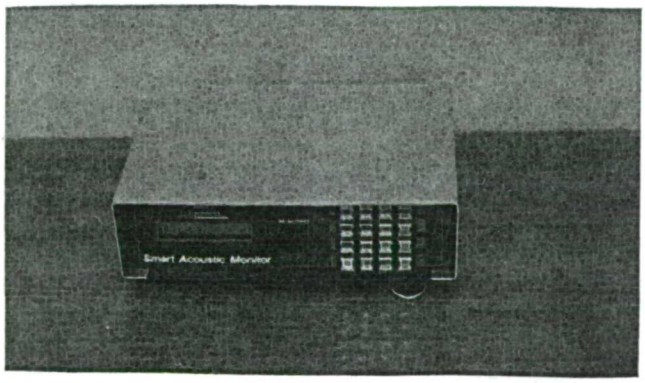


Fig. 5 -4. The Smart Acoustic Monitor.

The laser equipment was the same as in previous experiments. This is the fast axial flow 2 kW CO_2 Control Laser. The workpiece movement was controlled by the CNC workstation as shown previously in Fig. 3 -1. The laser beam was focussed onto the workpiece surface through a KCl lens with 125 mm focal length. The assistant gas, O_2, past through a converging conical nozzle with an orifice diameter of 1.6 mm. The nozzle standoff distance relative to the workpiece surface was 0.8 mm. The workpiece material was 1 mm thick of mild steel sheets. To study the relationship between the acoustic signals and cut qualities, the process parameters (laser power, gas flowrate and the cutting speed) were varied to get various cut edge qualities.

The quality assessment of the laser cuts was done by measuring the top kerf width, width of HAZ (average readings) and by visually examining the dross adhesion and surface roughness. The surface roughness was basically classified into three levels, i.e. rough, medium and smooth. The dross adhesion was classified according to the amount of the drosses into different grades, i.e. A- little dross; B- medium dross; C- heavy dross; D- very heavy dross. For those cuts with the same dross grade but with different dross size, they were further classified using the symbol "+", which means a little worse.

5.4. Results and Discussion

5.4.1. Factors affecting the overall signal strength

5.4.1.1. Signals detected by transducer P_1

(i). Detection principle

As discussed in 5.1, the generation of the acoustic signals through the final beam guidance mirror could be explained by the photon pressure theory and by the thermal stress waves theory. In order to make a comparison between the two theories, the following calculations are performed.

(i -1). Photon pressure theory.

Since the piezoelectric transducer P_1 was essentially unrestrained, it would detect only the fluctuations of the pressure imposing on the mirror, which accelerate the transducer and thus generate force imposing on it according to Newton's first law. Therefore, the magnitude of the photon pressure acting the transducer can be worked out from the acceleration.

a). Calculation of the deflection of the mirror: Considering the bending of circular plates subjected to loads disposed symmetrically with respect to the plate centre, the deflection of the plate in the case of a simply supported edge (Fig. 5- 5) is given as [208]:

$$W = \frac{q}{64D}(a^2 - r^2)\left(\frac{5+\nu}{1+\nu}a^2 - r^2\right) \qquad (5\text{-}12)$$

where

W = the deflection of the plate at the radial distance r (m);

q = a uniformly distributed load of intensity (N/m^2);

a = R = the radius of the circular plate (the mirror) (m);

r = polar radial coordinate in the plane of the plate (m);

ν = Poisson's ratio ;

D = flexural rigidity of the plate and is given as [208]:

$$D = \frac{Et^3}{12(1-\nu^2)} \qquad (5\text{-}13)$$

where

E =Young's Modulus (N/m^2);

t = thickness of the plate (m).

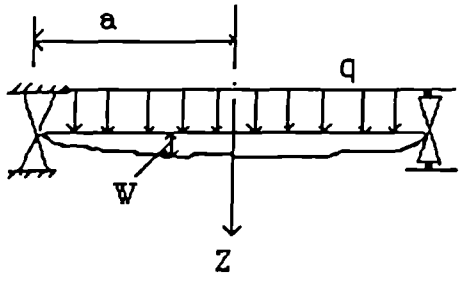


Fig. 5 -5. Illustration of a circular plate deflection.

Equation (5 -12) is accurate if the deflection of the plate is small compared to its thickness [208], which is the case of this study. Since the size of the mirror is slightly smaller than the mirror mount, which supports the mirror edges, the situation shown in Fig. 5 -5 can be approximately applied for this study.

Since the transducer was attached to the centre of the mirror, the central deflection of the mirror is of interest, i.e. r =0, therefore the Eqn.(5-12) becomes

$$W = \frac{qa^4}{64D} \frac{5+\nu}{1+\nu} \qquad (5\text{-}14)$$

Given data as below :

$a = R = 3.5 \times 10^{-2}$ m;

$E = 1.17 \times 10^{11}$ N/m^2 [208] ;

$\nu = 0.30$ [208] ;

$t = 1.5 \times 10^{-2}$ m ;

the flexural rigidity of the mirror, D, is calculated as $D = 3.62 \times 10^4$ (N.m). Therefore Eqn.(5 -14) is developed into

$$W = 2.64 \times 10^{-12} q \qquad (5\text{-}15)$$

b). Calculation of the acceleration: Suppose that the photon pressure imposed on the mirror varies in a sinusoidal way (in the positive region) and the frequency is about 100 kHz according to the detected acoustic signal spectrum (Fig.5- 6). The pressure can then be expressed as:

$$q = q_m \, |\sin(2\pi ft)| \qquad (5\text{-}16)$$

where

q_m = the amplitude of the pressure (N/m^2);

f = the frequency (Hz);

t = time (s).

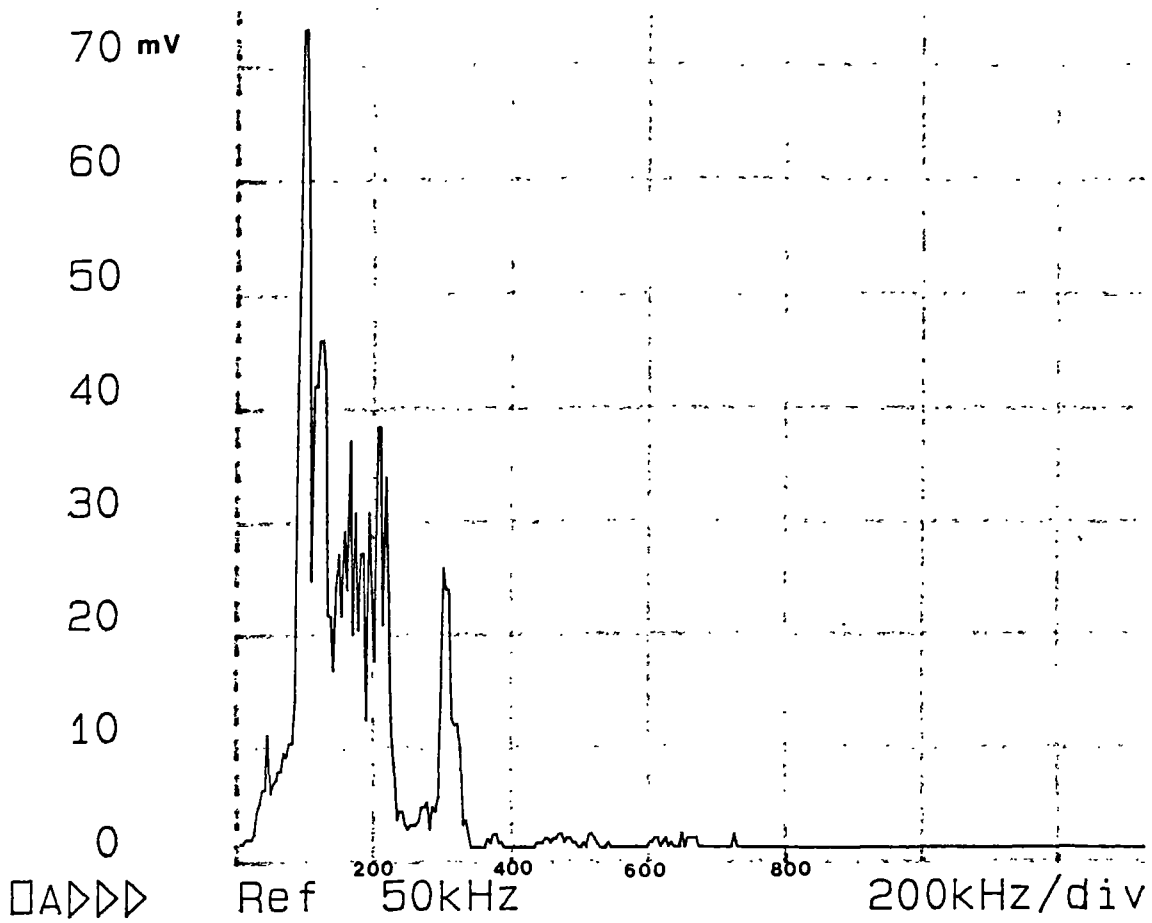


Fig. 5 -6. The acoustic signal spectrum analysis for a non-penetrating cut.

Suppose that the incident power (e.g. the back reflected beam energy) fluctuates at the frequency of 100 kHz with an amplitude of 10 W, i.e. the magnitude of the power density fluctuation over the whole mirror is $10/(\pi \times 0.035^2) = 2.6 \times 10^3$ $(W.m^{-2})$. The magnitude of the corresponding photon pressure imposing on the mirror is calculated according to Eqn.(5-10) as :

$$q_m = \frac{\sqrt{2} \times 2.6 \times 10^3}{3 \times 10^8} = 1.23 \times 10^{-5} \ (N.m^{-2}) \qquad (5\text{-}17)$$

The central deflection of the mirror becomes

$$W = 3.25 \times 10^{-17} \ |\sin(2\pi ft)| \qquad (5\text{-}18)$$

The acceleration of the mirror induced by this varying deflection can thus be calculated as

$$\begin{aligned} a^* &= d^2W/dt^2 \\ &= 3.25 \times 10^{-17} \ (2\pi \times 10^5)^2 \ |\sin(2\pi ft)| \\ &= 1.28 \times 10^{-5} \ | \ \sin(2\pi ft)| \end{aligned} \qquad (5\text{-}19)$$

which is also the acceleration of the transducer if it is directly attached to the mirror.

c). Calculation of the expected output from the transducer: According to Newton's law, the force imposing on the transducer is given as

$$\Delta F = ma^* \qquad (5\text{-}20)$$

where m is the mass of transducer and is about 20 g (2×10^{-2} kg). The magnitude of the force is thus calculated as 2.56×10^{-7} (N). This can be converted into the magnitude of pressure, ΔP, as

$$\begin{aligned} \Delta P &= \Delta F/A \\ &= 2.56 \times 10^{-7}/(3.14 \times (5 \times 10^{-3})^2) \\ &= 3.26 \times 10^{-3} \ (N/m^2) \end{aligned} \qquad (5\text{-}21)$$

where A is the contact area of the transducer with a radius of 5 mm. Since the transducer sensitivity after the preamplifier is 5.62 $V/N.m^{-2}$, the expected output from the transducer would be

$$3.26 \times 10^{-3} \times 5.62 = 18.3 \ (mV) \qquad (5\text{-}22)$$

which is lower than the amplitude of the detected signal strength ranging from 40 mV to 170 mV to be shown in later section. For the system under study, the transducer was not directly attached to the mirror but separated by a water cooling system, which would reduce the magnitude of the signal strength.

The photon pressure from the process-generated energy can also be calculated. According to Fig. 4 -3, the open circuit photovoltage is proportional to the intensity of illumination lux (1000 Lux = 4.75 mW/cm^2 as a typical value). Given an maximum output variation from a photodiode of 75 mV (Fig.4 -24), the corresponding illumination lux can be found out from Fig. 4 -3 about 0.08 lux (the amplification for the photodiode output was 1).

Since this amount of light was transmitted through the fibre which has a diameter of 1 mm, the light illuminating the whole mirror would

have an intensity given as (the magnitude):

$$I = \frac{A_2}{A_1} \times 0.08 \text{ (lux)} \qquad (5\text{-}23)$$

where

I = the magnitude of the light intensity, (lux);

A_1 = the cross section area of the fibre, i.e. $\pi/4$ (mm^2);

A_2 = the area of the mirror, i.e. 1.23 π x 10^3 (mm^2).

Therefore, I is calculated to be 394 lux, i.e. 394 x 4.75/1000 =1.87 (mW/cm^2) or 18.7 W/m^2. The magnitude of photon pressure is thus given as 1.414 x 18.7/c =8.8 x 10^{-8} Nm^{-2}. The central deflection of the mirror due to this pressure can be calculated according to Eqn.(5 -15) as :

$$W = 2.3 \times 10^{-19} |\sin(2\pi ft)| \qquad (5\text{-}24)$$

The acceleration can then be calculated as

$$a^* = d^2W/dt^2 = 9.07 \times 10^{-8} |\sin(2\pi ft)| \ (m/s^2) \qquad (5\text{-}25)$$

The magnitude of force is thus given as 1.81 x 10^{-9} (N), which can be converted into pressure: 1.81 x $10^{-9}/(\pi \times 0.005^2)$ =2.31 x 10^{-5} (N/m^2). The expected output from the transducer is thus given by

$$2.31 \times 10^{-5} \times 5.6 = 1.29 \times 10^{-4} \text{ (V)} = 0.129 \text{ (mV)} \qquad (5\text{-}26)$$

which is much lower than the signal strength detected. Hence this appears to show that the radiant heat generated during the processing is unlikely to be the cause of the acoustic signals detected in final mirror.

(i -2). Thermal stress waves

When the surface of the gold-coated mirror is subject to a sudden heating, there will be a strain generated in the surface layer. This layer may be represented by the depth of penetration, i.e. the skin depth, which is given as [210]:

$$\delta = \sqrt{\frac{1}{\pi f \mu \sigma}} \qquad (5\text{-}27)$$

where

f = frequency of the incident wave, (Hz);

μ= the permeability in gold $\approx 4\pi \times 10^{-7}$ [210], (H/m);

σ = electric conductivity of gold, i.e. 4.1×10^{7} [210], (1/m.Ω).

Given $f = 10^5$ Hz, the skin depth is calculated to be 2.5×10^{-4} (m).

Considering the heating of this skin layer of the mirror, the rate of the temperature change can be approximately determined by [3]:

$$\rho C_p \times A \times l \frac{dT}{dt} = P(1 - r_f) \qquad (5\text{-}28)$$

where

ρ = density of gold, 19.3×10^3 kg/m^3 [206];

C_p = heat capacity of gold, 135 J/kg.^{0}C [1];

t =time (s);

l =thickness of the layer, 2.5×10^{-4} (m);

A = area of the mirror, i.e. $\pi \times 0.035^2 = 3.85 \times 10^{-3}$ (m^2);

P = the incident power (W);

r_f =reflectivity of the mirror $\approx$ 0.99.

The linear expansion normal to the surface is given as :

$$dl/l = \alpha\, dT \qquad (5\text{-}29)$$

where

dl = the thermal expansion(m);

α = linear expansion coefficient of gold, 1.42×10^{-5} (1/^{0}C)[206];

dT =the temperature change (^{0}C).

This equation can be arranged as :

$$\frac{dl}{dt} = \alpha l \frac{dT}{dt} \qquad (5\text{-}30)$$

From Eqns. (5 -28) and (5 -30), the following equation is developed, i.e.

$$\frac{dl}{dt} = \frac{\alpha P(1 - r_f)}{\rho C_p A} \qquad \text{or}$$

$$\frac{d^2l}{dt^2} = \frac{\alpha P_m(1 - r_f)}{\rho C_p A} 2\pi f \cos(2\pi f t) \qquad (5\text{-}31)$$

where P was assumed to fluctuate in a sinusoidal way, i.e. $P = P_m \sin(2\pi f t)$ and P_m is the magnitude of the power oscillation. The magnitude of the thermal stress imposing on the mirror due to the oscillation of the thin layer is thus given as:

$$\Delta P = \frac{\Delta F}{A} = \frac{ma^*}{A} = \frac{\rho A l a^*}{A} = \frac{2\pi f l \alpha P_m(1 - r_f)}{C_p A} \qquad (5\text{-}32)$$

where m is the mass of the thin layer and is equal to ρ Al. Given the magnitude of the power fluctuation P_m= 10 W and f =10^5 Hz, the magnitude of the thermal stress is thus calculated as 4.3 x 10^{-4} ($N.m^{-2}$). Compared to the photon pressure given by Eqn.(5 -17), i.e. q =1.23 x 10^{-5} ($N.m^{-2}$), it is easily to see that the ratio between the thermal stress and the photon pressure is 35. Therefore the thermal stress could produce an acoustic signal with a strength value of 35 x 18.3 =641 (mV) (Eqn.(5-22)), which is higher than the detected signal but in the same order.

The thermal stress due to the radiant heat from the process can also be calculated according to Eqn.(5 -26) as 35 x 0.129 =4.5 (mV). This is far lower than the detected signal strength.

To sum up the above discussion, it is seen that there exist photon pressure and thermal stress waves when the mirror is subject to sudden heating. Both of which are likely caused by the fluctuation of the back-reflected beam energy. But the thermal stress is much higher than the photon pressure. This agrees well with reported results [211,212]. The effect of the process-generated radiant heat is small in both cases and is thus unlikely to produce the acoustic signals. Therefore, the acoustic signals detected in the final mirror appear to be mainly due to the thermal stress waves.

(ii). Effect of dross on signal strength

Figure 5 -7 shows a set of signals for cuts with different grades of dross adhesion. These cuts were obtained at different gas flowrates while the laser power and the cutting speed were kept the same. The cut edge quality was different mainly in the amount of the clinging dross particles as summarised in Table 5 -1.

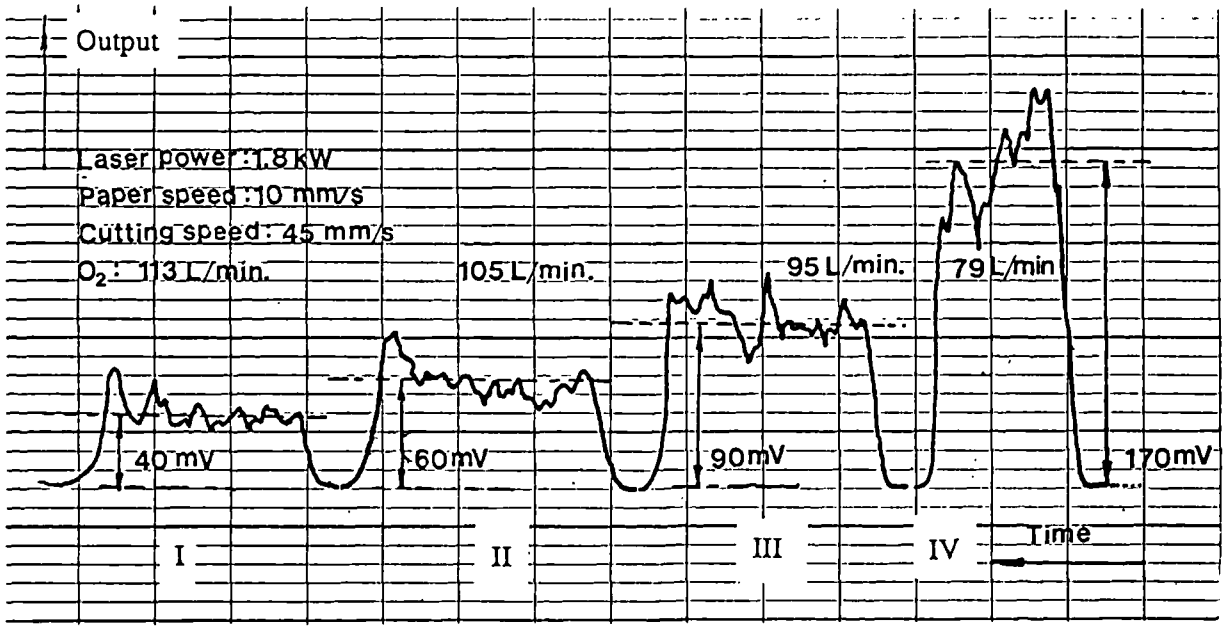


Fig. 5 -7. Effect of dross on acoustic signals (P_1).

Table 5 -1. Cut Quality Assessment

Sample number	Kerf width (mm)	HAZ width (mm)	Dross grade	Roughness grade	Comments on cut quality
I	0.65	0.30	A (blocking 10% of the kerf) *	smooth	good, little dross
II	0.66	0.55	B (blocking 40% of the kerf) *	smooth	HAZ variation and dross on one side
III	0.66	1.50	D (blocking 80% of the kerf) *	medium	large variation in HAZ + dross
IV					not cut through

* Figures were estimated when the kerf was top-viewed.

The back reflected optical energy (i.e. the process-generated lights) varied with the gas flowrate due to which affected the burning energy. However it is reasonable to say that the detected signals were different mainly due to the clinging dross effect, since the thermal stress caused by this process-generated lights was small as discussed before.

It is seen from Fig. 5 -7 that the overall signal strength varied significantly with the dross grade. In cut I where the about 10% of the kerf was blocked by the clinging dross particles, the overall signal RMS value was about 40 mV. In cut II and III where more clinging dross particles were observed, the overall signal RMS values were 60 mV and 90 mV respectively, which were significantly higher than that shown in cut I. If the cut was not penetrating, the overall RMS value reached 170 mV. This was similar to the case for laser welding, where strong acoustic signals were detected when the keyhole failed [187]. The effect of the clinging dross on the signal strength was expected, since the transducer P_1 mainly responded to the variations of the back reflected beam energy. A larger amount and size of the clinging dross would block more of the laser beam passing through the kerf and thus reflect more of the beam energy. In other words, a larger variation in the amplitude of the back-reflected energy would be produced, which caused stronger thermal stress waves.

Theoretically, the back reflections were also affected by the cut face roughness, i.e. a rougher surface would absorb more laser beam energy and thus reflects less of the beam back to the mirror. However, by comparing the two signals for cut II and cut III, this roughness effect could not be seen because the roughness was associated with more dross particles.

(iii). Effect of kerf width on overall signal strength

Figure 5 -8 shows signals obtained for two cuts with different kerf widths at the cutting speeds of 45 and 65 (mm/s) respectively. The cut edge quality is summarised in Table 5 -2. It is seen that both cuts had little dross clinging at the bottom edges, relatively constant HAZ and smooth surface. But they had different kerf widths, i.e. cut II had an average kerf width of

0.65 mm while cut I had a value of 0.40 mm. The laser power and the gas flowrate were set as 1.8 kW and 113 L/min. respectively.

Table 5 -2. Cut quality assessment

Sample number	Kerf width (mm)	HAZ width (mm)	Dross grade	Roughness grade	Comments on cut quality
I	0.40	0.45	A	smooth	good
II	0.65	0.30	A	smooth	good

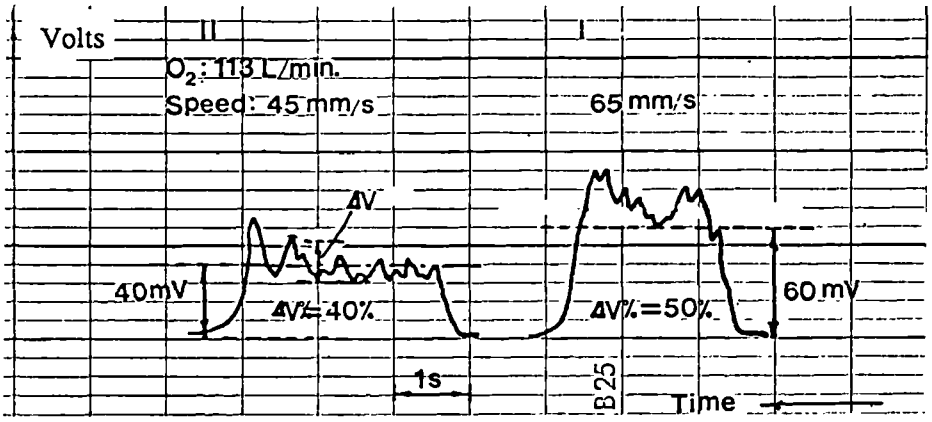


Fig. 5 -8. Kerf width effect on overall signal strength (P_1).

As can be seen from the signals that the overall signal RMS value of the narrow cut was 60 mV, which was higher than the wider cut with an overall signal RMS of 40 mV. This can again be explained by the effect of the back-reflected laser beam. At the cutting front, a larger portion of the laser beam was reflected for the narrow kerf and thus causing a stronger back reflection, which affected the amplitude of the thermal stress waves and thus the signal strength.

Since the cutting speed was different for the two cuts, the cutting front temperature was also different. The higher the cutting speed, the hotter the cut front and thus the more the radiant energy. It may thus be argued that why the stronger signal recorded for the narrow cut was not due to the hotter cut front. This was unlikely, since as discussed before the thermal stress imposing on the mirror was mainly caused by the back-reflected laser beam energy. The effect of the process-generated optical energy including the radiant energy from the cutting front was thus unlikely to be the cause of the detected acoustic signals. Therefore,

the difference in the overall RMS values of the two signals shown in Fig.5-8 were mainly caused by the kerf width effect.

This kerf width effect was also seen in Fig. 5 -9, where signals were obtained for two cuts with different kerf width and surface roughness. As discussed before, the surface roughness also affected the back reflections. Therefore, the lower signal strength of the signal for cut I was likely a combined effect of narrower kerf width and smoother surface. Table 5 -3 is a summary of the cut quality .

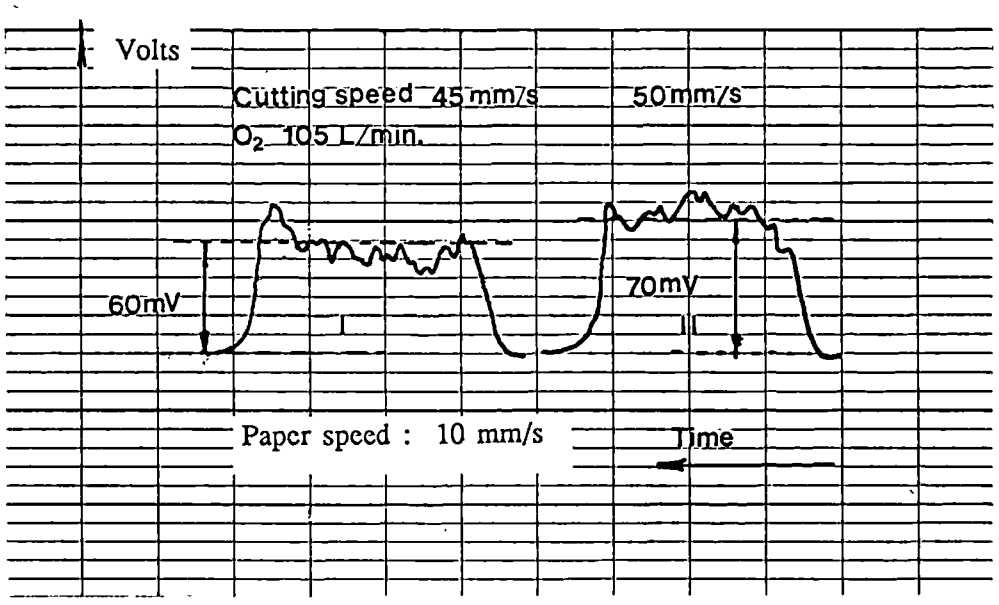


Fig. 5 -9. Kerf width and roughness effect on the signal strength (P_1).

Table 5 -3. Cut Quality Assessment

Sample number	Kerf width (mm)	HAZ width (mm)	Dross grade	Roughness grade	Comments on cut quality
I	0.66	0.55	B	medium	HAZ & dross on one side
II	0.50	0.55	B	smooth	HAZ & dross on both sides

5.4.1.2. Signals detected by the transducer P_2

The transducer P_2 was positioned close to the cutting nozzle at a distance of around 50 mm. At this distance, the transducer could sense the process-related acoustic waves transmitted through air without causing damage to the transducer due to, for example, the flying sparks generated in laser cutting. These process-related acoustic waves could come from the laser-generated plasma, the impact due to the interactions between the gas stream and the workpiece, the gas flow which causes the melt expulsion. The transducer could also sense the back-reflected energy which may strike on the transducer.

(i). Effect of dross on signal strength

The figure shown below is a set of signals for cuts with different grades of dross adhesion. These signals were recorded at the same time as those shown in Fig.5- 7. Therefore the assessment of the cut quality refers to Table 5 -1.

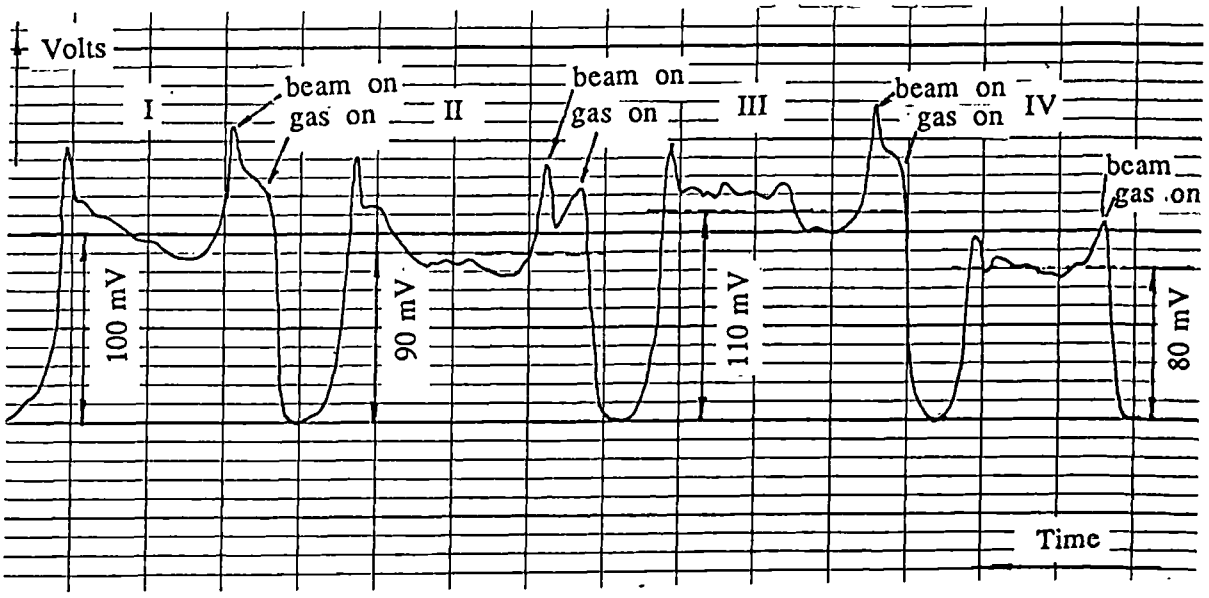


Fig. 5 -10. Effect of dross on acoustic signals detected by P_2.

a). Initial and final peaks: It is seen that the signals had initial and final peak values. The initial peak was a combined effect of the gas stream impact and the laser generated plasma. As clearly shown in the

signals of cut I, II and III, when the gas stream was striking the workpiece ("gas on") there was a strong response from the transducer. This response was intensified when the beam was turned on, which generated plasma (vaporisation pressure) and caused a stronger back-reflection initially. Signals then dropped to a lower value due to a variety of causes. For example, the laser-generated plasma was blown away by the flowing gas stream and fractions of the gas stream simply past through the cut kerf reducing the gas impact. The back reflections were also reduced since a portion of the beam past straight through the cut kerf. At the end of a cut, the gas impact was increased since the majority of the gas stream struck the surface allowing a reduced portion of the gas stream to pass through the already formed kerf. This was a possible cause of the final peak values. However, neither the initial nor the final peaks are of importance in identifying the process cut quality and therefore they are not considered further in the following text.

b). Relationship between dross grade and signal strength: It is seen that the overall signal strength varied for the different cuts, but no obvious correlations with the dross grade can be observed. This possibly due to the combined effect of the clinging dross and the gas impact. On the one hand, the clinging dross could block the gas stream passing through the kerf and thus cause stronger impact signals. The back reflections were also stronger due to the dross blocking effect. These two factors tended to increase the signal strength. On the other hand, since the clinging dross was mainly caused by insufficient drag forces of the gas stream as discussed in chapter three, these reduced gas dynamic forces could weaken the gas impact effect thus leading to the reduced signal strength. These contradictory effects were better illustrated by the signal of cut IV (not separated). The signal strength would have been higher than the others if only the dross effect were considered. It was in fact somewhat lower due to the reduced gas impact (lower gas flow rate).

(ii). Effect of kerf width on overall signal strength

Figure 5 -11 shows signals obtained at the same time as those shown in Fig. 5- 8. The cut quality is thus referred to in Table 5 -2.

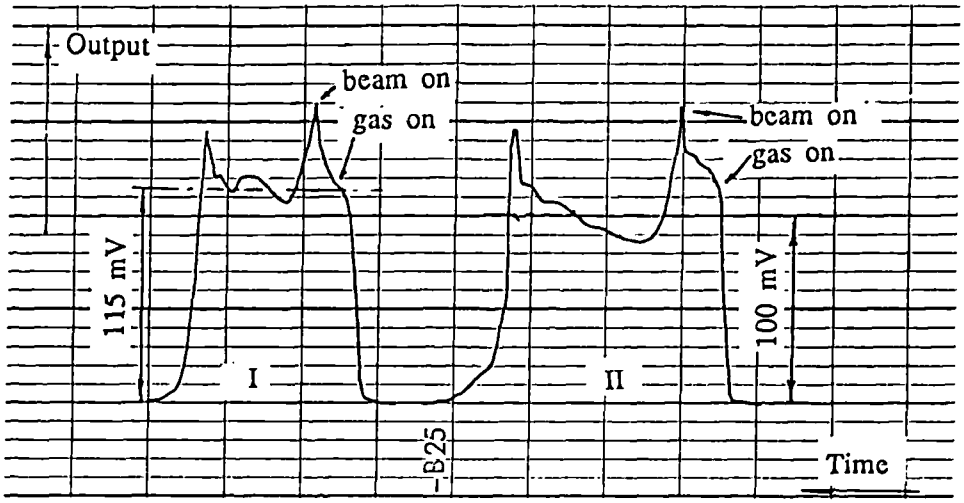


Fig. 5 -11. Kerf width effect on overall acoustic signal strength (P_2).

It is seen from these signals that the overall signal strength of the narrow kerf was 115 mV, which was higher than that of the wide kerf with a value of 100 mV. This can be understood from the interactions between the gas stream and the workpiece. When the cut kerf was narrower, a larger portion of the gas stream struck the workpiece leading to a stronger impact effect and thus stronger acoustic signals.

This kerf width effect can also be roughly seen from Fig. 5 -12. These signals were recorded simultaneously as those in Fig. 5 -9. The assessment of cut quality was referred to in Table 5 -3.

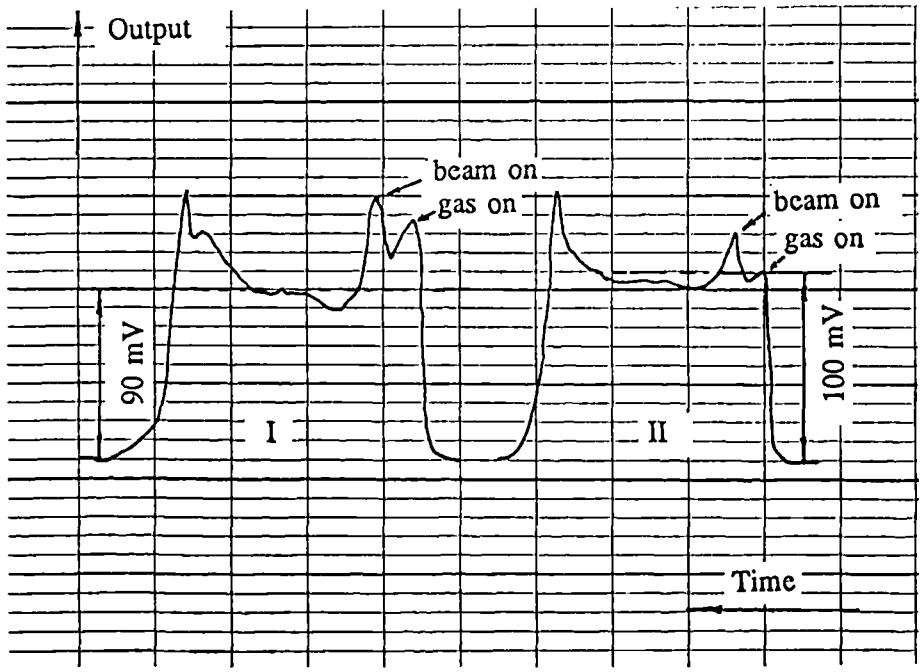


Fig. 5 -12. Kerf width effect on signal strength (P_2).

5.4.2. Signal variations with cut quality

This section looks mainly at the correlation between the variability of the signal and the cut quality.

5.4.2.1. Signals detected by P_1

(i). Signals from a bad cut:

Figure 5 -13 shows a signal from a bad cut, which was obtained at the cutting speed of 10 mm/s, the gas flowrate of 95 L/min. and the laser power of 1.80 kW. A summary of the cut edge quality is shown in table 5 -4. It is seen that the cut edge quality varied along the cut length although the operating parameters were set the same. The first one third of the cut was rough and with some clinging dross and variations in kerf width. The middle part (about one third) was not cut through, while the last part was irregularly blocked by clinging dross particles and had a rough surface. These variations in the cut quality were possibly due to the variations in the workpiece surface conditions which could change the workpiece absorptivity or due to the distortion of the workpiece which changed the focal position. The latter could be caused by some preheating effects at the slow speed cutting, i.e. the part in front of the cutting front was preheated due to the conducted heat from the process. This could cause some noticeable thermal stress in this area. The thermal stress could lead to the bending of the workpiece particularly when it was thin (such was the case of the workpiece under study which had a thickness of 1 mm).

Table 5 -4. Quality Assessment of the Poor Cut

Cut sections	Kerf width (mm)	HAZ width (mm)	Dross grade	Roughness	Comments
first part	1.2 mm	3.0	D	rough	kerf variations
middle part		5.0	D		not cut through
last part	1.6 mm	3.2	C	rough	irregular dross adhesion

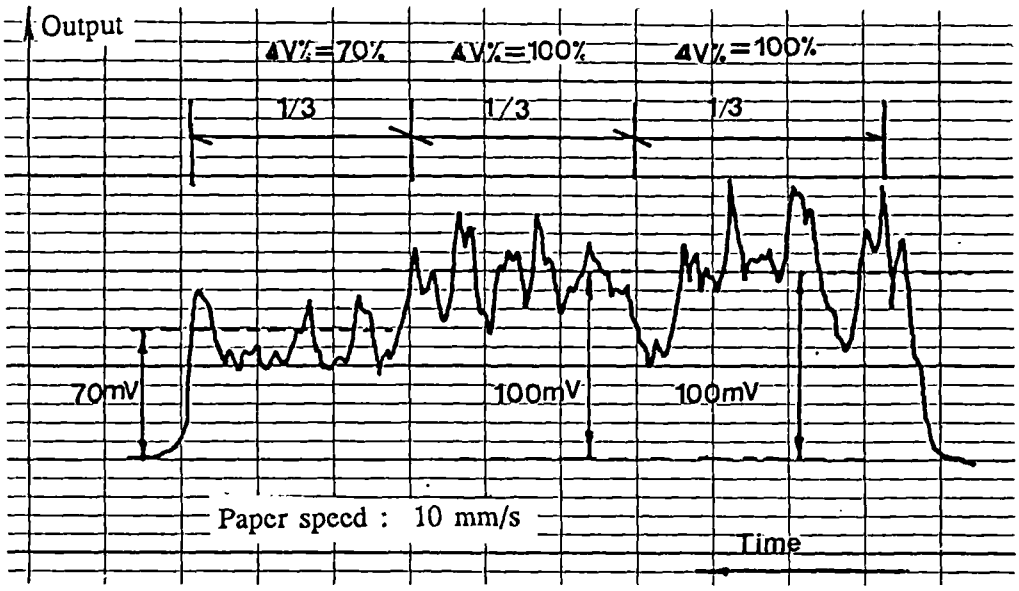


Fig. 5 -13. Signals from a poor cut (P_1).

It is clearly seen from the figure that there were large variations in signal strength along the whole cut. These signal variations were measured by the parameter $\Delta V\%$ as defined in chapter 4. In the first one third of the cut, the signal varied greatly in strength, i.e. $\Delta V\% \approx 100\%$ due to the variations in kerf width and in dross blocking effect. The rough surface may also cause some signal variations. The middle part was not cut through and thus similar to a weld. Holes, cracks and depth variations of the cut were responsible for the variations in the signal strength, since they all affected the magnitude of the back reflected energy. The signal variation, $\Delta V\%$, was also about 100%. The signal of the last part varied mainly due to the clinging dross effect. Since the cut kerf of this part was irregularly blocked by clinging dross particles, the back reflections varied accordingly leading to variations in the detected signal. However, the scale of this signal variation was smaller ($\Delta V\% \approx 70\%$) compared with the previous cut sections possibly due to the smaller clinging dross size and the less number of clinging dross particles (classified as grade C).

It is also observed that the overall signal strength of the three parts were different. The signals of first and middle parts had higher values (approximately 100 mV), while the signals of the last part had lower value (approximately 70 mV). This can be explained by the kerf width effect and dross effect. The first part was relatively narrow, while the middle part had too much dross (not fully penetrating, in fact). Both of these led to stronger back reflections and thus stronger signal strength.

(ii). Signals from cuts with too much dross:

Figure 5 -14 shows a set of signals of cuts with too much clinging dross. They were obtained at different cutting speeds and gas flowrates as shown on the graph. The summary of the cut quality is shown in table 5-5.

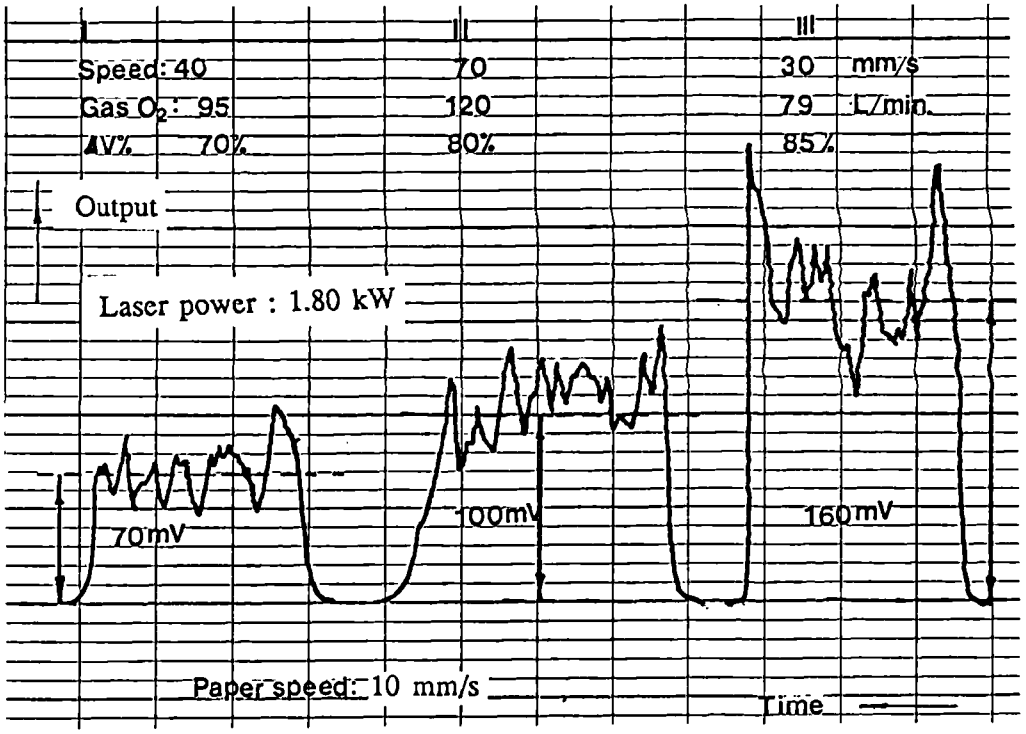


Fig. 5 -14. Signals with too much dross.

Table 5 -5. Cut quality assessment of cuts with too much dross

Sample	Kerf width	HAZ width	Dross grade	Roughness grade	Comments
I	0.66	2.50	D	smooth	one-sided dross and HAZ
II	0.62	3.50	D	medium	One-sided dross (bigger size than I)
III	0.70	4.00	D^+		majority of cut was blocked by dross (not separate)

It is clearly seen from the graph that there were large variations in signal strength for each cut. They were calculated as 70%, 80% and 85%

respectively in the order of the cut number. These variations were mainly due to the dross effect but may also be affected by roughness effect. Where the kerf was blocked the signal was strong, while where the cut was through the signal was weak. Thus the signal varied greatly with the grade of dross adhesion. Comparing cut I and II, the dross grade was similar but cut II had a rougher surface and the bigger dross size which possibly caused the wider HAZ. The signal variations of cut II were thus observed bigger than those of cut I. The overall signal strength was also different due to the combined effects of the dross grade and kerf width and varied in a similar way as those shown in Fig. 5 -7.

(iii). Signals from good cuts: Figure 5 -8 shows the signals for two good cuts. Compared with the above-discussed signals, these two signals had smaller variations due to more regular kerf width and smoother surface. The overall signal RMS values were also significantly lower with 40 mV and 50 mV respectively.

To sum up the above results, it can be concluded that the acoustic signals detected by the transducer P_1 did contain information about the cut quality. The detection unit has the further advantages of being independent of the cutting direction and non-interruptive of the beam. The following points can be drawn based on this study:

a). Good cut: the overall RMS $\approx$ 50 mV or less and $\Delta V\% \approx 50\%$;

b). Poor cut and cuts with too much dross: $\Delta V\% \approx 70\%$ or the overall RMS $\approx$ 70 mV or above.

5.4.2.2. Signals detected by P_2

As discussed before, the transducer P_2 responded to many things. The relationship between signal variations, signal strength and cut quality was thus rather difficult to observe. Figure 5 -15 shows the signals recorded at the same time as those shown in Fig. 5 -14. Although cut III was the worst cut among these three, it did not show a stronger signal (contrary to the signal shown in Fig. 5 -14). The other two signals had also no direct correlations with the cut quality. This was possibly due to the gas stream impact which affected the signal strength in two different ways as

mentioned earlier. On the one hand, increasing the gas flowrate increased the gas stream impact and thus the signal strength. On the other hand, increasing the gas flowrate also reduced the number of clinging dross particles (cut quality improved), which reduced the gas impact again. In other words, the signal strength was not directly related to the cut quality.

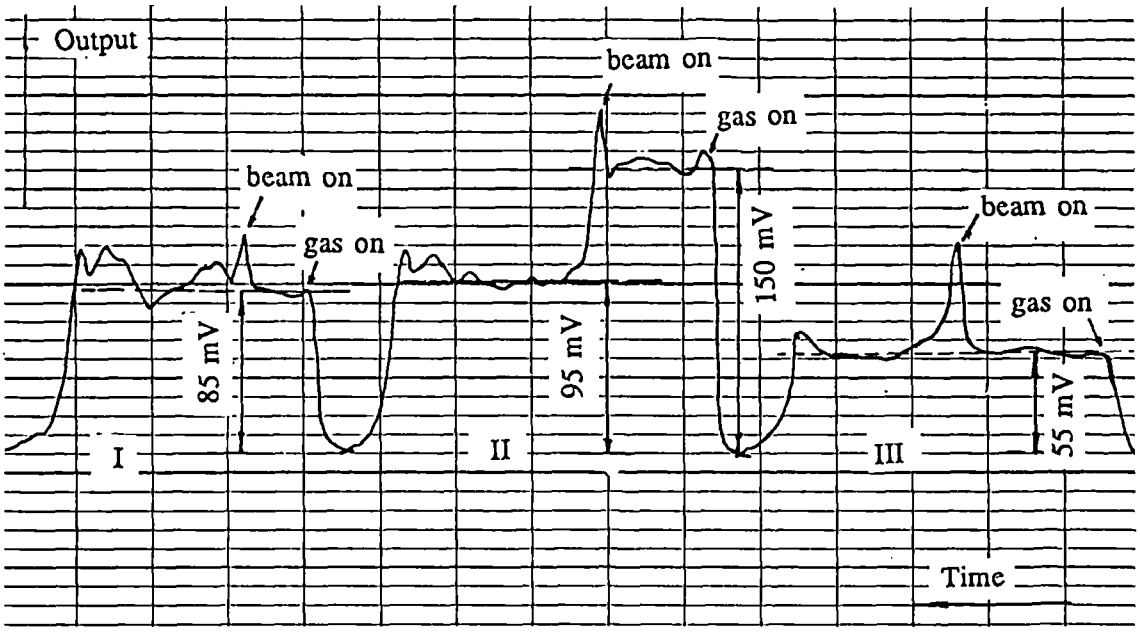


Fig. 5 -15. Signals with too much dross adhesion (P_2).

The extent of the gas stream impact on the overall signal strength can be seen from Fig. 5 -15, where the gas stream caused a strong signal response before the cutting started. The higher the gas flowrate the stronger the signal. This gas effect was however complicated during the processing, since the gas stream reacted with the melt, blew the melt out of the cut kerf and simply past through the kerf. To get a clearer concept of the gas stream impact, the following calculations can be performed.

If the kerf width is represented by ' w ' and the gas jet diameter on workpiece is ' b ', the signal strength may thus be represented by

$$I_S = \left(\frac{b - w}{b}\right) I_g \qquad (5\text{-}33)$$

where I_s is the expected signal strength which could be represented by the RMS value (mV), while I_g is the signal strength when the kerf width is zero. The latter is proportional to the dynamic pressure which is given as

$\rho u^2/2$, where ρ is the gas density and u the gas flow velocity at the workpiece surface. Within the potential jet region, which is usually defined to be smaller than 5d (d = diameter of the nozzle), the gas velocity, u , is approximately given as

$$u = u_{exit} \tag{5-34}$$

where u_{exit} is the gas flow velocity at the nozzle exit. The value of u_{exit} is determined by the nozzle diameter and the gas flowrate, F*, as below:

$$u_{exit} = \frac{4F^*}{\pi d^2} \tag{5-35}$$

The jet diameter on the workpiece, b , can be approximately given as

$$\frac{b}{2} = \frac{d}{2} + l\tan(\alpha) \tag{5-36}$$

where l is the nozzle standoff distance to the workpiece and α is defined as the gas stream expanding angle out of the jet and shown in Fig. 5 -16.

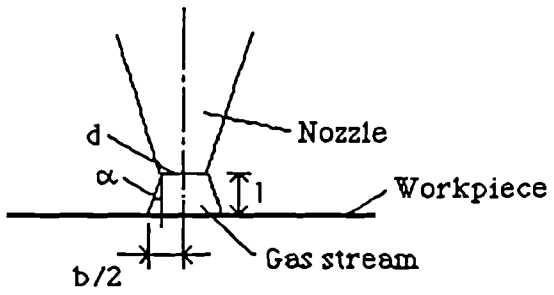


Fig. 5 -16. The angle of the flowing gas stream from the nozzle exit.

The value of α for free jet of turbulence flow is about 7^0 [207]. Therefore, the equation (5 -36) becomes

$$b = d + 0.25 \times l \tag{5-37}$$

The signal strength, I_s , can thus be expected from Eq. (5 -33) as

$$I_S = \left(\frac{d + 0.25 \times l - w}{d + 0.25 \times l}\right) A' \rho \frac{1}{2} \frac{16F^{*2}}{\pi^2 d^4} \tag{5-38}$$

where A' is a constant with the unit of $(mV)\cdot s^2\cdot m/kg$. Given d $=1.6 \times 10^{-3}$ (m); l $= 0.8 \times 10^{-3}$ (m) and $\rho = 1.301 \times 10^{-3}$ (kg/m^3) for oxygen, the equation (5 -38) is developed as:

$$I_S = A'' \left(\frac{1.8 \times 10^{-3} - w}{1.8 \times 10^{-3}}\right) F^{*2} \qquad (5\text{–}39)$$

where A" = A' x 1.6×10^8 $(mV\cdot s^2/ m^6)$.

Before the laser beam is switched on, i.e. w = 0, the value of A" can be calculated from Eqn.(5 -39) and tabulated as in Table 5 -6 shown below. It is seen that A" is approximately constant at different gas flowrates (an average of 3.5×10^7 was taken for the following calculation) therefore the expected signal strength during the process can be worked out from Eqn. (5 -39) and tabulated as in Table 5 -7.

Table 5 -6. Determination of the constant A"

Gas flowrate (L/min.)	Gas flowrate (m^3/s)	I_S (experimental results from Fig. 5 -15) (mV)	A" ($mV\cdot s^2 / m^6$)
79	1.3×10^{-3}	55 ± 5	$(3.3 \pm 0.3) \times 10^7$
95	1.6×10^{-3}	85 ± 5	$(3.3 \pm 0.2) \times 10^7$
120	2.0×10^{-3}	150 ± 10	$(3.8 \pm 0.3) \times 10^7$

Table 5 -7. Expected signal strength and dross blocking effect

Kerf width w (m)	I_{se} (mV) (experimental)	Gas flowrate F^* (m^3/s)	I_{sc} (mV) (calculated)	$\frac{I_{se} - I_{sc}}{I_{se}} \times 100\%$ (dross blocking effect)
0.70×10^{-3}	55	1.3×10^{-3}	36	35
0.62×10^{-3}	95	2.0×10^{-3}	92	3
0.66×10^{-3}	85	1.6×10^{-3}	57	33

It is seen that the calculated signal strength is a function of the kerf

width and the gas flowrate. Increasing the gas flowrate or decreasing the kerf width would increase the signal strength. Since the calculated values of the signal strength, I_{sc}, were based on the cuts free of dross, they were lower than the experimental values. The difference between them was mainly caused by the clinging dross particles, which could block a portion of the gas stream passing through the kerf and thus increase the gas impact. The calculated dross blocking effect decreases with increasing the gas flowrate due to the more efficient removal of the melt at a higher gas flowrate.

It is also seen from Table 5 -7 that by increasing the gas flowrate would have two contradictory effects on the signal strength. On the one hand, the signal strength could be increased due to the increased gas stream impact. On the other hand, the signal strength could also be decreased due to the reduced 'dross blocking effect'. Therefore, in the real cutting process, these three effects, i.e. kerf width, dross particles and the gas flowrate are combined together, which would make the signal analysis complicated. For example, the overall RMS values of the signals of the cuts I & II in Fig. 5 -15 were similar although the gas flowrates were different. Therefore, the signal detected by the transducer P_2 did not show direct correlation with the cut quality and would thus be difficult to be used as a control signal.

5.5. Chapter Summary

Two different arrangements using acoustic methods for in-process quality monitoring of laser cutting process were studied. Both methods employed piezoelectric transducers to record acoustic signals induced during laser cutting process. The first method positioned the piezoelectric transducer on the rear of the final mirror to detect the back reflections of the laser beam. This detection system provided reliable and fast information on cut quality and is independent of cutting direction. Therefore, there is a possibility for making it into a real-time quality inspection system.

The second method positioned the transducer close to the cutting nozzle to monitor the gas stream impact and the process-generated

acoustic waves. The signals were noisy and thus difficult to be related to the cut quality.

CHAPTER SIX

THERMAL METHOD FOR IN-PROCESS MONITORING OF LASER CUTTING

6.1. Introduction and Background

It has been demonstrated in chapter four that the light intensity emitted from the cut front as well as from the sparks had a strong correlation with the cut quality, i.e. steady signals were obtained from good cuts, while unsteady signals with large variations in light intensity were observed from poor cuts. Since the light emission from the cut front is proportional to the fourth power of its temperature for a given surface emissivity (Stefan-Boltzmann law), the cut front temperature is likely to be a sensitive indicator of the cut quality. In fact, as already discussed in previous chapters, the cut front temperature is controlled by the process parameters, e.g. the laser power, the cutting speed, the gas flowrate and gas composition. These parameters may change their values during the cutting process and thus cause variations in the cut front temperature. The temperature changes would further lead to the variation in cut quality. Therefore, in-process quality analysis can possibly be achieved by measuring the temperature changes of the cut front.

In laser cutting, the nozzle is usually positioned close to the workpiece so that the gas jet can blow the molten dross particles out of the cut kerf. Therefore, the nozzle temperature is directly affected by the state of the processing. In particular, the radiant heat from the cut front and the back reflected power are the main heat sources affecting the nozzle temperature.

The radiant heat from the cut front is governed by three parameters, i.e. the radiant area, the cut front emissivity and the temperature. The radiant area is related to the kerf width, which is mainly controlled by the cutting speed for a given laser power and gas flowrate as discussed in previous chapters (the assistant gas is assumed to be oxygen here and in the following discussion). Increasing the cutting speed would decrease

the kerf width and thus reduce the radiant area. The cut front emissivity (absorptivity) increases with the beam incidence angle (Fig. 1-10) and with the cut front temperature. The cut front temperature is again affected by the cutting speed. Increasing the cutting speed would cause more of the beam to strike the cut front thus raising the cut front temperature. It is thus seen that increasing the cutting speed would have two contradictory effects on the radiant heat: reducing the radiant area while increasing the cut front temperature. The latter effect would be more important at high cutting speeds, since then the laser beam traverse speed is dominant in controlling the heat input. The former effect would be more important at slow cutting speeds, since then the oxidation reaction is dominant in determining the heat input.

The radiant heat comes also from the clinging dross, HAZ and the process-generated plasma. Obviously, the quantity and size of the clinging dross particles and the extent of HAZ determine the amount of their radiant energy. In other words, the cut quality parameters affect the radiant heat during the processing. The heating from the plasma is likely to be small in laser cutting. Firstly because the majority of the material is removed as molten dross particles due to the strong gas jet, only a small portion of the material is evaporated which forms plasma. Secondly, any plasma is quickly blown away by the gas jet.

The back reflected power is mainly from the flying sparks and from the back reflected laser beam. The heating from the flying sparks is due to the direct interaction between the flying sparks and the nozzle. Since these sparks are usually ejected in some preferred directions depending on the cut quality, this form of direct heating could be related to the cut quality. For example, the molten dross is usually ejected downward from the cut kerf instead of flying upwards when a good cut is achieved. While for a poor cut, such as a cut with much clinging dross or even not fully penetrating, some of the molten dross would fly upwards contacting the nozzle. The back-reflected laser beam off the cut faces and dross particles may strike the nozzle and raise the nozzle temperature due to the beam/nozzle interaction. These back reflections are mainly controlled by the cut face reflectivity and shape, which are related to the surface

roughness, and affected by the clinging dross and the kerf width, which may have a blocking effect for the beam passing through the kerf. This blocking effect is small if there is no dross adhesion and the kerf width is wide. Therefore, the back reflected power is also related to the cut quality parameters.

From the above discussions, it may be stated that the cutting nozzle temperature is a function of the process parameters and the cut quality parameters. The nozzle temperature variations during the processing could thus indicate the state of the cut front.

The objectives of this chapter are therefore, first to find out factors affecting the nozzle temperature and secondly to correlate the nozzle temperature with the cutting performance.

6.2. Experimental Set-up

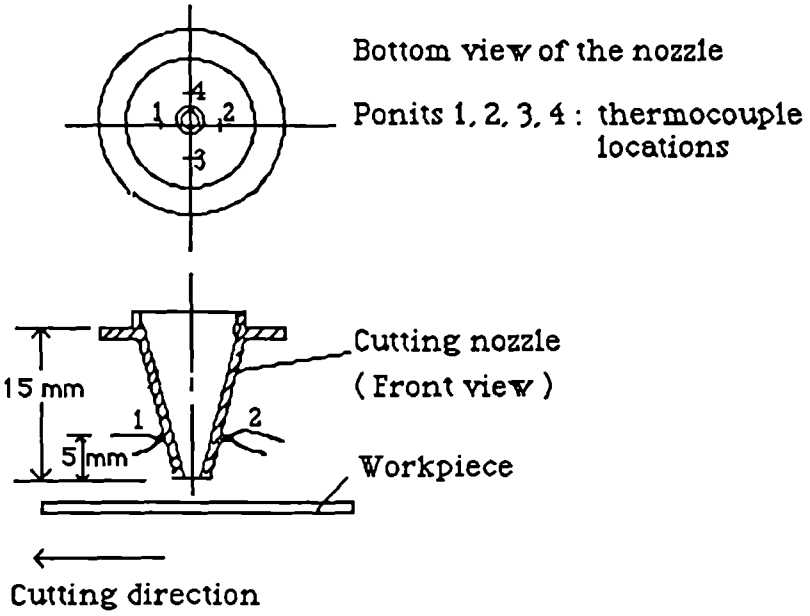


Fig. 6 -1. Construction of the hot nozzle.

The experimental set-up was the same as that shown in Fig. 2 -16. The laser used was the 2 kW CO_2 Control Laser. The laser beam was focussed by

a ZnSe lens with 125 mm focal length, and passed through a convergent cutting nozzle with an orifice diameter of 1.5 mm. The assistant gas was oxygen. The workpiece material was 3.0 mm thick mild steel.

The type K thermocouples (the same as those used in chapter two) were chosen as the nozzle temperature detectors and fixed onto the nozzle at different locations (Fig. 6 -1).

6.3. Results and Discussion

6.3.1. Causes for the temperature signals

According to the construction of the detection unit as described above, the thermocouple would indicate the nozzle temperature changes due to the radiant heat, the reflected power or beam clipping. The indication of the beam clipping has been previously discussed in chapter two. The effect of the radiant heat and the back reflected power on the nozzle temperature can be seen in the following experiment as shown in Fig. 6 -2. In this arrangement an aperture (a hole of 10 mm in diameter in a shiny steel plate) was positioned underneath the nozzle to reduce the amount of heat from both the back reflected power and the radiant heat. The distance between the nozzle and the workpiece was set as 5 mm (out of focus) to prevent it from being drilled.

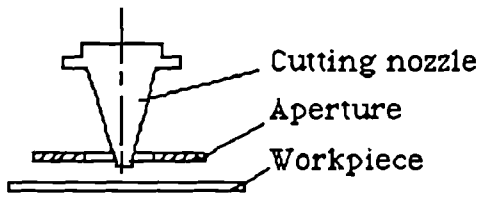


Fig. 6 -2. Experimental set-up for testing the back-reflected power.

Experiments were performed by firing the laser beam onto a piece of mild steel plate with and without the aperture respectively. The laser power and the beam "on" time were kept the same as 1.60 kW and 8 seconds respectively. The workpiece was stationary. The temperature signals recorded by a chart recorder were shown in Fig. 6- 3.

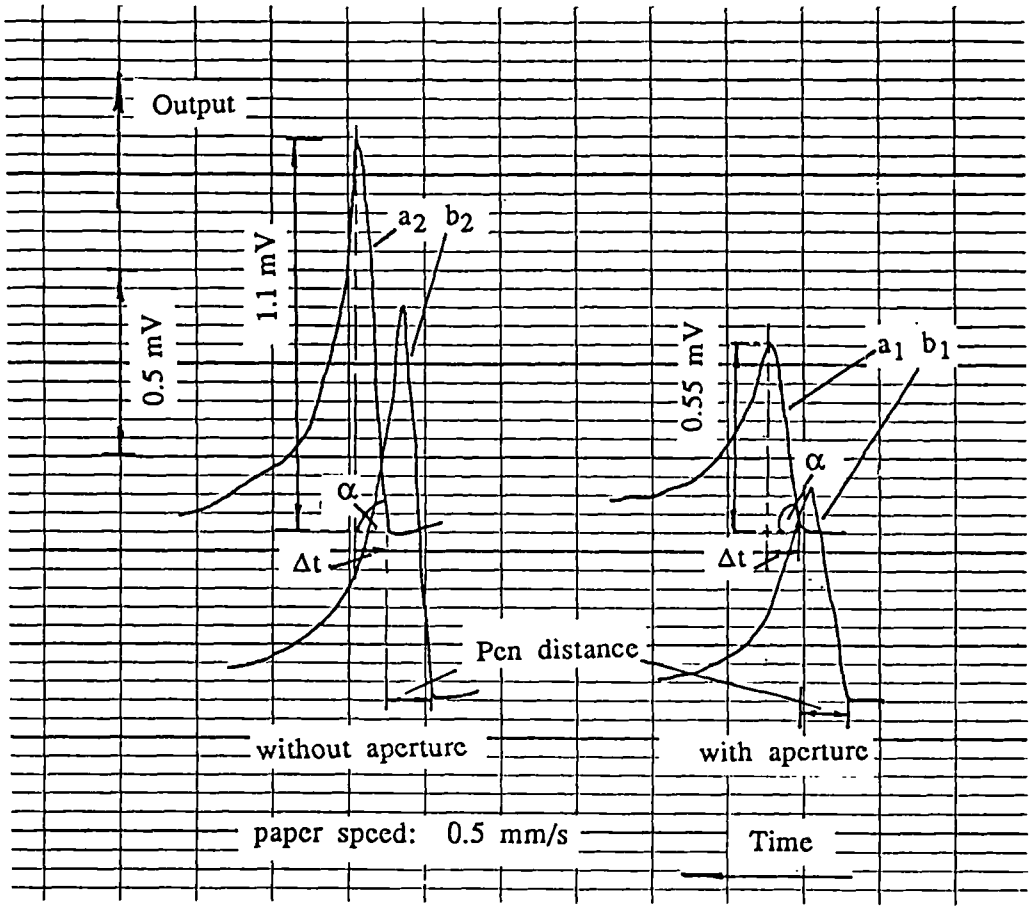


Fig. 6 -3. Temperature signals with and without the aperture.

The signals a_1 and a_2 were recorded by the thermocouple at location 1, while the signals b_1 and b_2 were simultaneously recorded at location 2. The time difference between the signals a_1 and b_1 (or a_2 and b_2) was due to the different starting positions of the two pens (pen distance). It is seen that the signal obtained without the aperture protection was nearly twice as strong as that with the aperture protection, i.e. the peak response values with and without the aperture were 0.55 mV and 1.1 mV respectively. This can be better illustrated by the rate of the temperature rise, which is approximately given by the gradient of the signal, i.e.

$$\tan\alpha = \frac{\Delta V}{\Delta t} \tag{6-1}$$

where

$\tan\alpha$ = the gradient (mV/s);

ΔV = the thermocouple output (mV);

Δt = the beam 'on' time (s).

For the signal without the aperture protection, the rate of the temperature change was calculated as $\tan\alpha$ = 1.1/8 = 0.14 (mV/s). Similarly, for the signal with the aperture protection, the rate of the temperature change was calculated as 0.55/8 =0.069 (mV/s). This clarifies that the temperature signal was caused by the combined effect of the radiant heat and back reflected power, and was sensitive to the amount of total heating.

It is also seen that the responses from the two thermocouples were similar. The reasons are: firstly, the workpiece was stationary and may thus give back reflections in all directions; secondly, the two thermocouples were symmetrically positioned on either side of the nozzle thus responding to the conducted heat from the nozzle with the same time scale. The responses from the two thermocouples could be different during the cutting process, since the back reflections may travel in some preferred angles depending on the cut quality.

6.3.2. Signal variations with cut quality

To investigate the possible correlation between the cut quality and the nozzle temperature signals detected by the thermocouples, various cut edge appearances with corresponding signals are needed. These were obtained by two ways: changing the nozzle/beam alignment or changing the preset parameters, i.e. the cutting speed and gas flowrate.

6.3.2.1. Signal variations due to the nozzle/beam misalignment

In this study, the nozzle position was moved relative to the beam while keeping the other parameters unchanged so that different cut edge appearances was obtained. Two thermocouples were used at one time and fixed at position 1 & 2 and 3 & 4 respectively as described in Fig. 6 -1.

The experiment was performed at the laser power of 1.63 kW, the cutting speed of 63 mm/s and the gas flowrate at 65 L/min.. The nozzle standoff distance to the workpiece was 1.0 mm. The cut edge quality was visually examined according to the quantity of the clinging dross particles, cut face roughness and variations in kerf width and the extent

of HAZ. The chart recorder scale was set differently, since one thermocouple was equipped with an thermocouple amplifier while the other was not (scale is marked on each figure).

(i). Signals from thermocouples at locations 1 and 2

a). Good cut: Figure 6 -4 shows two signals obtained for a good cut. The signal 'a' was recorded by the thermocouple at position 1, while the signal 'b' was from the thermocouple at location 2. The time difference between the two signals was again due to the different starting positions of the pens (this pen distance was different from that of Fig. 6 -3, since different pens were used). The cut face was smooth with regular striation pattern along the whole cut (Fig. 6 -5). The cut had constant kerf width and was free of dross.

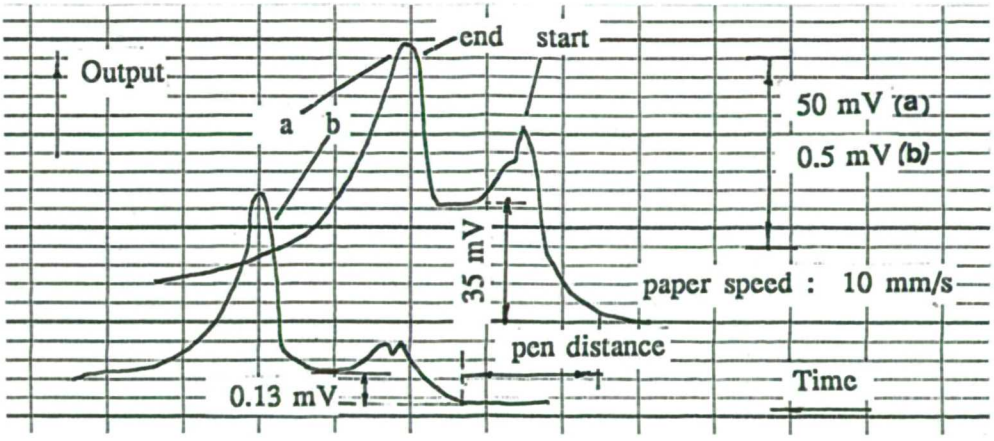


Fig. 6 -4. Signals for a good cut.

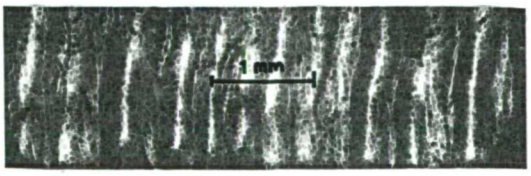


Fig. 6 -5. Cut face striation pattern for the good cut.

It is seen that each signal had two peak responses at the start and the end. The start peak was due to the burst of sparks at the formation of the initial "keyhole". The end peak was due to an edge effect. Namely, the heat tended to build up at the end of the cut due to the poorer conductivity of the air and thus gave more radiation. Some of the molten dross particles

may fly clear of the workpiece at the end of the cut contacting the nozzle and thus led to strong response from the thermocouple. If the beam was switched off before reaching the edge of the workpiece (a terminated cut), the end peak was not obvious (Fig. 6 -6). This supported the explanation of the above -discussed "edge effect". However, neither the start nor the end peak was of importance to the process cut quality. They will not be further discussed in the following text.

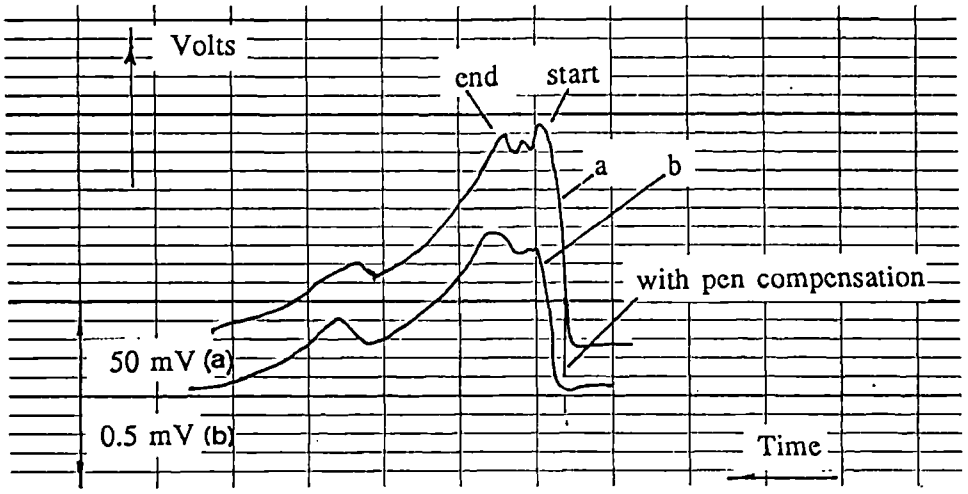


Fig. 6 -6. Signals from a terminated cut.

After the first peak response, the signals dropped to a lower level and levelled off. This can be explained by the changing reflected power as below. During the processing, the laser beam could behave in three different ways simultaneously. Firstly, a large portion of the beam interacted with the workpiece to generate heat, the majority of which was used to melt the material and give radiant heat. Secondly, a fraction of the beam was reflected off the cut face part of which may travel back to the laser cavity to disturb the beam mode - a phenomenon known as the optical feedback (chapter 5). Thirdly, the rest of the beam simply passed straight through the cut kerf. Since there was no clinging dross at the cut edge due to the sufficient gas drag effect, the dross blocking effect for the beam passing through the kerf was minimal. The back reflected beam power was thus low causing weak response from the thermocouples. Since the majority of the molten dross particles were ejected downwards for a good cut, the heating from the flying sparks was also minimised. Therefore, the signal dropped during the processing. The constant kerf

width and smooth surface contributed to the constant back reflected power and relatively stable radiant heat from the cut front and thus were responsible for the level-off of the signal.

The signal shape recorded by the two thermocouples was very similar, which indicated that the heating effect due to the back reflected power and the radiant heat was similar in either direction (without consideration of the start and the end peak responses). Although the overall signal strength of the two signals was different (the signal 'a' was from the output of the thermocouple amplifier described in chapter two, while the signal 'b' was directly from the thermocouple), the temperature indicated by the two thermocouples were however expected to be similar as calculated below. For the thermocouple 1 with the amplifier, the detected temperature change, ΔT, is given by

$$\Delta T = \frac{\Delta V}{\Delta S} \qquad (6\text{-}2)$$

where ΔV is the thermocouple amplifier output, i.e. the signal strength (mV); ΔS is sensitivity of the amplifier and equal to 10 $mV/^0C$ (chapter two). The signal strength, ΔV, was about 35 mV, the corresponding temperature change, ΔT, was thus calculated to be 3.5 ^0C.

The temperature detected by the thermocouple 2 can also be calculated. Since the sensitivity of the type K thermocouple was 0.04 $mV/^0C$ (chapter two) and the signal strength, ΔV, was approximately 0.13 mV, the temperature change, ΔT, was thus calculated to be around 3.3 ^0C. Therefore the temperature change detected by these two thermocouples was approximately the same.

b). Cuts with dross adhesion: Figure 6 -7 shows the surface striation pattern and dross adhesion of the two cuts. It is seen that there were some clinging dross particles at the bottom edges of both cuts. But the amount of dross adhesion for cut I was slightly more. The cut faces had quite regular striation pattern. The detected signals for the two cuts are shown in Fig.6-8.

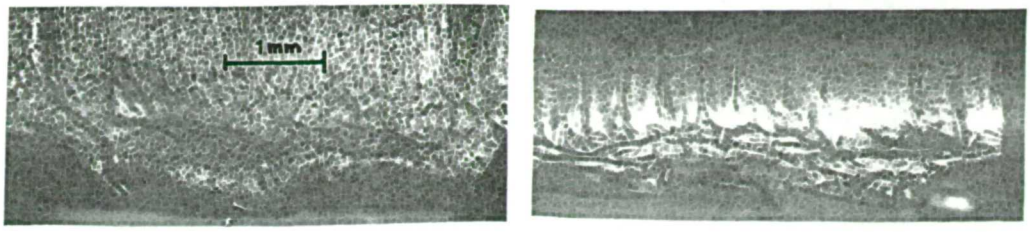


Fig. 6 -7. Dross adhesion and surface striation pattern.

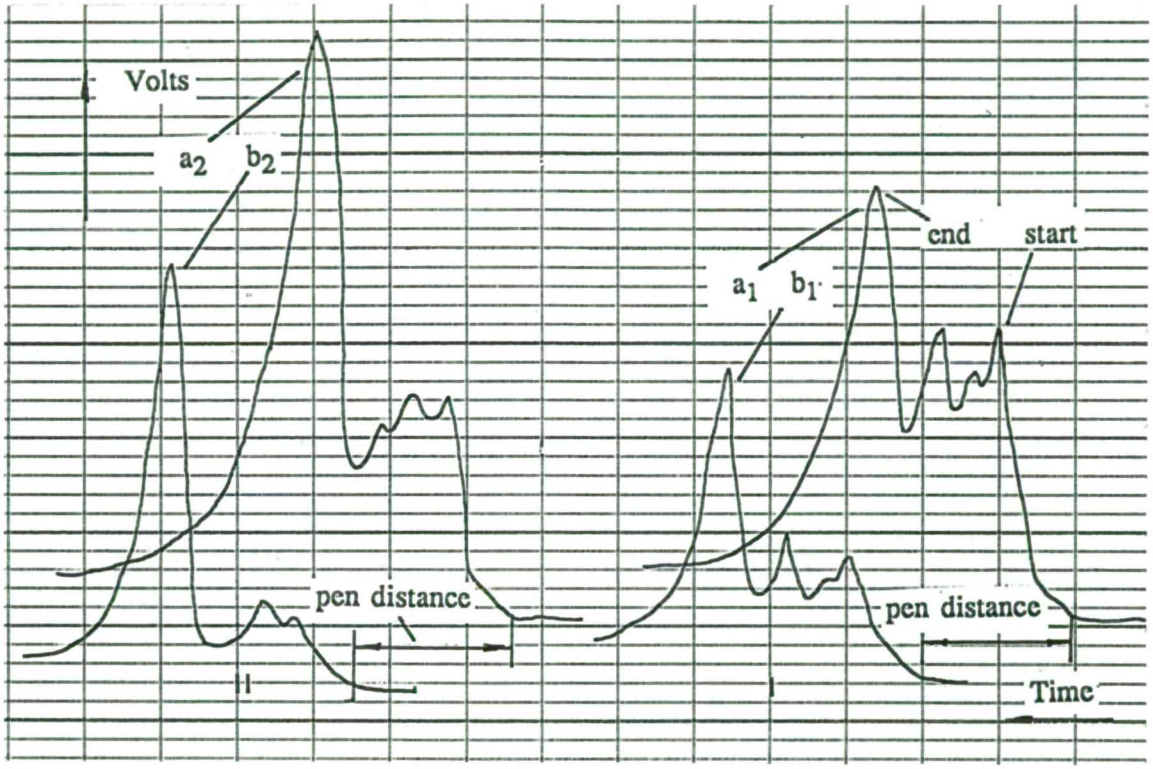


Fig. 6 -8. Signals for cuts with dross adhesion.

It is seen that there were some variations in signal strength (middle peaks) between the initial and the final peak responses. These middle peaks were due to the blocking effect of the clinging dross, which reflected more power upward heating the nozzle. These clinging dross particles also emitted heat as additional radiant sources. However, the number of the middle peaks were far fewer than the number of the clinging dross particles. This could raise two points. Firstly, the middle peak was likely due to the combined effect of several dross particles instead of a single one. Secondly, these middle peaks could not be correlated to the dross location on the workpiece indicating the slow response of the detection system. The response time was determined by

the heat conduction time of the nozzle and the thermocouple response time. The former was calculated in chapter two to be around 0.1 s. The latter was given as approximately 0.1 s (chapter two). Therefore the response time of the detection unit was about 0.2 s, which could not match the transient changes of the melt pool.

It is also seen that the responses from the two thermocouples were basically the same. This similarity indicated that the nozzle was approximately equally heated at both of the thermocouple locations.

c). Cut with too much dross: Figure 6 -9 shows the signal obtained for the cut with too much dross on one side of the edge (Fig. 6 -10) possibly due to the gas jet and the beam misalignment.

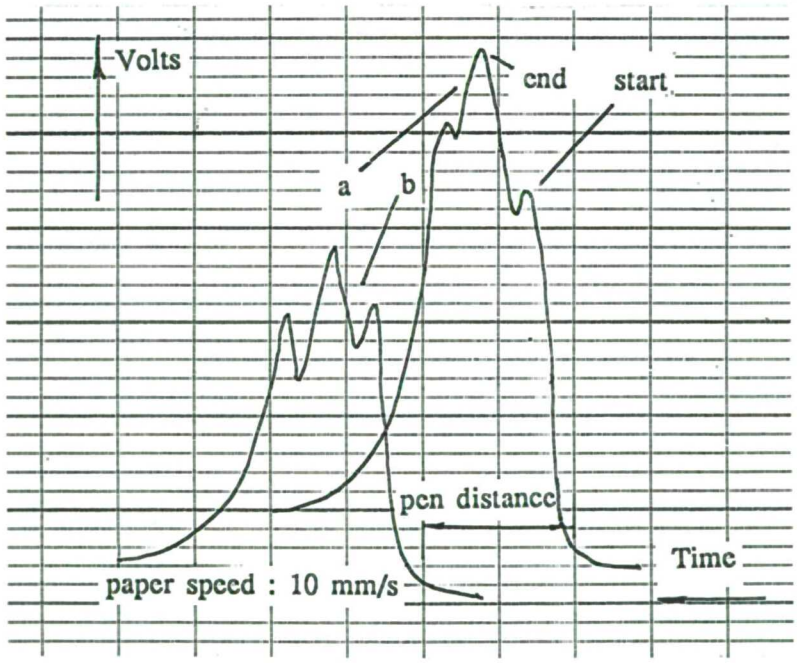


Fig. 6 -9. Signals for cut with too much dross.

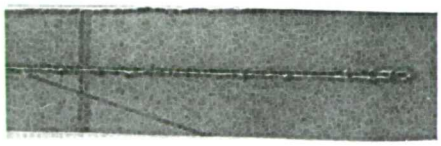


Fig. 6 -10. Dross adhesion on one side of the cut edge.

It is seen that both signals had similar shape as just discussed in b),

but the middle peaks were bigger. This was due to the larger quantity of the dross particles which caused a stronger blocking effect. These middle peaks could not be located against the clinging dross on the cut edge due to the slow response of the detection unit as discussed before.

Further movement of the nozzle position resulted in the beam clipping the nozzle, which as discussed in chapter two caused a strong signal (Fig.6-11).

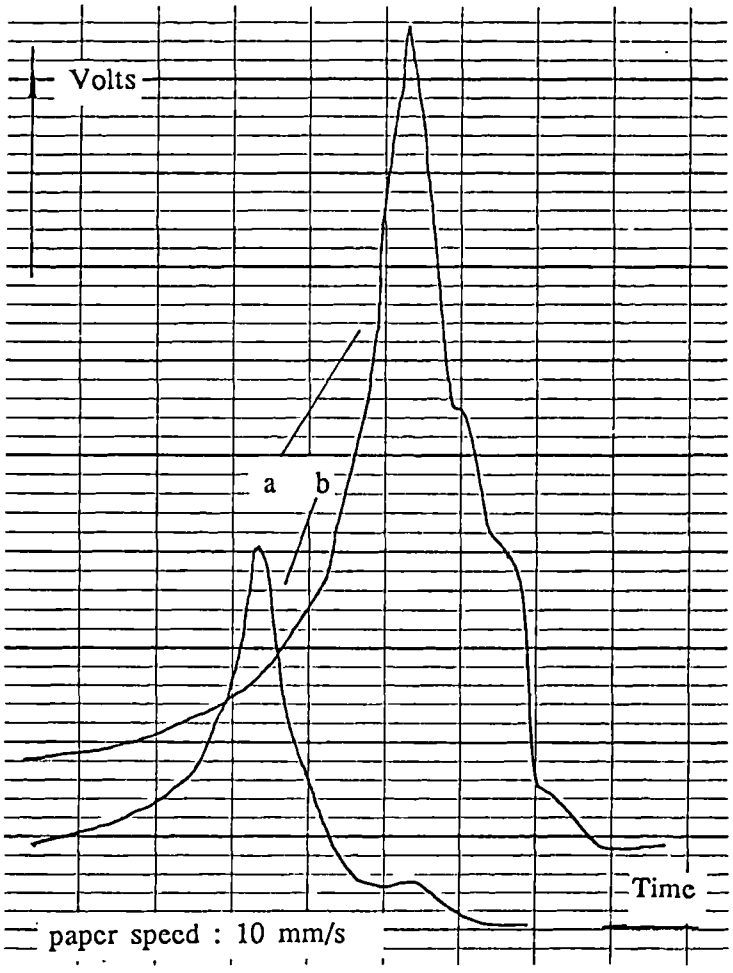


Fig. 6 -11. Signals when the nozzle clipped.

(ii). Signals from thermocouples at the location of 3 and 4

The following experiments were performed also by moving the nozzle while keeping the other parameters unchanged. The signals 'a' were recorded by the thermocouple 3 with the amplifier, while the signals 'b'

represented the response directly from the thermocouple at location 4.

a). Good cuts: Figure 6 -12 shows the signals for a cut with dross free , constant kerf width and smooth surface. It is seen that the two signals were basically the same due to the symmetrical position of the two thermocouples and due to the constant kerf width. The signals were also similar to those shown in Fig. 6 -4 having peak responses at the start and the end and weak responses during the processing.

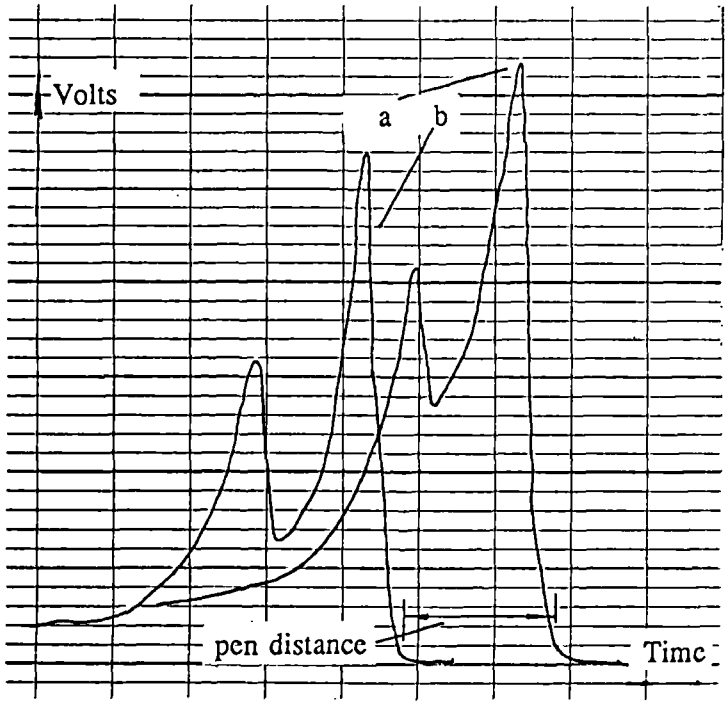


Fig. 6 -12. Signals recorded by the thermocouples at location 3 & 4 for a good cut.

b). Cut with dross adhesion on one side : Figure 6 -13 shows two signals for a cut with dross clinging on one side of the cut edge. It is seen that these signals were similar to those shown in Fig. 6 -9 having middle peak responses. But the number of the middle peaks could not be related against the clinging dross particles on the cut edges due again to the slow response time of the detection unit.

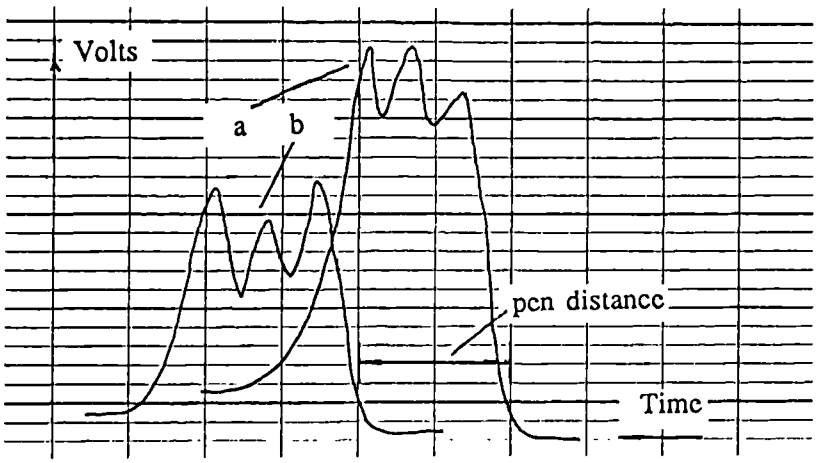


Fig. 6 -13. Signals for a cut with dross clinging on one-side of the cut edge.

In this cut, the clinging dross was observed on the same side as the thermocouple 4 (Fig. 6 -1), while little dross was observed on the side of thermocouple 3. However, the responses from the two thermocouples were similar. Theoretically, the responses were expected to be different, since the clinging dross was on one side of the cut edge, which reflected sparks and the beam in preferred directions. More radiant heat from the dross side was also expected. However, these phenomena could not be observed in this experiment, since the time constant of heat conduction of the nozzle was calculated to be in the same order of the thermocouple (chapter two). Therefore, the nozzle temperature would have become uniform by the time the thermocouple started to respond.

To sum up the above results and discussions, it is concluded that the thermocouple could not respond fast enough to indicate the transient temperature and thus could not give detailed information about the cut quality, e.g. the formation of the dross adhesion. It was also suggested that the thermocouple could not indicate the temperature difference at different locations. Therefore, only one thermocouple was used in the following experiments (the detected signals were thus at the same sensitivity).

6.3.2.2. Signal variations with process parameters

Since the cut quality was controlled by the cutting speed and the gas flowrate for a given laser power, various cut edges were obtained by changing these two parameters. The corresponding temperature signals

were recorded as follows.

(i). Signals at a wide range of cutting speed

The experiments were performed at the laser power of 1.65 kW and the gas flowrate of 93 L/min..

a). Good cut: Figure 6 -14 shows a set of signals for cuts with dross free, constant kerf width and smooth surface. These cuts were obtained at the cutting speeds of 33, 39 and 44 (mm/s) respectively. As can be seen from this graph, these three signals were similar in that they all had two obvious peak responses at the start and the end of each cut as discussed before. The signals dropped to a lower level once the cutting started due to the reduced reflected power and went up again near to the end of cut due to the edge effect.

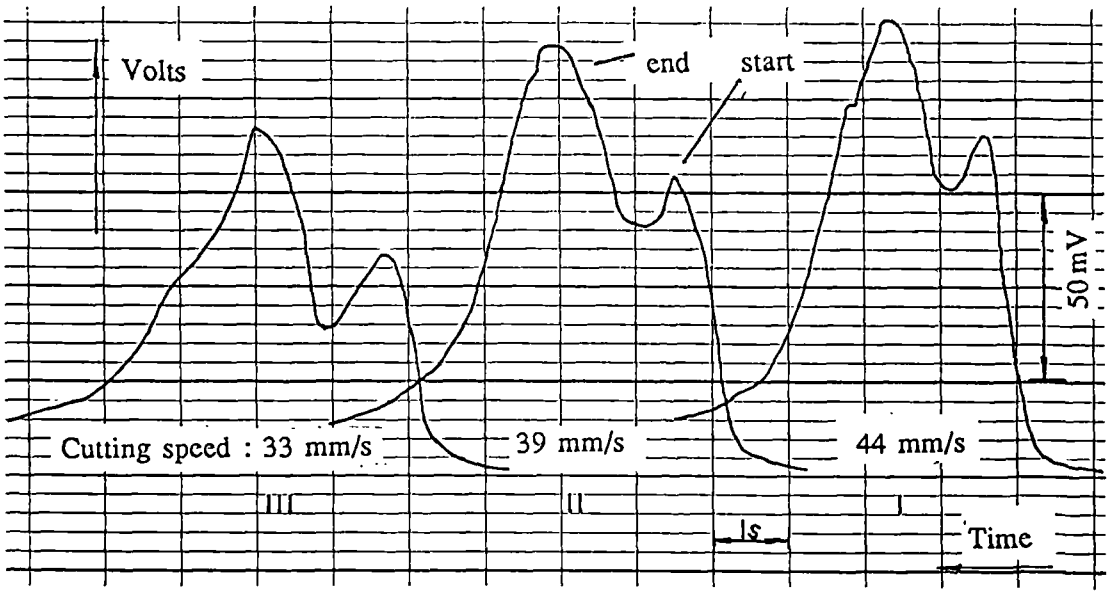


Fig. 6 -14. Signals at optimal cutting speeds.

b). Cut with clinging dross: Figure 6 -15 shows the signal obtained for a cut with dross adhesion. This cut was obtained at the speed of 51 mm/s. It is seen that the signal had some middle peaks possibly indicating the existence of the clinging dross particles. But they could not be located against the dross particles on the cut edge as before.

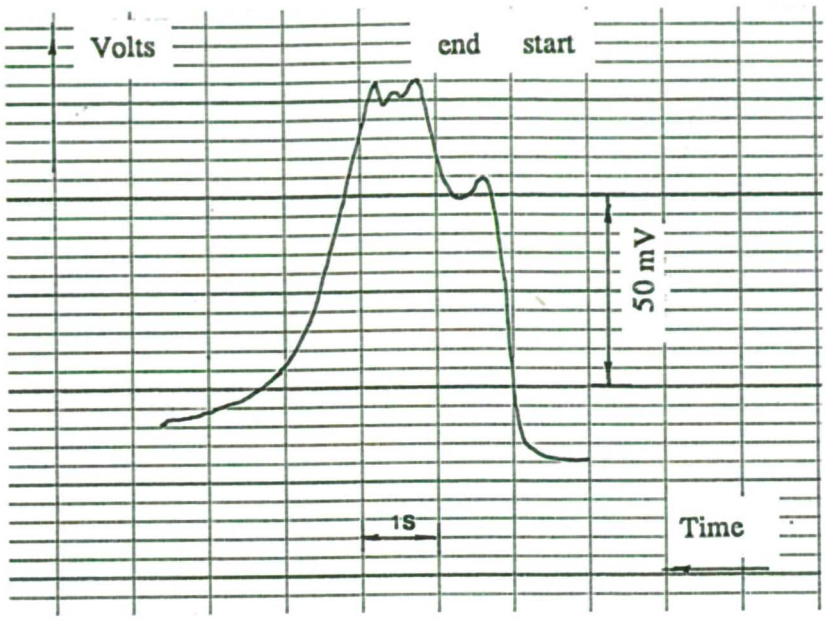


Fig. 6 -15. Signals at the cutting speed of 51 mm/s.

c). Rough cut: When the cutting speed was slow, a rough cut resulted as shown in Fig. 6 -16.

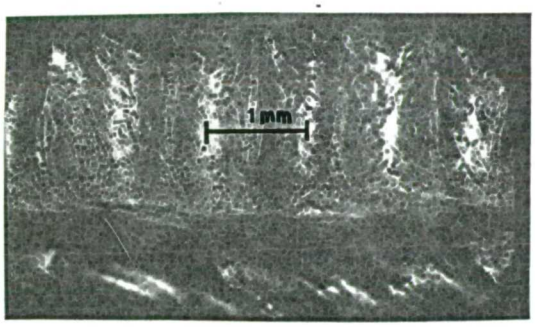


Fig. 6 -16. A rough cut.

It is seen that the cut had a coarse striation pattern and some clinging dross particles. The corresponding signal was recorded as Fig. 6 -17. The signal had some variations during the processing. In general, the radiant emission from the cut front was not stable at slow cutting speeds due to the dominant burning reaction as discussed in chapter four. This unstable emission led to variations in the radiant heat and thus in the signal strength. The rougher surface also caused varying amount of radiant heat and back reflected heat.

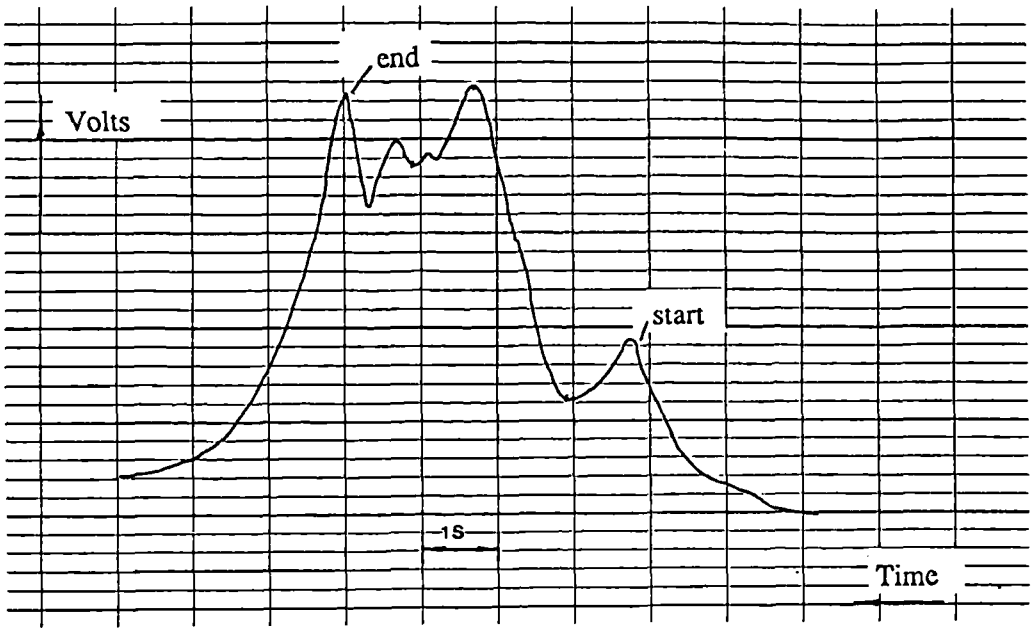


Fig. 6 -17. Signals at a slow cutting speed, 25 mm/s.

d). Not-through cut: When the cutting speed was too high, the assisted gas jet failed to blow the molten dross out of the cut kerf resulting in the cut failure. Since majority of the sparks were ejected upwards (the reflected power was thus increased) during the processing, the signal reached a high value as shown below in Fig. 6 -18.

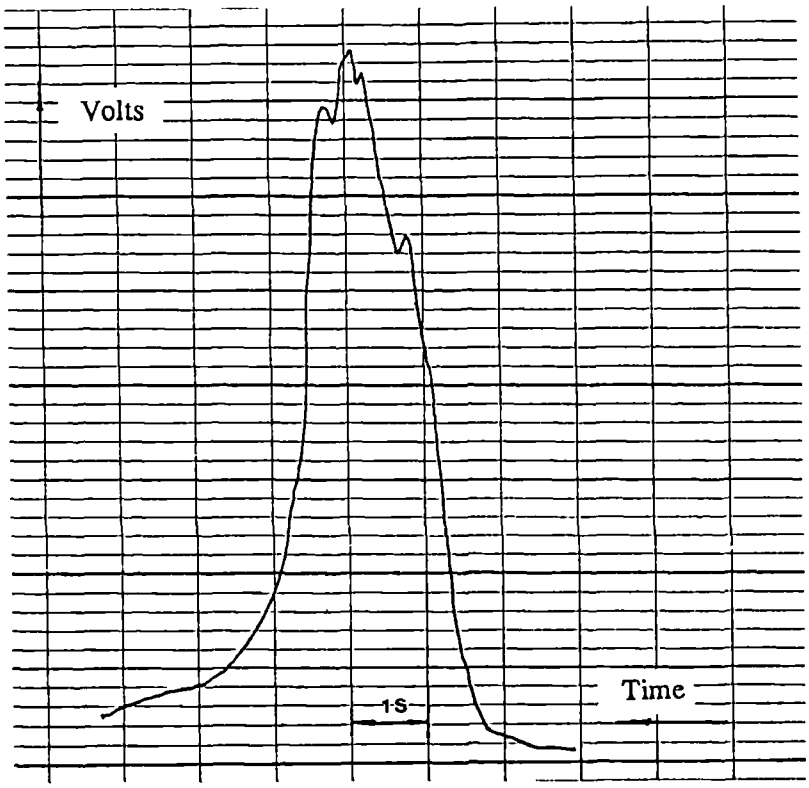


Fig. 6 -18. Cut at a high cutting speed, 75 mm/s.

(ii). Signals at different gas flowrates

In laser cutting, the cut quality, in particular the removal of the molten dross, is very much affected by the gas flowrate. Therefore, various cut edges were obtained at different gas flowrate. The following experiments were performed at the laser power of 1.75 kW and the cutting speed of 60 mm/s.

a). Signals at high gas flowrates:

Figure 6 -19 shows a signal obtained at the gas flowrate of 95 L/min.. The cut quality was good with no dross clinging. The signal was observed to be the same as before for a good cut, i.e. having two peak responses at the start and the end of each cut but no middle peaks.

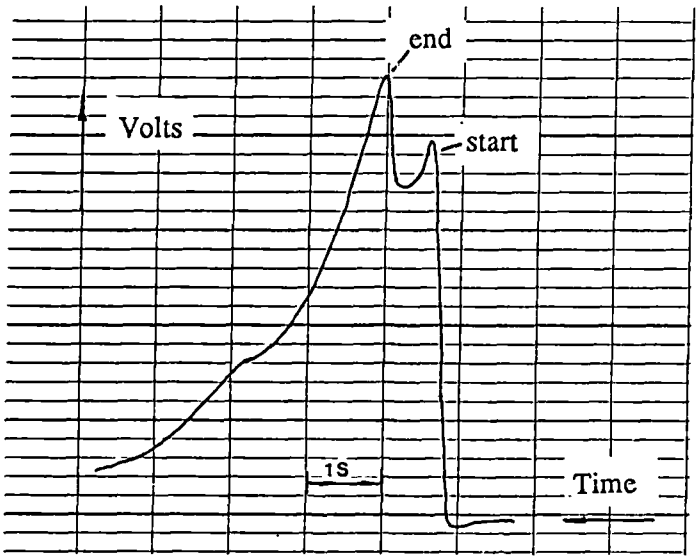


Fig. 6 -19. Signals at a high gas flowrate, 95 L/Min..

b). Signals at a low gas flowrate:

When the gas flowrate was low, the dross failed to clear resulting in the cutting failure. The recorded signal is shown in Fig. 6 -20, which had a single peak due to the massive back- reflected energy.

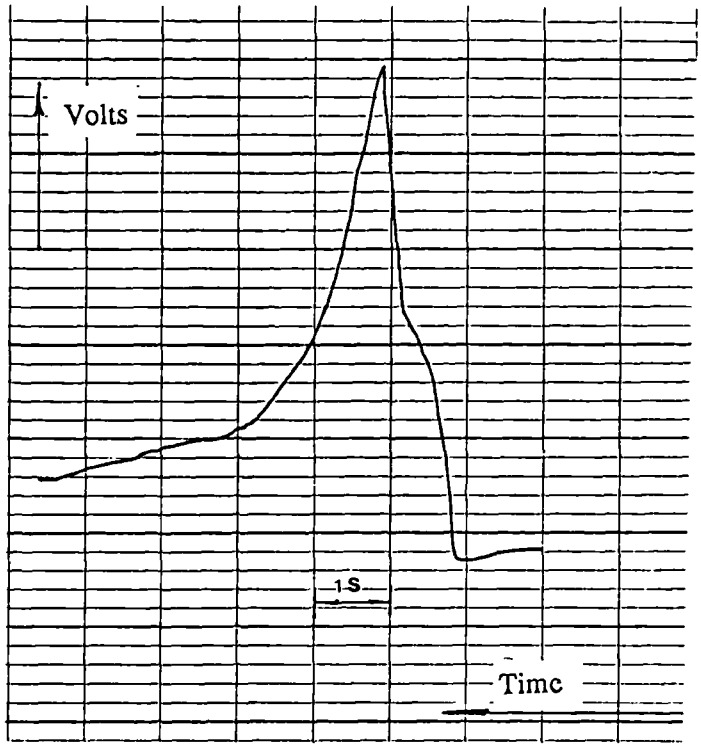


Fig. 6 -20. Signals at a low gas flowrate, 65 L/min..

6.3.3. Increasing the sensitivity of the detection unit

Attempts were made by putting the thermocouple close to the workpiece as shown in Fig. 6 -21, hoping that this would make the thermocouple respond quickly to the state of the processing.

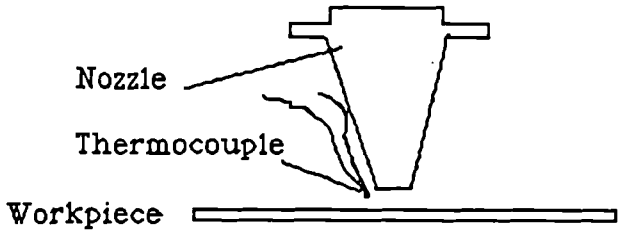


Fig. 6 -21. Experimental set-up for monitoring the plasma stability.

Unfortunately, the signals recorded were too noisy to be analysed. These noisy signals were possibly due to the vibration of the thermocouple itself due to the gas flow stream and showed no regularity. For example, under the same cutting conditions (the cut quality was similar), two different signals resulted as shown in Fig. 6 -22. Therefore, this attempt was not successful.

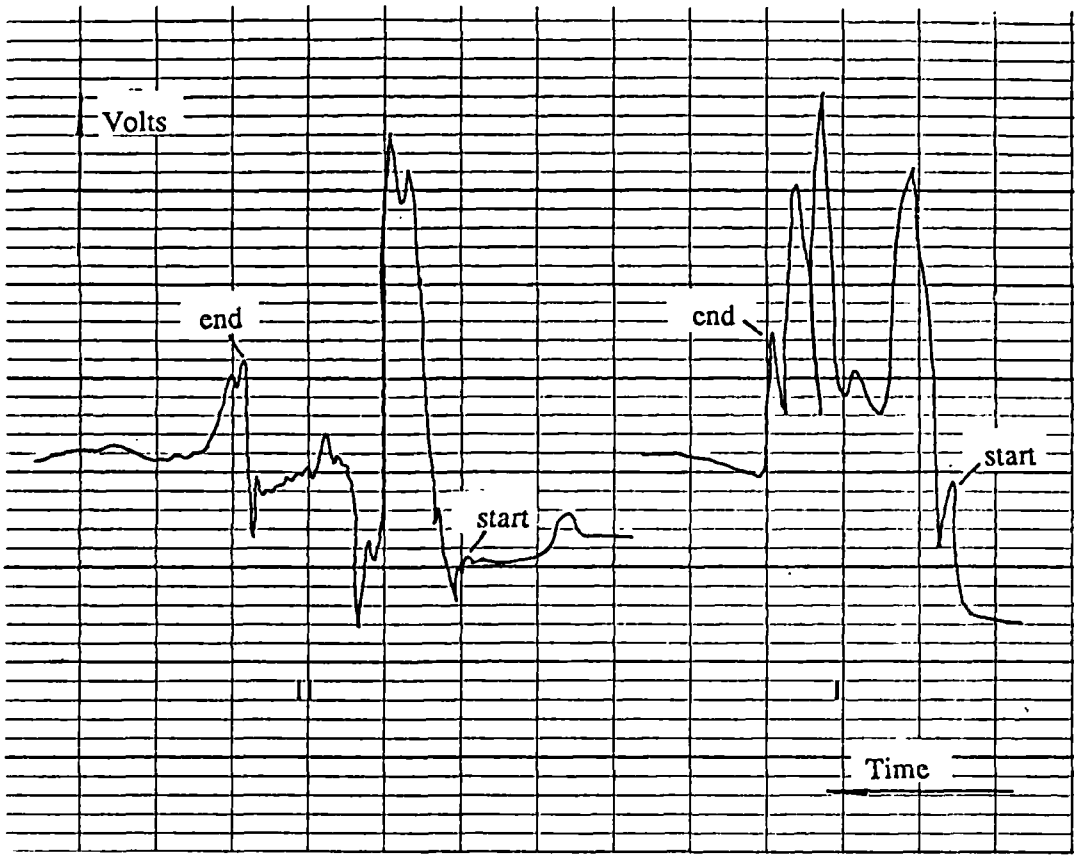


Fig. 6 -22. Signals obtained at the cutting speed of 40 mm/s, gas flowrate of 95 L/min..

6.4. Chapter Summary

Thermocouples were used to monitor the nozzle temperature during the cutting process. Different signals were obtained for various cut edge quality. For a good cut, the signal showed little variation in the signal strength. For a poor cut with dross adhesion, the signal showed some variation having middle peaks. For a not fully penetrating cut, the signal simply went up until the beam was switched off showing a single peak response. Therefore, the temperature signals contained some information about the cut quality. However, these signals did not contain detailed quality information due to the slow response of the detection unit, which could not catch the transient state of the cut front. Therefore, this method is not suitable for in-process monitoring applications.

However, the other thermal techniques such as the one using a radiation pyrometer already discussed in 1.5.3.3. may be used for in-process monitoring of the laser cutting process.

CHAPTER SEVEN
KERF SCANNING SYSTEM

7.1. Introduction

A cut with constant and narrow kerf width and clean cut square edges is always expected by industry from laser cutting and thus the laser cut kerf width is one of the main criteria for a good laser cut. The cut kerf width also has significance for economic reasons. A narrower kerf and clean cut edge would save material and make after-cut processes unnecessary. However, as already discussed in previous chapters, the laser cut quality including the kerf width and kerf appearance may vary due to such factors as the variations in laser power, assistant gas flow velocity, changes in material thickness and sample surface conditions during the laser cutting process. Therefore the monitoring and controlling of the cut kerf are necessary.

Methods for in-process quality analysis of the laser cutting process have been reviewed in chapter 1 and investigated in chapters 4, 5 and 6. Some of these methods, particularly the optical and the acoustic detections described in chapters 4 and 5, can provide real-time cut quality information, which would make on-line diagnosis and further on-line control of the cut quality possible. In this chapter, methods which could monitor and measure in real-time the individual quality parameters, particularly the kerf width, will be investigated.

The objective of this chapter is therefore to design an in-process kerf width measuring system. This will be discussed in two stages. First, a kerf scanning system for straight line cutting of a flat plate and second, a kerf scanning system for laser straight line cutting of an uneven plate.

7.2. Kerf Scanning System for Straight Line Cutting of a Flat Plate

7.2.1. Principle of the system operation

Figure 7 -1 shows the operation set-up of the laser kerf scanning system, while figure 7 -2 is the schematic diagram of the system. It is seen

that the scanning system comprises four major parts: a scanning device for causing a beam of light to scan repeatedly across a predetermined region, a He-Ne laser as the source of the light beam, a light sensitive detector for receiving light from the workpiece and for providing a signal representative of the intensity of the light received which allows the kerf width to be determined and a signal recording device.

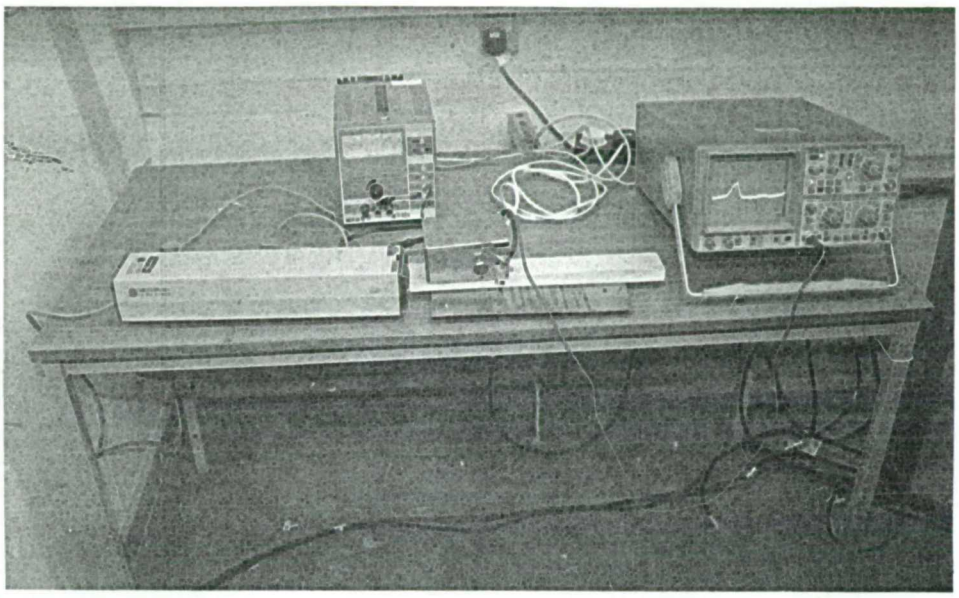


Fig. 7 -1. Operation of the laser kerf scanning system.

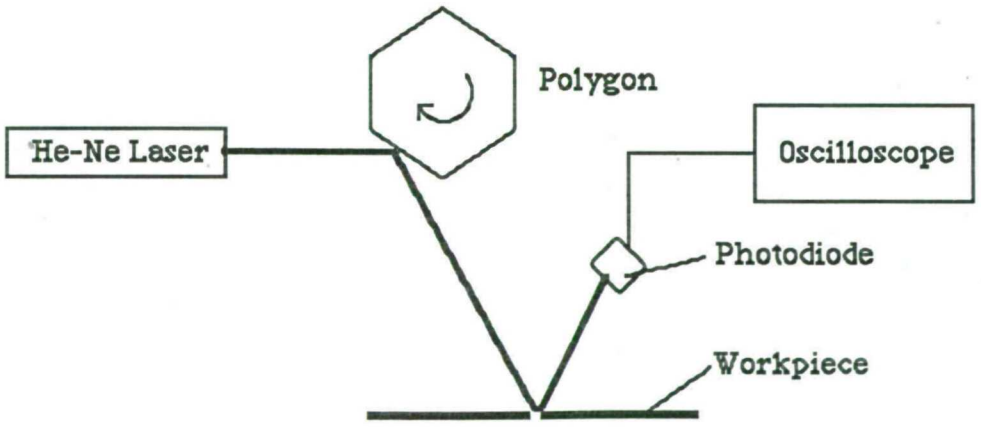


Fig. 7 -2. A schematic diagram of the scanning system.

The scanning device used was a rotating polygon. The He-Ne laser was manufactured by Spectra-Physics (Model 155A). It operated in the visible

spectrum having a wavelength of 6.328×10^{-7} m (632.8 nm), TEM_{00} power of 0.95 mW and a beam diameter of 0.70 mm at e^{-2} points. The rotating polygon had six facets (hexagon) with a radius of 10 mm and was driven by a synchronous motor selected from RS Component Co. Ltd.. The rotating speed was 250 revolution per minute (r.p.m.), i.e. 4.17 revolution per second (r.p.s.).

The light sensitive detector was a photodiode selected from Hamamatsu Ltd. (Model No. G1117). The photodiode was of the GaAsP diffusion type, which have a wavelength range of 300 - 680 (nm) with the peak wavelength of 610 nm which is close to that of the He-Ne laser. The effective area of the photodiode was 29.3 mm^2, which was large enough to cover the cut kerf area. The signal recording device was an oscilloscope, which recorded and displayed the signals.

Tracing the laser beam as it travels from beginning to end serves to illustrate the system's operation. First, the He-Ne laser is introduced parallel to the workstation and appropriately positioned so that it's beam strikes one of the facets of the hexagon. Then the beam is directed at continuous angles down to the workpiece as the hexagon rotates. The photodiode is positioned at a proper angle to receive the reflected beam from the workpiece. The received signal is then displayed on the oscilloscope. The position of the photodiode depends on the relative position of the hexagon and the workpiece, as to be discussed later.

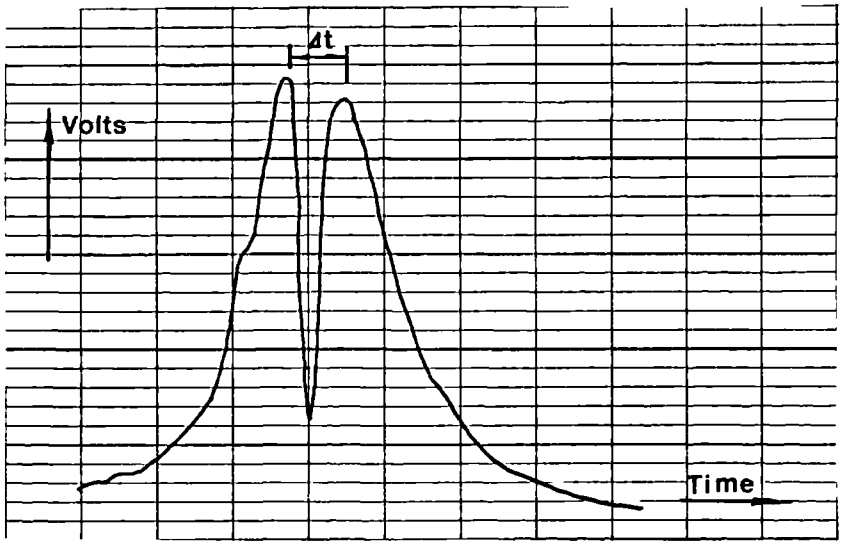


Fig. 7 -3. A typical signal scanning a clean cut kerf.

For this study, a piece of laser-cut mild steel sheet, 1 mm thick, was scanned. A typical signal when the He-Ne beam scans across a clean part of the cut kerf is shown above in Fig. 7 -3.

As can be seen, the photodiode starts to respond when the reflected beam reaches within the photodiode's viewing angle (the solid angle), which is a function of the effective area of the photodiode and the distance between the photodiode and the scanned kerf as defined in chapter four. The signal then rises as the beam moves closer to the photodiode, which leads to the increase of the reflected light intensity falling onto the photodiode. The first peak is formed when the beam meets one side of the cut edge. From then the signal falls down due to the existence of the kerf where most of the light vanishes instead of being reflected upwards. As the laser beam comes across the other side of the cut edge, the signal jumps up to form the second peak due to the reappearance of the reflected beam. Moving away from the kerf, the signal drops and finally reaches the original level when the beam is out of the photodiode's viewing angle. The entire cycle repeats as another beam comes into the photodiode's viewing angle. Since the rotating speed of the hexagon is 250 r.p.m., the scanning frequency of the beam crossing the kerf can be worked out as :

$$f_s = \omega * n \qquad (7\text{-}1)$$

where

f_s = the scanning frequency (Hz);

ω = the rotating speed of the hexagon (r.p.s.);

n = the number of facets of the polygon and is 6 in this case.

Therefore the scanning frequency is calculated to be 25 Hz. From the above-description, it is seen that the distance between the two signal peaks, i.e. the time interval, would indicate the width of the kerf. A wider kerf would result in a longer time interval.

7.2.2. Mathematical background

The relationship between the kerf width and the time interval measured from the two signal peaks, shown in Fig. 7 -3, can be

mathematically represented as follows.

To facilitate the calculation, a two-dimensional coordinate system is set in a X-Y plane as shown in Fig. 7 -4.

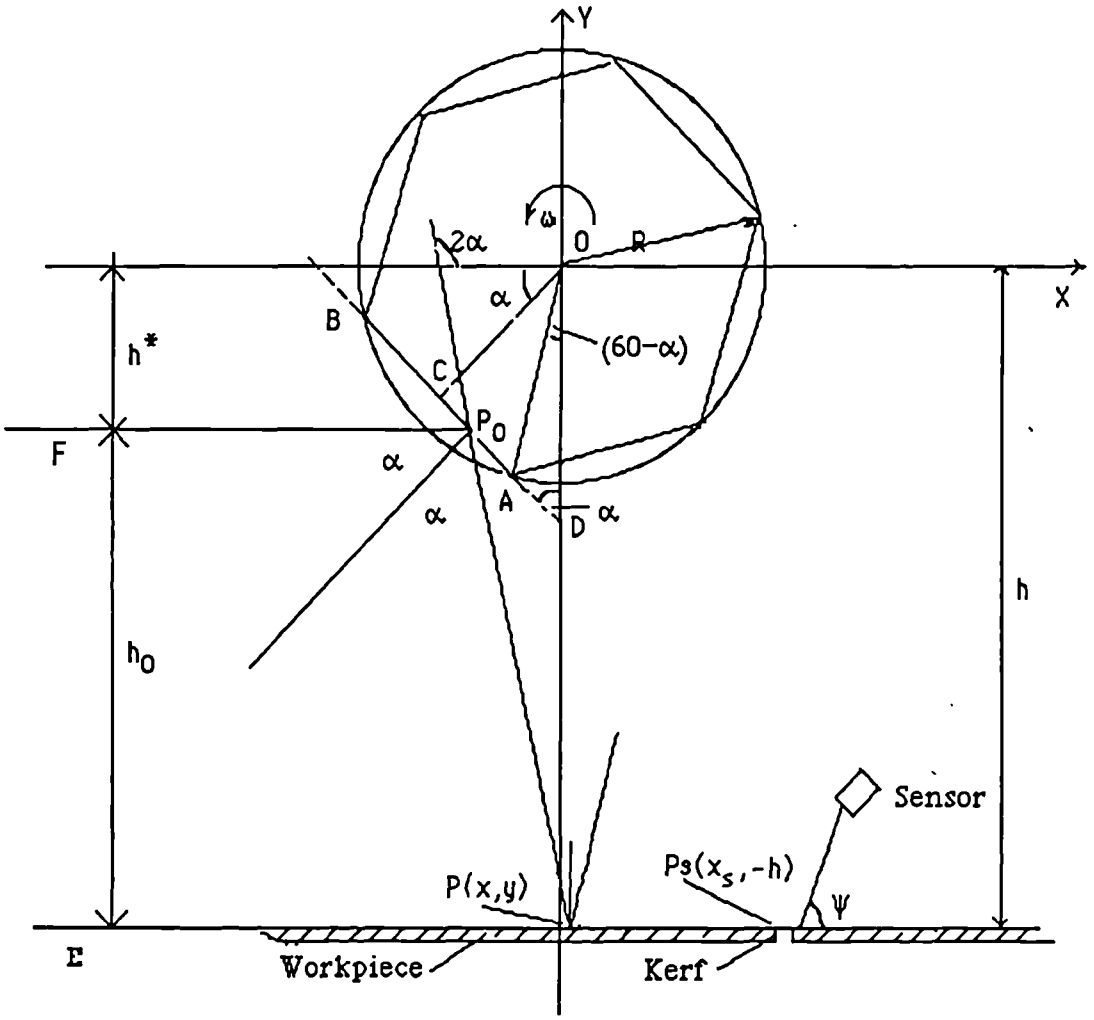


Fig. 7 -4. A geometric drawing of the scanning system.

The hexagon, inscribed in a circle of radius R, rotates at an angular velocity ω, and is positioned above the sample at a distance of h. The He-Ne laser beam FP_0 travels parallel to the X-axis for convenience and is a distance of h_0 from the workpiece. The photodiode is positioned at a fixed angle ψ. Line AB represents one of the facets of the hexagon. Line OC is normal to line AB. Thus the position of AB can be determined by the angle,

α , between line OC and X-axis (- X direction). The intersection point of AB and -Y axis is D. At an arbitrary angle α, the functions of line EP and the scanning beam line P_0P are given respectively as:

$$y = -h^* - h_0 = -h \tag{7-2}$$

and

$$y - y_0 = k(x - x_0) \tag{7-3}$$

where

$P_0(x_0,y_0)$ = the crossing point between the input He-Ne beam FP_0 and the hexagon facet, i.e. line AB;

P(x,y) = the point where the scanning beam meets the sample surface;

k = the gradient of P_0P , given as $\tan(2\alpha)$.

In order to find out the coordinates of P(x,y), point $P_0(x_0,y_0)$ needs to be worked out, which is given by

$$y_0 = -h^* \tag{7-4}$$

and

$$y_0 = k'x_0 + b \tag{7-5}$$

where

k' = the gradient of the line AB, given as $\tan(\pi/2 + \alpha)$, i.e. $-\cot\alpha$;

b = the y coordinate when x = 0, i.e. b = -OD.

The constant, b , can be worked out by applying the sine rule in the triangle ΔOAD as below :

$$\frac{R}{\sin\alpha} = \frac{OD}{\sin(\frac{2\pi}{3})} \tag{7-6}$$

or

$$b = -OD = -0.866R\csc\alpha \tag{7-7}$$

Thus the x coordinates of point $P_0(x_0,y_0)$ can be deducted from equations (7 -4) and (7 -5) as :

$$x_0 = h^* \tan\alpha - 0.866\frac{R}{\cos\alpha} \qquad (7\text{-}8)$$

Put the coordinates of $P_0(x_0,y_0)$ into the equations (7 -2) and (7 -3), then the point P(x,y) can be worked out as :

$$\begin{aligned} x &= (y + h^*)\cot 2\alpha + h^* \tan\alpha - \frac{0.866R}{\cos\alpha} \\ &= f(\alpha, h_0) \\ &= f(t, y) \end{aligned} \qquad (7\text{-}9)$$

where f(t, y) is a function of the scanning time and the y coordinate, since $\alpha = (\alpha_0 + \omega t)$ and $y = -(h^* + h_0)$, and α_0 determines the initial position of the hexagon.

This equation correlates the scanning distance over the workpiece surface with the scanning time. Given h* = 5 mm, R = 10 mm, $\alpha_0 = \pi/3$ and $\omega = (4.17 \times 2\pi \times 10^{-3})$ per millisecond, which were the values approximate to the testing built, the equation then becomes:

$$x = (y + 5)\cot(2.09 + 0.052t) + 5\tan(1.05 + 0.026t) - \frac{8.66}{\cos(1.05 + 0.026t)} \qquad (7\text{-}10)$$

By giving a few sets of values for x and t, plots of this function at two different y coordinates can be shown as Fig. 7 -5, where the scan length is limited within $\pm$ 50 mm.

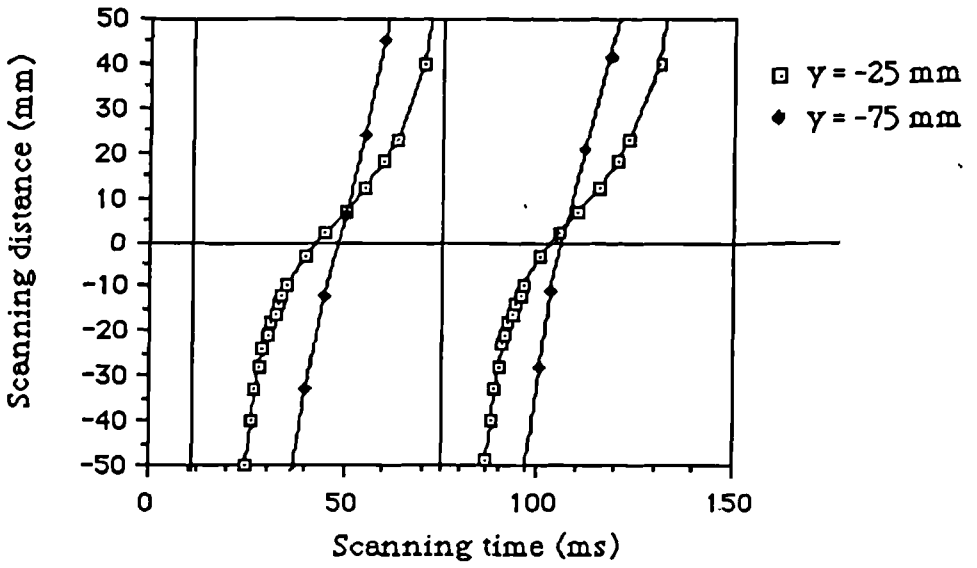


Fig. 7 -5. The correlation between the scanning distance and the scanning time.

It is seen from these curves that the scanned distance increases with the scanning time until when the beam strikes the change-over of the two facets of the hexagon, which is indicated by the vertical lines in the graph. The curve then repeats as the second facet comes across the beam showing an periodical function of the scanning time.

It is also seen that the two curves at the different y coordinates are different. In other words, the scanned distance is also a function of the distance between the workpiece and the hexagon, which may cause errors if a uneven workpiece is scanned. This will be discussed later.

Since the laser cut kerf width is usually within 2 mm, a more detailed graph showing the correlation between the scanning distance and the time is necessary. Given the position of the kerf as $P_s(x_s, -h) = P_s(18, -25)$, the corresponding scanning time past is found to be 60 ms. A graph is thus drawn from this point on at smaller time intervals as shown in Fig. 7 -6. The data were calculated according to the equation (7 -10) (y = -25 mm) and shown in table 7 -1.

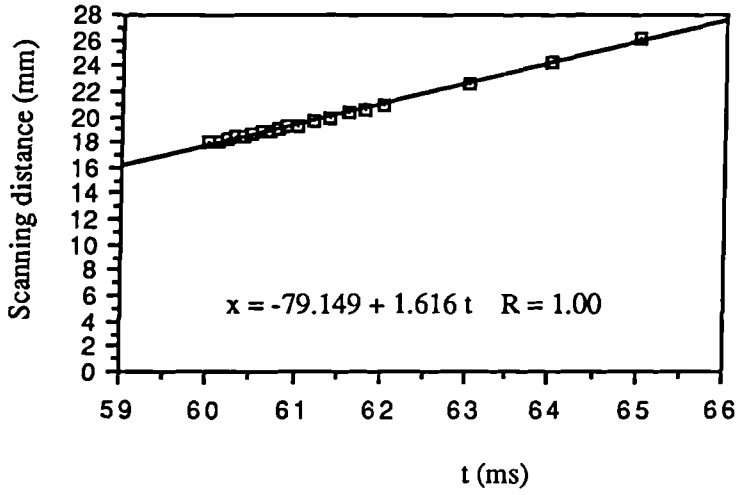


Fig. 7 -6. The theoretical correlation between the scanning distance and the scanning time within a short distance.

It is seen from the straight line fit ("least squares fit to points") that the scanning distance increases nearly linearly with the scanning time within a certain distance range (e.g. from 18 to 24 mm). Namely, the scanning velocity is nearly constant over this short distance. This equally suggests that the kerf width could be measured from the time interval over a short distance (such is the case of a laser cut kerf).

Table 7 -1. Values of x and t

t (ms)	60.0	60.1	60.2	60.3	60.4	60.5	60.6	60.7	60.8	60.9	61.0
x (mm)	18.00	18.11	18.25	18.38	18.52	18.66	18.80	18.94	19.09	19.24	19.38
t (ms)	61.2	61.4	61.6	61.8	62.0	63.0	64.0	65.0			
x (mm)	19.68	19.97	20.27	20.58	20.89	22.52	24.28	26.20			

7.2.3. Experimental results

In order to prove the theoretical relationship shown in Fig. 7 -6, the following experiments were performed by varying the kerf width while keeping the geometry of the system constant. The system geometry includes the relative position of the hexagon to the kerf and the viewing

angle of the photodiode, i.e. $P_s(x_s, -h) = P_s(18, -25)$, $h^* = 5$ mm, $\alpha_0 = \pi/3$ and $\psi = \pi/3$ (the solid angle of the photodiode). The experimental results are shown in Fig. 7 -7, where the time interval, Δt, was defined as the distance between the two signal peaks (Fig. 7 -3).

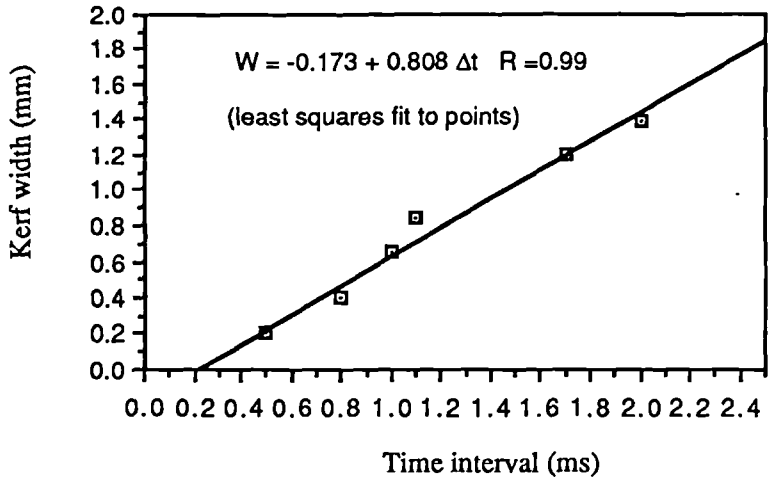


Fig. 7 -7. The empirical relationship between the kerf width and the time interval.

It is seen that the kerf width varied almost linearly with the time interval, which supported the above discussed theory. Therefore the scanning system can be used for observing the kerf width variations.

7.2.4. Scanning a cut with dross adhesion

When the part of a cut kerf with dross clinging at the bottom edge and with one-sided HAZ on the top was scanned, the signal obtained (Fig. 7 -8) was different from that shown in Fig. 7 -3.

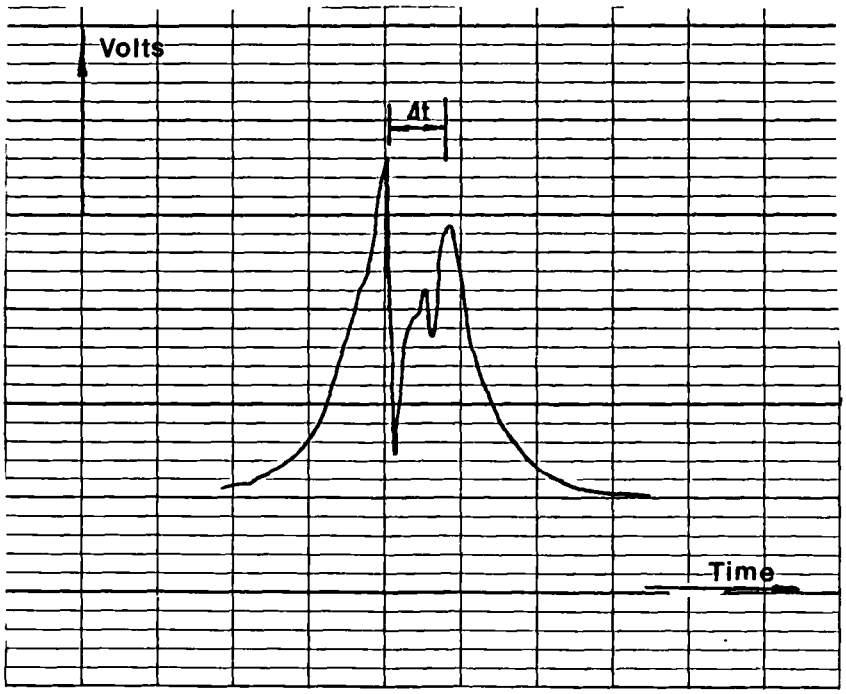


Fig. 7 -8. A typical signal scanning a cut with HAZ and dross adhesion.

It is seen that there is a middle peak response apart from the initial and the final peak responses discussed before. The first peak response can be explained as before due to the beam scanning the cut edge. The second peak was due to the back reflection from the clinging dross. When the scanning beam came across the other cut edge, the light intensity was increased again forming the final peak. This final peak was, however, not as high as the first peak. This could be explained as below. Since the HAZ area has been oxidised during the laser cutting process, the reflectivity was low compared with that of the unaffected area. Thus the light being reflected had a lower intensity, which led to the decrease of the sensor output.

It is thus seen that this scanning system could also be used for indicating the existence of the clinging dross particles and the HAZ.

7.3. Kerf Scanning System for Straight Line Cutting of an Uneven Plate

The above-described system would work well when a straight line cut on a flat sheet is made. However, a problem would arise if the plate being cut is uneven, since the scanning time across the cut kerf is dependent on y coordinates.

7.3.1. Two polygon system

It is easily seen from Fig. 7 -5 that the time interval Δt will be different for the same kerf width at different y coordinates. This is because the scanning velocity changes with the change of distance between the workpiece and the centre of the hexagon. Thus, if an uneven surface is cut, different signals would be observed even when there is no variations in the kerf width. To solve this problem, a two- polygon system is proposed as shown in Fig. 7 -9.

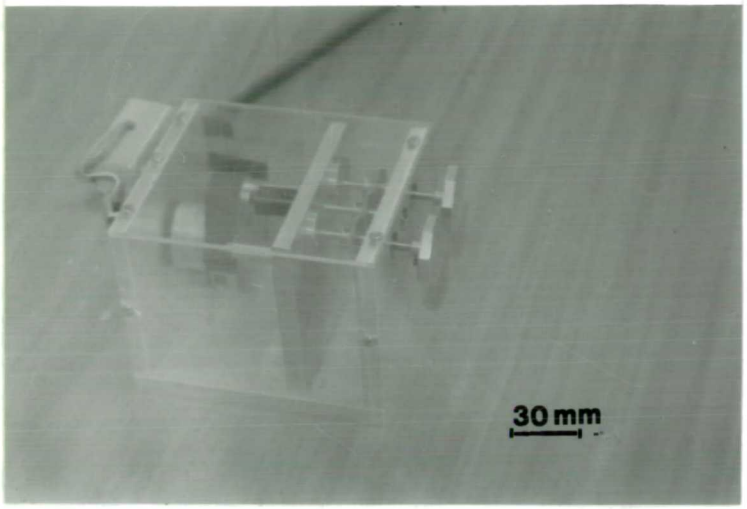


Fig. 7 -9. The two-polygon unit.

Basically, it consists of two polygons rotating at an equal angular velocity ω. After being reflected twice, the scanning beam will always be at the same angle to the Y axis. Thus the signals obtained would be irrelevant of y coordinates as calculated below.

7.3.1.1. Derivation to obtain the angle of the beam

As before, a X-Y coordinate system is set up to facilitate the calculation. A mathematical representation of the two-polygon system (two-hexagon system for the following calculations) is thus shown in Fig. 7-10.

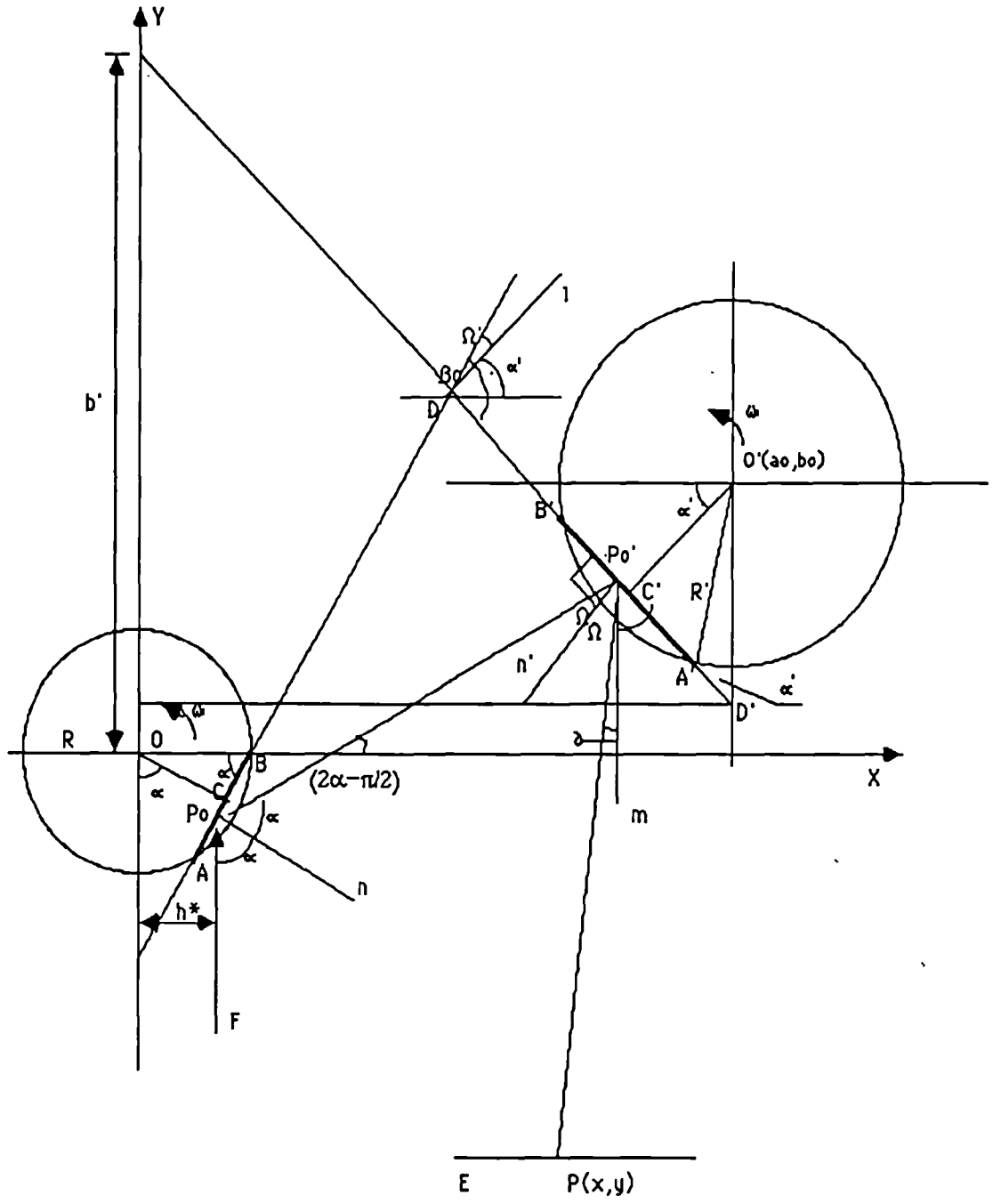


Fig. 7 -10. The mathematical representation of the two-hexagon system.

Line AB is one of the facet of the first hexagon. Its position is determined by the angle α as defined in 7.2. Similarly, line A'B' represents one of the facet of the second hexagon and positioned by the angle α'. The

two hexagons are synchronised to rotate at the same speed and the same direction. The angle between AB and A'B' is thus kept constant as β_0. The He-Ne beam FP_0 is parallel to the Y-axis at a distance of h*. At an angle α, the angle ∂ between the scanning beam, $P_0'P$, and the Y-axis is worked out as follows. Make line m parallel to the Y-axis and line l parallel to O'C', then

$$\partial = (\pi/2 - \Omega) - \alpha' . \qquad (7 - 11)$$

In $\Delta DP_0P_{0'}$,

$$\beta_0 = (\pi/2 - \alpha) + (\pi/2 - \Omega)$$

$$= \pi - \Omega - \alpha ,$$

or $$\Omega = \pi - \beta_0 - \alpha . \qquad (7 -12)$$

as $$\alpha' = \alpha - \Omega' ,$$

$$\Omega' = \beta_0 - \pi/2 ,$$

therefore

$$\alpha' = \alpha + \pi/2 - \beta_0 . \qquad (7 -13)$$

Put equations (7 -12) and (7 -13) into (7 -11), then the angle ∂ is given as

$$\partial = 2\beta_0 - \pi ,$$

$$= \text{constant} , \qquad (7 -14)$$

which means that the scanning beam has a fixed angle to the Y axis.

7.3.1.2. The relationship between the scanning distance along X-axis and the scanning time.

Given $\beta_0 = \pi/2$, then the scanning beam $P_0'P$ is parallel to the Y-axis and α' equals to α. Thus the x coordinate of the point P(x,y) equals to x_0'.

The point $P_{0'}(x_{0'},y_{0'})$ can be worked out from the following equations:

$$A'B' \quad : \quad y_{0'} = k'x_{0'} + b'$$

$$= - x_{0'} \cot\alpha + a_0 \cot\alpha + (b_0 - 0.866R'/ \sin\alpha), \qquad (7\text{-}15)$$

$$P_0P_{0'} \; : \; y_{0'} - y_0 = k(x_{0'} - x_0)$$

$$= -\cot 2\alpha \; (x_{0'} - x_0), \qquad (7\text{-}16)$$

Similarly, $P_0(x_0,y_0)$ is given as

$$y_0 = h^* \tan\alpha - 0.866R/ \cos\alpha,$$

$$= f(t), \qquad (7\text{-}17)$$

and

$$x_0 = h^*. \qquad (7\text{-}18)$$

Put Eqns. (7 -17) and (7 -18) into (7 -15) and (7 -16), x can be worked out as below :

$$x = x_{0'} = [h^* \cot 2\alpha + f(t) - \alpha_0 \cot\alpha - b_0 + 0.866R'/\sin\alpha]/(\cot 2\alpha - \cot\alpha)$$

$$=\varphi(\alpha)$$

$$=\phi(t). \qquad (7\text{-}19)$$

It is clearly seen that the scanning distance is irrelevant of y coordinates and a pure function of the scanning time.

A plot of the function in the positive region is shown in Fig. 7 -11, where R'= 40 mm, a_0 =100 mm, b_0 = 60 mm and the other parameters are the same as before.

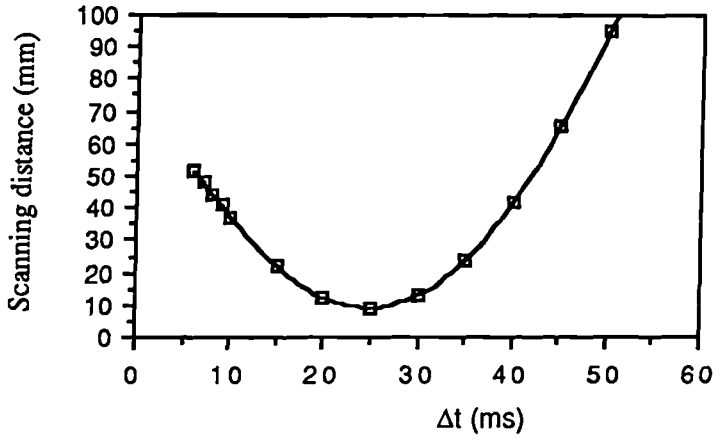


Fig. 7 -11. The correlation between the scanning distance and the scanning time in the two hexagon system.

It seems that there exists an approximately linear portion at the first part of the graph . Therefore a more detailed graph is plotted as shown in Fig. 7 -12.

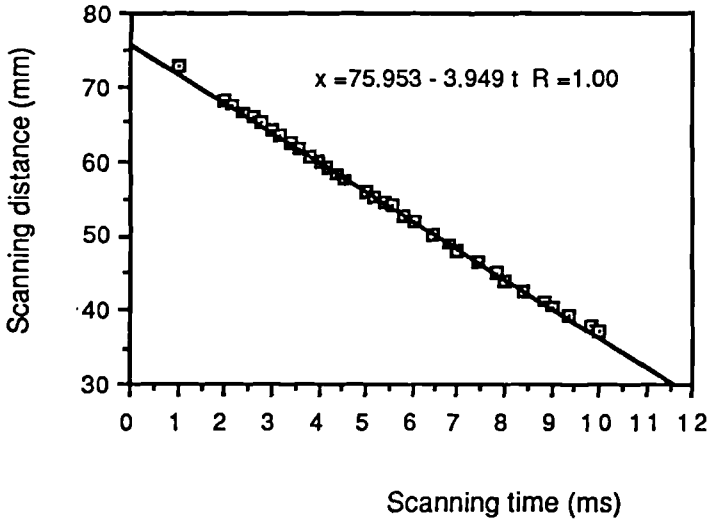


Fig. 7 -12. The nearly linear correlation between the scanning distance and the scanning time.

It is clearly seen that the scanning distance varies nearly linearly with the scanning time, i.e. the scanning velocity over the workpiece surface is close to constant over a scanning distance range of 35 - 75 mm.

7.3.2. Effects of the scanning beam size on the signal shape

The observed signal shape scanning a cut kerf is affected by the scanning beam size as shown in Fig. 7 -13.

Figure 7 -13a shows the signal when the He-Ne beam diameter (0.70 mm) is greater than the kerf width (0.45 mm). It is seen that a noisy signal with a small drop was observed. If an on-line analysis of the signal is required, it would make control programming difficult. When a computer analyses a signal in order to calculate the time interval between the two peak responses, the computer must first be able to identify the peak responses. Therefore a clear difference between the peak value and the lowest point is necessary.

When the beam size equals to the kerf width as seen in Fig. 7 -13b, signal was improved. But it did not drop down to the original level. This was due to the beam size being taken at e^{-2} points, i.e. the whole beam did not completely vanish in the kerf leaving some reflections.

While the beam size is smaller than the cut kerf (1.0 mm) as shown in Fig. 7- 13c, the signal is clean and right down to the original level. This would make the control work much easier. Therefore, the beam size should be as small as possible.

7.3.3. Design of an on-line kerf scanning system

7.3.3.1. Mechanical design of the two polygon system

The two-polygon kerf scanning system shown in Fig. 7 -9 requires that both of the polygons rotate at the same speed and in the same direction (clockwise or counter-clockwise) in order to keep the angle β_0 constant (Fig. 7 -10). In other words, these two polygons have to be synchronised and kept at the angle of $\pi/2$. This synchronisation requirement was achieved by using a three-gear system as shown in Fig. 7 -14, where gear 2 is the driving gear, while gear 1 and 3 are driven gears. They were chosen to have the same size and the same number of teeth so

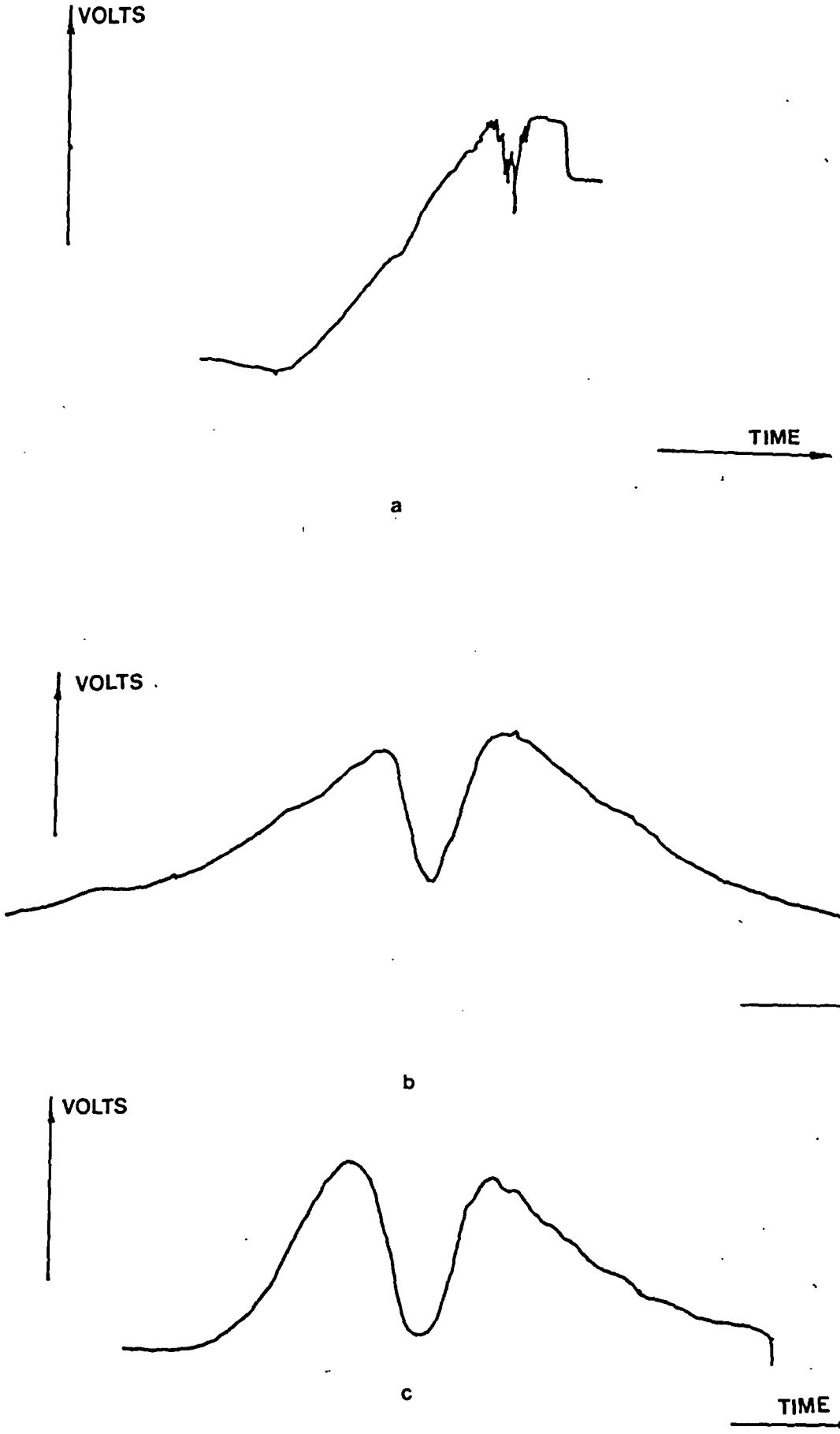


Fig. 7 -13. Effects of the scanning beam size on the signal shape.

that they rotate at the same speed and in the same direction. If the two polygon are coupled to these two gears respectively, the two polygon will also be synchronised. (The mechanical design was made by a third year student, the radii of the two polygons were made equal to 30 mm. Since smaller facets are much easier to be polished up to reasonable flatness and smoothness, both polygons were designed as octagons. This would not affect the above-discussed principle. This increased number of facets would however increase the beam scanning frequency according to the equation (7 -1)).

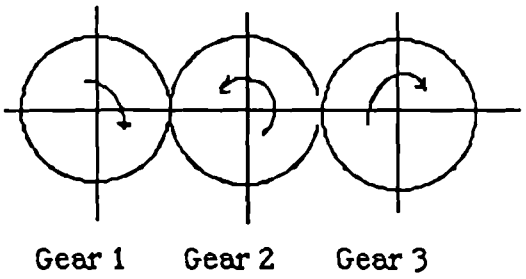


Fig. 7 -14. A schematic drawing of the synchronising system.

In consideration of the limited free space around a laser head assembly where the scanning system would be located, smaller gears would be preferable. Therefore two small size gears were selected from Hinchliffe Precision Component Ltd. (U.K.). The overall diameter of the gear is 20 mm. The materials is aluminium alloy.

Two polygons were firstly machined on a CNC machine in the Mechanical Engineering Workshop of Liverpool University. Then they were polished to give flat and reflective facets.

The motor which drives the driving gear 2 was the same as that of single polygon system having a rotating speed of 250 r.p.m.. A gearbox is used to increase the torque to overcome friction. The gearbox also steps down the motor speed to 60 r.p.m., i.e. the scanning frequency is thus 8 Hz. It was also ordered from the RS Component Ltd. (stock number: 332-868). The beam scanning frequency is determined by the cutting speed and the measuring accuracy required. Lower scanning frequency would be suitable for a slow cutting process.

The engineering drawings of the mechanical parts of the system are given in the Appendix C.

7.3.3.2. Requirements for an on-line application

When the two-polygon system is used in a real processing, the following points must be considered.

(i). Noise from the process

In a CO_2 laser cutting process, massive visible light is generated, which could cover the whole range of the frequency spectrum. These lights would interfere the detection of the scanning beam. Therefore a way to filter out the process-generated visible light is necessary. This can be achieved by putting a filter in front of the photodiode. The filter should have a passing frequency equal to that of the scanning beam so that all the other lights would be effectively filtered out. Although the process-generated light may also include the frequency of the scanning beam which cannot be filtered out, its light intensity would be much lower than the original scanning beam. In addition, the scanning beam source power can be chosen according to the real process.

(ii). Location of the photodiode

Since the process-generated sparks may damage the filter and the photodiode if they are close to the cut kerf, the location of the photodiode would be important. A basic requirement is to keep them a distance away from the workpiece. Since the scanning beam would vertically scan the workpiece, the reflected light would also be vertical, which requires the photodiode to be located in the beam path. This would be impossible, since the photodiode would block the scanning beam. To solve this problem, a window can be positioned in the beam path as shown in Fig. 7 -15. The top side of the window can be antireflection-coated to transmit the scanning beam, while the lower side of the window is reflective to reflect the reflected light to the photodiode.

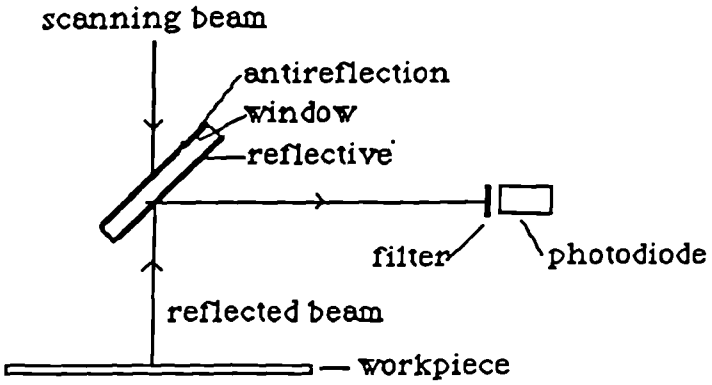


Fig. 7 -15. Location of the photodiode.

(iii). Introduction of the He-Ne beam

Since the He-Ne beam is required to be parallel to the Y-axis (Fig. 4-10), the He-Ne laser would have to be located underneath the first polygon. This makes the location of the system difficult due to the limited space around the laser head assembly. A better way to introduce the He-Ne beam is thus required. One solution to this would be to use a mirror as shown in Fig. 7 -16. By this arrangement, the He-Ne laser can be positioned horizontally.

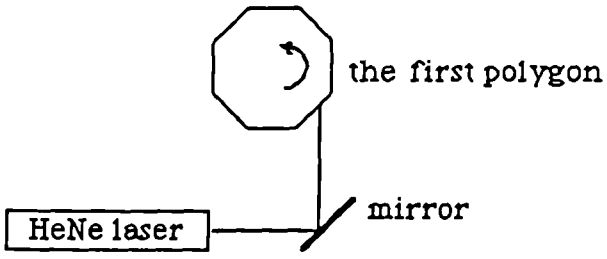


Fig. 7 -16. The introduction of the He-Ne beam.

(iv). Improvement of the scanning beam

As already shown in Fig. 7 -13, the scanning beam size affects the signal shape and may cause difficulties in the signal analysis process.

Therefore, improvement of the scanning beam is necessary. This can be achieved by either choosing a better beam source or using a focal lens to reduce the beam size as well as to increase the beam intensity (Fig. 7 -17).

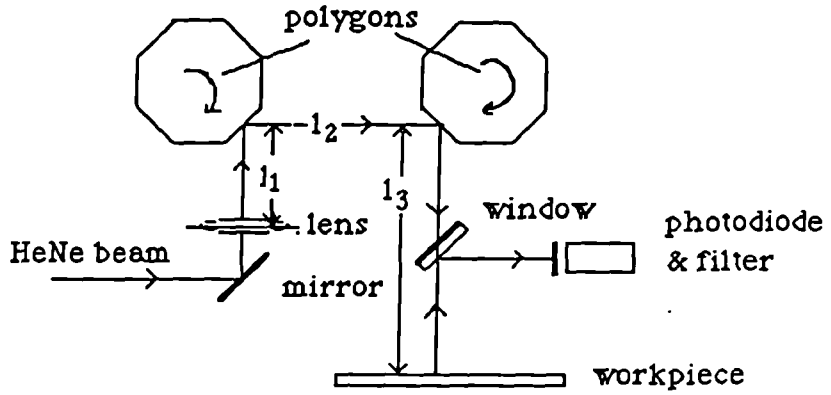


Fig. 7 -17. A schematic drawing of an on-line kerf scanning system.

In this figure, $l_1 + l_2 + l_3$ = focal length of the lens. By this arrangement, the scanning beam size can be greatly reduced. For example, if a lens with a focal length of 150 mm is used, the focussed beam diameter can be worked out according equation (1 -6) as

$$d = \frac{2\lambda f}{\pi r_L} = \frac{2 \times 0.633 \times 10^{-3} \times 150}{3.14 \times 0.35} = 0.17 \text{ (mm)} \qquad (7\text{-}20)$$

where

λ = the wavelength of the He-Ne beam , 0.633 x 10-3 mm;

f = the focal length of the lens, 150 mm;

r_L = the radius of the He-Ne beam, 0.35 mm.

Although the focal point of this focussed scanning beam is not necessarily on the workpiece surface for a profile cutting, the beam size would be reduced over a range of work positions.

Figure 7 -17 shows the operation principle of the whole kerf scanning system, which would be suitable for a straight line cut on a flat or an uneven plate. It would be also suitable for a curved line cut application as long as the radius of the curve is sufficiently large.

This two-polygon system is being further investigated to make it commercialise (the project is being funded by industry).

7.4. Chapter Summary

An off-line kerf scanning system for a straight line cut of a flat plate has been tested that can indicate quickly the variation of the kerf width. The system includes a He-Ne laser, a hexagon and a photodiode.

The design of an in-process two-polygon kerf scanning system has been discussed that would filter out the interference from the real process and could be used in a laser straight line cutting of an uneven plate. The theoretical work and the mechanical parts of the system have been presented.

7.5. Chapter Acknowledgement

A year III student, Miss M.M. Tan, working under the supervision of the author has assisted with the mechanical design of the two-polygon system.

CHAPTER EIGHT

ON-LINE QUALITY CONTROL OF LASER CUTTING

8.1. Introduction

In previous chapters, different methods have been investigated for in-process monitoring of the laser cutting process. The optical method using a photodiode and a 'see-through' mirror has been shown to be a satisfactory method of process monitoring. The acoustic method which used a pizeo-electric transducer on the back of the last mirror to monitor the back reflections from the workpiece also proved to be useful for the in-process quality analysis of the cutting process. The kerf scanning system which was discussed in chapter 7 could be used in real-time to provide on-line information on an individual quality parameter - kerf width. These methods can be further developed into an on-line control system of laser cutting.

As discussed in chapter one, laser cutting involves many factors which affect the cut quality. These factors can be summarised as Fig. 8 -1.

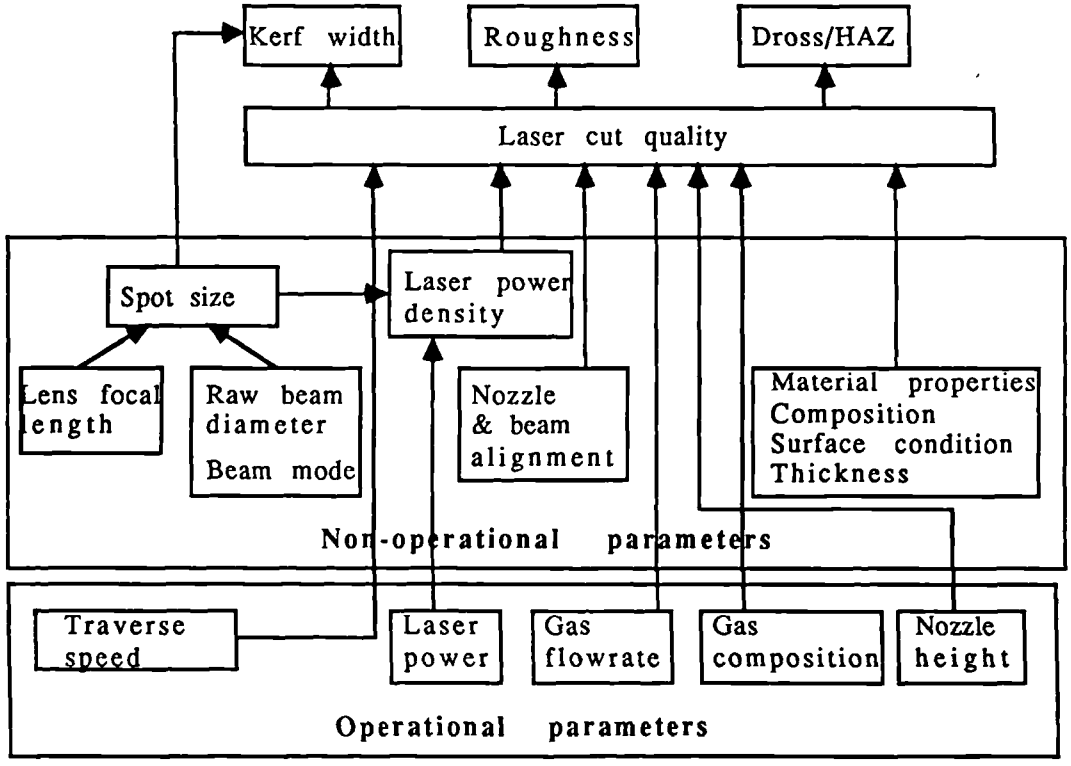


Fig. 8 -1. Laser cutting process parameter interrelations.

It can be seen that laser cut quality is affected by many parameters and are controlled by the operational parameters if the non-operational parameters are kept unchanged. In fact, at a suitable laser power level and gas flowrate, the cut quality can be controlled simply by varying the cutting speed (this of course assumes that all other parameters are properly set according to previous experience and kept unchanged during the processing). The correlation between the cut surface roughness and the cutting speed has already been shown in Fig. 1 - 13. Roughness is generally reduced with increasing the cutting speed up to a limited value. The correlation between the dross size and the cutting speed was shown in Fig. 1 -17. The size of the clinging dross particles was considerably reduced with increasing the cutting speed up to a maximum cutting speed after which the dross failed to be cleared away. The correlation between the kerf width and the cutting speed for pure oxygen assisted laser cutting was given in Fig. 3 -11. The kerf width increased nearly linearly with the reciprocal of the cutting speed. A common feature can thus be drawn from these figures, that is, the cut quality would generally be improved by increasing the cutting speed up to a limit for a given power level and gas flowrate. Further increase in the cutting speed would however lead to the incomplete penetration.

Similarly, the cut quality, in particular the extent of dross adhesion, can also be controlled by the gas flowrate at a suitable power level and a given cutting speed. The correlation between the gas flowrate and the dross adhesion for different gas mixtures has been investigated in chapter 3 and shown in Figs. 3 -24 to 3 -26. Increasing the gas flowrate (the gas velocity for a given nozzle exit diameter) would generally reduce the amount of clinging dross particles. If the gas velocity is too high, it may cause damages to the focussing optics and produce shock waves, which may reduce the cut quality.

Therefore, the cut quality can be controlled by controlling the cutting speed or the gas flowrate at a given laser power. In other words, cutting speed and gas flowrate can be used as control parameters. The objective of this chapter is therefore to discuss the possibility of developing an on-line laser cutting control system.

8.2. Principle of an On-line Laser Cutting Control System

A block diagram showing a proposed on-line laser cutting control system is given below.

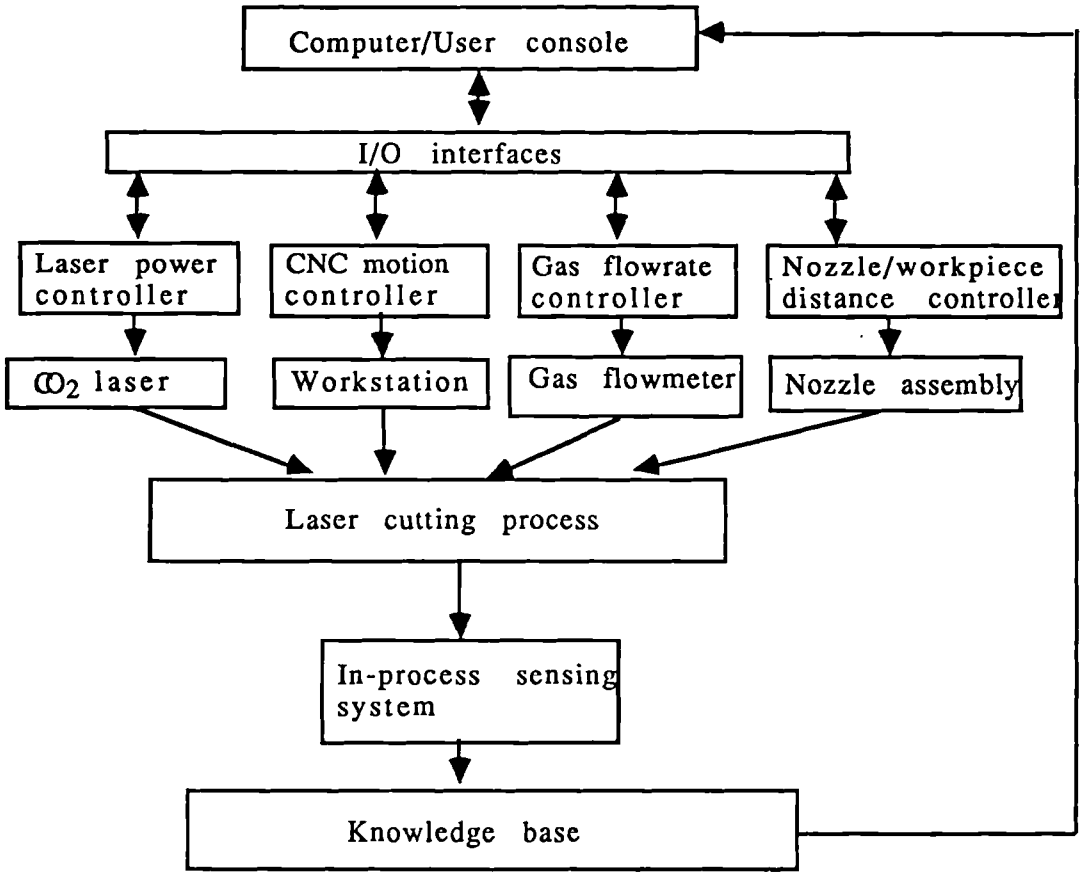


Fig. 8 -2. Block diagram of an on-line laser cutting control system.

The control system can be divided into two levels. The first level controls the operating parameters through the different controllers. The laser power can be controlled through the laser power controller, which is based on the operation of a LBA [164]. The cutting speed can be controlled by the CNC workstation shown in Fig. 3 -1. The gas flowrate can be measured with a gas flowmeter and controlled by a motorised valve. The nozzle/workpiece standoff distance can be controlled by one of the height sensing devices described in chapter one, for example the infrared sensing device. The second level will performs three main functions. Firstly, it compares the feedback signals from the process with the required signal (overall RMS or signal variations). Secondly, it searches

for rules regarding the signal and the cut quality (e.g. rules proposed in chapter 4) and rules correlating the operating parameters with the cut quality, for example the correlation between the cutting speed and the kerf width outlined in Fig. 3 -11, and finally produces instructions for the controllers to adjust the corresponding operating parameters. Obviously the second level would require the establishment of a rule-based data file which can be accessed on-line. It is second level which is discussed in this chapter.

The feedback signals are obtained through in-process sensing devices, which can be the axial optical detection system (chapter 4), the acoustic mirror system (chapter 5) or the kerf scanning system (chapter 7). These systems have been shown to be able to provide on-line information on the cut quality.

8.3. Possibility of Using the Axial Optical Detection Device in the Control System

As discussed in chapter four, axial detection by way of a photodiode and a 'see-through' mirror produced significant signals which were indicative of the laser cut quality. It has been shown that a good cut was obtained when the signal overall RMS was low and the signal was smooth. For a bad cut however, the signal was strong giving a high overall RMS value and showed large variations in the signal strength (represented by $\Delta V\%$). Some of the results were summarised as below, where the voltages refer to the output of the particular photodiode used in the experiment.

a). good cut: $\Delta V\% \approx 10\%$ and the overall RMS = 20 (mV); cut edge was clean and smooth;

b). ok : $\Delta V\% \approx 10\%$ and overall RMS = 40 (mV); cut with medium dross adhesion;

c). bad : $\Delta V\%$ nearly 100% or above and the overall RMS = 70 (mV); rough cuts or cuts with too much dross.

d). not cut: overall RMS > 85 mV.

It is thus possible to monitor the state of the cutting process according to the two signal parameters, i.e. $\Delta V\%$ and the overall RMS. If either of these two values are greater than the threshold values (e.g. V% = 10% and the

overall RMS = 20 (mV)), then proper actions can be taken according to rules concerning the metal cutting process. For example, rule 1: if the $\Delta V\%$ value and the overall RMS value are greater than the threshold, there is a large oscillation of the signals, then the cut possibly has a rough surface or much clinging dross (some other rules were also derived from the experiments as given in chapter 4). The computer then searches for rules or equations which represent the correlation between the dross adhesion and the operating parameters. For example, the correlation shown in Fig. 1 -17 can be applied, according to which the new speed can be calculated. The computer then sends instructions to the CNC controller to change the cutting speed to the calculated value. The processing is thus controlled to give optimum cut quality.

8.4. Possibility of Using the Acoustic Mirror Detection System in the Control System

As discussed in chapter five, the acoustic mirror detection system produced signals which were relevant to the state of the cutting process. For instance, the signal overall RMS varied significantly with the amount of the clinging dross particles as shown in Fig. 5 -7. For a good cut with little dross adhesion, the overall RMS value was 40 mV. With increasing the amount of the dross adhesion, the signal RMS increased to 60 mV for the cut with a small amount of the clinging dross on the side of the cut edge (still an acceptable cut). A signal of 90 mV was produced from the cut with medium dross on both sides of the cut edges (the surface was also getting rougher, a poor cut). When the cut was not penetrating, i.e. dross failed to be cleared from the cut, the overall signal RMS value reached 170 mV. The signal also showed variations in strength, e.g. for a poor cut $\Delta V\% \approx 70\%$ or above. A rule can thus be drawn from these results: if the signal RMS value is greater than the threshold (e.g. 60 mV with the transducer and amplifier used) or if $\Delta V\%$ is equal to or greater than 70%, then the cut has some clinging dross particles. Proper functions can thus be performed to reduce the signal RMS value and the $\Delta V\%$ value by, for example, adjusting the gas flowrate and the cutting speed.

8.5. Possibility of Using the Kerf Scanning System in the Control System

As discussed in chapter 7, the two-polygon kerf scanning system could

provide signals indicating the kerf width variations during processing. That is, the time interval measured between the two peak responses of the detected signal was a nearly linear function of the cut kerf width (Fig. 7-7). If a computer is used to calculate the time interval in real-time, then the kerf width can also be calculated. When the kerf width becomes greater than the required value, proper function can be taken to reduce the kerf width. For example, this can be done by increasing the cutting speed according to the the model shown in Fig. 3 -11.

8.6. Chapter Summary

The possibility of developing an on-line control system of laser cutting was discussed. The in-process sensing devices investigated by the author of the thesis including the axial optical detection device, the acoustic mirror detection system and the two-polygon kerf scanning system could all be used for such a control system.

CHAPTER NINE
CONCLUSIONS AND FUTURE WORK

9.1. Conclusions

The physical mechanisms involved in laser cutting are discussed in chapter one. Three theories exist to explain the formation of the striation pattern of a laser cut. These are: the sideways burning theory; the oscillation of the mass and temperature of the molten layer which covers the cutting front and the oscillation of the thickness of the molten layer. The author considers the sideways burning theory to be most effective in explaining the experimental results.

The main factors which affect the cut quality were also discussed. A good cut is usually characterised by: smooth cut surface, narrow heat affected zone (HAZ), free of dross adhesion and narrow kerf width. Laser power level, cutting speed and gas flowrate are among the most important process parameters which control the cut quality. Higher power level is suitable for cutting thicker materials. Increasing cutting speed would generally reduce the kerf width and improve the overall cut quality. Gas flowrate mainly affects the extent of the dross adhesion.

The potential for laser cutting can be greatly enhanced by automation and adaptive control in order to achieve high process efficiency and high cut quality. To realise adaptive control of laser cutting process three major developments are required: firstly, the development of in-process quality analysis systems; secondly, the design and development of electronically controlled parameter adjustment of the process parameters and finally the development of the process control hardware and software.

The in-process quality analysis of the cutting process is the most important stage towards the automation of laser cutting. The basic criteria of such a system are: reliable signals relating to the cut quality including the surface roughness, the kerf width, the extent of the HAZ and dross adhesion; a fast response time of less than about 3 milliseconds (in consideration of the typical frequency of the cut face striation, which is

usually in the order of a few hundreds of hertzs); be industrial applicable, e.g. a location which does not obstruct the practical process and independent of cutting direction. The state of art techniques for the in-process quality analysis have been extensively reviewed. Some of them, for instance, the registration of the shower of sparks by using a CCD camera provided reliable information of the cut quality. But it has the disadvantage of being positioned underneath the workpiece, which may not be practically applicable in industry and is subject to damage caused by flying molten debris and sparks. The use of an endoscope for direct observation of the cut kerf also indicated a promising source of signals relating to the cut quality, particularly the existence of the clinging dross particles. However, this method involved image processing, which was slow and expensive. The thermal detection by the use of a radiation pyrometer also provided good correlation between the temperature signal and the cut quality. However, it had the disadvantage of being cutting direction dependent. A number of new methods have been investigated, which constitute the main part of the thesis. These include optical methods, the acoustic mirror and a thermal method.

Two experimental studies of using optical sensors were presented in chapter four. The off-axis method by using a photodiode equipped with an extension tube produced reliable signals of cut quality. When a rough cut or a cut with a large quantity of dross particles were observed, the corresponding signal varied greatly in its amplitude $\Delta V\%$ and had a high overall RMS value. For a good cut, the corresponding signal was smooth with little variation. Since the photodiode had a fast response time (3.5 μs) well below the acceptable response time range of a few milliseconds, this method may be used for an in-process quality control of laser straight line cutting. When a curved line or a profile cutting is performed, however, this method would not be suitable since the detected signal was cutting direction dependent.

The axial detection method by way of a photodiode and a 'see-through' mirror produced significant signals regarding the cut quality. A good cut was obtained when the signal overall RMS was low and the signal was smooth. For a bad cut, however, the signal was strong giving a high overall RMS value and showed large variations in the signal strength

(ΔV%). Based on the material studied and the photodiode used, the following conclusions can be drawn:

a). good cut: ΔV% ≈ 10% and the overall RMS = 20 (mV); cut edge was clean and smooth;

b). ok : ΔV% ≈ 10% and overall RMS = 40 (mV); cut with medium dross adhesion;

c). bad : ΔV% nearly 100% or above and the overall RMS = 70 (mV); rough cuts or cuts with too much dross.

d). not cut: overall RMS > 85 mV.

Being omnidirectional in operation, i.e. independent of cutting direction and having a fast response time (3.5 μs), this method can be used in an on-line quality control system of laser cutting. It would also be useful for an adaptive control system on the basis that the process parameters (e.g. cutting speed and laser power) can be on-line adjusted (hardware development) and software for calculating the two signal parameters, i.e. ΔV% and the overall RMS and for calculating and setting the process parameters could be developed. The adaptive control system would obviously require a computer capable of high speed data processing and capable of interfacing with various process parameters controllers. A data file would also be needed which stores the correlations between the cut quality and the process parameters and the correlations between the cut quality and the sensing signals so that they can be accessed on-line for decision-making and correction.

High-speed film of the dynamic behaviour of the melt pool as presented in chapter four indicated a new burning pattern. The burning reaction speed and the laser beam traverse speed were observed to be alternatively advancing to each other in both low and high speed cutting, i.e., at one moment the burning speed is faster than the beam traverse speed while at the other moment the beam traverse is fatser than the burning speed. This phenomenum could be a good explanation of the formation of the surface striation pattern. A mathematical model can be set up by calculating the burning speed and comparing it to the laser beam traverse speed so that the observed burning pattern could be theoretically verified. This is suggested as a part of the future work.

Two arrangements of using piezoelectric sensors for in-process quality analysis of laser cutting were discussed in chapter 5. The first method by putting an piezoelectric transducer close to the cutting nozzle did not produce reliable signal of cut quality and will thus not be suitable for in-process quality control or adaptive control. The second method by way of putting the transducer onto the back of the final mirror (the acoustic mirror) produced signals which were relevant to the state of the cutting process and indicative of cut quality. For a good cut with little dross adhesion, the overall RMS value was low (40 mV for the study). For the cut with a larger quantity of the clinging dross particles on the side of the cut edge, the signal RMS increased to a higher value (60 mV). A very strong signal (170 mV) was produced when the cut was not penetrating, i.e. dross failed to be cleared from the cut. The signal also showed variations in strength, e.g. for a poor cut $\Delta V\% \approx 70\%$ or above. Because this method does not affect the laser beam and because of the observed fast response (in the range of 100 kHz), this system may prove suitable for in-process quality control and further for adaptive control. However, this method had a disadvantage of obtaining too much information(e.g. it was also affected by the variations of the main laser beam), which could make on-line data processing difficult.

The two theories, i.e. photon pressure and thermal stress wave, which are normally used for explaining the laser generated acoustic waves at the final beam guidance mirror were compared by calculating the amplitudes of the photon pressure and the thermal stress waves. The author prefers the thermal stress wave theory to the photon pressure theory, since the amplitude of the former was calculated to be 35 times higher than the latter.

The kerf scanning system using a single polygon and a photodiode was shown to be able to indicate the kerf width of a straight line cut to an estimated accuracy of $\pm$ 0.1 mm at the scanning frequency 25 Hz. However, it had the disadvantage of being suitable only for a straight line cutting on a flat plate as indicated in Fig. 7 -5. The two-polygon kerf scanning system overcame this problem. It basically consisted of two rotating polygons and a photodiode having a fast response time (3.5 μs). It may thus be useful for an in-process quality control of straight line cutting applications. However, software, which can on-line sample and analyse the signal and

send instructions for the process parameters to be adjusted, is required for an adaptive control system. This device could have commercial potential and a patent has been applied for. It needs however further developments for profile cutting applications. The scanning frequency may also need to be increased by either increasing the motor speed or /and by increasing the number of the facets of the polygons for high precision cutting applications.

The "hot nozzle" method, which used a thermocouple to measure the nozzle temperature, did produce some information on the cut quality. For a good cut, the signal showed little variation in the signal strength, while for a poor cut, e.g. not fully penetrating, a strong signal with a single peak response was detected. However, since the detection unit had a slow response time of 0.2 s, which is outside the acceptable level of a few milliseconds, this device may not be suitable for an in-process quality control system or adaptive control system. This, however, does not suggest that all the thermal methods not be suitable for in-process control.

A new method for nozzle/beam alignment was proposed in chapter two. It used a thermocouple to indicate the clipping state of the nozzle and to send back signals to the computer for controlling the movement of the motorised X-Y stage. Off-line testing suggested that the system may be used for the initial nozzle/beam alignment set-up with an estimated accuracy of $\pm$0.01 mm. It would require a minimum experience of laser beam alignment and may thus find its use in industry. It would, however, experience problems for on-line applications, since the process-generated energy will also affect the thermocouple output and may thus make the indication of the clipping state of the nozzle difficult.

A new approach to the improvement of laser cut quality was discussed in chapter three, where the effects of gas mixtures on laser cutting performance were investigated. Results are presented of cutting with pure oxygen, O_2/Ar, O_2/N_2 , O_2/He mixtures, and pure inert gases. The following points can be drawn:

(i). Kerf width was found to be approximately inversely proportional to the cutting speed. At the maximum speed, the kerf width was reduced

with the pure oxygen assisted cutting.

(ii). Clinging dross problems are principally controlled by gas velocity. Increasing the gas velocity would reduce the quantity of dross particles. At the maximum cutting speed, increasing the oxygen content would also reduce the amount of clinging dross particles.

(iii). The maximum cutting speed can be increased with the increase of gas velocity. Pure O_2 will cut faster at a given gas velocity. Helium gas mixtures had a somewhat lower cutting speed than the other gas mixtures. However, when the inert gas content was small (< 30%), Helium behaved similar to Ar and N_2.

(iv). There existed optimum speed ranges as a function of gas composition and gas velocity. For example, equation (3-18) showed the model which was produced at a high gas velocity.

The on-line adjustment of the gas composition would be too slow to match the cutting process. Therefore, the gas composition may not be suitable for acting as a control parameter in an adaptive control system. However, the gas pressure control could, in future, be part of an in-process control system.

The possibility of developing an on-line control system was discussed in the last chapter, where the optical device, the acoustic mirror and the kerf scanning system were shown to be suitable for such a control system. Considering the multi-parameter nature of the laser cutting process, the development of an adaptive control system may be pursued by using an expert system.

9.2. Suggestions for Future Work

The work reported in this thesis has indicated that the following future work would be worthwhile:

i). A mathematical model should be established to prove the new burning pattern observed in chapter four. It should essentially be able to calculate the burning reaction velocity and to compare it with the laser beam traverse velocity. This would hopefully prove the alternative advancing of the burning speed and the laser beam traverse speed. This

model could give an insight view of the laser cutting mechanism, particularly the formation of the surface striation pattern.

ii). Development of the two-polygon system to make it a commercial product. It would be more attractive to industry if it is developed to be suitable for profile cutting applications. The physical size of the device may be reduced to a minimum by choosing an approriate smaller motor and a gear box. The measuring accuracy of the system may be improved by increasing the scanning frequency for high precision cutting applications. This may be achieved by increasing the motor speed and the number of the facets of the polygons. Computer software needs developing for sampling and analysing the signals.

iii). Further development of the axial optical detection system into an on-line alarm system or an on-line control system. The design of the "see-through" mirror may be improved by reducing the hole diameter and by a proper design of the water cooling system. Computer software for calculating the two signal parameters $\Delta V\%$ and the overall RMS value may be developed. This software should be able to compare with the preset threshold values and to send commands for a alarm. A data file, as discussed earlier may be built up, which would make an on-line adaptive control possible.

iv). The nozzle/beam alignment system may be further developed for on-line applications. This may be achieved by symmetrically positioning four thermocouples in a ring above the focussing lens. Any shifting of the beam in one direction would cause the response of the thermocouple in that direction. Thus a proper adjustment of the beam guiding mirrors may to performed to keep the beam to be at the centre of the thermocouple ring.

iv). Software for on-line analysing the acoustic signals detected from the acoustic mirror will be required in order to make it suitable for an adaptive control system. This software should be able to distinguish the signals coming from the cutting process and signals due to the oscillation of the main laser beam itself.

REFERENCES

1. W.W. Duley, CO_2 Laser: Effects and Applications, Academic Press, New York, 1976.
2. J. F. Ready, Industrial Applications of Lasers, Academic Press, New York, 1978.
3. W.M. Steen and J. Kamalu "Laser Cutting", Chapter Two, Laser Materials Processing, (Ed.) M. Bass, North-Holland Publishing Co. (U.S.A.), 1983.
4. M. von Allmen, Laser-Beam Interactions with Materials, Springer-Verlag, Material Science, Vol. 2, 1987.
5. A. L. Schawlow "Laser Interactions with Materials", Laser-77, Opto-electronics, (Ed.) W. Waidelich, Munich, June 1977, pp 263 - 266.
6. D. Schuocker "Laser Cutting", Industrial Laser Handbook, (Eds.) D. Belforte and M. Levitt, PennWell Publishing Co., 1986, pp 87 - 106.
7. G. Hertziger "Influence of Laser-induced Plasma on Laser Materials Processing", Industrial Laser Handbook, (Eds.) D. Belforte and M. Levitt, PennWell Publishing Co., 1986, pp 108 - 115.
8. G. Hertziger "Physics of Laser Materials Processing", SPIE Vol. 650, 1986, pp188-194.
9. D. Schuocker "Dynamic Phenomena in Laser Cutting and Cut Quality", J. Phys. B 40, 9-14, 1986.
10. D. Schuocker, W. Abel "Material Removal Mechanism of Laser Cutting", Proc. SPIE 455, 88, 1984.
11. D. Schuocker and B. Walter "Theoretical Model of Oxygen Assisted Laser Cutting", 5th G.C.L. Symp., Oxford, 1984, pp 111 - 116.
12. D. Schuocker "Laser Cutting of Bulk Steel Due to Guided Flow of Radiation and Reactive Gas in the Workpiece", Proc. G.F.C.L., Italy, Sept. 1982, pp 647 - 654.
13. D. Schuocker "Reactive Gas Assisted Laser Cutting-Physical Mechanism and Technical Limitations", Industrial Applications of Laser Technology, (Ed) W. Fagan, SPIE Proc. 398, 1983, pp 388 - 392.
14. D. Schuocker "Physical Mechanism of Laser Cutting", Industrial Laser Annual Handbook, 1987, PennWell Publishing Co., pp 65 - 79.
15. Y. Arata "Dynamic Behaviour of in Laser Gas Cutting of Mild Steel", Trans. of J.W.R.I., Vol.8, No.2, Dec. 1979, pp 175 - 186.
16. G. Hertziger, Feinw , Messtech, 1983, 91, pp 156 - 163.
17. F.O. Olsen "Investigation in Optimising the Laser Cutting Process",

Lasers in Materials Processing, 1984, pp 64 - 80.

18. F.B. Thomassen and F.O. Olsen " Experimental Studies in Nozzle Design for Laser Cutting ", LIM-1, Birmingham U.K., 1983, pp 169 - 180.
19. M. Vicanek, G. Simon, H.M. Urbassek and I. Decker " Hydrodynamic Instability of Melt Flow in Laser Cutting ", J. Phys. D: Appl. Phys. 20, 1987, pp 140 - 145.
20. I. Decker and J. Ruge, SPIE Vol. 455, 1984, pp 81 - 87.
21. M. J. Adams, Metal Construction and British W. J., No.1, 1, Jan. 1970.
22. N. Forbes " The Role of Gas Laser in Metal Cutting with CO_2 Laser", Laser-75, Opto-Electronics, Munich, 1975, p 93.
23. G. Hertziger " Basic Elements of Laser Materials Processing ", SPIE 455, 1983, pp66-74.
24. G. Hertziger " Laser Materials Processing", 4th G.F.C.L., (Ed.) M. Onotate, 1984, p55.
25. E Beyer, G. Hertziger et.al. "Optical Feedback During Laser Materials Processing", Laser-83, Munich 1983, pp 259 - 263.
26. E. Beyer, O. Marten, K. Behler and J.M. Weick "Laser Optoeletronics", 17, 282, 1985.
27. M. Darchuk and L.R. Migliore "Guide Lines for Laser Cutting", Lasers & Applications, Sept. 1985, pp 91 - 97.
28. Y. Arata "Quality in Laser-gas-cutting Stainless Steel and Its Improvement", J.W.R.I., Vol. 10, No.2, 1981, pp 129 - 139.
29. J. Fieret "Aerodynamic Interactions During Laser Cutting", SPIE 1986, Canada.
30. M. Dijk et. al. "Reactive Gas Assisted Cutting with Pulsed YAG Lasers", ICALEO'85, Nov. 1985, pp 153 - 159.
31. H. Osada "Ultra-fine Cutting by CO_2 Laser", ICALEO'87, 1987, pp 157 - 161.
32. D. Belforte and M. Levitt (Eds.), Industrial Laser Annual Handbook 1986, PennWell Publishing Co..
33. D. Belforte and M. Levitt (Eds.), Industrial Laser Annual Handbook 1987, PennWell Publishing Co..
34. J.M. Weick "Laser Cutting of Steel in Manufacturing", LIM-1, 1983, pp 47 - 56.
35. J.T. Luxton "Optics for Materials Processing", Industrial Laser Handbook 1986, pp38-48.
36. M. Welch "Optics for Materials Processing: Practical Considerations", Industrial Laser Handbook 1986, pp 49 - 55.

37. D.M. Rossler "An Introduction to the Laser Processing of Materials", Industrial Laser Handbook 1986, pp 16 - 30.
38. J. Powell " The Influence of CO_2 Mode Quality on Cutting Performance ", Laser-4, Paris, Mar. 1988.
39. J. T. Luxton "Focussing and Depth of Focus of Gaussian and Higher Order Mode Beams". ICALEO'83, 1983, pp 31 - 36.
40. F.O. Olsen "Laser Cutting", SPIE 952, 1988, pp 512 - 582.
41. I. Spalding"Which Wavelength-How to select a suitable laser", LIM-4, May 1987, pp229-234.
42. I.P. Shkarofsky, RAC Review, 36, No.2, 336, 1975.
43. F.O. Olsen "Laser Cutting with Polarised Laser Beam", DVS-berichte 63, 1980, pp197-200.
44. F.O. Olsen "Studies of Sheet Metal Cutting with Plane-polarised CO_2 Laser", Laser-81, 1981, pp 227 - 231.
45. E.H. Berloffa "Laser Cutting-Principal System Aspects and Practical Results", SPIE Vol. 650, 1986, pp 289 - 293.
46. J. F. Ready "Development of Plume of Material Vaporised by Giant-Pulse Laser", Appl. Phys. lett., Vol.3, 1963, pp 11 - 13.
47. J.A. McKay and J.T. Schrilempf "The Spatial Distribution of Aluminium Targets by Laser Ignited Air Plasma", Appl. Phys. Lett., Vol. 33, 1978, pp 877 - 878.
48. E. Beyer and G. Hertziger et. al."Development and Optical Absorption Properties of a CO_2 Laser-induced Plasma During Laser Processing', SPIE 455, 1983, pp75-80.
49. J. Fieret "Circular and Non-circular Nozzle Exits for Supersonic Gas Jet Assist in CO_2 Laser Cutting ", LIM-3, Paris, 1986, pp 46 - 54.
50. B. A. Ward "Supersonic Characteristics of Nozzles Used with Lasers for Cutting", ICALEO'84, Boston, U.S.A., 1984, pp 94 - 101.
51. J Kamalu and W.M. Steen "The Importance of Gas Flow in Laser Cutting", Lasers in Metallurgy, (Ed.) K. Mukherjee and J. Mazumder, Oct. 1981.
52. W.M. Steen, Private Communication, 1987.
53. G. Sepold and R. Rothe "Laser-beam Cutting of Thick Steel", ICALEO'83, 1983, pp156-159.
54. J. Fieret "Overview of Flow Dynamics in Gas-assisted Laser Cutting", Optical and Optoeletronics Applied Sci. & Eng., Holland, April 1987.
55. S.E. Nielson "Laser Cutting with High Pressure Cutting Gases and Mixed

Gases", LIM-3, 1986, pp 25 - 43.

56. W.M. Steen "Thermal History of s Spot Heated by a Laser", Heat & Mass Trans., Letter 4, 167, 1977.
57. S. Kimura, J. Kinoshita et.al. "Thick Mild Steel Cutting with High Power CO_2 Laser", Proc. 2nd Int. Conf. on Metal Cutting, Wuhan, China, May 1985.
58. G.S. Settles "A direction Indicating Colour Schlieren System", A.I.A.A. J. 8, 1970,12, 2282 - 84.
59. M. Abbett "The Mach Disk in Underexpanded Exhaust Plumes", A.I.A.A, 8th Aerospace Science Meeting, new York, 1976.
60. I.S. Chang and W.L. Chow "Mach Disk from Underexpanded Axisymmetric Nozzle Flow", A.I.A.A. J. 12, 1974, 8, pp 1079 - 82.
61. C. Donaldson, R.S. Sanedeker "A Study of Free Jet Impingement", Part 1, J. Fluid Mech., 45 ,1971 , 2, pp 281 - 319.
62. I.P. Ginzberg et.al."Experimental Study of Underexpanded Jets Impinging Normally on a Plane Baffle", Fluid Mech. Sov. research 4, 1975, 3, pp 93 - 105.
63. G.T. Kalghatgi "The Occurrence of Stagnation Bubbles in Supersonic Jet Impingement Flows", Aerodynamics Quarterly, 1976, pp 169 - 185.
64. O.I. Gubanova et.al. "The Central Breakaway Zone with Interaction Between a Supersonic Underexpanded Jet and A Barrier", Fluid Dyn. 6, Mar. 1973, pp 298- 301.
65. G. Dionoro et.al."Inert-gas assisted Cutting of Low Carbon Steel Sheet Using High Power Laser System", G.F.C.L Proc., Sept. 1982, Italy, pp 629-638.
66. G. Daurelio "Copper Sheets Cutting: a New Goal on Laser Materials Processing", LAMP'87, Osaka, 1987, pp 261 - 266.
67. G. Daurelio et.al."Cutting Copper Sheets by CO_2 Laser", Lasers & Applics, Mar. 1986, pp 59 - 64.
68. C.M. Sharp "CO_2 Laser Cutting of Highly Reflective Materials", ICALEO'87, San Diego, 1987, pp 149 - 156.
69. A. Dillio "Laser Cutting of Al 7075 Sheets", LIM-2, Birmingham, 1985, pp 57 - 62.
70. M. Dell'Erba, G. Daurelio "High Reflectivity Metals Cutting by CO_2 Laser", 4th Cong. Nazionale Di Electronica Quantistica E Plasma 1, Italy, 1984, pp 27 - 32.

71. G. Daurelio "CO_2 Laser Applications for Cutting Alloying of Copper", Convegno Sulle, Tech. Appl., Conv., 1986.
72. G. Daurelio "Cutting Copper Sheets Using CO_2 Lasers", Int. Cong. Workshop on Modern Optics, Lasers and Laser Spectroscopy, Kanpur, India, 1987.
73. J. Powell "CO_2 Laser Cutting of Aluminium Alloys", LIM-5, 1988, pp 15 - 24.
74. W. Ulmer, Electro. Optical System Design, July 1974, 6, 33.
75. J. E. Harry, Industrial Lasers and Their Applications, McGraw-Hill Book Co. Ltd.(U.K.), 1974.
76. Jeanette Bellis (Ed.), Lasers: Operation, Equipment, Applications & Design, McGraw-Hill Book Co. Ltd., 1980.
77. J.T. Luxton , D.E. Parker, P.D. Plothwoski, Lasers in Manufacturing, IFS Ltd. (U.K.), Springer-Verlag, 1987.
78. J. Powell, I.A. Menzines, P.F. Scheyvaerts "An Appraisal of CO_2 Laser Cutting", Proc. Laser 4, Paris, 1988.
79. J. Powell "CO_2 Laser Cutting of Non-metallic Materials", LIM-4, 1987, pp 69 - 82.
80. W.W. Duley, Laser Processing and Analysis of Materials, Plenum Press, 1983.
81. J. Powell"Principles and Applications of CO_2 Laser Cutting", 2nd Conf.on Materials Engineering, Nov. 1985, London, pp 206 - 213.
82. H.R. Whittle "A Laser Based Fabric Cutting System", ATOM 220, Feb. 1975, pp 30 - 34.
83. S.H. Slivinsky "Laser Beam Interactions with Plastics", J. Appl. Phys., Vol.48, No.9, Sept. 1977.
84. A.A. Uglov et.al. "Cutting of Non-metallic Materials by a CO_2 Laser Beam", sov. J. Quant. Electron. 8(7), pp 884 - 887, 1978.
85. K.C.A. Crane, J.R. Brown "Laser Induced Ablation of Fibre/Epoxy Composites", J. Phys. D. , 14, 1981, pp 2341-9.
86. J. M. Ruselowski and J. Barrow "Production Laser Processing in the Automotive and Aerospace Industries", LIM-4, 1987, pp 83 - 102.
87. A. Gukelberger "Industrial Applications of High Power CO_2 Lasers-System Descriptions", SPIE Vol. 650, 1986, pp 254 - 261.
88. V.S. Kovalenko, Y. Arata et.al."Experimental Studies of Cutting Different Materials with a 1.5kW CO_2 Laser", Trans. J.W.R.I., Vol. 7, No.2,

1978, pp 101 - 112.

89. D.J. Doyle "Hazardous Byproducts of Plastics Processing with a CO_2 Laser", ICALEO'85, San Francisco, 1985.
90. J.E. Harry "Electrothermal Cutting Processes Using a CO_2 Laser", IEEE Trans. on Industrial Applications. Vol. 1A-8, No. 4, July/August, 1972, pp 418 - 424.
91. Coherent General-Commercial Literature.
92. Ferranti Industrial Electronics-Commercial Literature.
93. C. Esposito, G. Daurelio, Optics and Lasers in Engineering, 1981, 3, pp 161 - 171.
94. M. Lepore, C. Dell'Erba et.al., ICALEO'83, Los Angles, 9183, pp 160 - 165.
95. F.W. Lanua and B.C. Doxey "The Laser Cutting of Steel Rule Dies", Proc. of 2nd Int. Conf. on Product Development and Manufacturing Tech., London, 1973.
96. Laser Focus, 8(4), 14, 1972 .
97. "Lasers, Newest Plastics Fabrication Tool", Mod. Plast. 46(5), 1969, pp 71 - 74.
98. "Fabricating Plastics with Laser, Plant Design Processing, 10(3), 1970, pp 20 - 23.
99. "Take Another Look at Lasers", Plastics World, 29(1), 1971, pp 37 - 39.
100. "Another Genesco Garment Plant Will Expand Its Laser Cutting", Laser Focus, 8(6), 1972, pp 23 - 24.
101. "Laser Materials Processing Enters New Domain: Controlled Fracture", Laser Focus, 4(9), 1968.
102. W.S. W. Tandler"Production Roles for CO_2 Laser", Laser Focus, 7(3),1971, pp 24 -27.
103. L.S. Nelson "CO_2 Laser Enhances Study of Materials", Ceramic Age, 86(11), 1970, pp 38 - 39.
104. F.O. Olsen"Contribution to the Oxygen Assisted Laser Cutting", LIM-6, Birmingham, U.K., 1989, pp 67 - 79.
105. C.H. Miller and T.A. Osial"Status Report on 250 Watt CO_2 Laser for Applications in the Pulp and Paper Industry", 15th Annual IEEE Pulp and Paper Conf., Georgia, May 1969.
106. V. Sergi, V. Tagliaferri, and R. Teli"Cutting of Steel Sheet with a 2.5kW Laser", 5th G.C.L. Symp., Oxford, 1984, pp 117 - 124.
107. L. Bakowsky "New CO_2 Lasers of 1-4 Kilowatt Power with Axial Gas

Flow", LIM-2, 1985, pp 195 - 200.

108. V. Sergi, V. Tagliaferri, and R. Teli "Oxygen Assisted Laser Cutting of Low Carbon Steel Sheets", Proc. 4th G.C.L., 1982, pp655-665.
109. J. Clarke and W.M. Steen "Arc Augment Laser Cutting", Laser-78 Conf., London, Mar. 1978.
110. H.Y. Zheng, W.M. Steen and D. Brookfield "Effects of Gas Composition on Laser Cutting Performance ", Laser-5 Conf., London, April 1989, pp26-36.
111. B.D. Swift-Hook and A.E.F. Gick, Weld, Res. Suppl., 429 S, Nov. 1973.
112. K.A. Bunting and G. Cornfield , Trans. ASME of Heat Trans., Feb., 1975, p116.
113. M. Moriyasu, S. Hiramoro et.al." Adaptive Control for High Speed and High Quality Laser Cutting", ICALEO' 85, San Francisco, U.S.A., Nov. 1985, pp 129 - 136.
114. A. LaRocca, Private Communication, 1985.
115. S.E. Nielson, U.K. Patent Applic., GB 219 1434, 1986.
116. J-M. Weick and W. Bartel " Laser Cutting Without Oxygen and Its Benefits from Cutting Stainless Steel", LIM-6,1989, pp 81 - 89.
117. Petring, Abels, Beyer, Hertziger " Cutting of Metallic Materials with CO_2 High Performance Lasers", Feinwerktechnik & Mebtechnik, 9/88.
118. J. Gabzdyl and W.M. Steen " Nozzle-beam Alignment for Laser Cutting", ICALEO' 87, 1987, San Diego, U.S.A., pp 143 - 169.
119. Coherent Operations Manual for the " Euerlaser 325".
120. Handbook for the BOC Model 901 CO_2 Gas Laser.
121. H.Y. Zheng, Internal Report, Imperial College, London, 1987.
122. R. Nuss, S. Biermann, M. Geiger "Precise Cutting of Sheet Metal with CO_2 Laser", Laser Treatment of Materials, (Ed.) B.L. Mordike, 1987, pp 279 - 298.
123. V. M. Weerasinghe, W.M. Steen "In-process Monitoring of Laser Processing", ICALEO'85, U.S.A, 1985, pp 107 - 112.
124. W.M. Steen "Monitoring of Laser Materials Processing", SPIE Vol. 650, 1986, pp160-167.
125. G.C. Lim and W.M. Steen "Laser Beam Analyser", LIM-1, 1984, pp 161-167.
126. G.C. Lim " High-speed Beam Quality Measurement Technique and Results", ICALEO'87, 1987, pp 3 - 8.
127. G.C. Lim and W.M. Steen "Measurement of Temporal and Spatial Power

Distribution of a High Power CO_2 Laser Beam", Optics and Laser Tech., Vol. 14, June 1982, pp 149 - 153.

128. G. C. Lim and W.M. Steen "Instrument for Instantaneous in Situ Analysis of the Mode Structure of a High Power Laser Beam", J. Phys. E. Instrum., Vol.17, 1984, pp999-1007.
129. H.T. Inaba et.al. "Direct Observation of Output Beam Pattern from N_2-CO_2 Laser at 10.6 microns by Thermal Development Method", Infrared Physics: 145.
130. T.J. Ramos "Laser Beam Diagnostic for Metal Working Applications", ICALEO'84, 1984, pp 306 - 312.
131. A. Drenker, V. Sturm, H. Oebels, P. Loosen and F. Ruhl "Measurement of Laser Power", LIM-5, 1988, pp 241 - 246.
132. K. Konig, F.U. Meis, H. Willerscheid "Process Monitoring of High Power CO_2 Laser in Manufacturing", LIM-2, 1985, pp 129 - 140.
133. B.A. Ward "Laser Beam Measurement and Quality Assurance", 2nd Symp. on Exploitating the Laser in Engineering Production, Coventry, Sept. 1984, The W.I., U.K.
134. G. Sepold , W. Jupnter, R. Rothes, Paper A-29, Int. Conf. Weld Res. , 1980, Osaka, Japan, J.W.R.I. Publishing.
135. E. Beyer, G. Hertziger, R. Kramer, P. Loosen "Diagnostic System for Measurement of the Focused Diameter of High Powered CO_2 Lasers", SPIE Conf., 1986, pp 170 - 177.
136. P.B. Ulrich, U.S. Patent 4, 381,184, April 1983.
137. T. G. Miller, U.S. Patent 4, 325, 252, April 1982.
138. G.A. Shifrin, U.S. Patent 3, 487, 685, Nov. 1966.
139. T. G. Grow, U.S. Patent 4, 242,581 Dec. 1980.
140. Advertisement in Lasers & Applications, July 1986, p20. (Thermopile).
141. A.F. Gibson, M.F. Kimmitt, A.C. Walker, Appl. Phys. Lett 17 (1970).
142. Shirakura et.al., U.S. Patent 4, 474, 468, Oct. 1984.
143. W.M. Steen , V. M. Weerasinghe " Surface Engineering with Laser", Metal Soc., May 1985.
144. A.L Rasmussen, U.S. Patent 3,622,245, Nov. 1971.
145. D.N. Mansell, U.S. Patent 3, 738, 168, June 1973.
146. G.T. Pinson, U.S. Patent 3, 939,706, Feb. 1976.
147. V.M. Weerasinghe and W.M. Steen, U.K. Patent Applic. 84 12832, Feb. 1984.
148. M.K. Satheeskumar, C.P.G. Vallabhan, J.Phys. E. Sci. Instru. Vol. 18,

1985, pp 434 - 436.

149. M.I. Cohen, J.P. Epperson, "Advance in Electronics and Electron Physics", Suppl. 4, Academic, 68, pp 139.

150. A. Yamada et.al. , Precision Machinery (Japan), Vol. 48, pp 36 - 41.

151. I. Miyamoto, H. Maruo and Y. Arata "Intensity Profile Measurement of Focussed CO_2 Laser Beam Using PMMA", ICALEO' 84, 1984, pp 313 - 320.

152. McGee J. D. "Visual Display of Infrared Laser Output on Thermographic Phosphor Screens", IEEE Journal of Quantum Electronics, QE-3: 31, Jan. 1967.

153. T.J. Bridges "Observation of a CO_2 Laser by a High-Resulotion Thermographic Screen, Ibid. QE-3: 168, April 1967.

154. L. H. Skolnik, B. Bendiw and E.F. Gross "Infrared Vidicon Technique for Measuring Thermal Lensing from Laser Windows, Applied Optics. 13: 726.

155. C. Courtney, W.M. Steen "Measurement of the Diameter of Laser Beam", Appl. Phys. Vol. 17, pp 303 - 307, 1978. (Thermal time rise).

156. M. A. Ikeda, A. Yamada and K. Shginohara "Beam Profile Measurement of High Power CO_2 Laser", ICALEO'83, 1983, pp 16 - 21.

157. J. M. Davis "Calorimeter with a Highly Reflective Surface for Measuring Intense Thermal Radiation", Appl. Optics, Vol. 10, No.8, Aug. 1971. (Thermocouple mirror).

158. R. C. Crafer and P.J. Oakley "Review of Continuous Wave CO_2 Laser Beam Measurement Techniques and the Development of a High Intensity Beam Scanner", The Br. W.I. Res. Report, Oct. 1981, p 165.

159. D.U. Chang "A C-Radius Technique for Determination of Beam Profiles", ICALEO' 83, 1983, pp 22 - 30.

160. D. Meyehofer "Measurement of Beam Profile of a CO_2 Laser", IEEE Journal of Quantum Electronics, QE-4: 969, Nov. 1968.

161. E.V. Locke, R. Hella and L. Westra " Performance of an Unstable Oscillator on a 30 kW CW Dynamic Laser, IEEE Journal of Quantum Electronics, Dec. 1971, QE-7: 581.

162. I. Miyamoto, H. Maruo and Y. Arata "Intensity Distribution Measurement of Focussed CO_2 Laser Beam Using Acrylic Plastics", 3rd CISFFEL, 1983.

163. P. J. Oakley "The Measurement of Laser Beam Parameters", Inter. Inst. of Welding Doc., 1983, IV - 350 - 83.

164. L. Li, R. Hibberd and W. M. Steen "In-process Laser Power Monitoring and Feedback Control", LIM-4, 1987, pp 165 - 175.

165. "News Report", Lasers & Applications, July 1986, p 88. (Partial back end mirror).

166. W.P. Juptner "On-line Diagnostic for Laser Surfacing", SPIE Vol. 957, 1988, pp76 -81.

167. Advertisement on Lasers & Applications, Nov. 1983. (Pyroelectric by Molectron).

168. Adv. Lasers & Applications, Oct. 1985. (Pyroelectric array laser beam analyser by Spiricon Co.).

169. Adv. at Lasers & Applications, p 72, July 1983. (Silicon detector rotating device by Photon Tech. Ltd.)

170 J. Edwards "A Wide Range Monitor System for Laser Beam Profiles", J. Phys. E., Vol. 10. 1977. (Diode array)

171. M.K. Satheeshkumar "Use of a Photo-acoustic Cell as a Scientific Laser Power Meter", J. Phys. E., Sci. Instrum., Vol. 18, 1985, pp 435 - 436.

172. Koren Yorem, Computer Control of Manufacturing System, McGraw-Hill Book Co. (U.S.A.), 1983.

173. P. Anthony et. al. "Multi-dimentional Laser Process system", Proc. Conf. SPIE. Vol. 668, 1986, U.S.A., pp 265 - 274.

174. K. Sibsyama "Sensory Characteristics of the 'Melcut-3DCM,", ICALEO' 85, U.S.A., 1985.

175. W.M. Steen and L. Li"Some View Points on Laser Automation and Process Quality Control", Proc. Conf. Laser Tech. in Industry, (Ed.) O.D.D. Soares, SPIE Vol. 925, Portugal, June 1988.

176. N. Willmott, Ph.D thesis, Imperial College of London University, 1989.

177. I. Decker, M. Hansmann and J. Ruge "Facilities of Quality Control in Laser Cutting", SPIE Vol. 650, 1986, pp 279 - 284.

178. F. Olsen, K. E. Anderson, N. Raben and F. B. Thomassen "Investigation in Methods for Adaptive Control of Laser Cutting", LAMP' 87, Osada, May 1987, pp 267 - 272.

179. B. Burg, E. Lamotte, L. Foulloy and B. Zavidovique "A Smart Laser Cutter", SPIE Vol. 650, 1986, pp 271 - 278.

180. H.W. Bieler, A. Gasser, G. Hertziger, E. W. Kreutz et.al. "Methods of Adaptive Control in Surface Processing with Laser Radiation", ECLAT'88, Oct. 1988, German Welding Society, pp 46 - 53.

181. I. Miyamoto, T. Ohie and H. Maruo "Fundamental Study of In-process Monitoring in Laser Cutting", 4th Int. Colloquium on Welding and

Melting by Elec. and Laser Beam, Sept. 1988, France.

182. B. Burg, E. Lamotte, L. Foulloy and B. Zavidovique "How a Man and a Laser Robot Can Learn Mutually", LIM-3, 1986, Paris, pp 89 - 96.

183. B. S. Yilbas, Z. Yilbas, R. Davies and F. Begh "Measurement of PLasma Transmittance in Relation to CO_2 Laser Cut Quality of Stainless Steel", Laser-5, April 1989.

184. B. S. Yilbas, Symp. on Metal Forming'87, Poland, 1987, pp 95 - 99.

185. H. Y. Zheng, D. Brookfield and W.M. Steen "The Use of Fibre Optics for In-process Monitoring of Laser Cutting Process", ICALEO' 89, Orlando, Oct. 1989.

186. H.Y. Zheng, D. Brookfield and W.M. Steen "Kerf Scanning System for Laser Cut Quality Control", submitted to the Journal of Lasers in Engineering, (Ed.) B. L. Mordike, 1989.

187. V.M. Weerasinghe, J. Kamalu, W.M. Steen and R.D. Hibberd "Acoustic Signals from Laser Back Reflections", Laser-88, 1988.

188. M. Hansmann and I. Decker "Direct Observation of Laser Cutting Process", SPIE Vol. 801, 1987.

189. R. Diemann "Use of an Acoustic Emission Analysis (AEA) in Quality Assurance of Laser Spot Welding", ibid.

190. Optics Guide 4 , Melles Griot , 1988, Chapter one, pp 11 - 17.

191. L. Foulloy "A Rule Based Decision System for Robotization of Metal Laser Cutting", IEEE Intern. Conf. on Robotics and Auto., St. Louis, U.S.A., Mar. 1985, pp 192 - 7.

192. L. Li, Ph.D Thesis, Imperial College of London University, 1989.

193. P. D. Austin "High power CO_2 Laser Beam Diagnosis and Control ", SPIE Vol. 668, 1986, Quebec City, Canada , pp 232 - 235.

194. RS Data sheet No. 8638, 1988.

195. Manual on the Use of Thermocouples in Temperature Measurement, American Society for Testing and Materials, 1981.

196. B.C. Kuo "Step Motors as Control Device", Theory and Applications of Step Motors, e.d. (B.C. Kuo), West Publishing Co., USA, 1974, pp 1-4.

197. BBC Microcomputer Manual.

198. J. R. Simonson, Engineering Heat Transfer, the MacMillan Press Ltd., London, 1975.

199. W.W. Duley "Excimer Laser Etching of Organic Polymers", Proc. LAMP'87, Japan, May 1987, pp 585 -593.

200. J. P. Bentley, Principles of Measurement Systems, Longman London,

1983 .

201. Ozisik M. Necati, Radiative Transfer, A Wiley-Interscience Publication, 1973, pp 69-75.

202. J. Krautkramer and H. Krautkramer, Ultrasonic Testing of Materials, 2nd edn., Springer-Verlag London, 1977, Section 8.2.

203. S. G. Lipson and H. Lipson, Optical Physics, Cambridge University Press, 2nd edn., Cambridge 1981, section 4.5.

204. P. Loosen , L. Bakowsky, G. Herziger and F. Ruhl "Diagnostic of High Power CO_2 Lasers", Proc. Laser 83, Germany, 1984, pp 247-253.

205. L. Li, Internal Report, Liverpool University, 1990.

206. J.M. Coulson, Chemical Engineering, Vol.1, 3rd edn..

207. B.S. Massey, Mechanics of Fluid, 5th Edn., Van Nostrand Reinhold (U.K.) Co. Ltd., pp 291-292.

208. James McD. Baxter Brown, INtroductory Solid Mechanics, Section 15.

209. Max Garbuny, Optical Physics, Academic Press, New York, 1965.

210. Herbert, P. Neff. JR., Basic Electromagnetic Field, pp326.

211. C.J. Duthler "Explanation of laser-damage cone-shaped surface pits", Appl. Phys. Lett, Vol.24, No. 1, Jan. 1974.

212. R.M. White "Elastic Wave Generation by Electron Bombardment or Electromagnetic Wave Absorption", Communications, Oct. 1962.

213. P. Loosen, A. Drenker et.al. "Diagnostics of High Power Laser Beam", SPIE Vol.1024, Hamburg, 1988, pp26-34.

214. Shono S., Matsumoto O., and Beppu S. "Cutting of Thick Steel Plates by 5 kW CO Laser Beam ", ICALEO' 89, Orlando, U.S.A., Oct. 1989, pp 130 -139.

PUBLICATIONS

1. Zheng H. Y., Steen W. M. and Brookfield D. "Effects of Gas Composition on Laser Cutting Performance", Laser-5 conference, London, April 1989.

2. Zheng H.Y., Brookfield D. and Steen W.M. "The Use of Fibre Optics in In-process Monitoring of Laser Cutting Process", ICALEO'89, Orlando, U.S.A., Oct. 15 -20, 1989.

3. Zheng H.Y., Brookfield D. and Steen W.M. "An Experimental Study of the Relationship between In-process Signals and Cut Quality in Gas Assisted Laser Cutting", International Conf. of Optical Science and Engineering, Hague, Holland, March 1990.

4. Zheng H.Y., Brookfield D. and Steen W.M. "Kerf Scanning System for In-process Laser Cut Quality Control ", submitted for publication in the Journal of Lasers in Materials Engineering, ed. by B. L. Mordike, FRG.

5. U.K. patent application "Kerf Scanning System", No. 89175020, 1989.

APPENDIX A

Mr. N. Willmott and J. Gabzdyl cooperated with the author in producing this program.

APPENDIX A

```
10REM*********************************
20REM                                  *
30REM  NOZZLE ALIGNMENT WITH           *
40REM      THERMOCOUPLES               *
50REM                                  *
60REM  H. ZHENG, N. WILLMOTT           *
70REM                                  *
80REM           J. GABZDYL             *
90REM                                  *
100REM********************************
110:
120MODE0
130:
140REM********************************
150REM*                                *
160REM*     USER              PORT     *
170REM* BIT                   FUNCTION *
180REM*  2(2)                   XCLOCK *
190REM*  3(4)                   XDRCTN *
200REM*  4(8)                   YCLOCK *
210REM*  5(16)                  YDRCTN *
260REM********************************
270:
280:
290PROCconfig
300:
310REM:Thermocouple Threshold Value
320 TH=7000
330:
340PROCscanX
350:
360PROCscanY
370PRINT"The Centre of the Nozzle Has Been Found"
380:
390END
400:
410:
420:
470DEFPROCconfig
480?&FE62=&FF
490?U%=&FE60
500?U%=0
510ENDPROC
520:
530*
540DEFPROCscanX
550PROCfind
560A=N
570M=A: PROCretX
580PROCfind
590B=N
600C=(A+B)/2
610M=C:PROCretX
620ENDPROC
630:
640DEFPROCfind
650N=0
660PROCincX
670N=N+1
680T%=ADVAL(1)
```

```
690IF T%>TH GOTO 710
700GOTO 660
710ENDPROC
720:
730DEFPROCincX
740PRINT"X";
750FOR O=1 TO 8
760?U%=?U%EOR2
765REM SOFTWARE CLOCK 10 KHZ
766REM ONTIME 10MS
770FORQ=1TO 100:NEXTQ
775REM OFFTIME 40MS
780?U%=?U%EOR2
790FORQ=1 TO 400:NEXTQ
800NEXTO
810ENDPROC
820:
830:
840DEFPROCretX
850?U%=?U%EOR4
860FORI%=1 TO M
870PROCincX
880NEXTI%
890ENDPROC
900:
910DEFPROCscanY
920PROCfindY
930A=N
940M=A: PROCretY
950PROCfindY
960B=N
965PRINT"B=",B
970C=(A+B)/2
980M=C:PROCretY
990ENDPROC
1000DEFPROCfindY
1010N=0
1020PROCincY
1030N=N+1
1040T%=ADVAL(1)
1050IF T%> TH GOTO 1070
1060GOTO 1020
1070ENDPROC
1080:
1090DEFPROCincY
1100PRINT"Y";
1110FOR S=1TO 8
1120?U%=?U%EOR8
1130FORQ=1 TO 100:NEXTQ
1140?U%=?U%EOR8
1150FOR Q=1 TO 400:NEXTQ
1160NEXTS
1170ENDPROC
1180:
1190:
1200PROCretY
1210?U%=?U%EOR16
1220FOR I%=1 TO M
1230PROCincY
1240NEXTI%
1250ENDPROC
1260:
1270:
```

APPENDIX B

THE BOC MODEL 901 2 kW CO_2 GAS LASER

A CO_2 gas laser generally consists of an open ended gas discharge tube with a fully reflecting mirror at one end and a partially transmitted mirror at the other through which the output light beam emerges. A gas mixture of CO_2, N_2 and He usually flows through the discharge tube. Energy is supplied to the gas mixture by means of a DC electric discharge which is established in the laser tube.

The BOC 901 fast axial flow CO_2 laser was manufactured by Control Laser Ltd., providing a CW maximum power of 2 kW. The laser uses as its active medium a mixture of CO_2, N_2 and He with a ratio of around 1:1:8 (5 -10% : 10 -14% : 75 -85%). The molecule vibrations of carbon dioxide act as the lasing mechanism giving a laser beam with a frequency of 10.6 μm. The nitrogen is active in the excitation process to increase the excitation efficiency and helium which comprises about three quarters of the total gas mixture acts as an internal heat sink. This gas mixture is recirculated to reduce gas consumption by the laser.

The laser head carries four electric discharge tubes connected optically in series to effectively provide one long tube which is then folded in the middle by means of two mirrors in the form of a 'roof-top' prism, thus making the laser head shorter (Fig. B-1 and B-2). The four cathodes of the tubes are earthed and fixed to a central cathode box which is water cooled. This cathode box also acts as a gas manifold through which the laser gas from the four tubes is drawn. The gas in the laser tubes is heated by the discharge current and in order to remove this heat the gas itself is drawn rapidly from the laser tubes through the cathode manifold over the central heat exchanger by means of a large displacement Roots type blowers. The gas outlet of the blower is manifolded into two streams of gas and is at a higher pressure of 110 - 125 mmHg (Torr). The work done by the blower heats the gas again and this heat is removed by two further heat exchangers at either end of the laser head. These two end heat

exchangers are in boxes which again split the gas streams into two to supply each of the four discharge tubes. The cooled gas is then fed over the anodes and through adjustable annular gaps into four discharge tubes. The pressure difference across these annular gaps is used to generate the turbulent flow region to stabilise the electrical discharges, there is also a slight cooling effect due to the rapid expansion of the gas.

Inside the laser tubes, the electrical discharge tends to break up the CO_2 molecules as below:

$$CO_2 + E \leftrightarrow CO + O + E \quad \text{(E is excess energy)}$$

and

$$O + O \leftrightarrow O_2$$

$$O + N_2 \leftrightarrow N_2O$$

$$O + N_2O \leftrightarrow 2NO$$

Thus the discharge region generates CO, O2 and oxides of nitrogen. These gases tend to inhibit laser action and so a small proportion of the recycling gas flow is drawn off by vacuum pump for regeneration and recirculation. The gas drawn off by the vacuum pump is passed through five stages of oil filtration and allowed to flow through two reaction chambers in series. These reaction chambers are ovens, each containing a special catalyst heated to a particular temperature. The first reaction chamber causes removal of the oxides of nitrogen and the second converts the CO to CO_2 using the oxygen generated in the first process. After passing through these two chambers the gas is passed through a silica gel trap and a dust filter and then admitted to the laser by means of a solenoid valve and needle values.

Recirculating and regenerating does not however, maintain a sufficiently pure gas mixture indefinitely and it is necessary to introduce new and unused gas at intervals whilst dumping some of the used gas to atmosphere. It is therefore arranged for a 'flip-flop' formed by two timers, to allow variably timed amounts of new gas or regenerated gas back into the laser. Thus the recirculation rate can be altered. The new gas, when

required, is fed into the system by means of three regulators and choked orifices, these being adjusted to give the optimum gas mixtures.

The laser light emitted from the output window is allowed to strike a 45^0 mirror and is thus deflected into the water cooled calorimeter, which acts as a dump. A metered flow of water cools this cone and the difference between water inlet and outlet temperature is measured by means of thermocouples. The thermocouples output is displayed directly as watts of laser power by the digital voltmeter.

The laser beam can then be directed to the workstation through a series gold coated copper mirrors when the laser shutter is open; otherwise the laser beam is directed to the calorimeter. A 0.95 mW He-Ne laser is used for assisting the laser beam alignment. The He-Ne laser has a beam of 0.633 μm in wavelength which is visible red light, and the beam diameter is around 0.7 mm.

Figures B-1 and B-2 are the schematic diagrams of the laser.

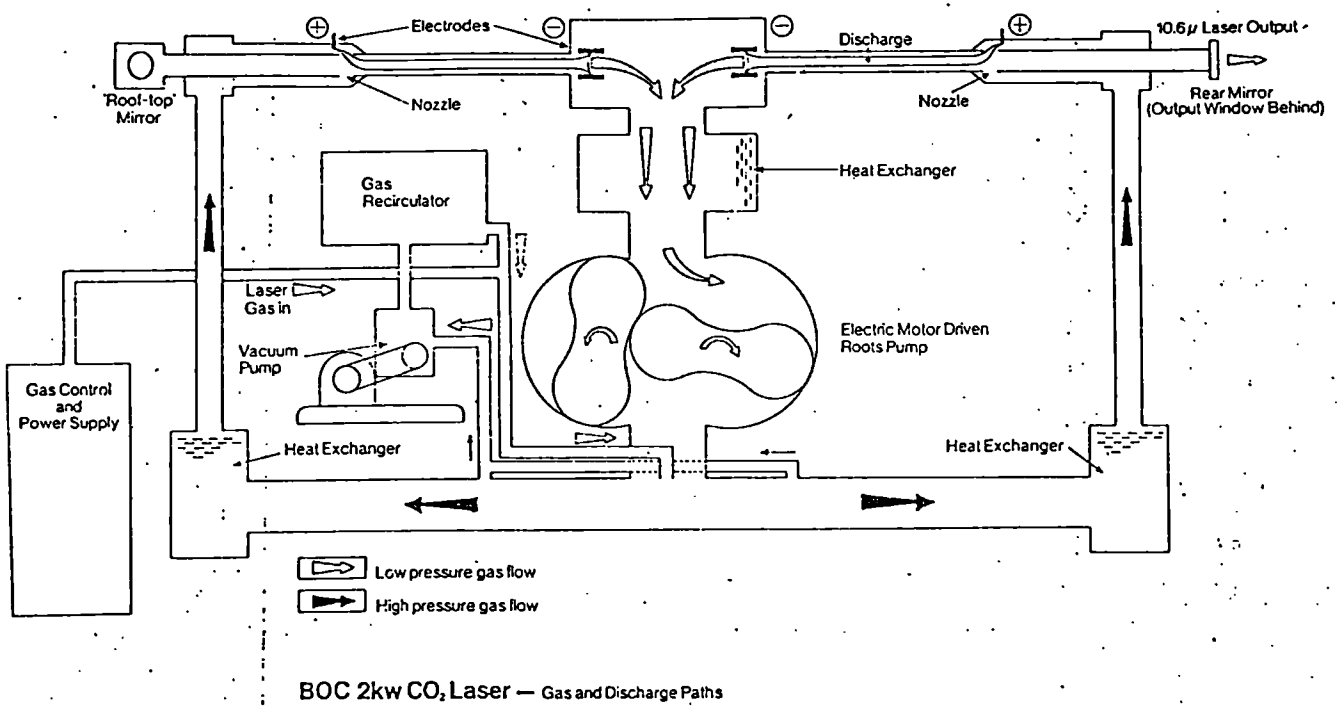


Fig. B-1. Laser Head Primary Gas Circuit.

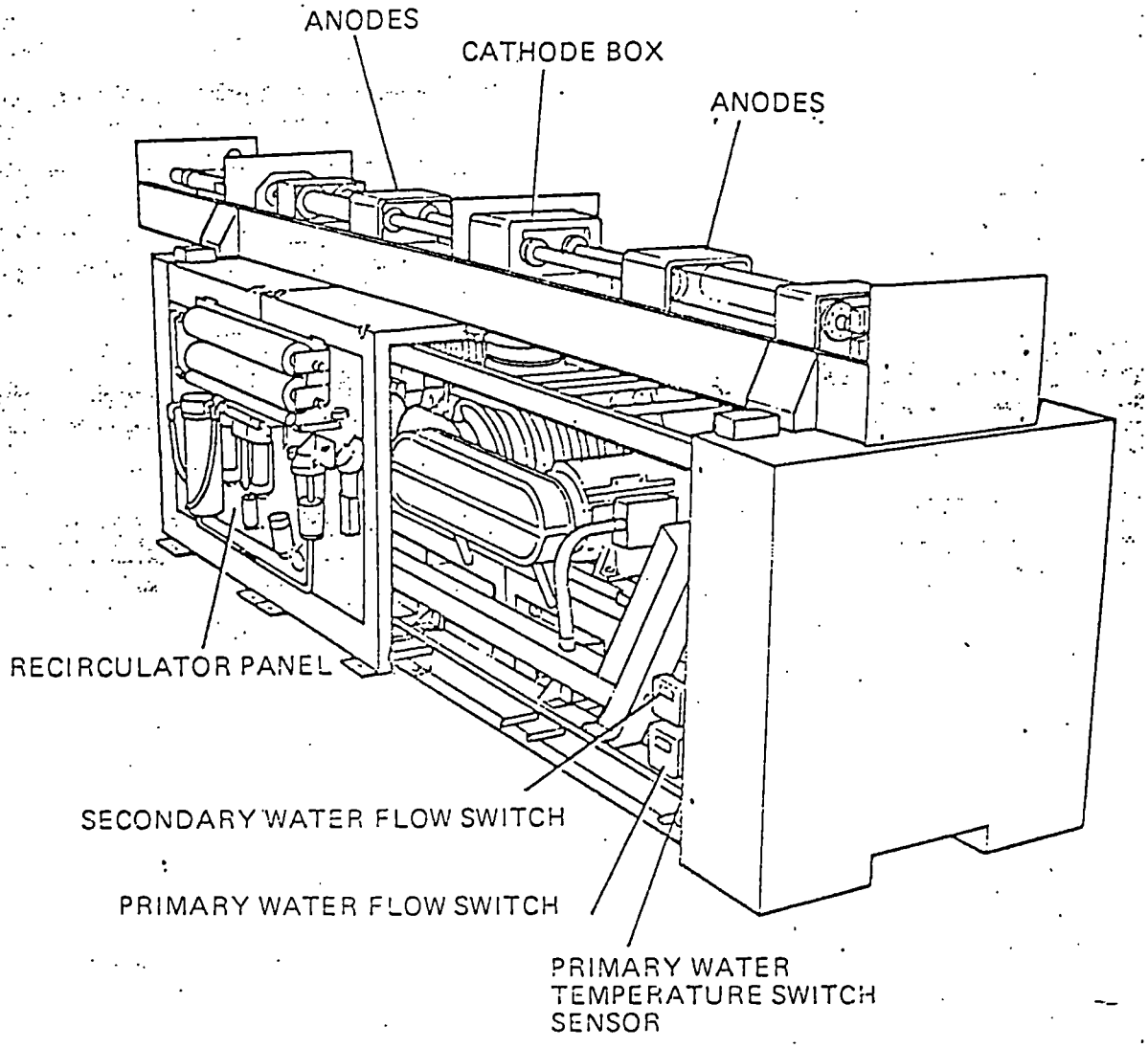


Fig. B-2. View of laser head with cover removed.

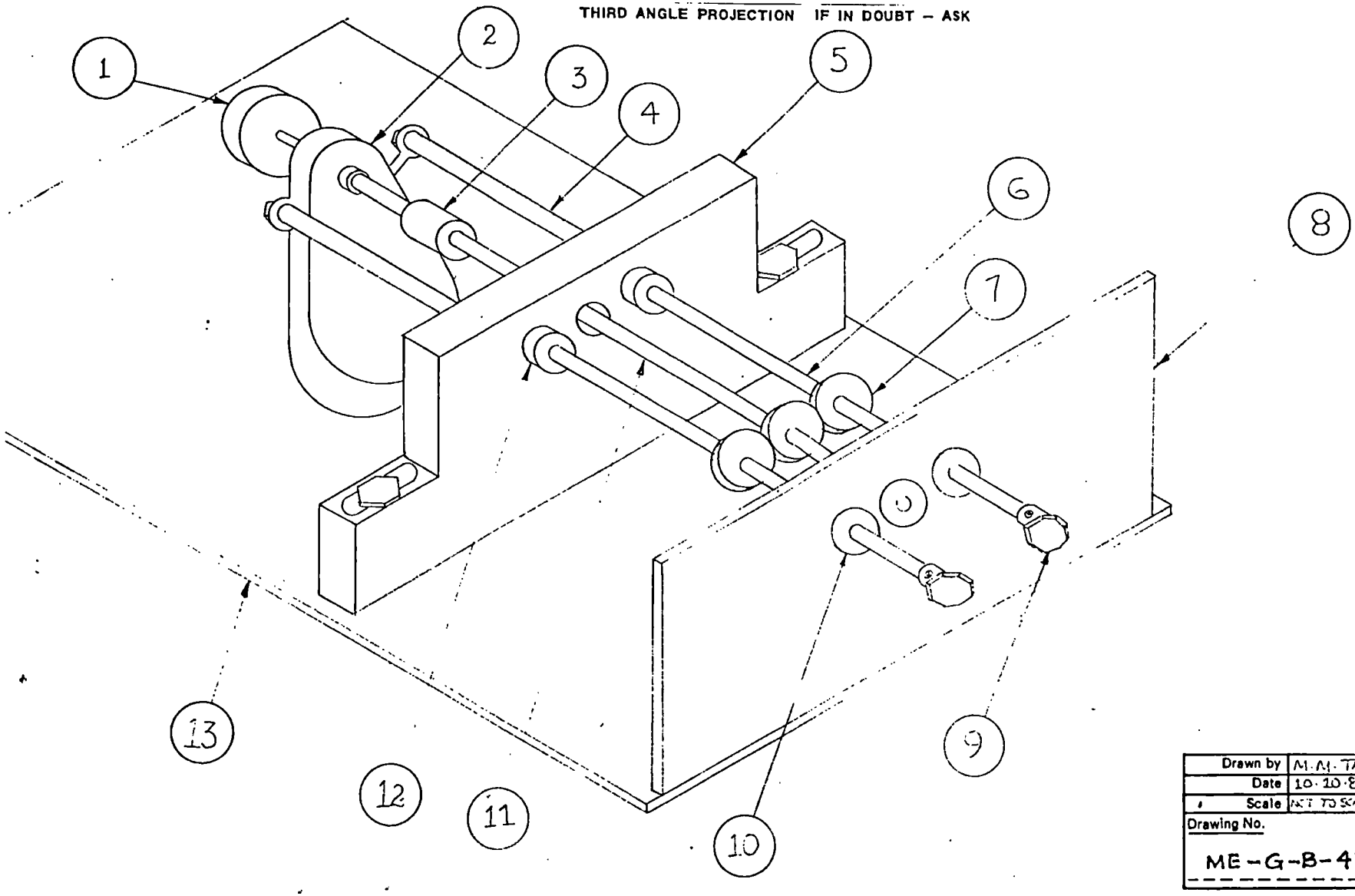
APPENDIX C

MECHANICAL DESIGN OF THE TWO-POLYGON SYSTEM

The isometric view of the assembly drawing of the two-octagon system is given in the drawings ME-G-B-413 & 413/1. The machining details of individual parts including the octagon, the gear and the box covers are given in the drawings ME-G-B-413/2 - 4.

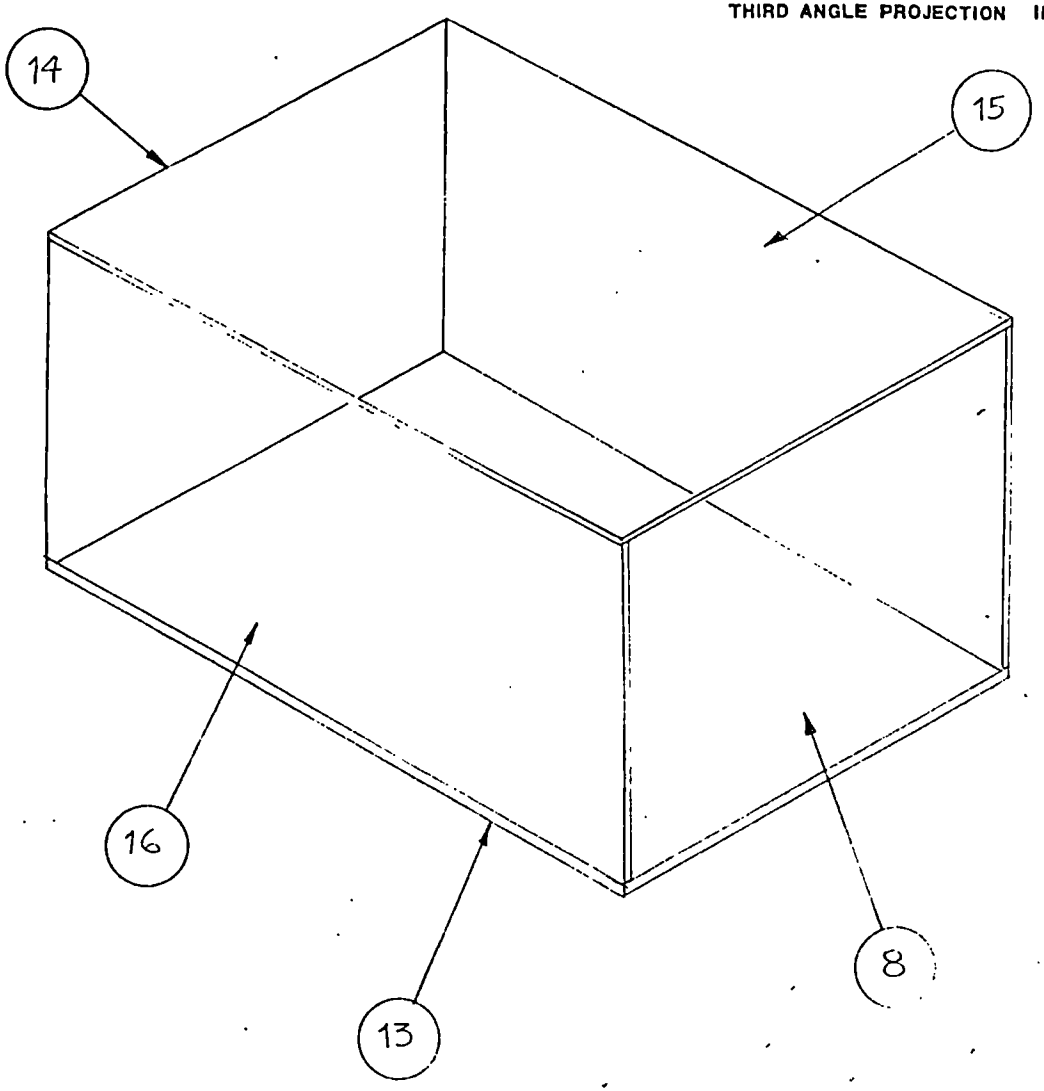
Miss M. M. Tan, a year III student, under the supervision of the author, did the mechanical drawings.

THIRD ANGLE PROJECTION IF IN DOUBT – ASK



Drawn by	M.M.TAN
Date	10.10.89
Scale	NOT TO SCALE
Drawing No.	ME-G-B-413

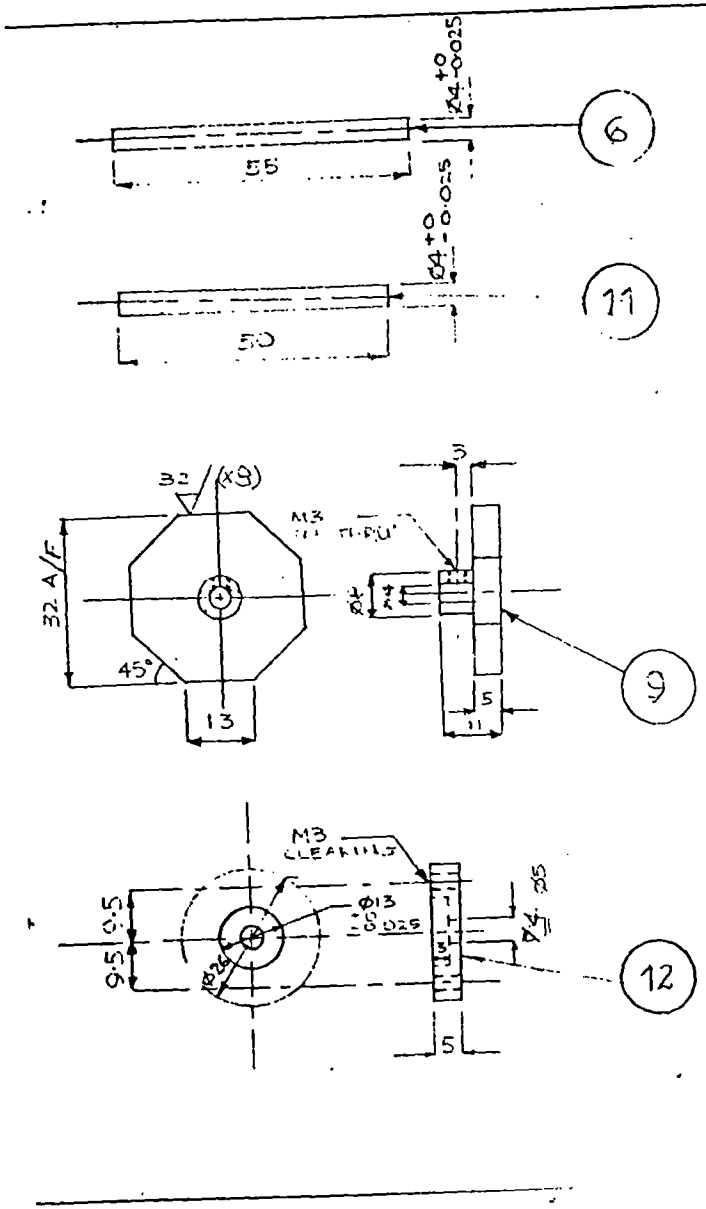
THIRD ANGLE PROJECTION IF IN DOUBT – ASK

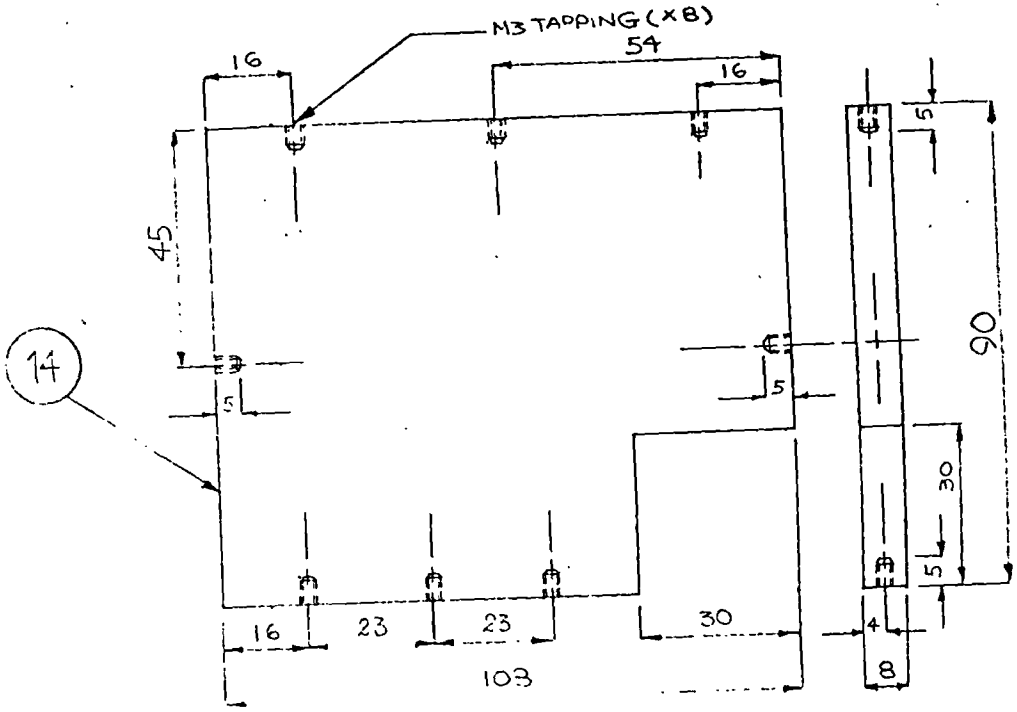


Drawn by	M M.TAN
Date	10·10·89
Scale	NOT TO SCALE
Drawing No.	ME–G–B–413/1

16	SIDE COVER	PSI	PERSPEX	2	
15	TOP COVER	PER	PERSPEX	1	
14	BACK COVER	AL	ALUMINIUM	1	
13	BASE	AL	ALUMINIUM	1	
12	SHAFT HOLDER	MS	MILD STEEL	2	
11	SHAFT 2	MS	MILD STEEL	1	
10	BALL BEARINGS			5	
9	OCTAGON	B	BRASS	2	
8	FRONT COVER	AL	ALUMINIUM	1	
7	GEAR			3	
6	SHAFT 1	MS	MILD STEEL	2	
5	SUPPORT PLATE	AL	ALUMINIUM	1	
4	MOUNTING BEE			2	
3	SHAFT COUPLING			1	
2	GEARBOX			1	
1	MOTOR			1	

THIRD ANGLE PROJECTION IF IN DOUBT – ASK

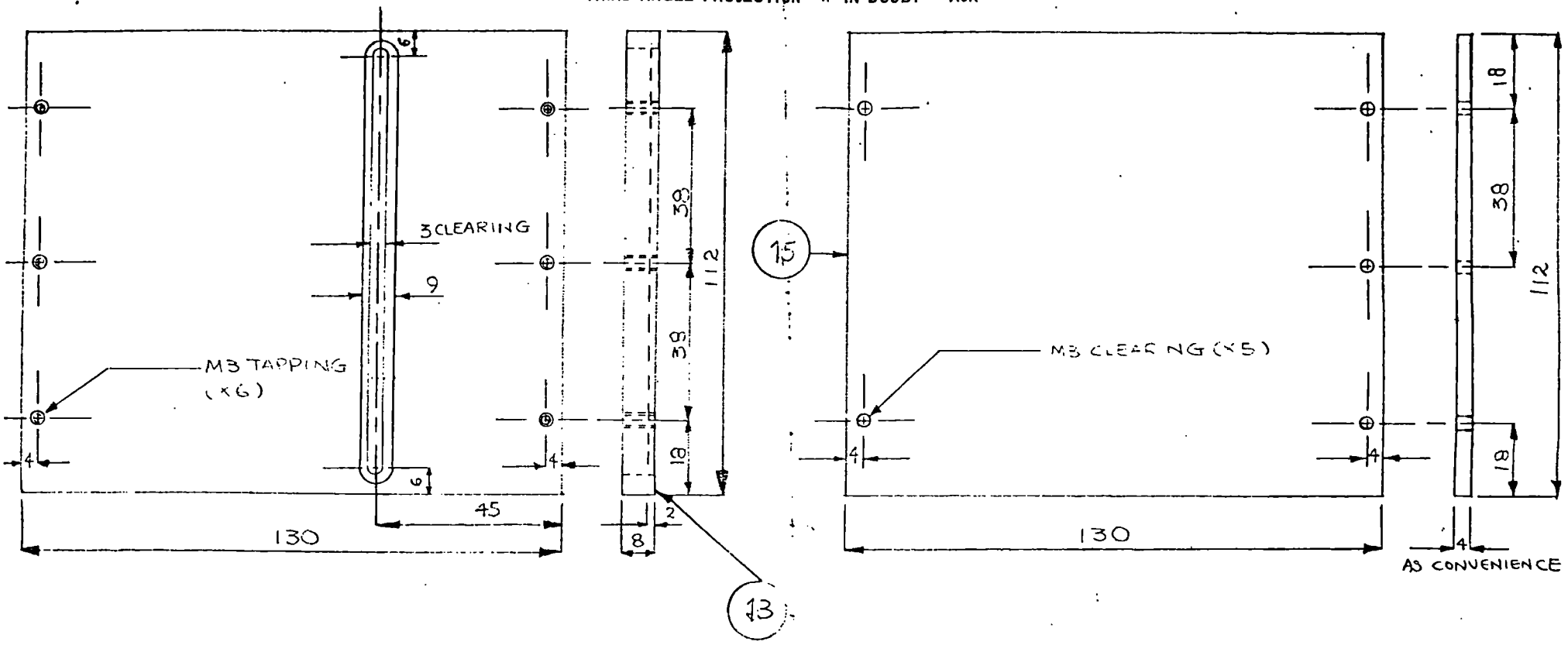


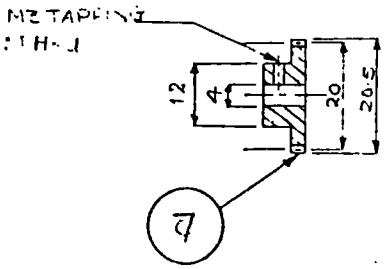


REMARKS	
Approved by	
Date	27-9-89
Drawn by	M.M.TAN
Date	
Scale	1 : 1
Drawing No.	ME-G-B-413/2

14	BACK COVER	AL	ALUMINIUM	1	
12	SHAFT HOLDER	M.S	MILD STEEL	2	
9	OCTAGON	B	BRASS	2	$\sqrt{}$ ON 8 SIDES
11	SHAFT 2	M.S	MILD STEEL	1	
6	SHAFT 1	M.S	MILD STEEL	2	

THIRD ANGLE PROJECTION IF IN DOUBT – ASK

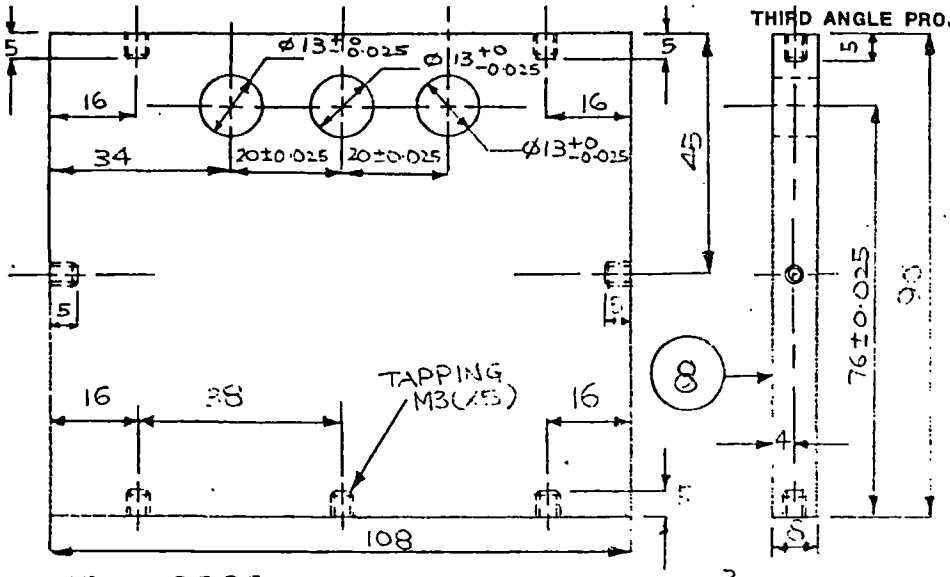


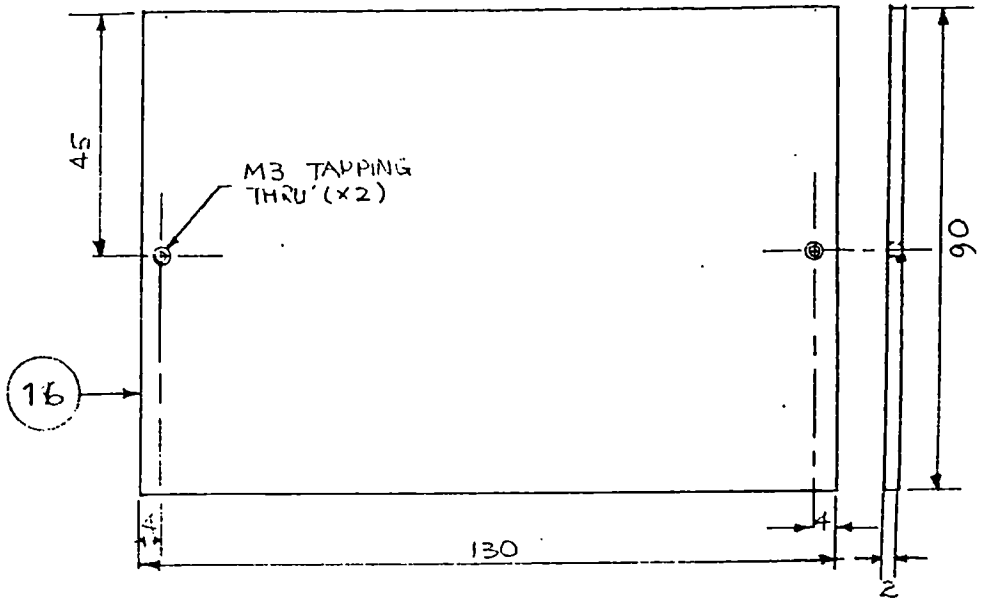


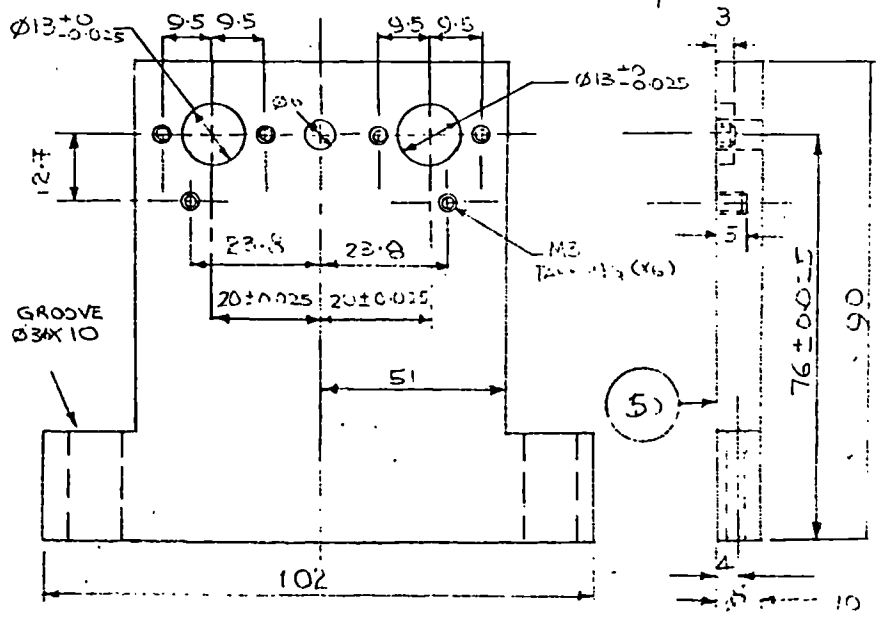
Drawn by	M.M.TAN
Date	27·9·89
Scale	1 : 1
Drawing No.	ME-G-B-413/3

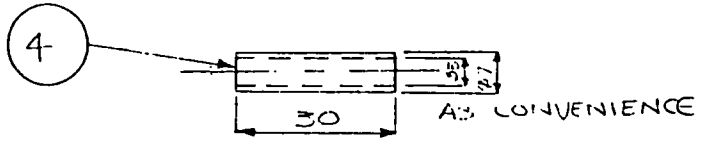
7	GLAR			3	TAP M3 ONLY
15	TOP COVER	PERSPEX	PERSPEX	1	
13	BASE	AL	ALUMINIUM	1	

THIRD ANGLE PROJECTION IF IN DOUBT – ASK









4	HOLLOW TUBE	AL	ALUMINIUM	2	
16	SIDE COVER		PERSPEX	2	
5	SUPPORT PLATE	AL	ALUMINIUM	1	
8	FRONT COVER	AL	ALUMINIUM	1	

Drawn by	M·M·TAN
Date	27·9·89
Scale	1 : 1
Drawing No.	ME-G-B-413/4